Western Australia School of Mines

Department of Exploration Geophysics

Analysis of the effect of CO_2 saturation on elastic properties of rocks using borehole seismic data from pilot carbon storage projects

Mohammed Saif Salim Al Hosni

This thesis is presented for the Degree of

Doctor of Philosophy

of

Curtin University

May 2016

To my parents, my wife and my brothers and sisters.

Declaration

"To the best of my knowledge and belief this thesis contains no material previously published by any other person except where due acknowledgment has been made. This thesis contains no material which has been accepted for the award of any other degree or diploma in any university."

Signature: 

Date: 15/05/2016

Abstract

Quantitative assessment of time-lapse seismic for CO_2 saturation distribution in the subsurface requires a rock physics model that predicts the changes in the elastic properties corresponding to the variations in the reservoir properties. However, the applicability of theoretical rock physics models (e.g., Gassmann's equation) at the seismic scale requires validation with field data. For this, high-resolution *in situ* seismic data can be used.

This thesis presents several approaches to investigate the applicability of theoretical rock physics models for time-lapse seismic analysis by performing quantitative and qualitative analysis of real and synthetic time-lapse borehole seismic for pilot CO_2 sequestration projects. First, a comprehensive analysis of the pre-existing data set for the Frio pilot CO_2 injection project is performed. For this project, a site-specific rock physics model is not yet established. However, the data shows that the high-resolution time-lapse seismic (e.g., vertical seismic profile and crosswell) integrated with other information (e.g., core and well log) can be used to constrain the velocity–saturation relation with considerable certainty.

Second, a tailored time-lapse VSP processing sequence is developed to obtain quantitative results for the CO_2 induced changes in the reservoir using three independent parameters (i.e., transit time delays, first arrivals amplitudes and reflections amplitudes). A modelling study is conducted to confirm the obtained elastic changes and investigate the effect of seismic resolution and gas plume geometry on the obtained geophysical parameters. The results show an agreement between the modelling and the field data for all the three independent parameters, thus, confirming the obtained velocity changes. Moreover, the effects of the plume size and seismic resolution are found to be pronounced on the reflection amplitude. Additionally, the seismic modelling allowed the approximate size of the CO_2 plume to be inferred using reflection behaviour from VSP. Next, a crosswell time-lapse traveltime tomography is performed to obtain a high-resolution P-wave and S-wave velocity changes upon CO_2 injection. The results show a substantial velocity reduction for both P-wave and S-wave at the injection well.

Subsequently, using the results from petrophysical data and time-lapse VSP seismic, the applicability of Gassmann's poroelasticity theory is investigated for the

Frio project. The results show a significant discrepancy between the rock physics model predictions derived using Gassmann's equation and the field data. Investigating the input parameters, uncertainty in CO_2 saturation and assumptions involved in Gassmann's poroelasticity theory suggest that invoking rock frame changes possibly induced by CO_2 injection could explain this discrepancy.

The S-wave velocities changes that accompany the large P-wave velocities from crosswell seismic is utilized to investigate the discrepancy observed. Thus, supported by the crosswell S-wave velocity changes a methodology to estimate changes in the rock frame is proposed. The rock physics model is defined based on rock microstructure diagnostic models which have physically meaningful parameters that can be updated based on the magnitude of the frame weakening obtained from the field data. Results show that rock frame weakening could be related to minute changes in grain contact cement. These changes could be induced by several mechanisms, with CO_2-brine-rock interaction (i.e., dissolution of rock frame forming minerals) as a possible cause. The obtained velocity-saturation relation could describe the field time-lapse velocity changes for both VSP and crosswell using a patchy saturation model.

Last, the Otway 2C project analysis is performed for a set of offset VSP data simulated in a full-waveform 3D time-lapse seismic model by incorporating the learnings from the Frio project. The sensitivity analysis reveals that time-lapse changes could be obtained using offset VSP data for the injection of 15,000 tons of CO_2/CH_4. The results show that the gas plume is detectable using transit time delays, first arrivals amplitudes, and reflections amplitudes. It is found that constraining the velocity-saturation relation using the transit time delays is possible if the receivers are at the injection well. However, the uncertainty in the measurement compared to the expected signal limit the interpretation of the velocity changes. Comparison between the Frio project and Otway 2C shows how the magnitude of the heterogeneity (e.g., P-wave velocity changes, thickness of the gas plume) in subsurface and the survey geometry control our ability to obtain quantitative geophysical data for rock physics modelling.

In summary, current time-lapse monitoring issues for CO_2 sequestrations, namely, quantitative and qualitative interpretation using real and synthetic borehole seismic data, rock physics modelling, CO_2-brine-rock interaction effects on the rock frame have been investigated. This research will benefit current and future time-lapse seismic monitoring of CO_2 sequestrations.

Acknowledgments

First, I would like to thanks my family for their patient during my studies, my mother my father and my wife.

I gratefully acknowledge Petroleum Development Oman (PDO) for granting me the scholarship of my PhD.

I would like to convey my sincere thanks to my supervisor Prof. Boris Gurevich for his guidance, comments, advice and outstanding supervision. I greatly benefited from his experience and scientific insights throughout my PhD.

I would like to thank my co-supervisor Assoc. Prof. Roman Pevzner for the support in the VSP processing and analysis. His input into my research results was invaluable, especially in the extraction of quantitative measurements from time-lapse VSP data.

I greatly thank Dr. Stephanie Vialle for her guidance and help with the understanding of the geochemical reactions and their possible effect on this research and valuable comments and review of my work.

Throughout my PhD studies I got support and valuable knowledge through discussions with my colleagues and staff. Thanks to Dr. Eva Caspari for her comments on the rock physics analysis, Dr. Stanislav Glubokovskikh for providing the synthetic data for the Otway research. Dr Qiaomu Qi for discussion on the velocity-saturation relation analysis giving great comments and suggestions to improve my work.

I wish to acknowledge the funding provided by the Commonwealth of Australia through its CRC Program to support CO2CRC research and by the sponsors of the Curtin Reservoir Geophysics Consortium (CRGC). I extend my thanks to Lawrence Berkeley National Laboratory (LBNL) for providing the data for this study with special thanks to Mr. Tom Daley for his support and collaboration in the analysis of the Frio project data.

Finally, I would like to thanks all my friends and colleagues.

List of publications

Journals

Al Hosni, Mohammed, Eva Caspari, Roman Pevzner, Thomas M. Daley, and Boris Gurevich, 2016, "Case History: Using time-lapse vertical seismic profiling data to constrain velocity–saturation relations: the Frio brine pilot CO_2 injection.": Geophysical Prospecting **64**, no. 4: 987-1000.

Al Hosni, M., S. Vialle, B. Gurevich, and T. M. Daley, 2016, Estimation of rock frame weakening using time-lapse crosswell: Frio brine pilot project: Geophysics, **(submitted)**.

Extended abstracts

Al Hosni, M., B. Gurevich, S. Vialle, and T. M. Daley, 2015c, Effect of CO_2 on Rock Properties: Frio Crosswell Case Study: Third EAGE Workshop on Rock Physics, EAGE. doi: 10.3997/2214-4609.201414393.

Al Hosni, M., B. Gurevich, and T. M. Daley, 2015b, Effect of CO_2 on bulk and shear moduli of rocks: Frio crosswell case study: 3rd International Workshop on Rock Physics.

Al Hosni, M., E. Caspari, R. Pevzner, T. M. Daley, and B. Gurevich, 2015a, Using time-lapse VSP data to constrain velocity-saturation relations: ASEG Extended Abstracts, **2015**, no. 1,1-4. doi:10.1071/ASEG2015ab153.

Contents

Nomenclature

Glossary of abbreviations

CCS Carbon dioxide capture and storage

CNC Constant-cement model

COC Contact-cement model

GH Gassmann-Hill

GW Gassmann-Wood

VSP Vertical seismic profiling

VSR Velocity-saturation relation

Indices, Sub- and Superscripts

CNC constant-cement model

COC contact-cement model

f pore fluid

Symbols

μ shear modulus

K bulk modulus

V_P compressional wave velocity

V_S shear wave velocity

CHAPTER 1. INTRODUCTION

1.1 CO_2 SEQUESTRATION REVIEW

In the past 15 years' carbon dioxide capture and storage (CCS) has been the focus of substantial research interest and is gaining further momentum currently as the world demands further action to reduce greenhouse gas emissions. Several CO_2 storage options are possible in the subsurface. These options are CO_2 injection into brine aquifers (offshore or onshore), using CO_2 for enhanced-oil-recovery (EOR), injection into depleted oil and gas reservoir and enhanced recovery of coal bed methane (Benson and Cole 2008).

The sequestration of CO_2 into brine aquifers and depleted hydrocarbon reservoirs has been recognized as a viable option in term of storage capacity, abundance and technological capabilities (Bachu and Adams 2003). Currently, there are several sequestration projects which are either in commercial operation (large scale) or experimental (small scale) such as Sleipner, In Salah, Ketzin, Otway, Frio and Nagaoka (Michael et al. 2010). The first large-scale commercial CO_2 sequestration project started in 1996 in the Sleipner field in the North Sea offshore Norway. The CO_2 was injected in the Utsira sand which is a brine aquifer at a depth of about 1000 m (Arts et al. 2004). The injected CO_2 volume was so significant that the CO_2 plume was easily detectable using surface seismic. However, quantitative interpretation of seismic data is still an ongoing challenge, especially for characterisation of thin CO_2 layers (Chadwick et al. 2010).

CO_2 injected into the subsurface requires a verification strategy to be certain that it remains trapped in the subsurface within the desired geologic formation and does not migrate into overlying layers, fresh water aquifers or into the atmosphere (Benson and Cole 2008, Michael et al. 2010, Wildenborg et al. 2013). Consequently, detailed geological characterization, CO_2 flow simulations and various modelling aspects (e.g., geophysical, geochemical, geomechanical) are implemented ahead of actual injection in any proposed storage site (Xu, Apps, and Pruess 2004, Ghomian, Pope, and Sepehrnoori 2008, Hosseini et al. 2012, Delshad et al. 2013, Klein et al. 2013, Hovorka

et al. 2001). Then, the injection is only performed if the modelling results provided an assurance of CO_2 containment within the desired formation.

Such studies are based on geological and geophysical information about the subsurface, which are always incomplete due to various inherent uncertainties (e.g., geological complexity, dynamic versus static model, fluid flow properties, tools resolutions and inversion) (Wildenborg et al. 2013). Thus, the model must be refined after the actual injection is performed. To achieve this, a monitoring campaign which account for the actual CO_2 distribution in space and time during and after the injection is needed. Monitoring technologies may include downhole pressure and temperature, well logs, geochemical sampling and tracer's injections and active time-lapse seismic methods. In particular, time-lapse seismic has been identified as an effective tool for such requirements as it has the potential to track CO_2 plume extent over time (Wildenborg et al. 2013, Michael et al. 2010, Lumley 2010).

Demonstration or experimental small-scale CCS projects are aimed at investigating the aspects of CO_2 injection and monitoring in a controlled environment (Kazemeini, Juhlin, and Fomel 2010, Hovorka, Sakurai, et al. 2006, Kikuta et al. 2005). This comes from the fact that a firm scientific knowledge needs to be established regarding the coupled mechanisms in the subsurface such as geochemical, hydrological and geomechanical processes (Benson and Cole 2008), using various monitoring methods. Moreover, such small-scale projects could be viewed as an analogue to CO_2 leakage scenarios. Among these experimental projects, the ones involving the injection of CO_2 into brine aquifers such as the Frio brine pilot, and recently the Otway 2C CO_2 injection projects, which are utilized in this research, present a valuable opportunity for time-lapse monitoring research. This is because of the absence of the complexity of hydrocarbon fluids that may have properties similar to those of the injected CO_2 in the reservoir, which could mask the CO_2 effect on the elastic properties and further complicate the monitoring campaign (Lumley et al. 2008).

In the last decade, time-lapse seismic was used successfully to detect CO_2 plumes extent and saturation distribution using both surface seismic, Vertical Seismic Profile (VSP) and crosswell seismic (Lüth et al. 2011, Arts et al. 2004, Daley et al. 2008, Ajo-Franklin et al. 2013, Saito et al. 2006). However, quantitative interpertation of time-lapse seismic data is still challenging (Lumley et al. 2008).

1.2 MOTIVATION

Interpretation of the time-lapse seismic data is often qualitative and the use of time-lapse data to estimate the change in the spatial distribution of saturation and pressure, so-called quantitative interpretation, remains a challenge (Lumley 2010).

A common practice to quantitatively relate observed time-lapse seismic changes to reservoir properties is using a rock physics model that predicts the changes in the elastic properties corresponding to the changes in the reservoir properties (Johansen et al. 2013). A conventional way is to use Gassmann poroelasticity theory (Gassmann 1951) to calculate fluid substitution effects assuming a uniform fluid saturation (i.e., low-frequency range) (Smith, Sondergeld, and Rai 2003, Han and Batzle 2004). However, at the seismic scale the applicability of the Gassmann equation (Gassmann 1951) is still not well understood and may require validation using *in situ* field data (Han and Batzle 2004).

This is because of the many assumptions involved in Gassmann's poroelasticity theory such as the homogeneity of the medium at both microscopic and macroscopic scale and micro-scale isotropy of both the dry rock frame and the fluids. These assumptions are not likely to hold for almost any sedimentary rocks (Brown and Korringa 1975). In other words, effective rock properties calculated at one scale (e.g., from well logs) using Gassmann's poroelasticity theory (Gassmann 1951, Biot 1956) might not be applicable at other seismic scales (e.g., surface seismic, VSP and crosswell). This is because at the seismic scale the seismic wave samples larger volumes of rocks compared to well logs. For this, a verification of the applicability of Gassmann's equations using in situ field data is in order. This problem arises in many time-lapse monitoring projects such as enhanced oil recovery (EOR), production monitoring (Yang et al. 2014, Lumley 2001) and more recently CO_2 sequestration monitoring (Arts et al. 2004, Ivanova et al. 2012, Daley et al. 2008).

Another assumption of Gassmann's poroelasticity theory (Gassmann 1951, Biot 1956) is that the rock frame properties do not change with a change of the pore fluid (Mavko, Mukerji, and Dvorkin 2009). However, recently many studies have discussed the geochemical interactions upon CO_2 injection that may result in changes in the rock frame strength in both carbonate and sandstones (e.g., Vanorio, Nur, and Ebert 2011, Marbler et al. 2013, Le Guen et al. 2007, Hangx, Spiers, and Peach 2010, Adam et al.

2015) depneding on their microstructure and mineralogy (Vialle, Dvorkin, and Mavko 2013, Steefel and Maher 2009, Molins et al. 2012, Wellman et al. 2003). Such rock frame changes masked within the time-lapse response caused by the fluids replacement, especially with V_P, may cause large errors in the quantitative interpretation of time-lapse seismic as we will show in Chapter 6.

Other than the porous rock frame properties, the fluids properties and their spatial distribution in the pore space of the rock is an important factor as it could have a large effect on the elastic wave velocities response (Knight and Nolen-Hoeksema 1990, Batzle and Wang 1992). CO_2 properties (i.e., bulk moduli, density and viscosity) change based on temperature and pressure. If the pressure and temperature in the reservoir are above the CO_2 critical point, then the CO_2 would be in a supercritical state (Span and Wagner 1996). In such state CO_2 properties are difficult to estimate especially if the CO_2 is present with other fluids such as brine or hydrocarbons (Maxim Lebedev 2013). This is discussed in more details in section 2.3.

The "Velocity-saturation relationship" (VSR) is often referred to in quantitative assessment of CO_2 saturation using P-wave velocity with Gassmann's equation (Mavko, Mukerji, and Dvorkin 2009). When two or more immiscible fluids exist in the pore space, then, Gassmann equation for uniform saturation might be inapplicable (Johnson 2001). In such cases the VSR will be dependent on many factors of which the geometrical distribution of fluid phases within the porous media, frequency of the seismic measurement, permeability of the rock and fluids viscosity are key parameters (Mavko, Mukerji, and Dvorkin 2009); with the geometrical distribution of the fluid phases as the most challenging quantity to estimate or obtain for *in situ* conditions. Because the wave elastic response here is frequency dependent, then measurement at different frequency could have different wave elastic response ranging from "uniform" response where the fluids mixture can be assumed uniform to a "patchy" response with the fluids completely unmixed. It is often required either to calculate or assume if the VSR is patchy or uniform for a given measurement frequency, as depending on this the prediction of the fluid saturation can differ greatly, especially at low saturations and for CCS saturations due to the often large compressibility difference between brine and injected CO_2 at reservoir conditions (Daley et al. 2008, Konishi et al. 2008, Caspari, Müller, and Gurevich 2011, Ajo-Franklin et al. 2013, Ivanova et al. 2012).

A motivation for this research is that geophysical data acquired during CO_2 sequestration in saline aquifers such as Ketzin, Nagaoka, Otway and Frio (Michael et al. 2010) provide high-resolution *in situ* data for calibration with theoretical rock physics. Thus, they present an attractive opportunity to investigate the applicability of theoretical models at the seismic scale. The use of high-resolution Vertical Seismic Profiling (VSP) rather than surface seismic in such small scale projects minimizes typical time-lapse monitoring challenges by providing better vertical and lateral resolution associated with high-frequency content and high signal-to-noise ratio (O'Brien, Kilbride, and Lim 2004). Moreover, crosswell seismic could provide a high-resolution image of the subsurface for calibrating rock physics models to obtain CO_2 saturation effects on rocks. The challenges described above are best investigated using an inversion and modelling schemes as shown in Figure 1-1. This is an iterative process, and several cycles of refining the inversion and modelling schemes to match with the time-lapse data may be required.

The studies conducted in this research are summarised in Figure 1-2 and they all aim to investigate the challenging aspect of CO_2 monitoring discussed above to ultimately understand the CO_2 saturation effect on the elastic properties of rocks. The main objectives of this research are given in the next section.

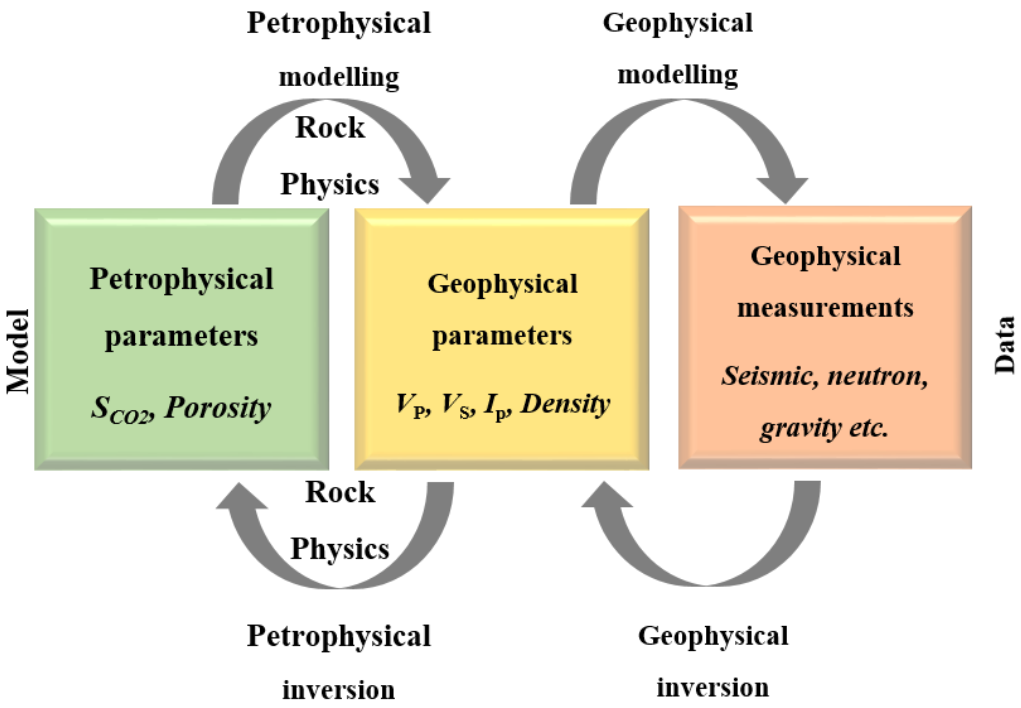

Figure 1-1: Time-lapse CO_2 monitoring from geophysical data to geophysical and petrophysical parameters. Modified from JafarGandomi and Curtis (2012).

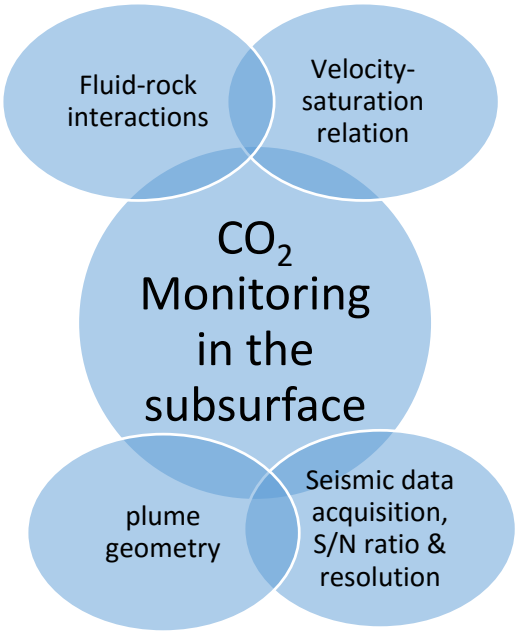

Figure 1-2: Aspects of CO_2 monitoring covered in this research.

1.3 OBJECTIVES

The focus of this research is the analysis of the effect of CO_2 saturation on the elastic properties of rocks using borehole seismic data. For this the following objectives are proposed:

- Study the effect of resolution and CO_2 plume geometry on the obtained parameters seismic.
- Quantify the effect of CO_2 saturation on seismic velocities from field seismic data.
- Investigate the effect of CO_2-brine-rock interaction on the rock frame properties.
- Estimate CO_2 saturation at both VSP and crosswell seismic scale from field data.
- Investigate the time-lapse signal obtained from offset VSP from a 3D time-lapse synthetic and its use to recover the velocity-saturation relation used in the synthetic modelling.

To achieve these objectives, we investigate two CO_2 injection projects using several theoretical and practical approaches for CO_2 time-lapse monitoring using several synthetic and real data sets. The choice of Carbon Capture and Storage (CCS) projects for this research and the data driven approach is given next.

1.4 APPROACH

This research uses field data, seismic modelling and rock physics modelling to achieve the proposed objectives stated earlier. We utilize available data for two pilot CO_2 injection project; that is the Frio-I brine pilot and Otway 2C sequestration project. Because each project is unique based on data availability, data quality, objectives, previous learnings etc., the approach is project specific.

The main objective for the Frio project is establishing a site-specific rock physics model for the injection interval and investigate its applicability at the field scale using time-lapse VSP and crosswell seismic. This is because previous analysis was based on an analogous rock physics model for the formation and quantitative interpretation of the time-lapse data is still an ongoing research (Daley et al. 2008, Doughty, Freifeld,

and Trautz 2008). Moreover, recent geochemical studies conducted highlighted the possibility of fluid-rock-interaction which could affect the rock frame properties in the Frio project (Kharaka et al. 2006, Ilgen and Cygan 2016). These effects must be taken into account in rock physics modelling for time-lapse quantitative interpretation. For this we revisit multiple datasets provided by LBNL, which were not published elsewhere and those available in the literature. The step-by-step approach we applied is as follows:

- Investigation of the reservoir rock petrophysical properties and analysis of field observations which my aid constraining the choice of a rock physics model and subsequent VSR (Chapter 3). We start by analysing the petrophysical data from available literature and that provided by LBNL. A quality control of the well logs and core data is performed. Then, we perform lithological and sedimentary microstructure evaluation using well log crossplots.
- Obtain high resolution quantitative measurement of velocity changes caused by CO_2 injection from the time-lapse seismic data (VSP and crosswell). For the VSP data, we expect the resolution of the seismic and plume geometry would have an effect on the estimated velocity changes. For this, the effects of seismic resolution and gas plume geometry on the obtained measurement are investigated at the VSP scale closely. Crosswell traveltime tomography is then performed to verify their results and to be utilized later the rock physics modelling (Chapter 4).
- Investigate the applicability of Gassmann's poroelasticity theory (uniform saturation) at the field scale by first creating a site-specific rock physics model of the Frio formation. Then, the petrophysical data and quantitative data from seismic are integrated to verify the model applicability and investigate causes of discrepancy (Chapter 5).
- We estimate quantitatively rock frame weakening possibly induced by CO_2-brine-rock interaction. This is achieved by employing the changes in V_S calculated from crosswell traveltime tomography. Then, a rock physics model based on rock microstructure diagnostics is proposed which allows the frame microstructure to be updated based on the magnitude of the rock frame weakening. A velocity-saturation relation is defined after

incorporating rock frame weakening effects. The results of this approach are to be compared to those obtained using Gassmann's poroelasticity theory. Finally, CO_2 saturation at both the VSP and crosswell scale is estimated using both patchy and uniform saturation models (Chapter 6).

The Otway 2C project has a similar injection depth as the Frio brine pilot project, both involve the injection of a relatively small amount of CO_2 in a fully brine saturated interval (for Otway 2C several stages of monitoring are proposed and palnned to be conducted after the injection of a predefined CO_2/CH_4 mixture volume of 5000, 10,000 and 15,000 tons) and part of the monitoring campaign would invlove the use of sparse-VSP shots for monitoring. Due to these similarities, we aim to utilize the learning from the research conducted in Chapter 4,5 and 6 for the Frio data set in a sensetivity analysis of the Otway 2C project in Chapter 7. For the Otway 2C project a site-specific rock physics model has been defined previously (Caspari et al. 2015) but not yet verified if it can be constrained using offset VSP time-lapse seismic data. Moreover, a comprehensive synthetic seismic data set is available which incorporate the rock physics model and reservoir simulation results for a realistic CO_2/CH_4 gas injection (Pevzner et al. 2015, Glubokovskikh et al. 2016). The approach for Otway 2C study is as follows:

- Investigate the time-lapse signal that could be obtained from offset VSP as a sensitivity study for the proposed field data geometry to be conducted. This involves assessing the strength of the time-lapse signal that could be observed. Then, the associated P-wave velocity changes are estimated from the VSP data obtained signal.
- We compare the synthetic data results the parameters used in the model.
- Finally, the feasibility of using these attributes in constraining the rock physics model is discussed taking into account the proposed field data geometry.

An illustrated workflow of the approach utilized in this research is shown in Figure 1-3.

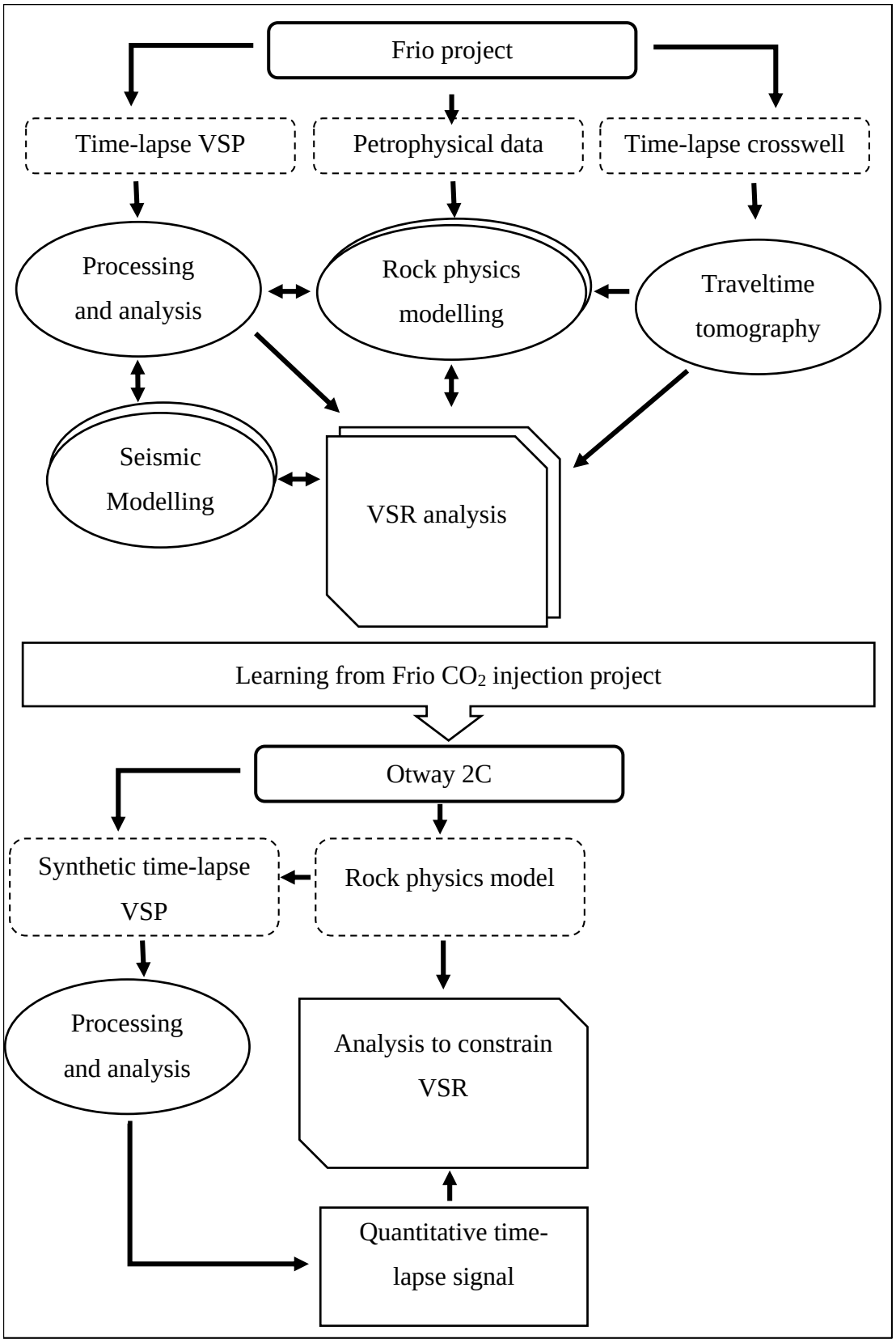

Figure 1-3: Flow chart of the research approach for the Frio project and Otway 2C project. The data provided is presented with dashed outline.

1.5 THESIS OUTLINE

The thesis is organized in eight chapters with each chapter targeting an aspect of my research with a number of objectives to be accomplished at the end. The thesis is structured as follows:

Chapter 2: This chapter is an evaluation and summary of the theoretical models, which will be implemented throughout my research. The focus here is presenting the underlying theory and concepts for the rock physics modelling, seismic methods, seismic theory and seismic modelling related to this research. As these concepts are well-established and published, the aim is to provide an overview of these concepts to underpin this research.

Chapter 3 gives an overview of the Frio CO_2 injection project geophysical data obtained and geological and petrophysical information available. The objective of this chapter is to provide a comprehensive treatment of the petrophysical measurements obtained from previously published work on the Frio project and the data set provided by LBNL. Moreover, a quality control over the available data is performed to verify their accuracy.

Chapter 4 deals with the processing of the time-lapse VSP and crosswell data of the Frio CO_2 injection project to obtain geophysical parameters for quantitative interpretation that will be carried out in Chapter 5 and 6. Here a modelling study is performed to assess the effect of resolution and CO_2 plume geometry on the obtained geophysical parameters using time-lapse VSP. This is illustrated by investigation of reflection amplitude change for different models and comparing to field observations. The majority of the chapter is focused on the VSP method as it provides several high accuracy independent measurements.

Chapter 5 investigates the applicability of Gassmann's fluids substitution theory for the Frio CO_2 case study. The first part deals with utilizing the geophysical and petrophysical parameters obtained in Chapter 3 and 4, respectively, to obtain a constrained rock physics model for the "Frio-C" injection interval. Then, the velocity-saturation relation predicted from this rock physics model is compared to the geophysical parameters obtained from the VSP time-lapse data (e.g., V_P, I_P and reflection amplitude).

Chapter 6 utilizes an approach to obtain the elastic properties of the Frio "C" based on the rock microstructure diagnostic. The motivation for this chapter is driven by the observed large discrepancy between the site-specific rock physics model obtained in Chapter 5 and the real data at both the VSP and crosswell scales which suggested that rock frame weakening occurred after CO_2 injection.

Chapter 7 investigates the application of the learnings from the Frio CO_2 injection project to the Otway 2C injection project. A review of the previous work and rock physics model of the injection interval is provided. Then, a realistic synthetic time-lapse VSP data set (provided by Curtin University staff) is analysed with a similar approach to that utilized earlier for the Frio project to obtain the CO_2 plume extent and velocity changes. The results obtained from the synthetic study are utilised to analyse the possibility of using time-lapse VSP data to recover the velocity-saturation relationship used for the modelling. The results are finally discussed in the context of the seismic response magnitude and for constraining the rock physics model of the formation.

CHAPTER 2. BACKGROUND THEORY AND CONCEPTS

In this chapter, a summary of the theoretical concepts and methods used in this thesis is given. The chapter consist of three main topics:

The first topic (section 2.1) is a brief description of the trapping mechanism of CO_2 in the subsurface and as they are related to many of the underlying aspects of this research.

The second topic (section 2.2) deals with the elastic properties of the porous rock frame. We first present the elastic bounds for both mineral and fluids mixtures. Then, we deal with the theoretical models used to derive reservoir rock elastic properties, mainly grain contact models. Next, we discuss fluid properties at reservoir conditions in section 2.3. Then, we present Gassmann's fluid substitution equations and the concepts of uniform and patchy saturation in section 2.4.

The third topic (sections 0, 2.6 and 2.7) deals with the elastic wave propagation and theoretical concepts of the seismic method. We describe briefly some of the seismic theory concept, the elastic wave equation and modelling methods of interest in this thesis. Then, the VSP method is described in more details here as it is used extensively in this research. Finally, a review of the crosswell method is given.

All models and concepts treated here are described briefly to underpin this research since these models are well-established and treated in several publications which will be referenced as appropriate in each section.

2.1 CO_2 trapping mechanisms

Understanding the mechanisms that allow the trapping of CO_2 in the subsurface, their effectiveness, capacity and effects on subsurface rocks is essential for any CO_2 injection project planning. An important concept is the amount of CO_2 trapped by each mechanism and how it affects the CO_2 plume distribution in the subsurface (Gershenzon et al. 2014). The CO_2-brine displacement mechanism that could be in

effect after injection into the subsurface as stated by Bachu, Gunter, and Perkins (1994) are:

- Microscopic: pore scale (molecular diffusion and dispersion).
- Macroscopic: well scale (mixing of CO_2 and water around the injection well).
- Megascopic: aquifer scale (gravity segregation by density and viscous fingering due to mobility difference).

In this research the macroscopic scale displacement mechanism is important as many measurements utilized in this research will be that acquired at or close to the injection well. The trapping mechanisms are described below and a summary of their contribution over time is shown in Figure 2-1.

2.1.1 Stratigraphic and structural trapping

The presence of a structure which prevents CO_2 from migrating to the surface is usually considered a pre-request for any CCS project. Structural trapping here refers to the presence of a thick non-permeable layer, which could effectively prevent upward migration of CO_2 to the surface or unwanted location in the subsurface, while stratigraphic traps refer to a unit which may trap CO_2 due to pinch-out of a porous formation overlain by non-porous sealing units. In many cases, shaley formations can provide an effective sealing capacity of CO_2 due to their very low permeability. Usually, the CO_2 will be trapped below such a structural trap as a thin layer which may migrate along the barrier depending on the structural relief. This trapping mechanism usually dominates in the early stages of a CO_2 sequestration project as Figure 2-1 shows.

2.1.2 Solubility trapping

CO_2 could dissolve in water forming an acidic solution thus removing the CO_2 fluid phase. In such cases solubility trapping could halt CO_2 plume migration as once CO_2 is dissolved into brine, it becomes driven by the hydrodynamics of the aquifer rather than its buoyancy (Bachu and Adams 2003). CO_2 solubility is dependent on many factors such as pressure, temperature, salinity and the contact surface area between the CO_2 and the fluid phase (Bachu and Adams 2003).

2.1.3 Mineral trapping

Mineral or geomechanical trapping is the most preferred type of trapping mechanisms as it could immobilize CO_2 by precipitation of minerals. It occurs when dissolved CO_2 reacts with rock-forming minerals. The dissolution of carbonate initially dominates the reaction (if present) which may increase the porosity of the rock frame as:

$$CO_2\,(g) + H_2O + CaCO_3\,(s) \Leftrightarrow 2Ca^{2+} + 2HCO_3^{-}. \quad (2\text{-}1)$$

Such interaction is considered rapid and could result in changes in the microstructure of the rock frame within a short timeframe especially near the injection well (Kharaka et al. 2006). This reaction contribution in CO_2 trapping is not shown in Figure 2-1 as although this process is very rapid; it could be volumetrically insignificant depending on the initial minerals assembly of the porous rock (Ilgen and Cygan 2016). Then, dissolution of feldspar becomes the dominant reaction and carbonate participation takes place (Benson and Cole 2008). An example of a possible reaction of silicate minerals with CO_2 is the CO_2-Calcium feldspar reaction:

$$CaA1_2Si_2O_8[\text{Ca feldspar}] + CO_2 + 2H_2O \rightarrow AI_2\,Si_2\,O_5\,(OH)_4\,[\text{kaolinite}] + CaCO_3\,[\text{calcite}]. \quad (2\text{-}2)$$

This method of trapping is a long-term process, and simulation studies from several studies indicated that up to 90% of the injected CO_2 could be trapped over the period of thousands of years (Bachu, Gunter, and Perkins 1994). CO_2-fluid-rock interaction and their possible effects on the porous rock frame and time-lapse monitoring will be discussed in more details in Chapter 6.

2.1.4 Capillary or residual trapping

This trapping mechanism includes residual trapping, the hysteresis of the relative permeability and hysteresis due to capillary pressure (Gershenzon et al. 2014, Saadatpoor, Bryant, and Sepehrnoori 2010). The mechanism occurs predominately at the trailing edge of the CO_2 plume as brine imbibes into the CO_2 plume. This type of trapping could result in a significant volume of CO_2 trapped especially in dipping formations. Also, another type of trapping that could be classified in this category and

referred to as local capillary trapping could also be of great importance (Saadatpoor, Bryant, and Sepehrnoori 2010). It is induced by heterogeneity intrinsic to sedimentary rocks (i.e., capillary entry pressure is larger than average) thus causing CO_2 to be trapped underneath it. This type of trapping has an advantage over residual trapping in that the CO_2 trapped could have a saturation which is larger than the residual CO_2 saturation. Moreover, in the case of seal integrity failure of a structural trap this CO_2 will not migrate upwards (Saadatpoor, Bryant, and Sepehrnoori 2010). These trapping mechanisms may give rise to CO_2 patches in the subsurface at different scales. Recent studies from the Frio-I brine pilot CO_2 injection project have shown that the small amount of CO_2 injected (1600 tons) in the formation has been trapped efficiently by this mechanism (Daley et al. 2008, Xu et al. 2010).

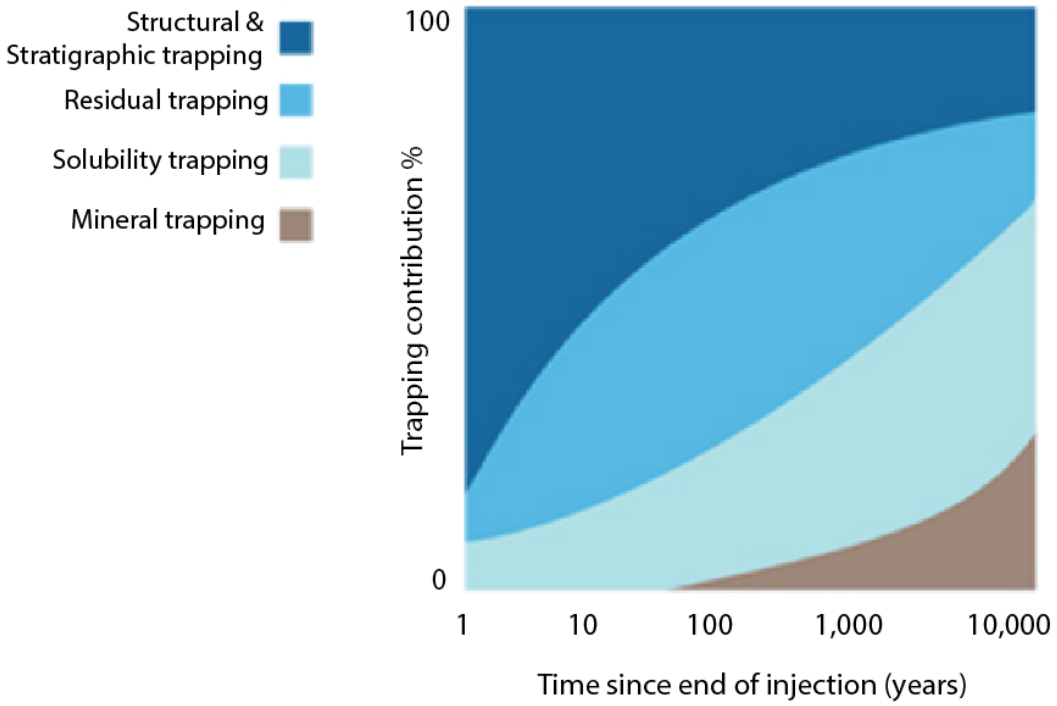

Figure 2-1: Trapping mechanisms and their contribution to store CO_2 with time. The relative contribution of each process is dependent on many factors such as mineralogy, fluid-rock interaction and fluid-flow. From CO2CRC. (2016).

2.2 EFFECTIVE ELASTIC PROPERTIES

Rock physics relationships play an important role as a link between reservoir rocks, pore fluid properties and geophysical measurements. Rock physics relationships provide the link between elastic measurements at different frequencies and the intrinsic

properties of the rock such as porosity, pore fluids and mineralogy (Jalal Khazanehdari 2010). A rock physics model is defined by knowing the elastic properties of the rock frame and the fluid phases. Here we present the theories and approaches that are used in this thesis to derive the elastic properties of the rock frame and fluids mixtures. The rock frame response to fluids replacement is discussed later in section 2.4.

2.2.1 Bounds and mixing laws

The elastic properties of a mixture of several elastic constituents are defined by three main components; the volume fraction of the each constitutes, their elastic moduli and the geometry of each constitute (Mavko, Mukerji, and Dvorkin 2009). However, the geometrical arrangement of the constitutes is never known exactly. Thus, several theories were developed to overcome this by considering upper and lower limits or using ideal geometries for the constitutes.

The bulk modulus of the rock matrix can be calculated if the mineral composition of the rock is known; otherwise, indirect calculations can be used. Core data are the best source of mineral constitutes analysis, then if not available well logs such as gamma ray can be used to calculate simply the volume fraction of assumed minerals such as clay and quartz (Smith, Sondergeld, and Rai 2003).

2.2.1.1 Voigt, Reuss bounds and the Voigt-Reuss-Hill average

The Voigt and Reuss bounds are the simplest bounds that can be used to predict theoretically the effective elastic moduli of a mixture of constitutes of grains and pores. The bounds need two input parameters which are the volume fraction of the constitutes and their elastic moduli (Mavko, Mukerji, and Dvorkin 2009).

The Voigt bound represents the stiff or upper bound and represent the case of isostrain average because it results in the ratio of average stress to the average strain with the same strain assumed for all constitutes (Mavko, Mukerji, and Dvorkin 2009). The Voigt bound written for M_V effective elastic moduli N constitutes, with f_i representing the volume fraction of each phase and M_i as the effective elastic moduli of each phase:

$$M_V = \sum_{i=1}^{N} f_i M_i. \tag{2-3}$$

The Reuss lower bound or the isostress average gives the ratio of the average stress to the average strain with the same stress assumed for all constitutes. This Reuss bound M_R is written as:

$$\frac{1}{M_R} = \sum_{i=1}^{N} \frac{f_i}{M_i}. \tag{2-4}$$

The bound in the Reuss average can describe a modulus M such as K, μ then utilize them to compute any other moduli (Mavko, Mukerji, and Dvorkin 2009).

The Voigt-Reuss-Hill (VRH) average is the simple arithmetic average of the Voigt and Reuss bounds. This average is useful as it usually gives good results as we usually seek an estimated value rather than a range in many of the calculations (Mavko, Mukerji, and Dvorkin 2009). The VRH average M_{VRH} is written as:

$$M_{VRH} = \frac{M_V + M_R}{2},$$

with M_V and M_R representing the Voigt and Reuss averages, respectively.

2.2.1.2 Hashin-Shtrikman bounds

The Hashin-Shtrikman bounds (Hashin and Shtrikman 1963) are the narrowest bounds that can be predicted for an isotropic mixture of grains and pores without specifying any geometrical details of the constitutes in relation to each other's. The result for the effective elastic moduli will always be within the bounds for any volume fraction of constitutes. These bounds are very useful as they limit the possibility of going out of the physically possible results for any combination of constituents (Mavko, Mukerji, and Dvorkin 2009). The upper and lower bounds are written as:

$$\mathrm{K^{HS+}} = \Lambda(\mu_{\max}), \quad \mathrm{K^{HS-}} = \Lambda(\mu_{\min}), \tag{2-5}$$

$$\mu^{HS+} = \Gamma\big(\zeta\,(K_{max}, \mu_{max})\big), \quad \mu^{HS-} = \Gamma\big(\zeta(K_{min}, \mu_{min})\big), \tag{2-6}$$

where

$$\Lambda(z) = \left\langle \frac{1}{K(r) + 4z/3} \right\rangle^{-1} - \frac{4}{3}z,$$

$$\Gamma(z) = \langle \frac{1}{\mu(r) + z} \rangle^{-1} - z,$$

$$\zeta(K, \mu) = \frac{\mu}{6} \left(\frac{9K + 8\mu}{K + 2\mu} \right),$$

with, μ_{max} and μ_{min} as the maximum and minimum shear modulus of the constitutes; K_{max} and K_{min} as the maximum and minimum bulk modulus of the constitutes; r representing the different constitutes and ‹.› is the average over the medium (Mavko, Mukerji, and Dvorkin 2009).

The bounds are more precise if used for mixture with elastic moduli of the same order of magnitude. Thus, using the Hashin-Shtrikman bounds with one of the constitutes being a fluid or gas gives less useful bounds due to the large separation between the upper and lower bounds. We illustrate the bounds discussed here and in the previous section for the bulk moduli and shear moduli in Figure 2-2 and Figure 2-3, respectively, for two constituents of which one is a fluid or gas.

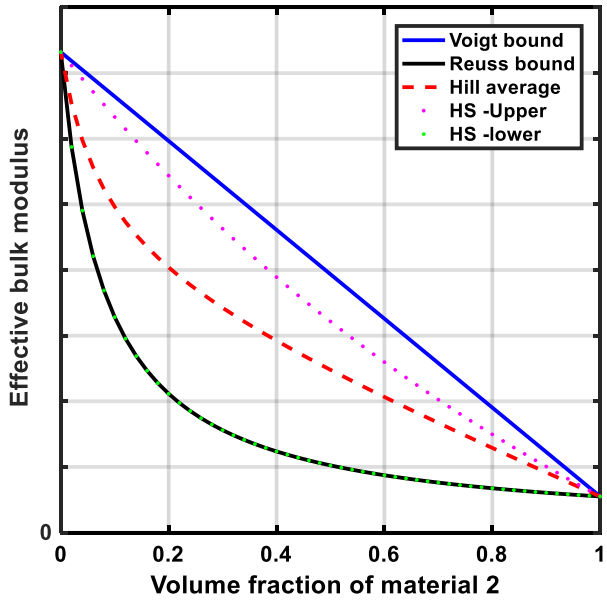

Figure 2-2 The effective bulk modulus for two constitutes of which the second is fluid or gas using Voigt, Reuss bounds and their average. Also shown the Hashin-Shtrikman (HS) lower and upper bounds. If one of the constituents is a fluid or gas the Reuss bounds is equal to the Hashin-Shtrikman lower bound.

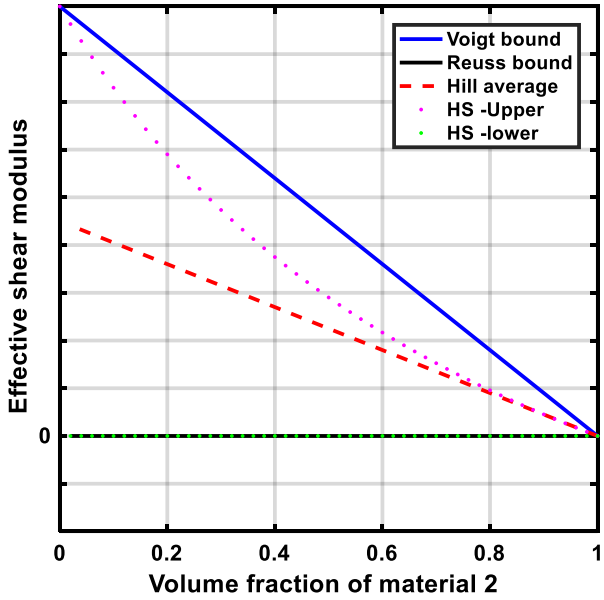

Figure 2-3 The effective shear modulus for two constitutes of which the second is fluid or gas using Voigt, Reuss bounds and their average. Also shown the Hashin-Shtrikman bounds. The Reuss bound is equal to the Hashin-Shtrikman lower bounds in this case.

2.2.1.3 Wood's formula

Wood's formula represents the case where we have a fluid suspension or a fluid mixture with the heterogeneities being small compared to the wavelength of the seismic wave. Wood's formula (Wood 1955) for estimating the velocity (V) is given by:

$$V = \sqrt{\frac{K_R}{\rho}}, \tag{2-7}$$

with K_R as the Reuss average of the composite as

$$\frac{1}{K_R} = \sum_{i=1}^{N} \frac{f_i}{K_i}, \tag{2-8}$$

and ρ as the density of the composite written as

$$\rho = \sum_{i=1}^{N} f_i \rho_i, \tag{2-9}$$

with f_i, K_i and ρ_i as the volume fraction, bulk moduli and densities of the various constituents, respectively.

2.2.2 Dry frame elastic properties

The porous rock frame elastic properties are the low-frequency drained modulus of a rock (Smith, Sondergeld, and Rai 2003). This value is used in fluid substitution to predict the elastic moduli of the saturated porous rock. The value for the frame bulk modulus can be calculated using many approaches. The most accurate is usually measurements performed on core plugs samples; other approaches involve using simplified theoretical models, bounds and empirical relationships.

In here, we present the elastic contact theory models. These models fundamentally have two end members. The zero porosity end member that is primarily the mineral properties, while the high porosity end member is calculated using elastic contact theory (Avseth, Mukerji, and Mavko 2010). Then the interpolation between these two end members could describe elastic properties of the rock frame at other porosity values between those two end members. It is well noted in the literature that this interpolation could be inadequate for situations where there is only small amount of cement present, as this would give rise to a substantial increase in the frame stiffness, which is not predicted by such an interpolation (Avseth, Mukerji, and Mavko 2010).

These contact models are usually applicable for a range of porosities that does not exceed the critical porosity (ϕ_c). If values exceeded this critical porosity, one must consider this due to the large difference in the elastic moduli behaviour beyond ϕ_c. The critical porosity separates the rock frame behaviour from a load-bearing (frame-supported) at porosities lower than ϕ_c and as a suspension (fluid-supported) if the porosity is higher than ϕ_c as shown in Figure 2-4 (Nur et al. 1998).

We note here an important aspect of contact theory models which are known to overestimate the shear moduli that is controlled by the tangential contact stiffness (Avseth and Bachrach 2005, Makse et al. 2004, Makse et al. 1999). Thus, in this research, we calibrate the effective shear moduli obtained from contact models by a shear reduction factor. This shear reduction factor takes into account the grains which have no tangential contact stiffness. In general, we assume these models to be satisfactory and provide a reasonable approximation after calibration with field data.

In the next subsections, we provide the theoretical background of some of the contact theory models which will be used in my research.

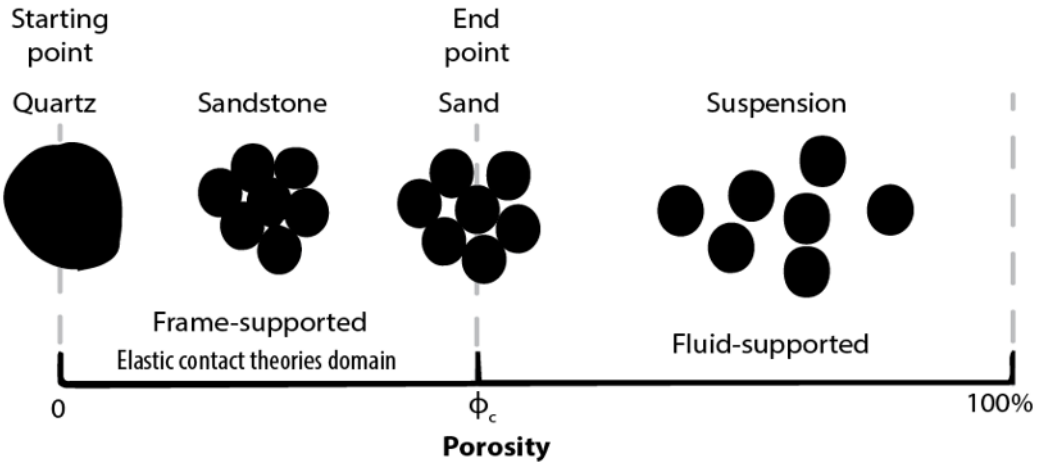

Figure 2-4 The physical meaning of critical porosity and the domain of contact medium theories. No frame support is present at values higher than the critical porosity. Modified after (Nur et al. 1998).

2.2.2.1 The Hertz-Mindlin Model

The classical Hertz-Mindlin model gives the effective modulus of random pack of spheres at normal compression with the radius of the contact area, a and the normal displacements, δ (Mavko, Mukerji, and Dvorkin 2009) as

$$a = \left[\frac{3FR}{8\mu}(1-\nu)\right]^{1/3}, \quad \delta = \frac{a^2}{R}, \tag{2-10}$$

with μ as the shear modulus of the grains and ν is their Poisson ratio.

The force acting between two particles in a random pack of identical spheres under a hydrostatic confining pressure is

$$F = \frac{4\pi R^2 P}{C(1-\phi)}, \tag{2-11}$$

then

$$a = R\left[\frac{3\pi(1-\nu)}{2C(1-\phi)\mu}\right]^{1/3},$$

with the normal stiffness defined as

$$S_n = \frac{4\mu a}{1-\nu}. \tag{2-12}$$

The shear stiffness is defined as

$$S_\tau = \frac{8\mu a}{2-\nu}. \tag{2-13}$$

Giving an effective dry frame of random identical sphere packing as

$$K_{eff} = \left[\frac{C^2(1-\phi)^2\mu^2}{18\pi^2(1-\upsilon)^2}P\right]^{1/3}, \tag{2-14}$$

and an effective shear modulus as

$$\mu_{eff} = \frac{5-4\upsilon}{5(2-\nu)}\left[\frac{3C^2(1-\phi)^2\mu^2}{2\pi^2(1-\upsilon)^2}P\right]^{1/3}. \tag{2-15}$$

In the case of a frictionless spheres with η=0, thus S_τ=0 the effective bulk and shear moduli are written as

$$\begin{aligned} K_{eff} &= \frac{C(1-\phi)}{12\pi R}S_{n,} \\ \mu_{eff} &= \frac{C(1-\phi)}{20\pi R}S_{n,} \\ \frac{K_{eff}}{\mu_{eff}} &= \frac{5}{3} \end{aligned} \tag{2-16}$$

and the effective Poisson ratio is, ν_{eff}=0.25.

2.2.2.2 Contact-cement and constant cement models

The contact-cement model was proposed by Dvorkin and Nur (1996). The model is based on the cementation theory (Dvorkin, Mavko, and Nur 1991, Dvorkin, Nur, and Yin 1994) and the contact model of Hertz and Mindlin. The model requires an input of the starting critical porosity and a contact per grain (coordination number). The dry frame elastic moduli given (Dvorkin and Nur 1996) as

$$K_{COC} = \frac{1}{6}(1-\phi_c)M_c\hat{s}_n, \tag{2-17}$$

$$\mu_{COC} = \frac{3}{5}K_{COC} + \frac{3}{20}C(1-\phi_c)\mu_c\hat{s}_\tau, \tag{2-18}$$

with M_c and μ_c as the P-wave and S-wave modulus of the cement, respectively. The $\hat{s}_n$ and $\hat{s}_\tau$ are proportional to a two-grain contact normal and shear stiffness, respectively. These two parameters depend on the grain properties and the amount and properties of the contact cement as follows (Mavko, Mukerji, and Dvorkin 2009)

$$\begin{aligned}
&\hat{s}_n = A_n\alpha^2 + B_n\,\alpha + C_n \\
&A_n = -0.024153\,\Lambda_n^{-1.3646} \\
&B_n = 0.20405\,\Lambda_n^{-0.89008} \\
&C_n = 0.00024649\,\Lambda_n^{-1.9868} \\
&\Lambda_n = \frac{2\mu_c}{\pi\mu}\,\frac{(1-\upsilon)(1-\upsilon_c)}{(1-2\upsilon_c)},
\end{aligned} \tag{2-19}$$

$$\begin{aligned}
&\hat{s}_\tau = A_\tau\alpha^2 + B_\tau\,\alpha + C_\tau \\
&A_n = -0.01(2.26\upsilon^2 + 2.07\upsilon + 2.3)\,\Lambda_n^{0.079\upsilon^2+0.1754\upsilon-1.342} \\
&B_\tau = (0.0573\upsilon^2 + 0.0937\upsilon + 0.202)\,\Lambda_\tau^{0.0274\upsilon^2+0.0529\upsilon-0.8765} \\
&C_\tau = 0.0001(0.0573\upsilon^2 + 4.945\upsilon \\
&\qquad\qquad + 3.1)\Lambda_\tau^{0.01867\upsilon^2+0.4011\upsilon-1.8186} \\
&\Lambda_n = \frac{\mu_c}{\pi\mu},
\end{aligned} \tag{2-20}$$

where μ and υ are the shear modulus and Poisson ratio of the grains, respectively. μ_c and υ_c are the shear modulus and Poisson ratio of the cement, respectively.

The contact cement model provides schemes for cement deposition based on the parameter α which is the ratio of the radius of the cement layer to the grain radius. Relating this parameter to the porosity of cemented and uncemented sand, we could obtain two schemes. Scheme 1 assumes all cement is deposited at grain contact, which would significantly increase the stiffness of the rock frame as given in equation (2-21). Conversely, scheme 2, assumes the cement to be deposited as a shell around the grains as in equation (2-22).

$$\alpha = 2\,[\frac{S\phi_0}{3n(1-\phi_0)}]^{1/4}, \tag{2-21}$$

$$\alpha = 2\,[\frac{2S\phi_0}{3n(1-\phi_0)}]^{1/2}, \tag{2-22}$$

here S is the cement saturation that is the fraction of pore space occupied by cement (in the originally uncemented sand).

We can see that the contact-cement model predicts that all cement is contributing at grain contact in both schemes. Thus, one of the most significant results of the cementation theory is that cement at grain contact causes a sharp increase in the rock frame strength for the first few percent of cement. However, pore filling material could sometimes be of little contribution and do not strengthen strongly the rock frame. For such cases, the constant-cement model by Avseth et al. (2000) could be used to describe the elastic properties of the rock frame.

The constant-cement model departs from the contact-cement model from the porosity of the cemented sand obtained using the contact-cement model at $\boldsymbol{\phi}_b$ given an initial critical porosity ($\boldsymbol{\phi}_c$) using either Scheme 1 or 2. The elastic moduli for the constant-cement model (Avseth et al. 2000) are written as

$$K_{CNC} = \left(\frac{\boldsymbol{\phi}/\boldsymbol{\phi}_b}{K_{COC} + \frac{4\mu_{COC}}{3}} + \frac{1 - \boldsymbol{\phi}/\boldsymbol{\phi}_b}{K_s + \frac{4\mu_{COC}}{3}} \right)^{-1} - \frac{4\mu_{COC}}{3}, \tag{2-23}$$

$$G_{CNC} = \left(\frac{\boldsymbol{\phi}/\boldsymbol{\phi}_b}{\mu_{COC}+z} + \frac{1-\boldsymbol{\phi}/\boldsymbol{\phi}_b}{\mu_s+z} \right)^{-1} - z,\ z = \frac{\mu_{COC}}{6}\,\frac{9K_{COC}+8\mu_{COC}}{K_{COC}+2\mu_{COC}}, \tag{2-24}$$

with K_s and μ_s as the mineral phase bulk and shear moduli, respectively; K_{COC} and μ_{COC} are the bulk and shear moduli for the cemented sand calculated from the contact-cement model equations in (2-17) and (2-18). The constant-cement model is described in more details and utilized in Chapter 6.

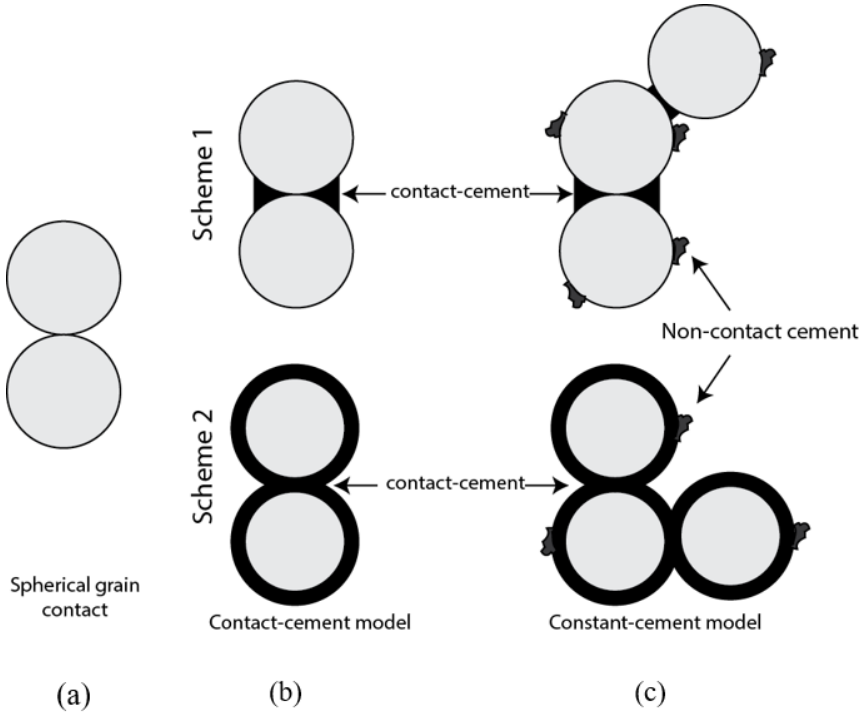

Figure 2-5: Schematic representation of the contact models discussed. (a) initial sand pack, (b) contact-cement model scheme 1 and 2, (c) constant-cement model for scheme 1 and 2. Figure 2-6 shows the models in the rock microstructure diagnostic template. Modified after Dvorkin and Nur (1996).

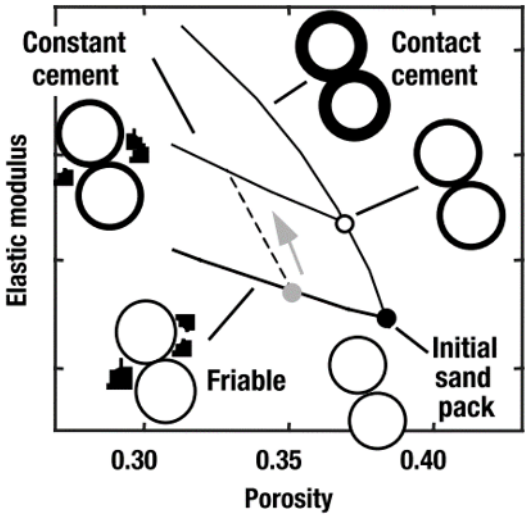

Figure 2-6: Rock microstructure diagnostics and schematic representation of the three theoretical models for high porosity sands. The thickening of the circles represents the addition of cement from the initial sand pack. The slope of the contact cement line depends on the type of cementation. From Avseth et al. (2000).

2.3 FLUID PROPERTIES

The fluids in the rock pores influence the rocks elastic properties substantially. Fluid properties change with changing composition, pressure and temperature parameters. Their properties are calculated using a combination of thermodynamic relationships, empirical trends or direct lab measurements. Accurate fluid properties (e.g., density, bulk modulus and viscosity) are essential for modelling a porous rock behaviour in term of seismic velocities, rock density, dispersion and attenuation of the seismic waves (Batzle and Wang 1992).

In this research, we deal with CO_2 (or CO_2/CH_4 mixture) and brine as all the projects investigated involve injection of CO_2 into brine aquifers. Brine density is a function of salinity, temperature and pressure. Thus, for brine properties we use the equations of Batzle and Wang (1992) if experimental values are not provided in the literature or the data we have for each CO_2 injection project reservoir conditions and brine salinity.

CO_2 properties are difficult to obtain especially if CO_2 is at a supercritical state. If *in situ* or lab measurements are not available for the CO_2 properties, given knowledge of the reservoir pressure and temperature, we refer to use the

thermophysical properties of fluid systems (The National Institute of Standards and Technology 2014) that is based on the CO_2 equation of state by Span and Wagner (1996). CO_2 has a critical point that is at the temperature of 31°C and a pressure of 7.4 MPa (Yam and Schmitt 2011). Above this pressure and temperature point CO_2 is considered at a supercritical state and has the physical properties of both gas and liquid as Figure 2-7 shows. Note that the transition in the physical properties for pressure and temperature above this critical point is close the liquid state for density and gas state for the bulk moduli.

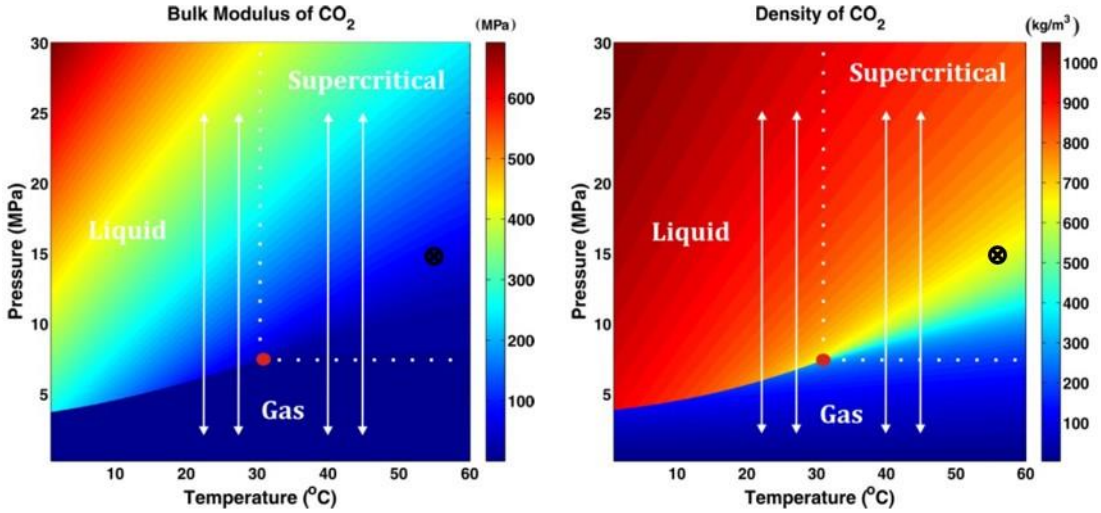

Figure 2-7: CO_2 bulk modulus and density phase diagram based on the equation of state of Span and Wagner (1996). The Frio reservoir conditions are indicated by the black crossed circle. Modified from Yam and Schmitt (2011).

2.4 FLUID SUBSTITUTION

Fluid substitution is an algorithm designed to compute elastic moduli of a rock saturated with one fluid from the moduli of a rock saturated with another fluid (Avseth, Mukerji, and Mavko 2010). These effects could be the results of changes in the fluids composition, temperature and pressure (Batzle and Wang 1992) and distribution within the pore space (Avseth, Mukerji, and Mavko 2010). Thus, we discuss the next the theories and concepts related to fluid substitution.

2.4.1 Biot-Gassmann's poroelasticity theory

The Biot-Gassmann equations Gassmann (1951), (Biot 1956) are the most used equations for the prediction of changes in elastic properties - mainly bulk modulus- due to variable pore fluid saturations (Han and Batzle 2004). Gassmann's equations can be written in many forms, one being as

$$\frac{K_{\text{sat}}}{K_{\text{g}} - K_{\text{sat}}} = \frac{K_{\text{dry}}}{K_g - K_{\text{dry}}} + \frac{K_{\text{f}}}{\phi(K_{\text{g}} - K_{\text{f}})}, \tag{2-25}$$

and

$$\mu_{sat} = \mu_{dry}, \tag{2-26}$$

where K_{sat} is the saturated rock effective bulk modulus, K_{dry} is the effective bulk modulus of dry rock, K_{g} is the bulk modulus of mineral material [sometimes referred to as K_{grain}], ϕ is the porosity, μ_{dry} is the dry rock shear modulus and μ_{sat} is the effective shear modulus of the saturated rock (Mavko, Mukerji, and Dvorkin 2009). Equation (2-26) state that the shear moduli is independent of the fluid saturation. This equation comes from the underlying assumptions used to derive Gassmann's equation (Han and Batzle 2004, Berryman 1999). There are several assumptions involved when applying Gassmann's equation (Mavko, Mukerji, and Dvorkin 2009) as:

- Gassmann's equation assumes a homogenous and isotropic rock. That is, both for the rock frame and the fluid.
- Pores are connected and allow for pressure equilibration. This pressure equilibration must be within a length scale which is much greater than the pore space and much less than the wavelength of the seismic wave passing through (Smith, Sondergeld, and Rai 2003). This assumption of Gassmann is very important, because it is dependent on both formation properties and the frequency of the seismic measurement. As such, Gassmann's equations could be valid for seismic frequencies, but may or might not be for sonic frequencies.
- The drained frame properties do not change with the change of pore fluid.

Several extensions of Gassmann's equations have been introduced to account for many situations (e.g., anisotropy, mixed mineralogy, clay-filled rocks etc.), those are conveniently stated in Mavko, Mukerji, and Dvorkin (2009). The grain bulk moduli

could be obtained by any of the elastic bounds discussed in section 2.2.1.1 and 2.2.1.2 given knowledge about the mineralogical composition of the rock.

Gassmann's equations are often used to obtain the dry frame elastic properties by utilizing wireline log data (V_P, V_S, ρ) or core measurements. This is achieved by inverting Gassmann pore-elasticity theory (Gassmann 1951) given in equation (2-25) for the dry frame (i.e., drained) bulk modulus K_{dry} while the shear modulus μ_{dry} is kept constant for both the dry and saturated frame (Smith, Sondergeld, and Rai 2003) as

$$K_{\text{dry}} = \frac{\left(\frac{\phi K_{\text{g}}}{K_{\text{f}}} + 1 - \phi\right) K_{\text{sat}} - K_{\text{g}}}{\frac{\phi K_{\text{g}}}{K_{\text{f}}} + \frac{K_{\text{sat}}}{K_g} - 1 - \phi} \tag{2-27}$$

$$\mu_{sat} = \mu_{dry}, \tag{2-28}$$

where, K_g is the grains bulk modulus, K_f the fluid bulk modulus, K_{sat} and μ_{sat} are the bulk modulus and shear modulus calculated from the fluids saturated rock measurements and ϕ is porosity.

2.4.2 Elastic moduli of partially saturated rocks

Gassmann's equations defined earlier are strictly valid for a single fluid occupying all of the pore space in a representative volume of the rock. Thus, if two or more immiscible fluids exist in the pore space (e.g., CO_2 and brine) then an effective fluid mixture bulk moduli can be used using Wood's equation (Wood 1955) given in section 2.2.1.3 to substitute in Gassmann's equations to obtain the so called "Gassmann-Wood" (GW).

Wood's equation assumes that the pressure between the fluids is equilibrated in the porous rocks for a given wavelength. Thus, Gassmann-Wood is only valid when the fluids are mixed at a very fine scale as such that the fluid patches length scale (d) is much smaller than the critical fluid-diffusion scale L_c, defined as

$$L_c \approx \sqrt{\tau D} = \sqrt{\frac{D}{f}}, \tag{2-29}$$

with f as the frequency and D is the diffusivity given by

$$D = \frac{kK_{fl}}{\eta}, \tag{2-30}$$

with η as the viscosity, k is the permeability and K_{fl} is the fluid bulk modulus.

Conversely, if $d >> L_c$, and the fluids heterogeneities (patches) are separated with no pressure communication, then, each fluid patch will have its own bulk moduli, however, the shear moduli will be spatially uniform and unaffected by fluid changes for the different patches as given by equation (2-26). Then the effective bulk modulus can be calculated using the so-called Hill's equation (Smith, Sondergeld, and Rai 2003)

$$K_H = \left[\sum_{i=1}^{N} \frac{x_i}{\left(K_i + \frac{4}{3}\mu\right)}\right]^{-1} - \frac{4}{3}\mu, \tag{2-31}$$

where N is the number of patches with different fluid content and K_i, is the saturated bulk modulus for i^{th} component given by Gassmann's equation (2-25) and x_i is the volume fraction of this component. The uniform (i.e., Gassmann-Wood) and patchy (i.e., Gassmann-Hill) bounds are given in Figure 2-8.

This means that partial saturation may occur depending on the combination of diffusion length scale and heterogeneity scale of the partially saturated formation. Taking the diffusivity and frequency as constants for a given case, the geometrical distribution of the fluids phases (e.g., brine and CO_2), that is whether the fluids are finely mixed or if CO_2 form patches, can result in a different seismic velocity response (Cairns et al. 2010). Alternatively, changing the frequency of the seismic wave can result in a different seismic velocity response. Thus, if the a patch size with $d \sim L_c$, then at such an intermediate frequency, patchy saturation models such as white White (1975) and the continuous random media (CRM) models (Toms et al. 2006) could be used to predict the seismic response of a partially saturated porous rock for the region between the GW and GH bounds in Figure 2-8.

White (1975) assumes that there are two concentric spheres with the volume of the outer sphere equals the volume of an elementary cube. The computed bulk modulus from White's model is an average and does not take into account gas pockets interactions (Carcione, Helle, and Pham 2003). Dutta and Odé (1979) proposed a more rigorous solution for White's model based on the pore-elastic equations of Biot (1962)

and they corrected White's model for the low-frequency limit. This modified model is referred to as White and Dutta-Odé (WDO) model.

All these models assume a regular distribution of fluids patches in the medium. However, it is known that fluids patches in case of injection into subsurface reservoirs will be dependent on many factors such as the heterogeneity of the rock (Müller and Gurevich 2004). Thus, a realistic approach is to introduce random patches rather than periodical which is geologically plausible.

Random distribution of fluids in a porous rock is considered more realistic and reasonable than periodic distribution in case of patchy saturation (Müller and Gurevich 2004, Toms, Mueller, and Gurevich 2007). Two models were developed to describe the effect of random distribution of mesoscopic fluid heterogeneities (Toms et al. 2006). The random patchy saturation model was developed as a 1D model where it described the system as an alternating fluids layers of random thicknesses by Müller and Gurevich (2004). Following this, a 3D random patchy saturation model was developed as an extension of the 1D model with a more realistic fluid patches system (Toms, Müller, and Gurevich 2005). The 1D patchy saturation dynamic-equivalent P-wave modulus $H_{1D}(\omega)$, is written by Müller and Gurevich (2004) as

$$H_{1D}(\omega) = H_{GW}\left[1 - isk_D \int_0^{\infty} B_{MM}(r) e^{ik_D r} dr\right], \qquad (2\text{-}32)$$

and the effective slow P-wave number (k_D) is given as

$$k_D = \sqrt{\frac{i\omega}{k}} \frac{\sum_{i=1}^{2} \sqrt{\eta_i N_i}\, S_i}{\sum_{i=1}^{2} N_i S_i}, \qquad (2\text{-}33)$$

where S_i is the saturation of the ith fluid phase and N_i is the poroelastic coefficient of the ith fluid phase. s characterizes the degree of inhomogeneity of the medium as

$$s = \frac{H_{GH}}{H_{GW}} - 1, \qquad (2\text{-}34)$$

with H_{GH} and H_{GW} as the P-wave modulus of the Gassmann-Wood and Gassmann-Hill theories, respectively.

The 1D model generalized for the 3D porous medium effective frequency-dependent P-wave modulus given by Toms, Mueller, and Gurevich (2007) as

$$H_{3D}(\omega) = H_0\left(1 - \Delta_2\Delta_1 k_D^2 \int_0^\infty B_{MM}(r)e^{ik_D r}dr\right)^2, \qquad (2\text{-}35)$$

with H_0 as the undrained P-wave modulus of the homogenous poroelastic background medium supporting k_D. The dimensionless coefficients are given as

$$\Delta_1 = \frac{L}{H}\,\Delta_2 \quad \text{with} \quad \Delta_2 = \frac{\alpha^2 M \sigma_{MM}^2}{2H}, \qquad (2\text{-}36)$$

with σ_{MM} as the normalized variance of the fluid storage coefficient.

The given effective P-wave modulus in equation (2-35) is only valid for weak contrast in the fluid moduli. Toms, Mueller, and Gurevich (2007) derived the effective P-wave modulus by introducing a scaling factor function as

$$H_{SC} = H_{GW}\left[1 + \frac{H_{GH} - H_{GW}}{H_{high} - H_{low}}\,\frac{H_{eff} - H_{low}}{H_{GW}}\right], \qquad (2\text{-}37)$$

with H_{low} and H_{high} as the low and high-frequency limits derived from H_{eff} given by

$$H_{low} = H_0(\Delta_2 - 1)^2,\ H_{high} = H_0(1 - \Delta_2 + \Delta_1)^2. \qquad (2\text{-}38)$$

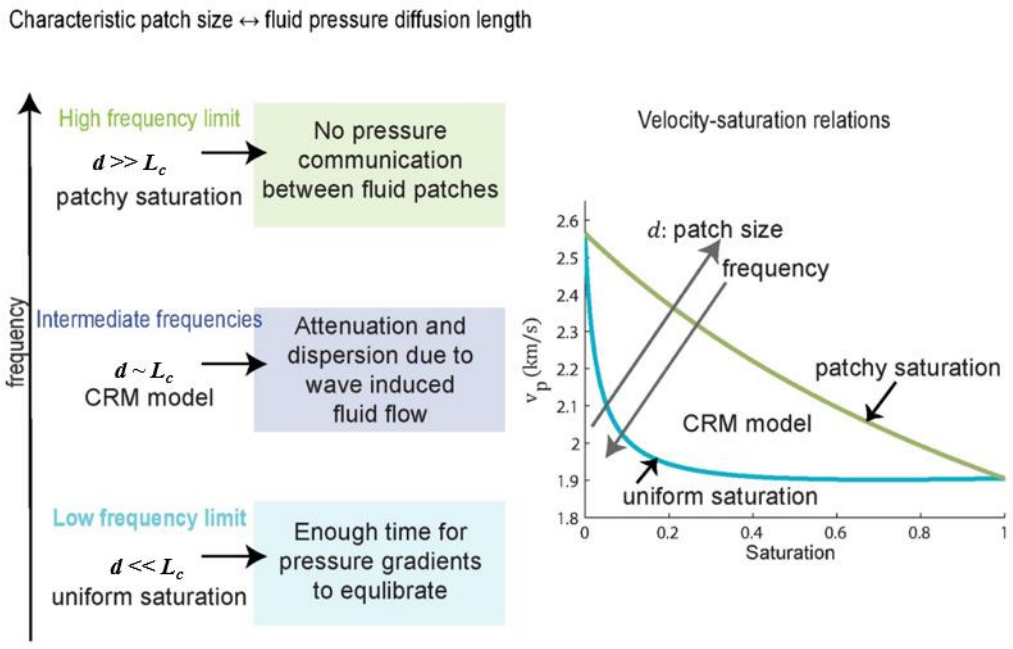

Figure 2-8: Velocity-saturation relations classifications used in this research. From Caspari (2013).

2.5 SEISMIC THEORY AND ELASTIC WAVES

We summarise here some of the concept of the elastic waves, seismic modelling and modelling softwares utilized in this research. Seismic waves travel through the earth as a spherical wave that propagates outward from a seismic source. The velocities of seismic waves in a homogeneous elastic medium are expressed simply as:

$$V_P = \sqrt{\frac{K + {}^{4}/_{3}\mu}{\rho}}, \tag{2-39}$$

and

$$V_S = \sqrt{\frac{\mu}{\rho}}, \tag{2-40}$$

with V_P and V_S as the compressional and shear wave's velocities respectively. K, μ and ρ representing the bulk modulus, shear modulus and density of the rock.

The seismic wave decays due to two reasons, first is due to spherical spreading or spherical divergence with the seismic energy being inversely proportional to the square of the distance from the source. Second, the seismic energy may be attenuated by various attenuation mechanisms such as intrinsic attenuation or scattering. When the seismic energy reaches an interface between two half-spaces, for normal incidence with the acoustic impedance of the first layer as $I_{P1}=\rho_1 V_{P1}$ and the second layer as $I_{P2}=\rho_2 V_{P2}$, then the transmission coefficient (T_p) at normal incidence is defined as

$$T_p = \frac{2I_{P1}}{I_{P2}+I_{P1}}. \tag{2-41}$$

The P-wave reflection coefficient R_p at the layer's boundary is defined as

$$R_p = \frac{I_{P2} - I_{P1}}{I_{P2} + I_{P1}}, \tag{2-42}$$

then,

$$R_p + T_p = 1. \tag{2-43}$$

For non-normal incident and elastic medium, the reflection and transmission equations that governs their amplitude are given exactly by Zoeppritz equations (Yilmaz 2001b). The treatment of these equations and their approximations are beyond the scope of this

review and the theoretical treatment and a practical usage of these approximation can be found in many publications (Aki and Richards 1980, Avseth, Mukerji, and Mavko 2010).

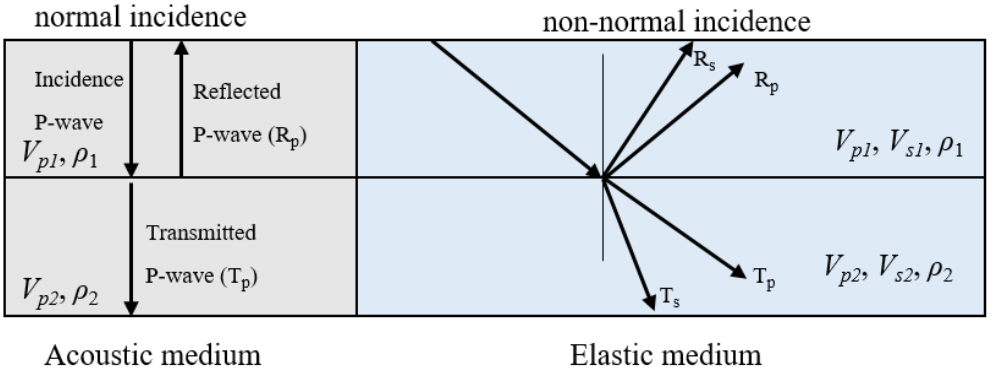

Figure 2-9: Wave types in the acoustic and elastic medium.

2.5.1 Seismic modelling

Seismic waves travel through the earth in a complex manner. In active seismic methods, the seismic waves are generated by a source (e.g., hammer, air gun, vibrator etc.) and travel through the earth, then recorded by seismic receivers. The recorded waves have information about the subsurface, normally in the form of reflection amplitudes. The Earth is bound to have complex features such as faults, salt diapers, pitchouts of sedimentary layer (geological) or those made by subsurface activities such as oil and gas production or enhanced oil recovery and sequestration of CO_2, etc. To be able to understand these subsurface features we need to model the seismic response of the subsurface.

For this, several physical models have been developed to describe seismic wave propagation in the subsurface to perform seismic modelling; that is the acoustic and the elastic wave models. The acoustic model ignores coupling between P-waves and S-waves while the elastic model accounts for this coupling and provide a more realistic treatment of wave propagation in the subsurface. Seismic modelling is one of the most powerful tools in seismic interpretation. It allows us to predict the seismic response recorded by seismic receivers if we provided a model of the subsurface that is 1D, 2D or 3D model (Kosloff and Kessler 1990). Three main seismic modelling categories are commonly used based on the way they approach solving or approximating the wave equation and assumptions about the wave propagation. These are, direct methods,

geometrical optics methods and analytical methods. A description of each method is beyond the scope of this review, but one could refer to Kosloff and Kessler (1990) for more details. We will emphasise here only on the direct methods that employ approximations of the wave equation solution in a predefined discretised numerical grid that is given by a finite numbers of points (Kosloff and Kessler 1990). The advantage of such approach is that if the grids are sufficiently fine, a high accuracy solution is obtained. However, this is computationally very costly. The finite-difference (FD) or full-waveform modelling is one of the mostly used direct methods in seismic modelling. The method entails the discretization of both space and time variables. For further treatment of the finite-difference modelling method several publications are available (e.g., Carcione, Herman, and Ten Kroode 2002, Kosloff and Kessler 1990).We provide next a description of the elastic modelling schemes for the software packages used in this research.

2.5.2 Seismic modelling software

In order to study the effect of velocity-saturation relation and heterogeneity scale and compare that to field data synthetic modelling is essential. Initially, we used a 1.5D full waveform elastic modelling provided in the OASES software for horizontally stratified media (Schmidt and Tango 1986). The software package is a numerical solution of the elastic wave propagation in a stratified medium for homogenous and isotropic layers (Schmidt and Tango 1986). The code accounts for 3D wave propagation effects, however, because of the underlying simplified horizontal layering it cannot account for wavefield from complex structural geological features such as dipping, synclines or truncation and those caused by fluids injection into the subsurface, such as CO_2 plumes of finite extent. For this reason, after using OASES in the initial research we have seen the need to extended the work to stimulate a 2D Earth model which account for the limited extent of the CO_2 plume (Al Hosni, Caspari, et al. 2015). Moreover, although the OASES code allows the calculation for the poroelastic wave equation (specifically, dispersion and attenuation of the fast P-wave caused by mode conversion between the fast and slow P-waves) it will not be utilized in this research as previous work on similar scenarios have shown that the poroelastic effects on the seismic waves are negligible, at least for small-scale heterogeneities (Caspari et al. 2015).

Finite-difference modelling is widely used to solve the elastic waves equation for 2D and 3D models of the subsurface. In this research we utilize Tesseral® seismic modelling software for 2D and 2.5D full-waveform elastic seismic modelling. A full description of the finite-difference full waveform modelling approach in Tesseral® is given in Technologies' (2012).The 2.5D modelling simulates 3D wave propagation in a 2D Earth. Thus, 2.5D modelling offer a correct 3D response (given that the true subsurface is constant along Y, which is approximately adequate for many sedimentary basins). A complete treatment of the 2.5D modelling method is provided in (Costa, Neto, and Novais 2006, Kostyukevych et al. 2008, Xiong et al. 2013).

Although 2D and 2.5D modelling provides the ability to model the finite plume extent, it does not account for the full 3D geometry of the plume (i.e., out of plane reflections, transmission and diffractions etc.) which are not present in the 2D model itself. Thus, for a true subsurface 3D wave propagation response the model must be built correctly in a 3D space. Thus, in this research synthetic data created using a full 3D waveform modelling for the Otway 2C project are used as the requirements to build a realistic 3D model of the subsurface were available. The modelling is performed by using the open source SOFI3D seismic modelling with finite-difference (Bohlen et al. 2015, Bohlen 2002) using the supercomputing facility provided by Pawsey Supercomputing Centre. The time-lapse 3D (4D) finite-difference modelling aspects as provided for this research (Chapter 7) are given in Glubokovskikh et al. (2016).

2.6 VERTICAL SEISMIC PROFILING (VSP): METHOD, PROCESSING AND RESOLUTION

Most of the research in this thesis is based on the analysis of Vertical Seismic Profile (VSP) data. VSP is a seismic method where sensors are set in a borehole and sources are set on or close to the surface. It provides a high-resolution image of the subsurface near the borehole where the measurement is being taken. An advantage of VSP compared to surface seismic methods is that both downgoing and upgoing wavefields can be recorded, thus more information is obtained about the subsurface. The downgoing and upgoing wavefields are identified according to their travel time as shown in Figure 2-10. The VSP method provides better vertical and horizontal resolution than surface seismic in most cases, as the frequency content is higher and receivers are placed close the reflectors. Moreover, VSP can provide crucial

information about the seismic velocities of the subsurface (from direct arrivals) which are essential for time to depth conversion (seismic-to-well tie) and for calibrating sonic well logs velocities. For this reason, in the field of CO_2 sequestration, VSP is an essential option especially for small scale injection or at the early stages of injection when the injection volume is small.

Conversely, the VSP method have some limitations in that the spatial coverage of VSP method is limited based on the well and shot location. Moreover, using time-lapse VSP for reservoir characterization is not trivial as VSP images different part of the subsurface for each source-receiver pair and due to the lack of redundancy "fold" in the data. Typically, 3D VSP is used to overcome some of these challenges (O'Brien, Kilbride, and Lim 2004), nevertheless, still if the object to be imaged is of large lateral extent, then surface seismic is a preferred choice. For pilot CCS projects, the objective is to perform high-resolution characterization of the CO_2 effect in the subsurface and the lateral extent of the CO_2 plume is expected to be small, thus, VSP method is the preferred tool.

In this section, we go through the main processing steps for VSP data (zero-offset or offset). The processing steps discussed are essential for single vintage or time-lapse processing. These processes can be summarized as first arrivals picking, wavefield separation of upgoing and downgoing, NMO correction or migration (if applicable). Moreover, the resolution of the VSP method is discussed thoroughly as it is of interest in this research.

2.6.1 Picking First arrivals and horizontal components orientation

First arrival picking is one of the most crucial steps in the processing of VSP data. A great effort is done to ensure the picks will flat the direct arrival for subsequent steps such as extraction of wavelet for deconvolution and spatial filtering for upgoing waves separation. For dynamite sources, the wavelet is treated as minimum phase and the first arrivals are picked at the onset of the seismic signal (energy) as it provides the true propagation time (Chen et al. 2013). This picking criterion means that we are ignoring absorption and attenuation effects on the velocity (Chen et al. 2013), however for processing the VSP it flattens the downgoing wavefield and allow for their separation (subtraction) with median filtering.

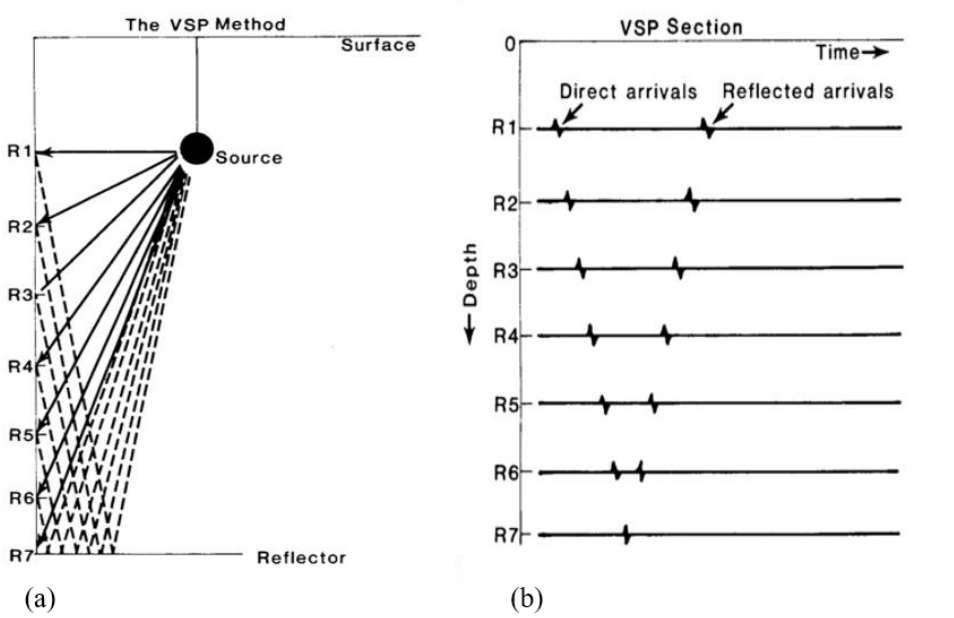

Figure 2-10: (a) Schematic diagram of a typical vertical seismic profiling experiment. (b) Ideal data set for the diagram in (a). From Balch et al. (1982).

A common processing step for multi-component VSP processing is the orientation of the components. This step is performed to remove tool rotation and bring all recorded wavefield to a similar orientation (Kramer 1996). The orientation is carried out after Hodogram analysis of the P-wave first arrivals which allow determining the polarization of the particle motion in the horizontal plane (Kramer 1996).

2.6.2 Upgoing wavefield separation

This is the main step after first break picking to obtain reflections (upgoing wavefield) from VSP data. The main approach in separation the upgoing wavefield from the downgoing is using median filtering (Kommedal and Tjøstheim 1989). In this work, we use the Alpha-Trimmed mean filter instead of median filtering. The filter is a sliding window with a given length L where the alpha-trimmed mean is calculated by sorting the input values within the window in an ascending order then removing a fixed fraction α ($0 \leq \alpha \leq 0.5$) from both ends. The mean is then calculated for the remaining values (Bednar and Watt 1984). This approach reduces the effect of outliers (which could be amplitude spikes in the signal, such as a faulty geophone), thus usually providing better stable results. An example of the difference between using a median filter and alpha-trimmed mean filter is shown in Figure 2-11 with the same length of operator L. In this research we refer to both methods as median filtering for simplicity.

The VSP data is flattened using the time picks for P-waves first arrivals (downgoing), S-waves or any unwanted coherent signal. Then the value calculated from the filter operator is subtracted from the data. An example of the subtraction of downgoing waves is shown in Figure 2-12. Other methods of wave separation could also be used such as *f-k* filtering (frequency-wavenumber filtering). *f-k* fileting allows separating coherent events in the frequency-wavenumber domain by passing or rejecting the energy between two apparent velocities (Kommedal and Tjøstheim 1989). A more comprehensive review of *f-k* filtering is given in (Yilmaz 2001a, Kommedal and Tjøstheim 1989).

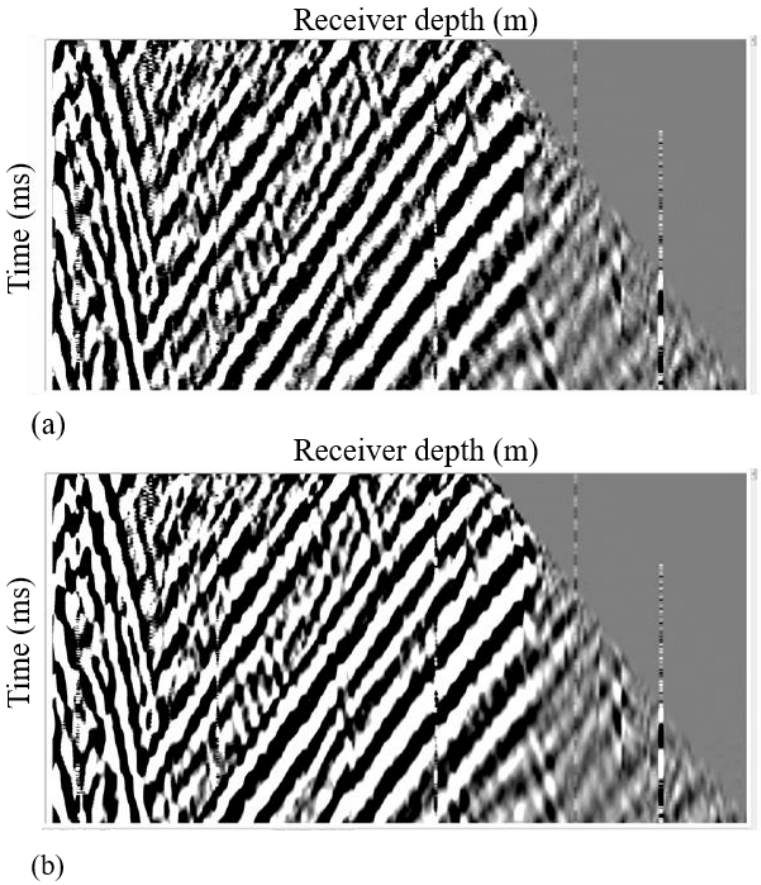

Figure 2-11: An Example showing the difference in the results of waves separation using (a) median filter and (b) alpha-trimmed mean filter with α=0.3. (b) Shows less smeared results and better continuity of events.

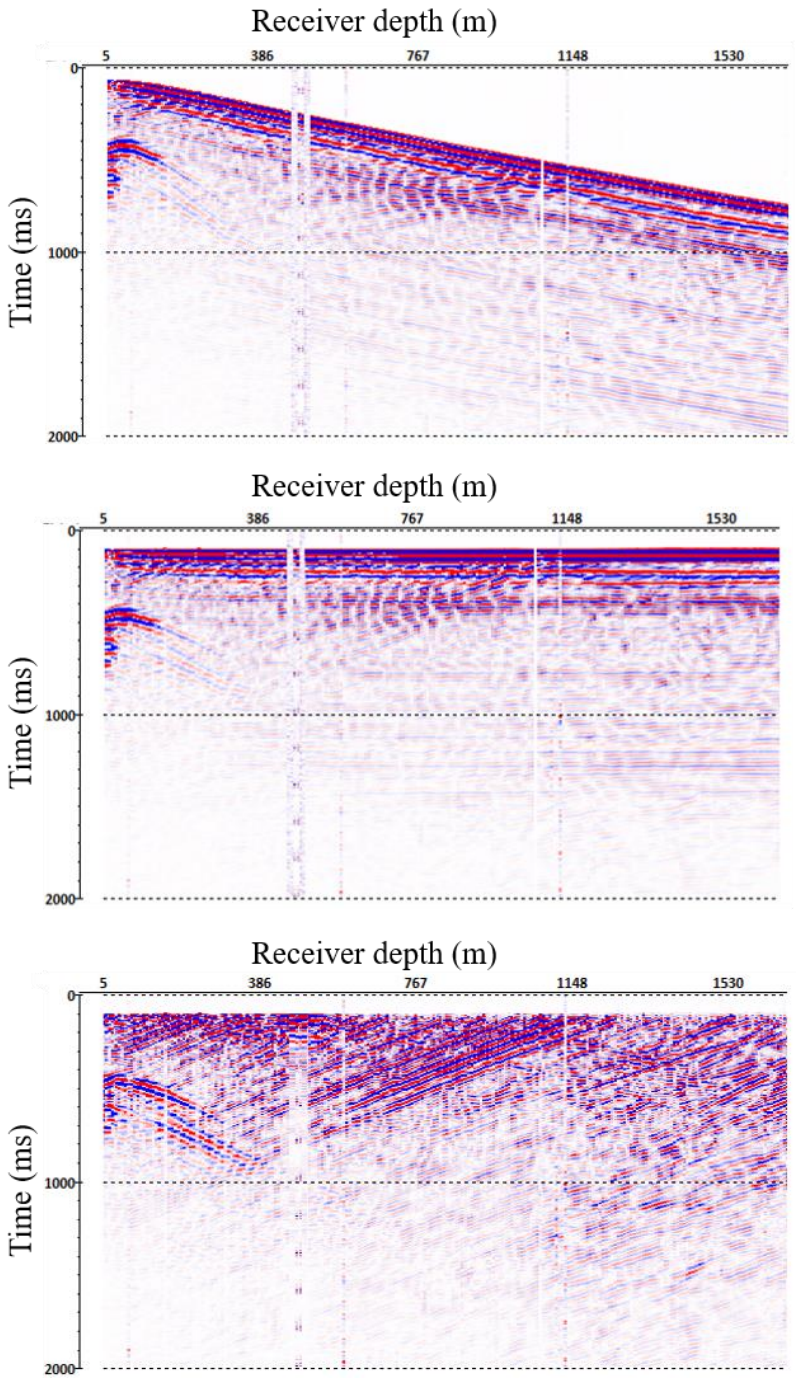

Figure 2-12: Upgoing waves separation. (a) Raw shot, (b) flattened using P-waves first-breaks and (c) results after applying an alpha-trimmed filter.

2.6.3 Deconvolution

Deconvolution is mainly utilized for multiple elimination and enhancing the frequency content of the data. To perform the deconvolution operator on the upgoing wavefield the wavelet of the source is required. Fortunately, in the case of VSP the source wavelet could be extracted from the first arrivals (downgoing wavefield). This is done by flatting the data using the first arrivals picks and summing over an N number of traces. In this summation the coherent signal is enhanced while the non-coherent signal is attenuated. A comprehensive review of deconvolution is found in Yilmaz (2001a).

2.6.4 Velocity analysis

In VSP records the P-wave velocity can be easily calculated from the traveltime of the first arrivals picks. Similarly, interval S-wave velocities could be obtained using the time picks of the S-wave. The velocity obtained is the interval velocity (V_{inter}). It is calculated between any two receivers at depths d_1 and d_2 respectively (for a vertical well) and the travel time pick for the seismic wave (event) at for the same receivers t_1 and t_2, respectively, as:

$$V_{inter} = \frac{|\, d_2 - d_1|}{|t_2 - t_1|} \qquad (2\text{-}44)$$

The velocity obtained depends on the accuracy of the first breaks pick performed and the depth interval used for the calculations. If the receivers used are further apart the interval velocity obtained is smoother, lower in resolution and less sensitive to the accuracy of the time picks. However, if the interval is small, then the interval velocity will be very sensitive to the accuracy of the time picks.

2.6.5 VSP-CDP transform and VSP migration

An important information in the VSP data is the location in the subsurface from which the recorded reflection originated. This is can be done by either a simple VSP-CDP transformation or by performing migration (Wiggins, Ng, and Manzur 1986). VSP-CDP mapping utilizes the velocity structure from either VSP or well logs to position the recorded reflections to its supposed subsurface position. The assumptions involved are that the velocity structure is correct and the recorded event comes from one single point in space (Wiggins, Ng, and Manzur 1986). These limitations appear useful as they can aid building the velocity model which best agree with the reflected

events (Wiggins, Ng, and Manzur 1986). VSP migration is more powerful than VSP-CDP transform in that it can handle dips, and it is supposed to map reflection to their true subsurface position given a correct velocity field of the subsurface (Wiggins, Ng, and Manzur 1986). A comprehensive treatment of VSP-CDP transform and migration could be found in the in the following literature (Hardage 1985, Wiggins, Ng, and Manzur 1986, Chen et al. 2000).

2.6.6 Repeatability analysis

To get an estimate of the repeatability of our time-lapse reflected data and the time-lapse signal caused by the injected CO_2, we use the NRMS (Kragh and Christie 2002) for the seismic sections for the base and repeat surveys as

$$NRMS = 200\ \frac{RMS(repeat - base)}{[RMS(repeat) + RMS(base)]} \qquad (2\text{-}45)$$

and the root mean square (RMS) of a seismic trace (x_t) for a number of samples in a time window (N) is defined as

$$RMS(x_t) = \sqrt{\frac{\sum_{t_2}^{t_1}(x_t)^2}{N}} \qquad (2\text{-}46)$$

The NRMS repeatability metric is a very sensitive method to changes in the seismic signal (Picotti et al. 2012). The range of NRMS values spans from 0% to 200% for similar form and polarity wavelet and opposite polarity wavelet, respectively. Thus, it provides quantitative information about the time-lapse signal in comparison to the background noise. In general, if the time-lapse signal NRMS values are smaller than the background noise level, quantitative interpretation becomes unviable.

2.6.7 VSP method resolution

The resolution of any seismic method is important if we would like to interpret the seismic amplitudes quantitatively. The bandlimited nature of the seismic waves and their shape imposes a limit on our ability to resolve objects in the subsurface

(Simm, Bacon, and Bacon 2014). In many cases, when referred to seismic resolution, one would think in the vertical resolution, that is resolving "thin beds". However, when dealing with situations such as injection of CO_2, production and EOR for which the lateral extent of their effect is small, the lateral resolution becomes an important factor.

2.6.7.1 Vertical resolution

Vertical resolution governs the ability to resolve two reflections vertically. The wavelength (λ) is governed by the frequency of the seismic wave (f), the velocity of the medium (v) as

$$\lambda = \frac{v}{f}, \tag{2-47}$$

then, as a rule of thumb, the vertical resolution is set to be equal to the tuning thickness that is

$$tuning\ thickness = \frac{\lambda}{4} \tag{2-48}$$

The tuning thickness is that where the amplitude response is largest, that is the maximum constructive interference between the top and bottom reflections of a reservoir (Avseth, Mukerji, and Mavko 2010).

Detectability is another term that is also of importance when trying to "see" a high contrast layer or "anomaly" in the subsurface. In this case, although this thin layer or "anomaly" is not totally resolved, we are able "detect" its response from the background (Simm, Bacon, and Bacon 2014). The detectability limit depends largely on the signal-to-noise ratio of the data and the magnitude of the acoustic impedance contrast (Simm, Bacon, and Bacon 2014). Detectability limits for gas (in sand) have been reported to be about $\lambda/20$ to $\lambda/30$ (Simm, Bacon, and Bacon 2014). Thus, for CO_2 injection into high porosity brine formations the detectability is expected to be high due to the large impedance contrast expected between brine saturated and CO_2 saturation porous rocks. In many cases, a wedge model is used to investigate the vertical resolution or tuning thickness and detectability of thin beds and their seismic response as shown in Figure 2-13.

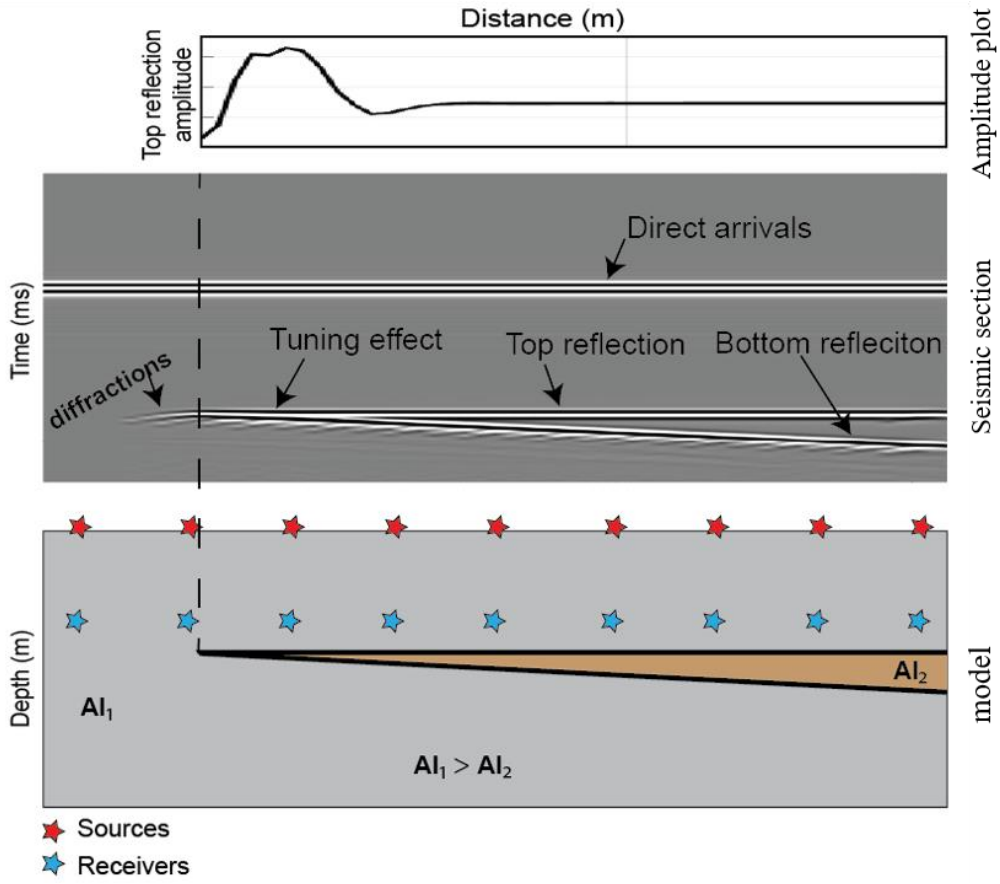

Figure 2-13: A drawing of a wedge model example for the tuning effect on the seismic amplitude for multiple zero-offset VSP experiments. At some thickness (tuning thickness) a maximum constructive interference occur, indicated by the peak in the reflection amplitude plot (top).

2.6.7.2 Horizontal resolution

The horizontal resolution of seismic methods is dependent of the Fresnel zone. The Fresnel zone defines the area in which diffractions energy interfere constructively to produce a reflection (Sun and Bancroft 2002). Broadband data synthetic studies have shown that the reflection response is independent of the reflector size if it is larger than the Fresnel zone (Spetzler and Snieder 2004). However, if the reflector size is smaller than the size of the first Fresnel zone interference between primary and diffractions from edges occur depending on the size of the Fresnel zone and the arrival time of the primary and diffractions (Knapp 1991). The first Fresnel zone in VSP at zero offset assuming constant velocity for a horizontal reflector is given by Hardage (1985) as

$$r^2 = \lambda \frac{ab}{a+b}, \tag{2-49}$$

where r is the radius of the first Fresnel zone, a is the source-to-reflector distance, b is the reflector-to-geophone distance and λ is the wavelength of the seismic wavelet, see Figure 2-14. This equation is only valid where a and b are much larger than λ and r.

For the purpose of this research, as an approximation we use equation (2-49) to estimate the Fresnel zone, as diffraction and Fresnel zone volume analysis are beyond the scope of this research. The amplitude evolution as the reflector approaches the Fresnel zone radius is shown in Figure 2-15.

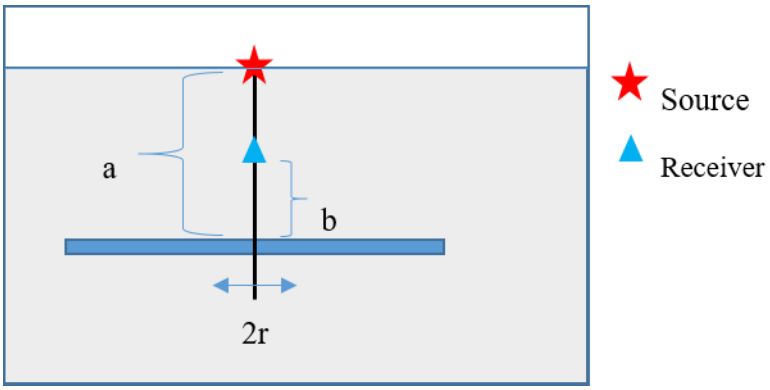

Figure 2-14: Illustration of the Fresnel zone for zero-offset VSP case for a constant velocity media.

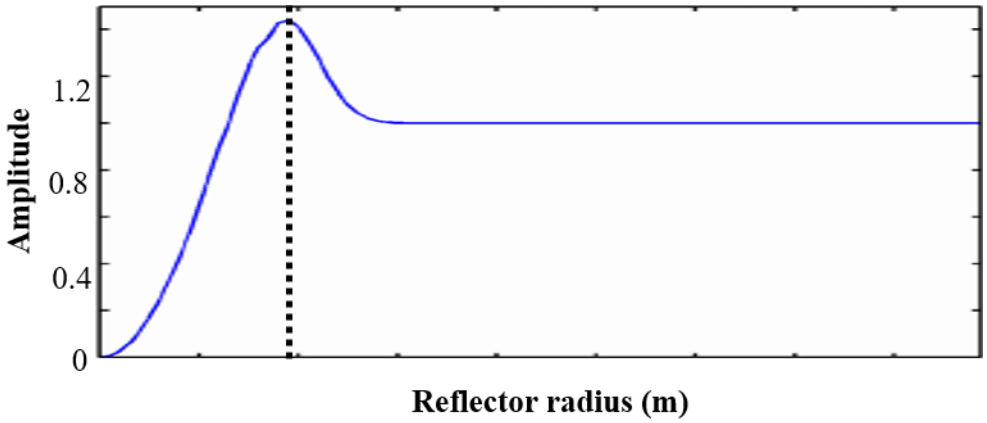

Figure 2-15: Illustration of the amplitude evolution in zero-offset VSP case as the reflector radius changes. The peak amplitude corresponds to the radius of the Fresnel zone with maximum constructive interference occurring. Modified from (Sun and Bancroft 2002).

2.7 CROSSWELL SEISMIC

The need for high-resolution images of the subsurface for reservoir characterization is more important than ever for more detailed understanding of the reservoir behaviour in oil production and CO_2 injection. Crosswell seismic surveys were an answer to this need. Crosswell seismic is a method where seismic sources are place in a well while the receivers are located in another well. Figure 2-16 shows a schematic of a typical crosswell survey. This results in a high-resolution image of the rock mass between wells thus avoiding attenuation of high frequencies by the overburden compared to other seismic measurements such as surface seismic and VSP (Stewart and Domenico 1991). The operational disadvantages of crosswell seismic involve first the need of two boreholes within a short distance from each other's. Second, only the plane between the two wells utilized in the survey is imaged, thus restricting the coverage. Third, is the difficulty of using seismic sources in borehole conditions and depth at which the sources and receivers could be deployed (Stewart and Domenico 1991).

The processing of crosswell seismic usually involves picking the first arrivals for tomographic traveltime inversion. Traveltime tomography is used to obtain a map of seismic velocities in the rock volume that is covered by the seismic raypaths (Ivansson 1986). The main source of uncertainty and errors in the traveltime

tomography are related to the raypath coverage, inversion method and the signal-to-noise ratio in the picking of the traveltime data (Zhou et al. 1993). Common the case, the tomographic inversion is challenged by the non-uniqueness of the solution and that sharp changes in velocity may not be accurately resolved (Guoping 1994). A thorough treatment of the crosswell method, picking first arrivals and tomography is available in several publications (e.g., Hardage 1992, Bregman, Bailey, and Chapman 1989, Peterson, Paulsson, and McEvilly 1985, Zhou et al. 1993).

In CCS sites, crosswell seismic imaging have proven to be very successful as a tool for imaging CO_2 plume as it provide high-resolution data for reservoir characterization (Freifeld et al. 2009). Recent studies in many pilot CO_2 injection project have successfully utilized the method to infer velocity changes and ultimately estimate CO_2 saturation (Daley et al. 2008, Onishi et al. 2009, Ajo-Franklin et al. 2013, Saito et al. 2006).

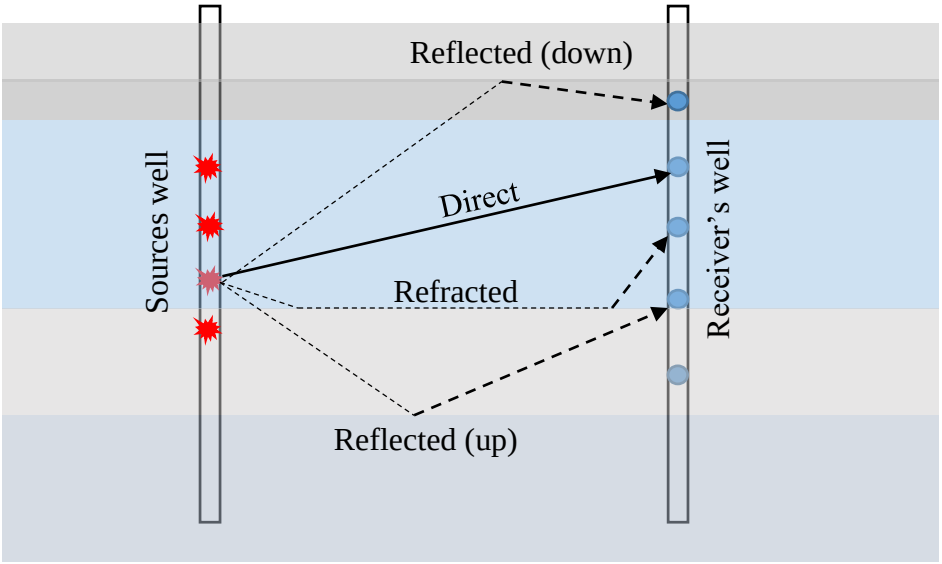

Figure 2-16: Schematic diagram of a typical crosswell seismic experiment design and seismic raypaths. From Stewart and Domenico (1991).

CHAPTER 3. FRIO BRINE PILOT PROJECT

Many CO_2 sequestration projects were initiated in the last decade (Michael et al. 2010). Small-scale pilot projects are of special interest because of the detailed information obtained and rigorous analysis of data to demonstrate the ability to monitor effectively CO_2 in the subsurface using various technologies. One of the initial stages of any carbon dioxide sequestration project is to determine the reservoir properties and its applicability to CO_2 storage. Deep saline aquifers have the largest CO_2 capacity for worldwide sequestration solutions and are considered less challenging for monitoring purposes compared to injection into depleted hydrocarbon reservoirs (Michael et al. 2010).

Traditional seismic monitoring techniques such as 4D surface seismic, time-lapse VSP and crosswell need to be assessed within the schemes of each CO_2 sequestration project. To establish a relationship between geophysical data (e.g., seismic, well logs, etc.) and reservoir petrophysical properties of interest (i.e., saturations) an understanding of the reservoir rock physics model is required. This includes the rock frame, pore fluids and their interaction. Each measurement scale could provide complimentary information to verify and refine the theoretical models used and subsequent interpretation of the seismic data. To this end, integration of geophysical data from different scales will be essential.

The Frio Brine Pilot CO_2 injection project (from here referred to as Frio project) was heavily instrumented with traditional and novel monitoring technologies (e.g., saturation logs, fluids sampling, time-lapse crosswell and VSP). Moreover, several laboratory measurements were taken including core porosity, permeability and thin section analysis. As we have discussed previously, the velocity-saturation relation and saturation estimates are still not well understood in this site (Doughty, Freifeld, and Trautz 2008). Moreover, previous studies have shown large change in P-wave and S-wave velocities upon CO_2 injection (Daley et al. 2008).

In this chapter, we introduce a comprehensive review and analysis of the Frio project available data from the literature. This includes geological and petrophysical data from previous studies. The work includes both literature review and my analysis

of the data for subsequent research objectives in Chapter 4, 5 and Chapter 6 as outlined earlier in Chapter 1.

3.1 PROJECT BACKGROUND

The Frio project took place in Dayton, Texas (United States of America) at the South Liberty field, see Figure 3-1. The project aimed at the injection of about 1600 tons of supercritical CO_2 into the Frio Formation "C" sandstone interval over the period of 10 days. Two wells were used, which are around 30 m apart on the surface; one well served as an injection well and the other as an observation well (Daley et al. 2008).

The injection well, Frio Brine Pilot Test TCEQ No.5X2500071 was drilled in May 2004. The well was cased from the surface to a depth of 813 m for initial logging and core recovery. The observation well that is an inactive oil well was drilled during the 1950s (Sun Gulf Humble Fee 4) with only legacy electrical logs. The well was originally producing from a deeper interval than the proposed injection depth for CO_2 and has a total depth of about 2717 m. Thus, the well was plugged back at a lower interval to separate it from the CO_2 injection interval used in the experiment. Thus, the producing interval did not interact with the interval of interest for the Frio experiment and the well casing, and cement integrity has been verified as being in good condition (Sakurai et al. 2006, Kharaka et al. 2009).

The Frio "C" sandstone perforation is about 6 m thick in the depth range of 1528 -1534 m at the observation well. In the newly drilled injection well that is 30 m, down-dip the Frio "C" sandstone perforation is set between 1541-1546 m giving a total perforation interval of about 5 m. This choice of perforation interval was based on the log data that suggested the presence of a low permeability layer at the depth of 1546.5 m at the injection well (Doughty, Freifeld, and Trautz 2008). However, after injection saturation logs and crosswell analysis suggested that the CO_2 migrated below the lower shaley-sand layer as shown in the schematic in Figure 3-2. The logs for the injection well cover the interval between 1115 – 1745 m (MD), except for the density logs that goes almost up to the surface.

The Frio formation used as an injection unit is part of a regional aquifer that covers vast areas in the US Gulf Coast (Kharaka et al. 2009). The Frio "C" unit used

for CO_2 injection is a high porosity and high permeability poorly consolidated sandy layer and is fully brine bearing with no hydrocarbon, thus no hydrocarbon complexities are involved (Hovorka and Knox 2003).

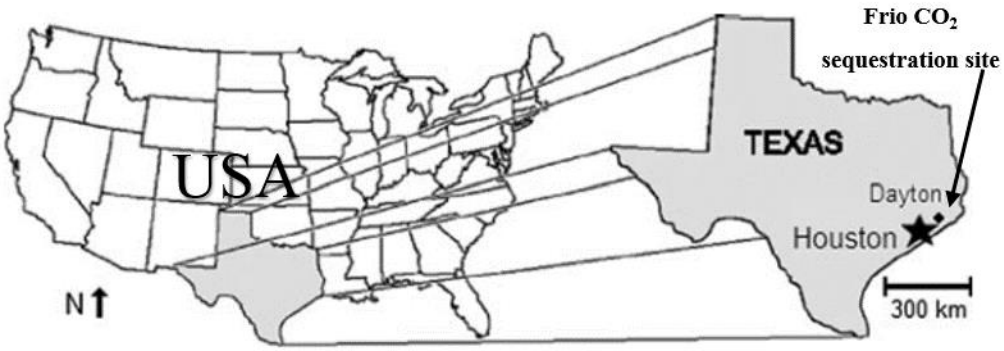

Figure 3-1: Map showing the location of the Frio brine pilot, in Dayton South Liberty field, from Doughty, Freifeld, and Trautz (2008).

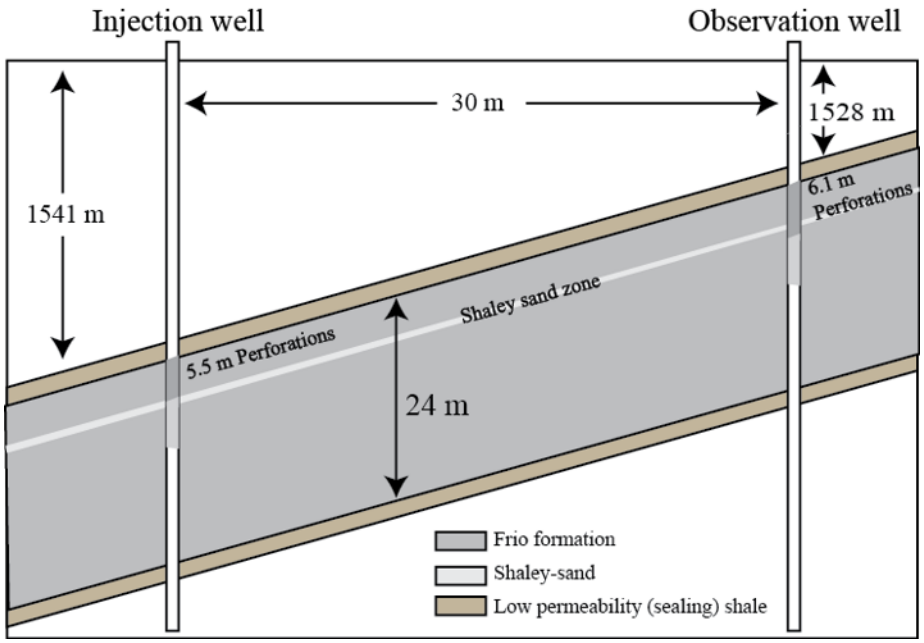

Figure 3-2: The Frio experiment, wells and perforation zones shown.

Several papers have been published on the Frio pilot site. Comprehensive analysis of the time-lapse seismic surveys and geochemical monitoring performed are available in several publications (e.g., Daley et al. 2008, Doughty, Freifeld, and Trautz

2008, Daley, Myer, and Majer 2005, Hovorka, Benson, et al. 2006, Kharaka et al. 2006). However, a site-specific rock physics model was not created for the Frio formation and the velocity-saturation relation was not constrained. This was due to limited availability of data during initial project research (Daley et al. 2008). The main data sets analysed for the Frio brine pilot as summarised in Figure 3-3 are:

- Core data.
- Well logs.
- Crosswell (Time-lapse).
- VSP (Time-lapse).

We note here that the previous studies although concluded the ability of monitoring CO_2 in the subsurface at the Frio-I project using several geophysical methods, quantitative analysis of the results were challenged by the following:

- Absence of a site-specific rock physics model (rock frame elastic properties).
- The type of velocity-saturation relation (patchy or uniform fluid distribution) is not known.
- Possibility of rock frame changes.
- Reservoir modelling results suggest a limited size of the CO_2 plume (Ghomian, Pope, and Sepehrnoori 2008) which could be smaller than the vertical and horizontal resolution of the VSP method, thus time-lapse VSP interpretation is expected to be challenging, especially for reflection amplitudes.

Thus, we integrate several data sets for quantitative interpretation, starting by examining the geological and petrophysical data separately in this chapter, while the seismic data is processed and interpreted in Chapter 4, and the rock physics models constrained using these data are given in Chapter 5 and Chapter 6.

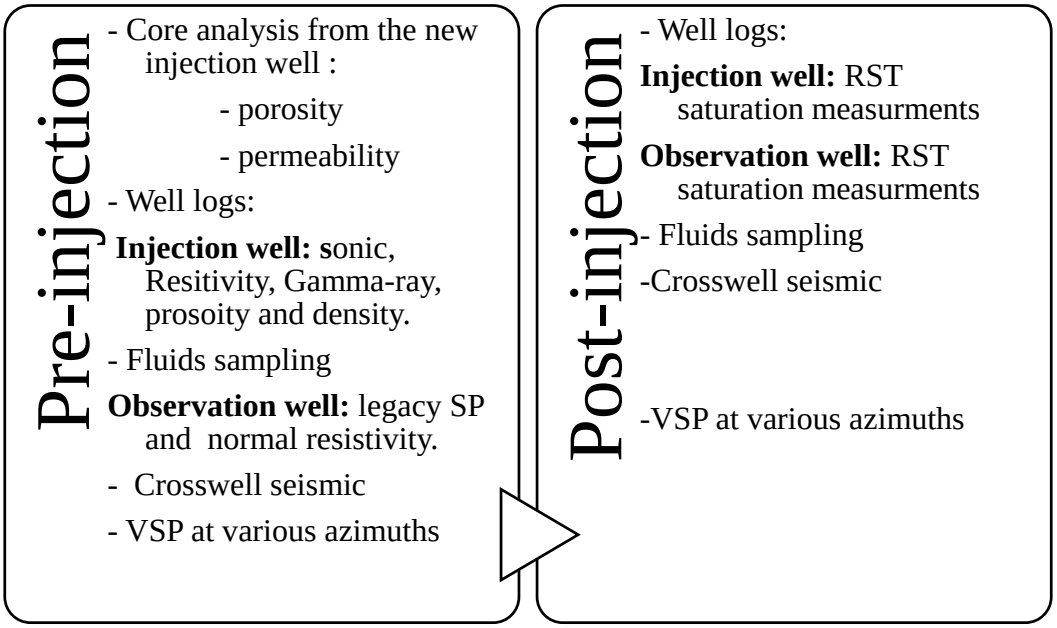

Figure 3-3: Data available for the Frio-I brine pilot project before and after injection (Utilized for this research).

3.2 GEOLOGICAL REVIEW

The Frio formation is a fluvial-deltaic deposited in the Oligocene epoch (Galloway, Hobday, and Magara 1982). The Frio "C" sandstone is about 24 m thick, which covers the depth of interest in this project. The formation at the injection interval is characterized by a fine moderately sorted sandstone with complex mineralogy and is poorly indurated. The upper part of the Frio "C" is part of a cross-bedded fluvial system while the lower part of the injection interval is a low permeability marine burrowed flooding surface (Hovorka, Doughty, and Holtz 2004).

The Frio formation is under the thick Anahuac Formation, which acts as a regional seal in the area. In addition, a local seal of thickness 0.6 - 1 m is present above the injection interval, which is composed of shale as we have shown in Figure 3-2. This minor seal is part of the Frio "C" interval and is expected to also act as a barrier of CO_2 migration upward to the overlying thin sandstone layer used as a monitoring layer for CO_2 leakage, (Hovorka, Sakurai, et al. 2006). The 3D seismic survey covering the area showed that the formation is within a fault-bounded compartments above the flank of a salt dome (Hovorka, Sakurai, et al. 2006, Hovorka and Knox 2003). The fault block is estimated to be around 800 m in width and about 2500 m in length

(Doughty, Freifeld, and Trautz 2008), see Figure 3-4. The mineral composition of the sandstone inferred from thin-sections is that it is mainly quartz with around 20% orthoclase and plagioclase feldspar and some altered rock fragments; Other minor components include calcite, micas, organic material, clay and local matrix (Hovorka, Benson, et al. 2006). The Frio "C" injection zone interval (top 10 meters) have minor amounts of illite/smectite, calcite, and iron oxyhydroxides (Kharaka et al. 2009).

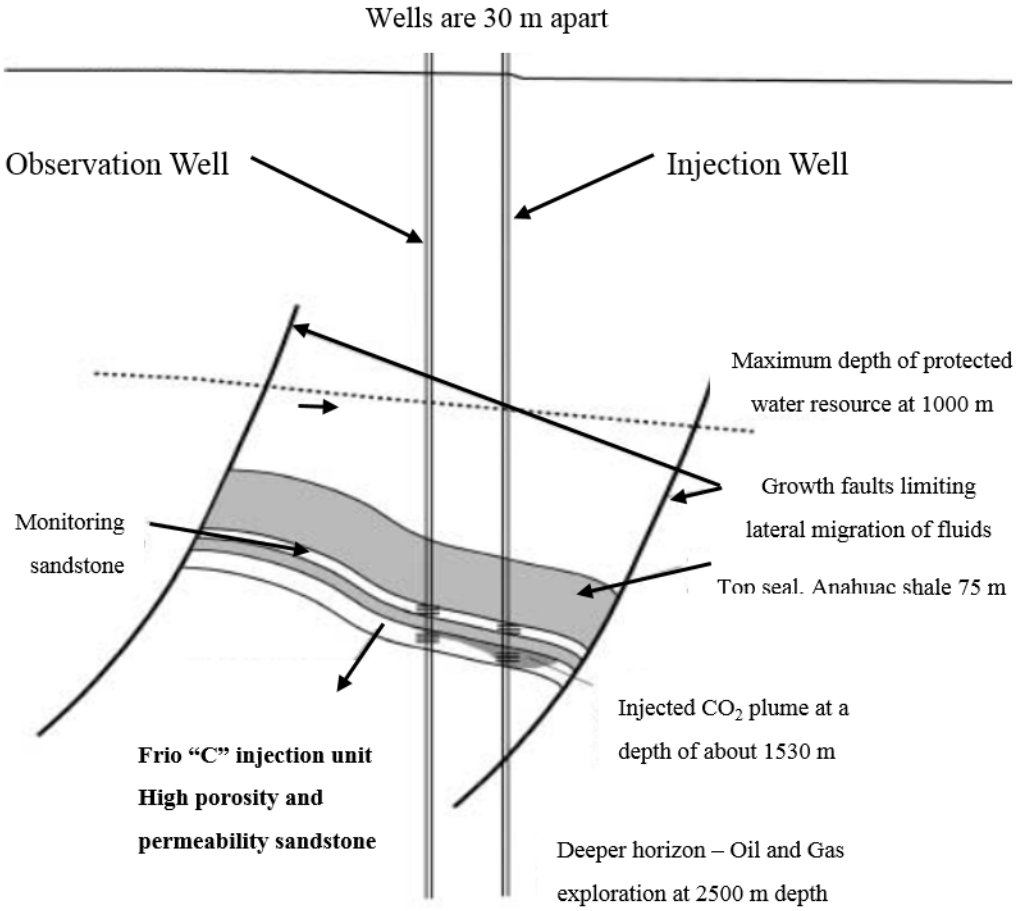

Figure 3-4: A zoom-out drawing of the Frio CO_2 injection experiment. The regional seal is the Anahuac formation and a subregional seal is present above the perforations in both wells. Modified after Hovorka and Knox (2003).

3.3 PETROPHYSICAL DATA AND QUALITY CONTROL

3.3.1 Reservoir temperature and pressure

Temperature and pressure data at reservoir conditions were measured extensively as they play the main role in controlling the properties of the injected CO_2.

Also, they were valuable in applying environmental corrections for measured CO_2 saturation using (Pulsed Neutron Capture) PNC logs (Sakurai et al. 2006). Initially, the cold liquid CO_2 was heated to a temperature between 10 - 21°C before injection. It is assumed that the CO_2 injected do not change significantly the reservoir temperature as it equilibrated rapidly after injection as the amount of CO_2 injection is considered small. Thus, reservoir temperature is assumed constant at about 55°C to 57°C (Daley et al. 2008). The CO_2 was pumped into the formation through the perforations at a constant rate of 140 litres/ minute (Sakurai et al. 2006).

We calculated the overburden pressure (*Pb*) using the available density log. The density log extends almost to the surface thus we apply the following equation with the density ρ in (Kg/m^3) and the depth increment Δd in meters to give an overburden pressure in (kPa),

$$Pb(kPa) = 0.01 \times \sum \rho . \Delta d \qquad (3\text{-}1)$$

Pore pressure (*Pp*) was calculated in the field using a pressure gauge at the reservoir interval (Sakurai et al. 2006). The pressure and temperature are presented in Table 3-1. The pressure data are important as a change in the effective pressure (*Pb* - *Pp*) after fluids injection could change the seismic wave velocities, hence the time-lapse response. Here we present the effective pressure calculated before and after CO_2 injection respectively by taking the borehole pressure shown Figure 3-5. For a change in pore pressure of 0.1 MPa (1bar) this will correspond to an effective pressure change from 17.54 MPa to 17.43 MPa; this is about 0.1 MPa effective pressure decrease. The results suggest that the effective pressure change is minimum and reservoir changes related to pressure variations should be minimum. This will be further investigated from a rock physics perspective in Chapter 5 and Chapter 6.

Temperature °C	**~55 to 57**
***Overburden Pressure, MPa**	**32.26**
Initial pore pressure, MPa	**14.72**
After injection equilibrated pore pressure	**14.83**
Maximum injection pressure, MPa	**28.82**

Table 3-1: Average pressure and temperature at the injection interval of the Frio experiment. From (Sakurai et al. 2006, Daley et al. 2008).*Calculated from density log.

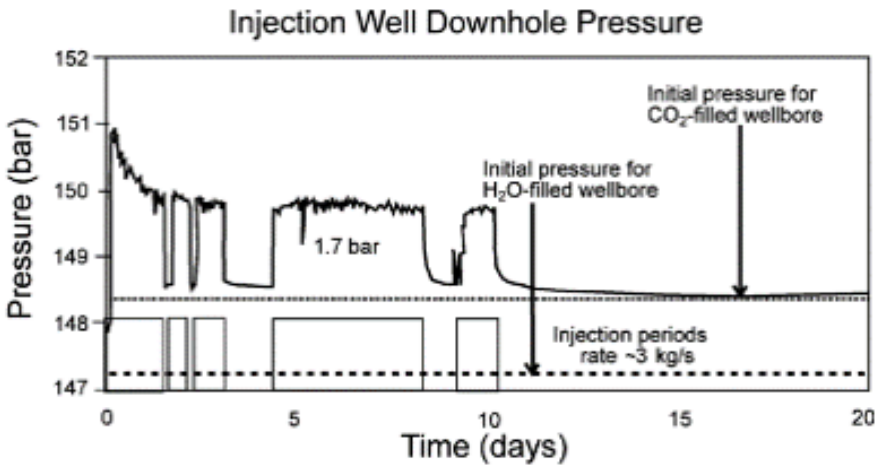

Figure 3-5: Downhole pressure change during and after CO_2 injection at the injection well. From (Hovorka, Benson, et al. 2006).

3.3.2 Core data: porosity, permeability and microstructure

The core data for the Frio brine pilot projects were taken from the newly drilled injection well to provide site-specific petrophysical information (Hovorka, Sakurai, et al. 2006). Three standard cores were retrieved, two from the Frio "C" interval in the depth range of 1539.24 to 1540.15 m (MD) and one from the Anahuac shale formation as shown in the core image in Figure 3-6. The core samples were kept frozen in dry ice containers prior to analysis (Sakurai et al. 2006). The core measurements for porosity and permeability indicated high-quality reservoir properties for the Frio "C" as shown in the thin section images in Figure 3-7. Average core porosity for the upper 10 meters of the interval of interest is about 32%. Capillary pressure test on cores

showed that CO_2 can be injected effectively using low pressure above formation pressure due to the high permeability of the formation (Sakurai et al. 2006). We examine the microstructure of the Frio "C" using thin section obtained from the recovered cores. Looking at the thin sections in Figure 3-7 we observe that cement content at grain contact (i.e., grain contact cement) is minimum and that there is "pore-filling" materials which appear away from grain contact.

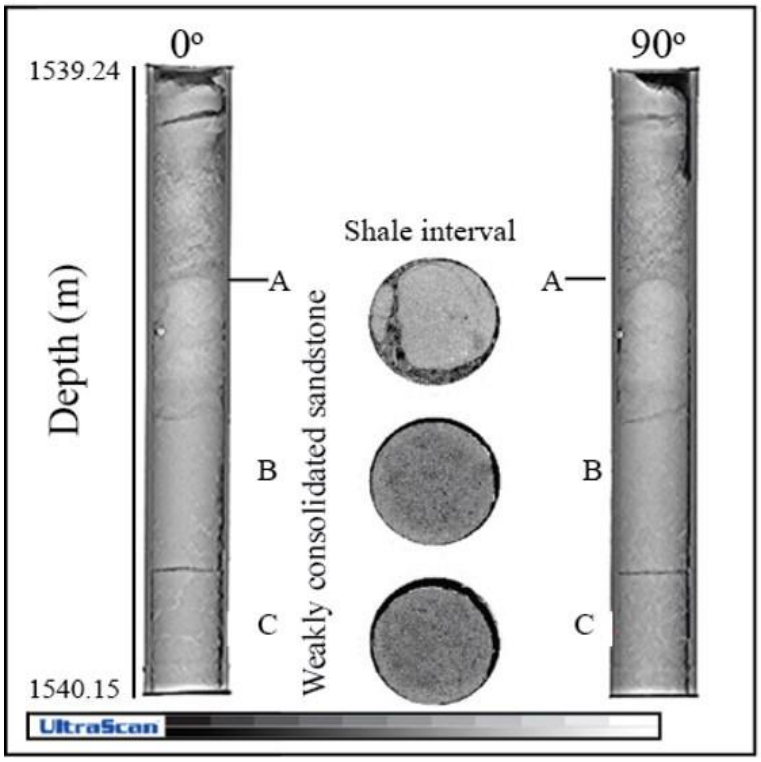

Figure 3-6: CAT-scan image for the Frio-C upper interval. The shaley interval shown is part of the sealing layer above the injection zone. The sandstone interval is weakly consolidated with high porosity. Modified after (Sakurai et al. 2006).

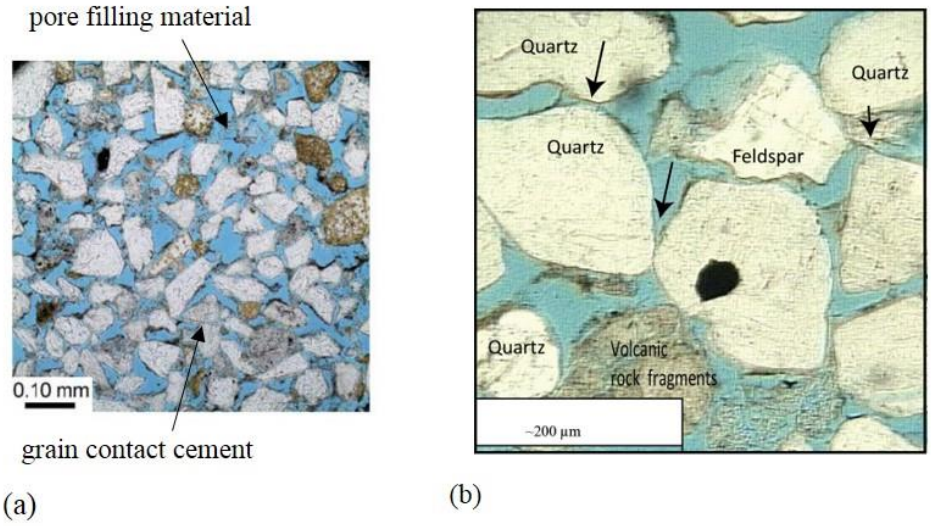

Figure 3-7: Thin section for the Frio "C" high porosity and permeability sandstone (upper interval). Minimum cement is present and point contact is indicated by arrows in the image. In addition, the mineralogical constitutes are indicated on the thin section in the right. (a) from Sakurai et al. (2006) and (b) from McGuire (2009).

3.3.3 Well logs

Several aspects of the logs measurements taken at the Frio brine pilot wells must be addressed before interpreting the logs results in my research. The overall quality of the logs for the injection well is acceptable; however, several corrections were made to the raw logs due to wellbore environment and the poorly consolidated nature of the sediment around the injection zone (Sakurai et al. 2006). Table 3-2 shows a list of the main logs acquired in both wells. The log values are measured with 15 cm interval. Several logs were derived from that existing such as V_P/V_S ratio, volume of shale (Vshale), Figure 3-10.

	Measurement	symbol	Injection well	Observation well
Well Logs acquired	P-wave Velocity	V_P	BL	-
	S-wave velocity	V_S	BL	-
	Density	ρ	BL	-
	Caliper	CALI	BL	-

	Permeability	κ	BL	-
	Spontaneous potential	SP	BL	Legacy (BL)
	Neutron porosity	NPHI	BL	-
	Gamma Ray	GR	BL	-
	Porosity	ϕ	BL	-
	Resistivity	*Ohm.m*	BL	-
	Sigma (RST)	Sigma	TL	TL

Table 3-2: well logs data available for the Frio-I project. (BL) indicate only baseline measurement is available, while (TL) indicate time-lapse logs is available.

The Well logs available must be verified in term of quality and consistency. One method of verification and calibration of well logs is to compare with data collected from core measurements. We calibrated the porosity logs using core data presented by Sakurai et al. (2006). This involved investigating the parameters for calculating porosity log ($\boldsymbol{\phi}_{log}$) from density, sonic logs and neutron. After investigation the following equation was applied in the calculation of porosity from density log (ρ_{log}) with grains density (ρ_{grains}) of 2585 Kg/m^3, brine density (ρ_{brine}) of 1030 Kg/m^3, results are shown in Figure 3-8:

$$\boldsymbol{\phi}_{log} = \frac{(\rho_{log} - \rho_{grains})}{(\rho_{brine} - \rho_{grains})} \qquad (3\text{-}2)$$

To validate and check the P-wave and S-wave velocities obtained from the logs, we compare the sonic velocities with those obtained from interval VSP velocities. In sonic logs calibration, VSP is regarded as a low resolution but high accuracy measurements, compared to well logs, which are high-resolution measurements, but sometimes may be of low accuracy (Dillon and Collyer 1985). Thus, a combination of the two gives confident in the accuracy of the velocities measured. As the VSP interval velocities are at a different scale compared to the sonic logs, an upscaling of the log velocities is performed using Backus averaging (Mavko, Mukerji, and Dvorkin 2009). A good match is observed for both V_P and V_S with the VSP interval velocities as Figure 3-9 shows. These analysis confirms that we could use the logs confidently, specifically in creating the subsurface model for the forward modelling in (Chapter 4, section 4.5) and rock physics modelling in Chapter 5 and Chapter 6.

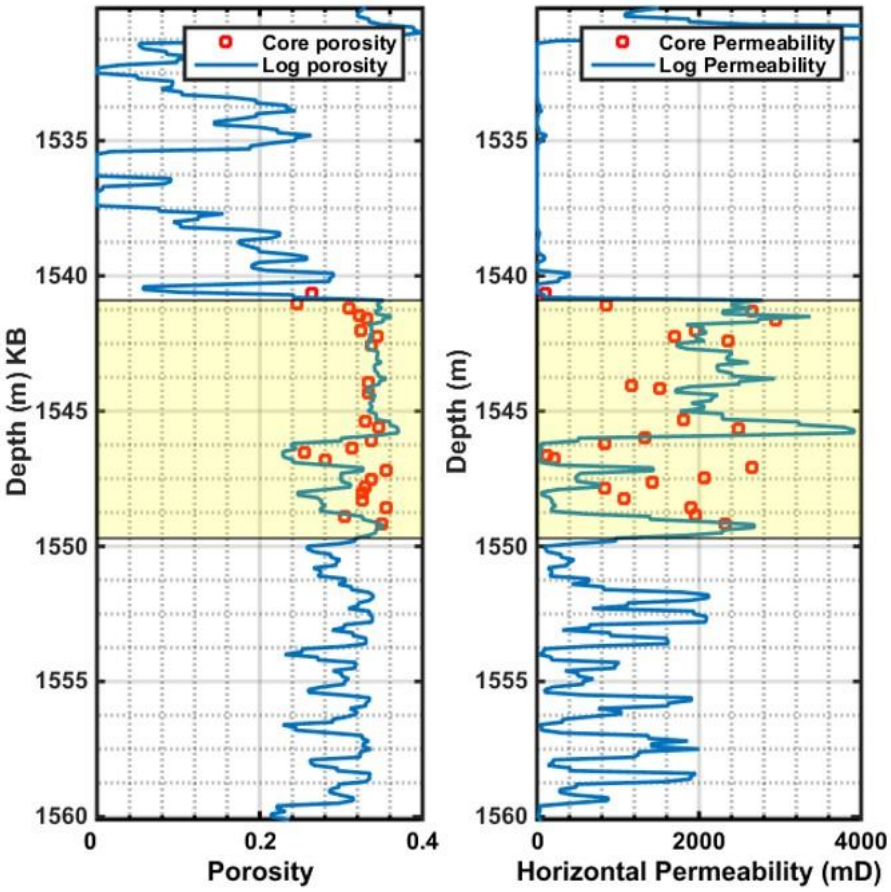

Figure 3-8: Porosity and horizontal permeability for the injection well. The red squares represent lab core measurements taken from (Doughty, Freifeld, and Trautz 2008). Interval of interest is shaded. At the top of the perforation zone is a low permeability shale, siltstone and sandstone layer.

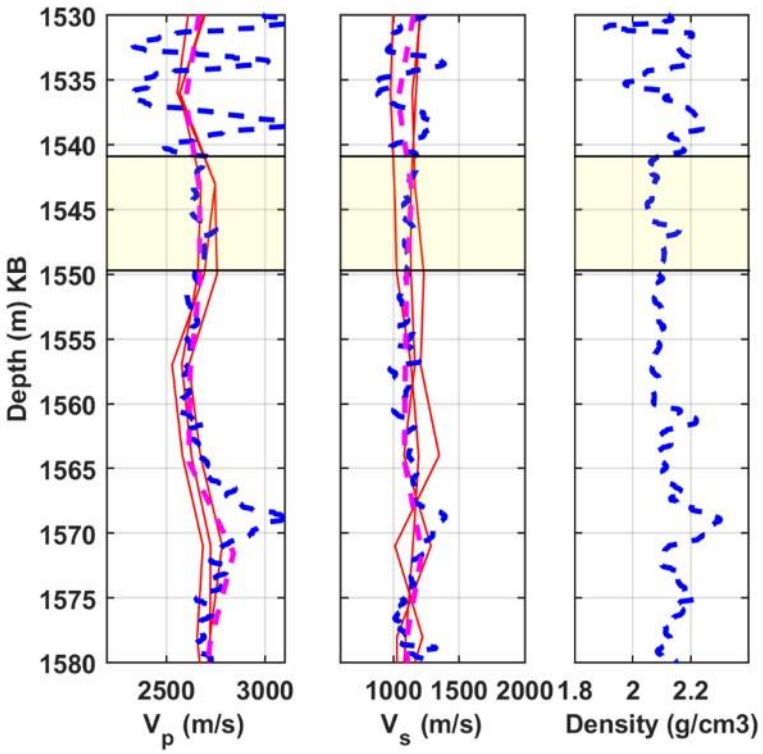

Figure 3-9: Baseline V_P and V_S logs in the injection well with the interval of interest shaded. Dashed magenta is the upscaled logs measurement by Backus averaging and the red lines are the interval velocities from VSP near offset shots.

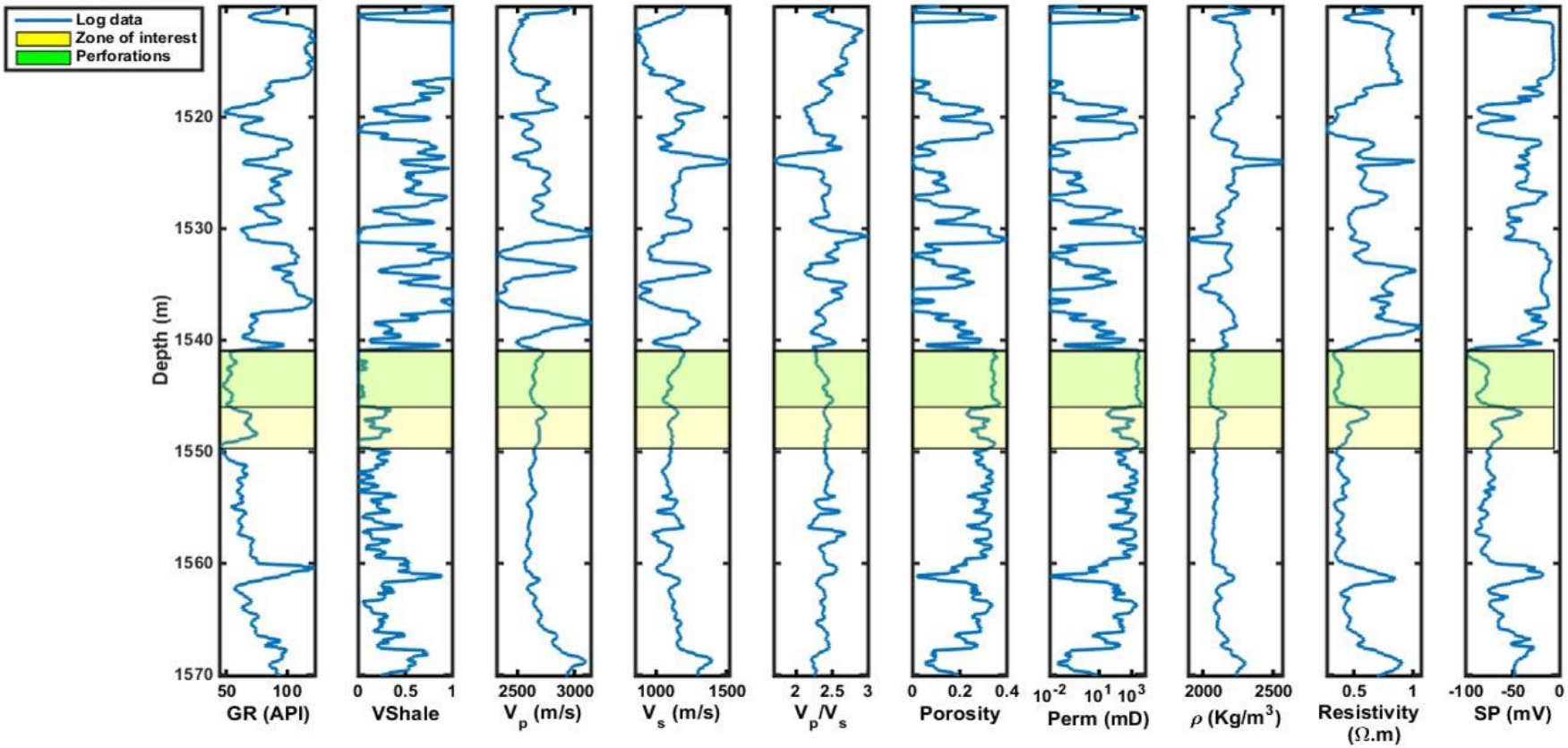

Figure 3-10: well logs and derived logs for the injection well. The interval of interest is the shaded areas. Perforation interval shaded in green (over the zone of interest in yellow).

3.3.4 Reservoir Saturation Tool (RST) log

One way to measure CO_2 saturation in the borehole is to use Pulse Neutron Capture (PNC) method. This method relies on the difference in the thermal capture cross-section of brine and CO_2 (Sakurai et al. 2006). The Reservoir Saturation Tool (RST) log which uses the pulsed neutron method with sigma (capture unit c.u.) to estimate water saturation was tested using the retrieved cores samples with the Frio formation brine. (Sakurai et al. 2006) showed that this method would work well as the formation is characterized with high porosity. More importantly, their results showed a large contrast in the sigma Σ (c.u.). For the average Frio interval porosity of 32% they obtained a Sigma of 6 c.u. for full CO_2 saturation and about 23 c.u. for full brine saturation see Figure 3-11.

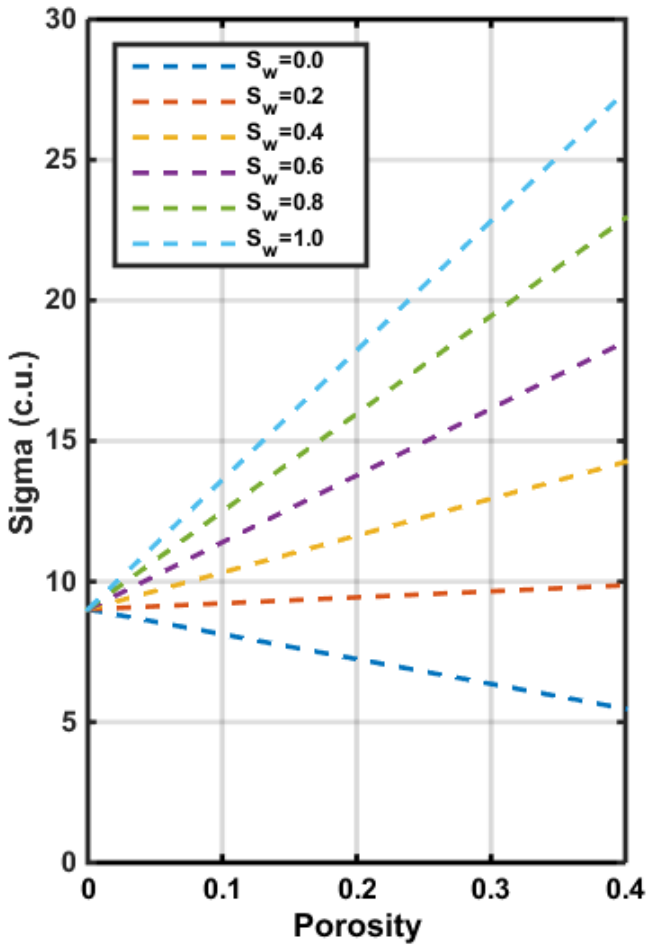

Figure 3-11: Crossplot of porosity and Sigma (c.u.) for the relationship of CO_2 and water saturation. Data from (Sakurai et al. 2006).

Several RST logs were measured at various times after CO_2 injection. The measurements were taken for the injection well just after the end of injection on 15th October 2004, then on 9th December 2004 and finally on 23rd February 2005.

A baseline measurement was taken on 26th September 2004 for the observation well, then on 8th October 2004 just after the breakthrough of CO_2 and after that on 14th October 2004 at the closing of the injection. Furthermore, RST logs were taken for the observation well on 2nd November 2004, then 9th December 2004 and finally on 23 February 2005, see Figure 3-12.

A critical aspect of the RST measurements for runs 2 and 3 in the injection well and runs 4 and 5 for the observation well is that both wells were sealed off by cement after the injection of freshwater to prepare them for the post-injection crosswell and VSP surveys. These measurements were corrected for fresh water effects, but for the injection well the measurement after casing were not reliable over the perforation zone as Figure 3-12 shows (Hovorka, Benson, et al. 2006).

Date	Injection well	Observation well
26th September 2004	-	Run 1, Baseline
8th October 2004 (day 4)	-	Run 2, CO_2 breakthrough
14th October 2004 (day 10)	End of Injection	Run 3, Before end of injection
15th October 2004 (day 11)	Run 1	-
2nd November 2004 (day 29)	-	Run 4 (monitor VSP on 25/11/2004)
9th December 2004 (day 66)	Run 2	Run 5
23rd February 2005 (day 142)	Run 3	Run 6

Table 3-3: RST measurements dates for the Frio-I project, the (day) represent the days after injection started. Data from (Hovorka and Cohen 2006, Sakurai et al. 2006).

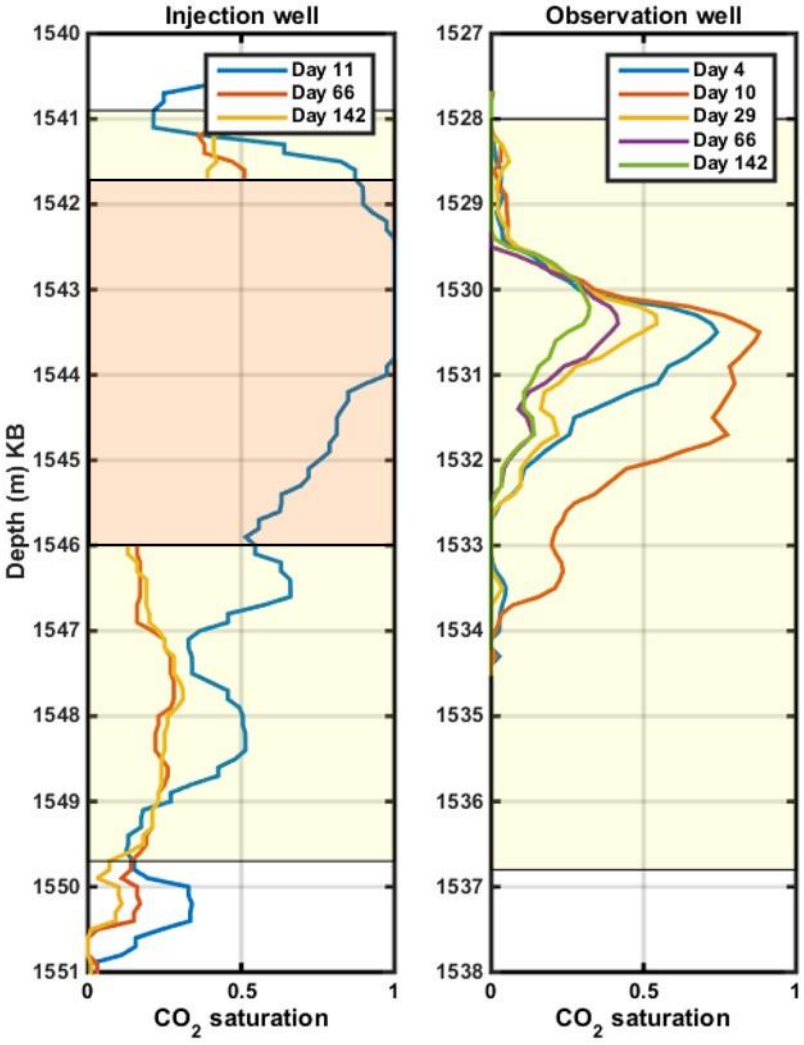

Figure 3-12: Injection well RST logs and interpreted CO_2 saturations. The red shaded area is the perforation interval within the Frio "C", while the shaded area shows the Frio "C" high porosity and permeability interval of interest. Injection well RST logs for days 66 and 142 are not reliable over the perforation zone due to wellbore issues encountered after casing. The RST results show a substantial increase in CO_2 saturation in day 11 just after CO_2 injection stopped.

3.4 FRIO "C" RESERVOIR PROPERTIES

The change in the elastic properties of the sedimentary reservoir due to fluid changes are influenced by the mineralogy, porosity and pore geometry (Johnston 2013). We presented earlier in Figure 3-7 thin sections from the Frio "C" and indicated some of the mineralogical constituents present. Here we aim to investigate the sedimentological trends of the Frio "C" sandstone using the well log data.

In order to highlight the Frio "C" reservoir properties we present in Figure 3-13 two crossplots of V_P versus Porosity and V_P versus V_S, which are often used in lithological and sedimentary microstructure evaluation (Avseth, Mukerji, and Mavko 2010). The sorting trend indicated in Figure 3-13 (a) is actually showing an upward coarsening trend (if colour coded with depth). The separation of clean sandstone, shaley sandstone and shale is difficult by looking only at Figure 3-13 (a) without showing the shale volume. However, Figure 3-13 (b) shows a trend for these three categories, which is typical in the V_P versus V_S domain. We note here that for the shaley sand which can be classified as shale with <0.3 shale volume (i.e., clay volume) the trend is explained to be adding pore-filling material between the grains which do not contribute significantly to the frame stiffness. An observation here is that the injection interval elastic properties do not vary significantly, however as noted by many studies, sandstones with similar elastic properties but different microstructure could have different response to fluid changes (Dvorkin, Nur, and Yin 1994, Dvorkin and Nur 2002). The histograms in Figure 3-14 illustrate the main formation properties distribution. It is clear that apart from the variation in shale volume and porosity for the lower part of the interval of interest, all parameters vary within a small range, hence, the reservoir is essentially homogenous. These analyses are of particular importance to understand the microstructure of the rock frame, as we will present later in Chapter 6.

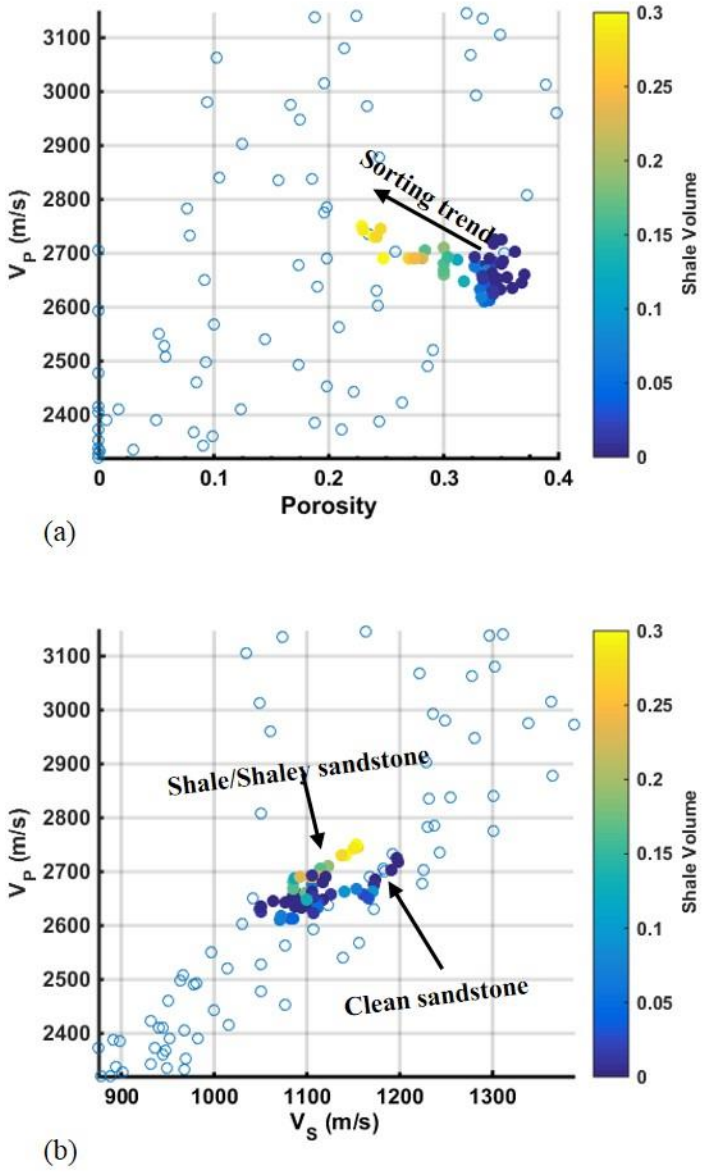

Figure 3-13 Cross plots of (a) V_P versus Porosity and (b) V_P versus V_S. The filled data points are for the injection interval shaded in Figure 3-10, while the empty circles are for the 10 m interval above the injection interval. A sorting trend is indicated in (a) for the reservoir. The interval above the injection do not show a preferred trend as it is composed of shale, siltstone and shaly sandstone. In (b) we can see a separation between the clean and Shale/shaley sandstone intervals.

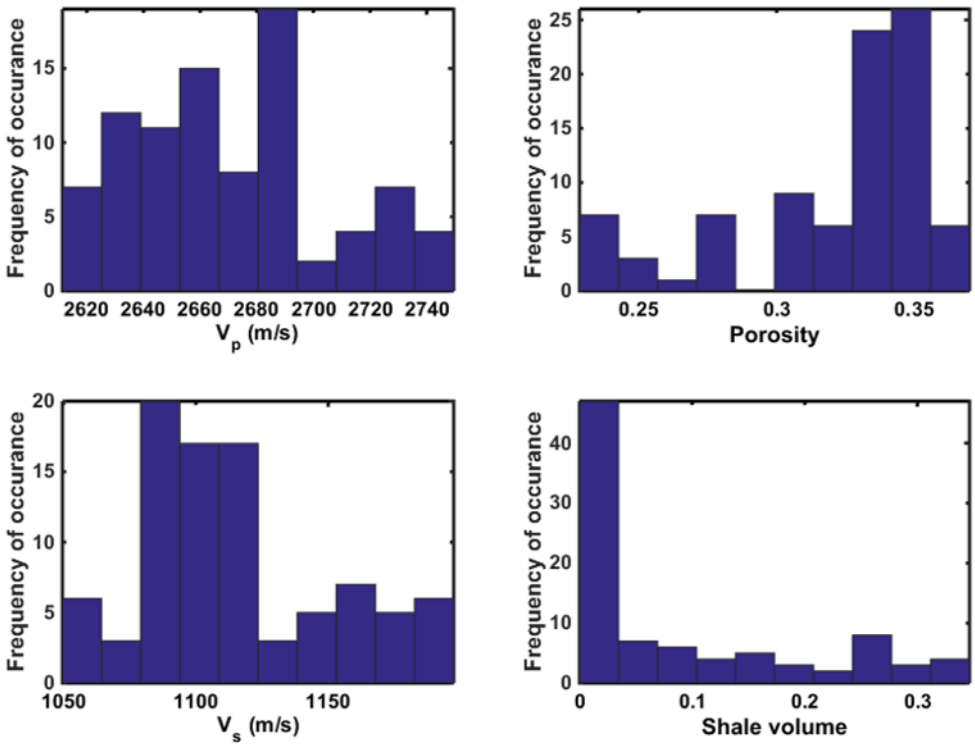

Figure 3-14 Histogram for the Frio "C" logs at the injection well in the interval (1540.9 – 1549.7 m).

3.5 CONCLUSION

We presented in this chapter a comprehensive review of the Frio CO_2 sequestration project and the measurements acquired. The field data acquired for the Frio project show a great opportunity for a rock physics analysis using petrophysical and seismic data. We focused here on the petrophysical data as the seismic monitoring aspects will be treated in Chapter 4. The data presented is aimed to be a basis for later rock physics modelling and interpretation in Chapter 5 and 6. The availability of baseline logs and core data will allow the choice of a rock physics model, while the time-lapse seismic data which will be treated in Chapter 4 will be used to constrain and confirm the rock physics models predictions. With the availability of such an extensive data sets, we have found that the Frio project is an excellent opportunity to study velocity-saturation relation using both theoretical rock physics and seismic data for both the VSP and crosswell scales at reservoir conditions.

CHAPTER 4. FRIO TIME-LAPSE VSP AND CROSSWELL: PROCESSING, MODELLING AND QUANTITATIVE RESULTS

Time-lapse (TL) Surface seismic is considered a good monitoring method for oil and gas production projects, enhanced oil recovery and large-scale CO_2 injection projects (Tabakov and Baranov 2007), however, when working with a small scale project such as the Frio brine pilot several limitations come into play. A first limitation is the high cost of 3D surface seismic, a second limitation is the resolution of surface seismic compared to the expected plume thickness and lateral extent of the injected CO_2. Fortunately, a high-resolution multi-azimuth VSP survey was conducted as a monitoring and verification method for the Frio brine pilot CO_2 sequestration project.

Another seismic monitoring method, which was applied in the Frio project, is crosswell seismic. The advantage of crosswell seismic over VSP is that it uses higher frequencies and the waves travel a shorter distance meaning that higher frequencies are not attenuated as much hence provides higher spatial resolution (meters to 10's meters) compared to VSP which is in the spatial scale of 10's to 100's of meters. For both the VSP and crosswell the baseline survey was conducted before CO_2 injection and a repeat survey was acquired about six weeks (42 days) after the end of CO_2 injection. Similar geometry for source and receivers were used in both surveys (Doughty, Freifeld, and Trautz 2008).

The Frio project has favourable conditions for monitoring using time-lapse VSP and any other time-lapse seismic monitoring method due to the expected large change in the elastic properties upon CO_2 injection. As presented in Chapter 3, the formation is mainly a high porosity, poorly consolidated sandstone (which could entail a weaker dry-frame), fluid change from brine to CO_2 implies a large change in fluids compressibility, saturation and impedance. Only the structural dip is not close to ideal. We assess these parameters using the reservoir risk assessment sheet described by Hottman et al. (2000) for time-lapse VSP, with score of 5 as the most favourable conditions, Table 4-1.

Reservoir Parameters	Ideal score	Frio brine pilot VSP
Porosity	5	5
Dry-rock bulk modulus	5	5
Fluid compressibility contrast	5	4
Fluid saturation changes	5	4
Predicted impedance change	5	4
Structural dip	5	2

Table 4-1: TL-VSP reservoir parameters-risk sheet for the Frio CO_2 injection pilot.

The first objective from the processing of the Frio VSP and crosswell data is to obtain the time-lapse changes in the reservoir seismic properties (i.e., obtain geophysical parameters from Geophysical data) to constrain the rock physics model of the formation and consequently the velocity-saturation relation as will be shown in Chapter 5. The second objective for the VSP data processing and modelling is to investigate how the resolution of the VSP method and expected plume geometry could affect the interpretation of the data, especially reflection amplitudes. As far as I know, these objectives were not part of any of the previous studies on the Frio project.

For the time-lapse VSP data to avoid redundancy, only the detailed processing sequence of one shot (shot 1, North azimuth) will be shown, however the final results will contain that for all shots where the data quality permitted. In the case of the crosswell tomography the data will be reprocessed after confirmation of the time picks which were supplied by LBNL and their tomography results are published in several papers (e.g., Daley et al. 2008, Doughty, Freifeld, and Trautz 2008, Ajo-Franklin, Minsley, and Daley 2007).

This chapter will partially contain some of the work published in (Al Hosni, Caspari, et al. 2015, Al Hosni, Gurevich, and Daley 2015, Al Hosni, Gurevich, et al. 2015) and these references will not be cited anymore in this chapter.

4.1 FRIO VSP DATA

The Frio VSP survey geometry was designed with the objective of mapping CO_2 distribution around the vicinity of the injection well. Eight shots were acquired with various azimuths in the range between 110 m to 1500 m from the observation well, Figure 4-1. The receivers (3-component geophones) were set in the injection well and Dynamite charges weighing 1.6 kg each used as sources at depth of 18.2 m below the surface (Daley, Myer, and Majer 2005, Zhou 2010). The receiver's depth is referenced to ground level (GL). The receiver coverage in the injection well extended from the surface to a total well depth of 1686 m for shots 1 and 3 and from 1072 to 1686 m for other shots.

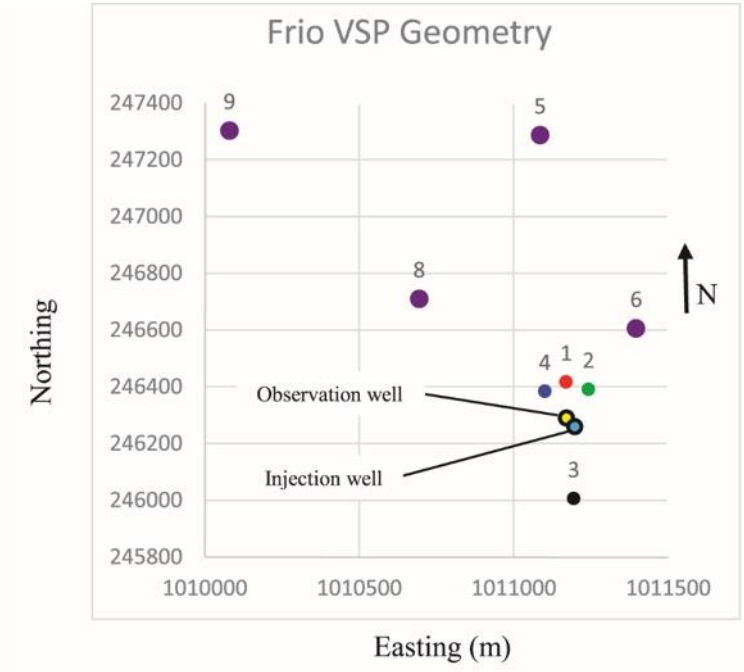

Figure 4-1: VSP acquisition geometry for the Frio brine pilot. A total of 8 shots were acquired as shown by the numbered circles.

Shots Number	Northing (y)	Easting (x)	Distance from receivers well (m)	Azimuth
1	246416.59	1011169.94	130	North
2	246390.97	1011242.07	111	Northeast
3	246005.75	1011194.05	284	South
4	246383.65	1011100.74	135	Northwest
5	247287.09	1011085.32	1003	North
6	246605.72	1011396.18	373	Northeast
8	246710.18	1010693.85	656	Northwest
9	247303.24	1010079.85	1508	Northwest
Receivers well Location	246289.86	1011197.17	0.0	-

Table 4-2: Shot points distance from the injection well (receiver's well) at the Frio site.

4.2 FRIO TIME-LAPSE VSP PROCESSING

In this section, we present the processing sequence applied to the VSP data. Only shot 1 processing is shown here. However, similar flow is applied to the remaining shots as data quality permits to extract the needed information for the analysis, namely first arrivals (amplitudes and arrival time) and reflection amplitudes. It is worth noting that for time-lapse VSP the processing flow is not clearly established and each study would have its own flow depending on the objectives, field conditions and acquisition parameters (Cheng, Huang, and Rutledge 2010). Thus, the processing here is tailored to obtain the information mentioned above and not for imaging per se.

4.2.1 Data preparation and pre-processing

The first step in working with the VSP data is assigning the geometry and sorting of traces. The Frio VSP data was acquired with a receiver string having a spacing of 7 m. For each shot point, the data was recorded at different receiver positions and then interleaved to create a denser spacing of 3.5 m at the injection interval (Daley et al. 2008, Daley, Myer, and Majer 2005). This introduced static shifts and amplitude differences, which are a source of unwanted noise in our time-lapse study, see Figure 4-2 (a). Thus, in order to avoid such effects, we take only one string position for each interval with a receiver spacing of 7 m, Figure 4-2 (b). This ensured that only one source energy (wavelet) is recorded for each depth interval. The raw shot record for

Frio VSP after pre-processing is shown in Figure 4-3 for the baseline and monitor (shot 1).

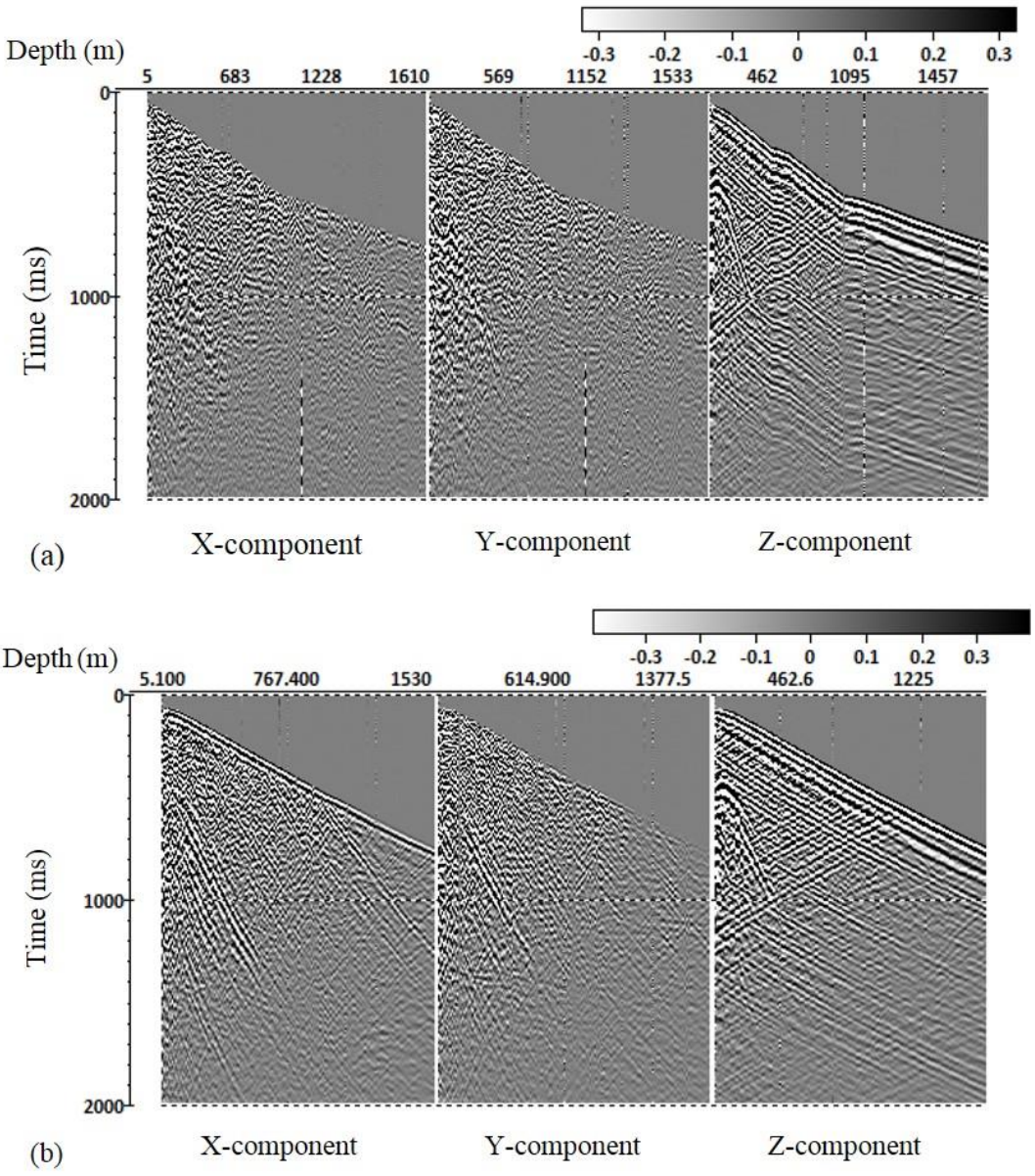

Figure 4-2: Baseline VSP data for shot 1. Three-component (3C) data before pre-processing (a) and after (b). Better coherency and less statics obtained after using only one receiver spread for each interval. Also, note the X and Y horizontal components after tool orientation showing better continuity.

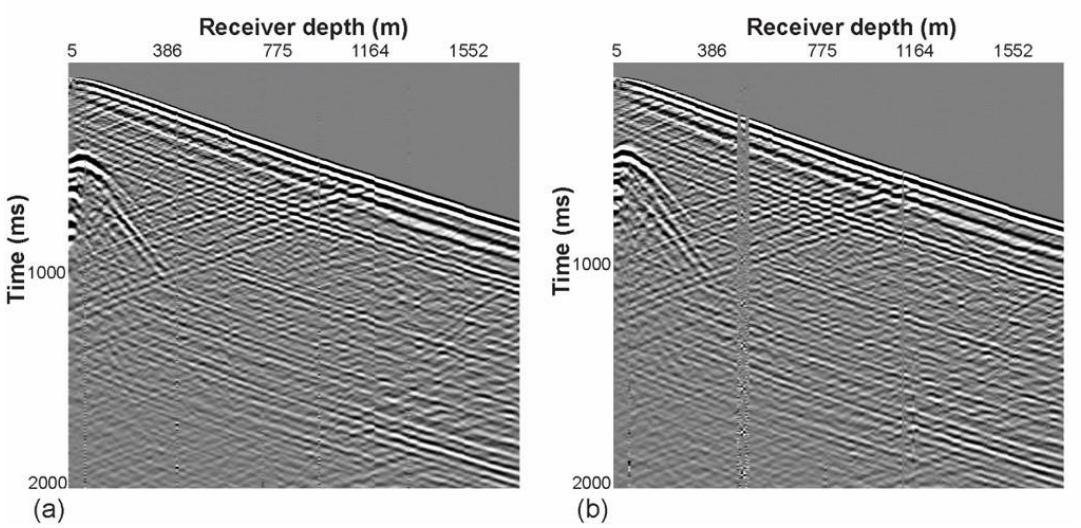

Figure 4-3: Raw shot record for Frio VSP after pre-processing (Z-component). Shot 1, (a) Pre-injection, (b) post-injection.

4.2.2 Picking first arrivals and component orientation

We pick the first breaks for the data at the onset of the seismic signal. This criterion for picking is possible for the Frio VSP data due to the high signal-to-noise ratio of the data in the vicinity of the first arrivals. Due to changes in the wavelet form with depth the time picks obtained for the Frio data are not accurate for shallow receivers. However, as the depth increase the time picks become more stable. Before picking, the data is resampled to 0.1 ms. This allow for accurate picking and it will be our picking uncertainty. However, (in a time-lapse sense) as we will show later in the analysis section (4.4.1), this does not mean that the first breaks will have a 0.1 ms uncertainty as the data could have variations due to statics and other acquisition noise. The picking is performed by first normalizing the data in the vicinity of the first arrivals then applying an automatic picking function that finds a specific threshold amplitude in a time window over the first arrivals. Manual editing of the picks was performed for traces which exhibit noise in their first arrivals as shown by the red arrow in Figure 4-4. After picking the first breaks, data orientation is performed. The horizontal components (X and Y) show better continuity after orientation, see Figure 4-2.

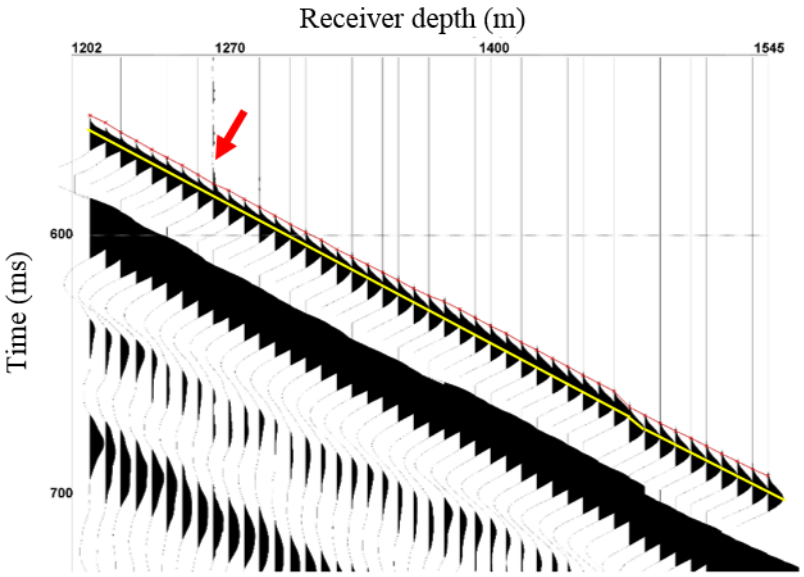

Figure 4-4: First breaks picks after resampling to 0.1 ms (red line). Picking is performed at the onset of the signal. Note the high signal-to-noise ratio of the data in the vicinity of the first breaks. For transmitted wave amplitudes we pick the first peak maximum (yellow line).

4.2.3 Upgoing- wavefield separation

The wavefield separation for the Frio VSP shots is performed using the alpha-trimmed mean filtering, described in section 2.6.2. The first step is to remove the downgoing wavefield. For comparison we show the wavefield separation for both the pre-injection and post-injection data sets besides each other in Figure 4-5. First, the data is flattened using the first arrivals time picks (i.e., subtracting the first arrival time picks for each trace) Figure 4-5(c,d), then the filter is applied, that is subtracting the value obtained. This result in the removal of the downgoing wavefield energy Figure 4-5 (e,f). Then, the data is returned to its original timing as shown in Figure 4-5 (g,h). This only removes the downgoing wavefield, however, other coherent (unwanted waves) are present such as S-waves. For this, a similar procedure is performed but using the time picks for those waves. We apply a bandpass filter on the data after

spatial filtering as such procedure is expected to introduce some frequency notches. The filter is set with a low-cut ramp of 5-10 Hz and a high-cut ramp of 70-90 Hz.

The events for shallow receivers (above 500 m) appear to be very contaminated with low-frequency noise, thus a surgical mute for those receivers will be performed at the final processing step. Moreover, as we know the depth of injection, the processing is focused on obtaining the best reflection results for the area of interest in the VSP data, that is the depth interval of 1000-1540 m. Figure 4-6 shows shot 1 after separating the upgoing wavefield for the baseline and monitor surveys. Some unwanted coherent and incoherent noise still remain in the data, however, for the depth of interest the results are sufficient to perform the next processing step, which is deconvolution.

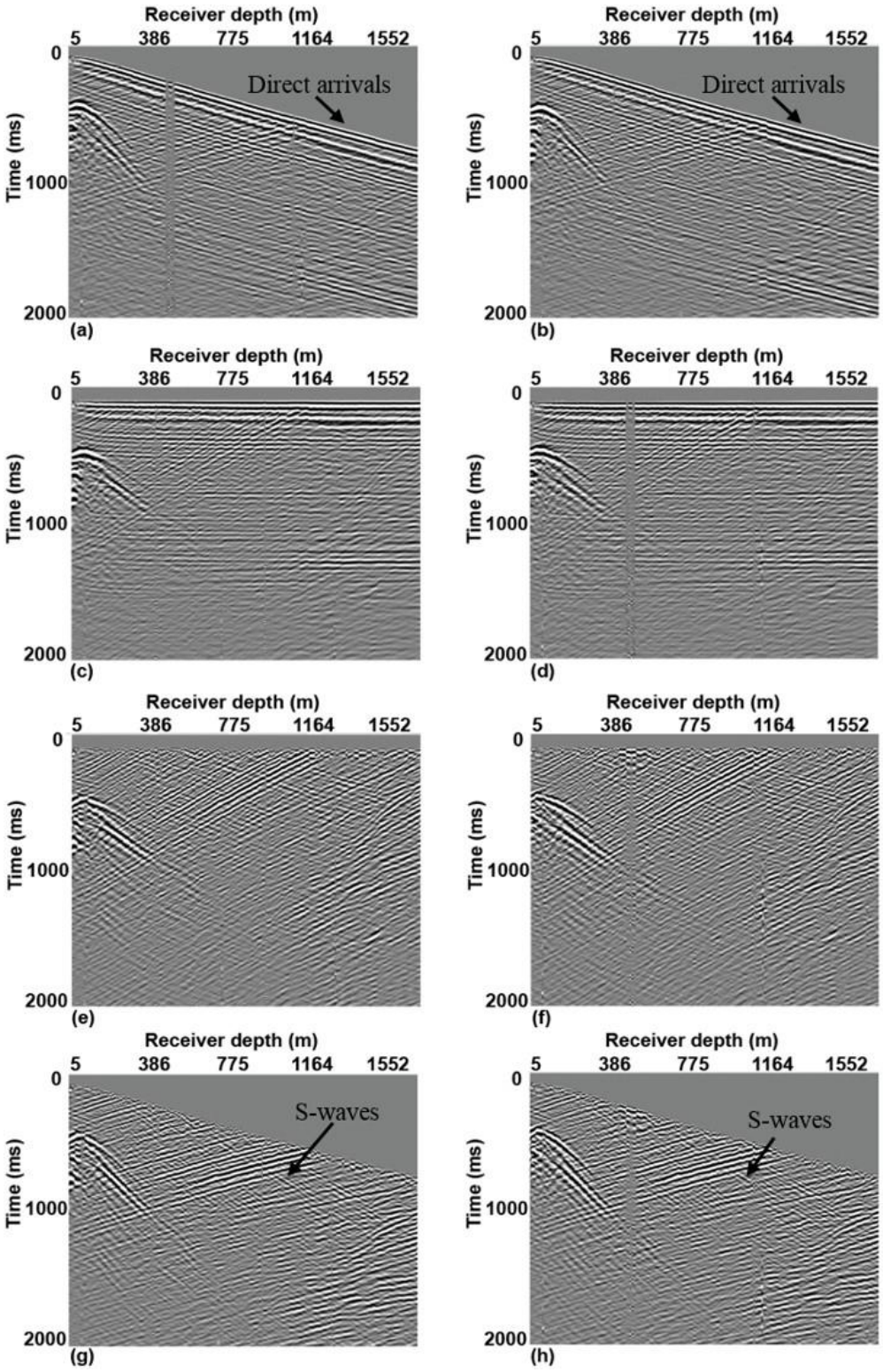

Figure 4-5: Upgoing wavefield separation by removing the downgoing wavefield using median filtering for the pre-injection (left column) and post-injection (right column) VSP data, shot 1. S-waves appear crossing the reflections as indicated in (g and h).

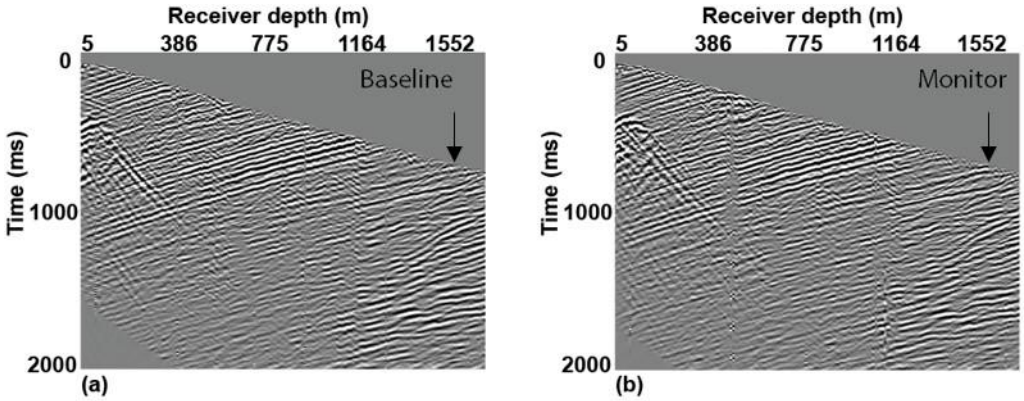

Figure 4-6: Upgoing wavefield after removing the downgoing wavefield, S-waves and other unwanted coherent signal for shot 1, (a) baseline and (b) monitor.

4.2.4 Deconvolution

For the Frio VSP data set, several dynamite shots were used to produce the seismic record, thus the source wavelet is expected to be different for each shot and varies with depth as the wavelet decays. Present in Figure 4-7 are the wavelets obtained for each receiver interval for the baseline VSP data. The frequency content for the first ensemble wavelet and the last are presented in Figure 4-8. Note the loss of the high frequencies from the data with depth. Such a filtration process of high frequency "broadens" the wavelet thus reducing the vertical resolution of the VSP data.

Deconvolution is applied to the VSP data for both the pre-injection and post-injection surveys using the ensemble wavelets for each vintage at the reservoir depth, Figure 4-9. We could look at deconvolution here as an equalization operator and a filter for the two vintages of data (baseline and monitor) as it is a process that help in removing multiples and bringing the wavelets closer to a spike. Looking at the injection interval indicated in Figure 4-9 (a,b), the reflection due to the CO_2 plume can be seen. The frequency of the VSP signal recorded is up to 50 Hz for shallow receivers with a dominant frequency at about 30 Hz. At the reservoir depth the dominant frequency is about 25 Hz, however, signal up to 50 Hz can be recovered from the data after deconvolution, Figure 4-10.

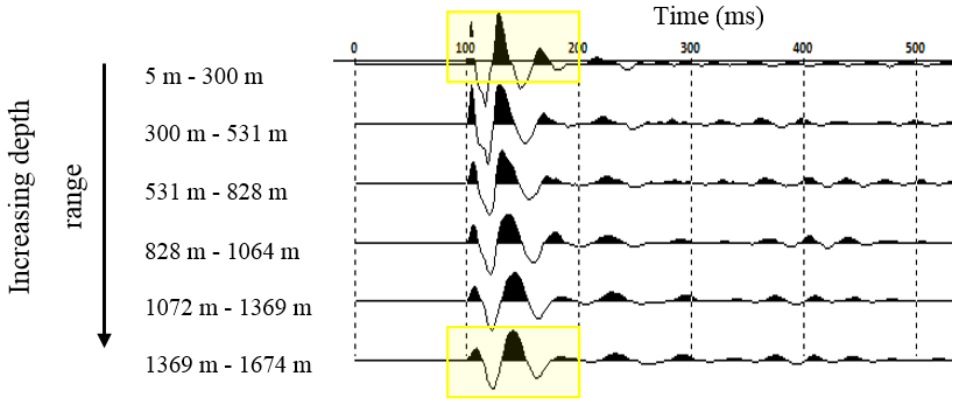

Figure 4-7: Wavelet change with depth for Shot 1 for each receiver level. The frequency content of the resulting wavelet decrease with depth, see Figure 4-8.

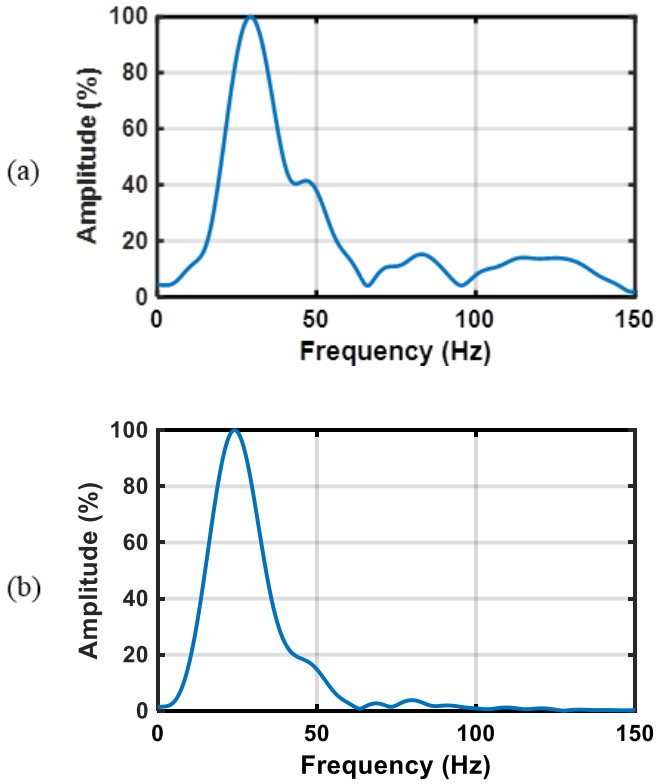

Figure 4-8 Amplitude spectrum for the ensemble wavelets for depth range (a) 5 m to 300 m and (b) 1369 m to 1673 m. wavelets are shown in Figure 4-7.

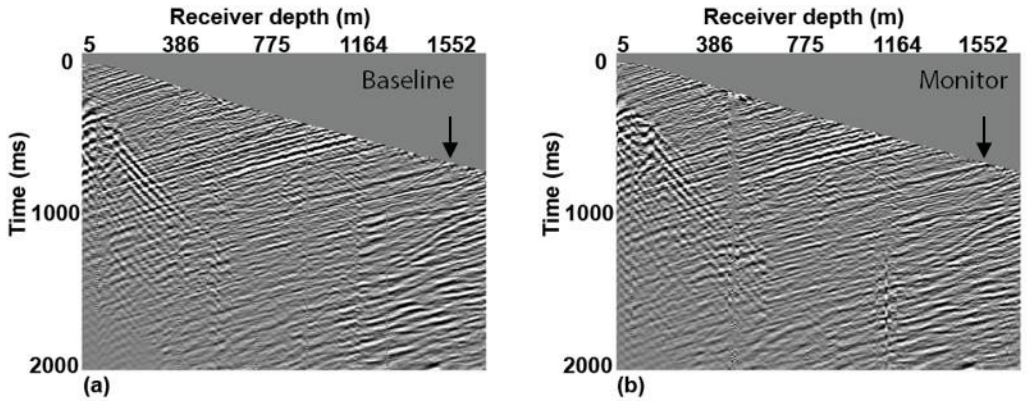

Figure 4-9: Results of applying deconvolution on the upgoing wavefield for shot 1 in Figure 4-6 for (a) baseline and (b) monitor survey. The injection interval is indicated by the arrows. Note the better delineation of the plume reflection compared to Figure 4-6.

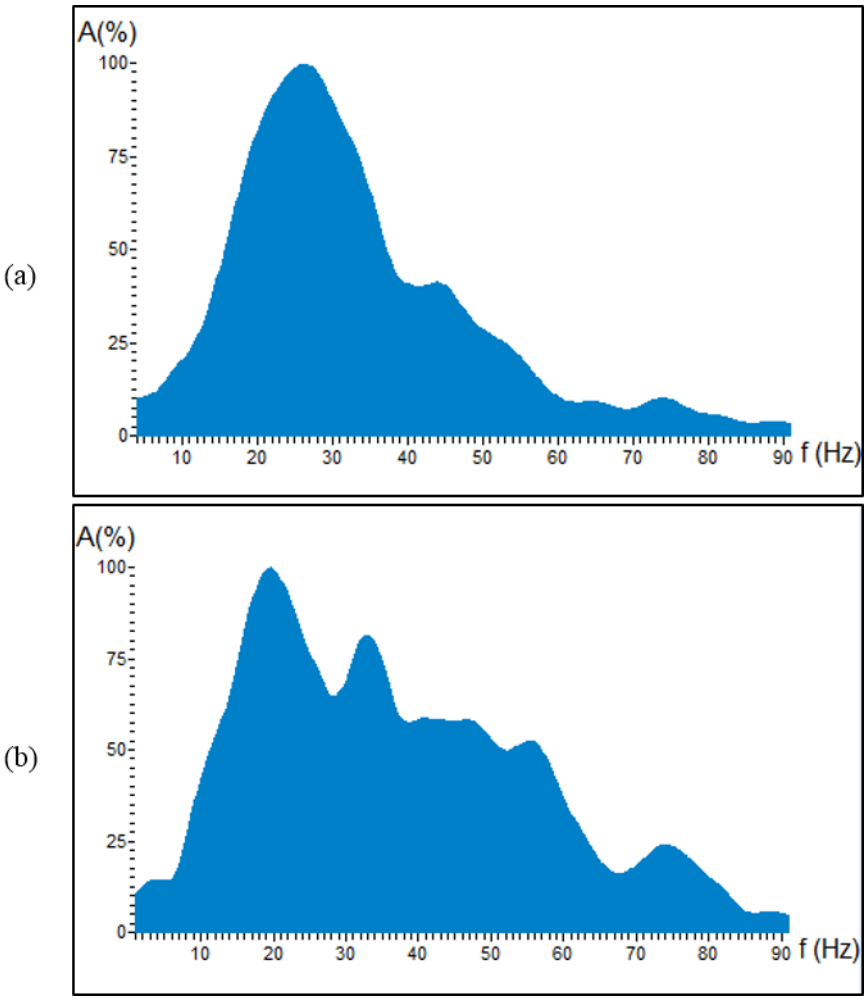

Figure 4-10: Amplitude spectrum in the same reservoir window (a) before, and (b) after deconvolution. Note the flatter "broadband" frequency content of the data after deconvolution.

4.2.5 Interval velocity analysis

We perform the velocity analysis of the VSP data for the first arrivals P-waves to obtain the interval velocities. The P-wave's velocities are essential for NMO corrections, VSP-CDP transform and migration. The velocities are calculated as described in Chapter 2, section 2.6.4. The intervals for which the velocity will be estimated in are chosen interactively as shown in Figure 4-11. S-wave velocities are also estimated from the VSP records. As many shots are available, the redundancy of the data provided assurance and estimate of the accuracy of the velocity estimate, especially for similar azimuth shots. The interval velocities were used earlier in Chapter 3 (Figure 3-9) to constrain V_P and V_S well logs.

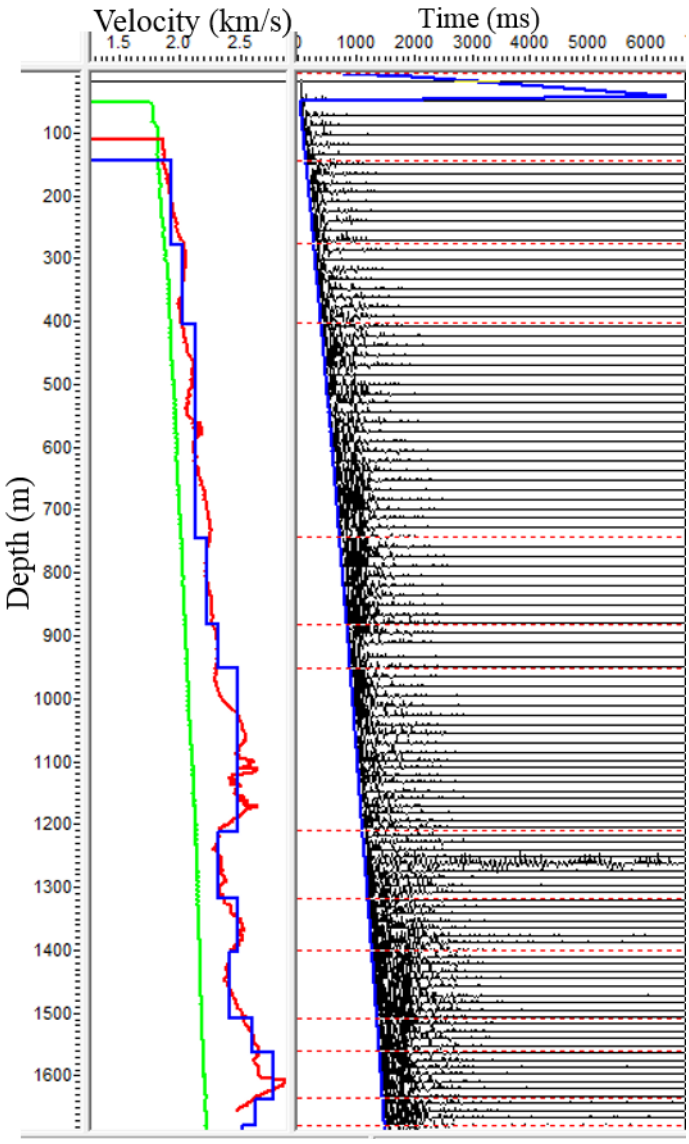

Figure 4-11: Interactive velocity analysis of the first breaks (P-wave) for shot 1. Interval velocities (blue line), per receiver velocity (red line).

4.2.6 NMO correction and enhancing reflections

NMO is performed to bring the event to a common traveltime (i.e., bring source and receiver to the same lateral position) in order to ease the comparison of the reflection results. We apply the NMO using the P-wave's interval velocity as obtained in the previous section. The NMO corrected sections are shown in Figure 4-12. In order to enhance the reflections a median filter is applied on the NMO corrected sections (Figure 4-13). These present the final sections for reflection analysis.

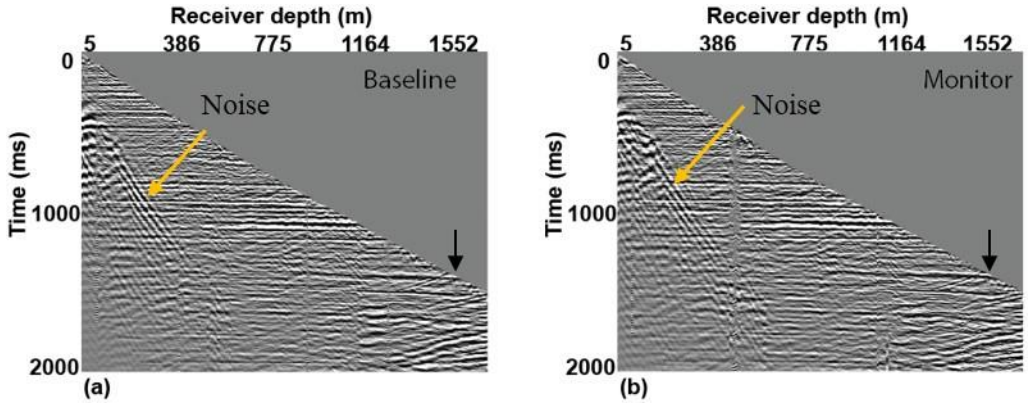

Figure 4-12: NMO corrected reflections for (a) baseline and (b) monitor surveys. The injection interval indicated by the black arrows.

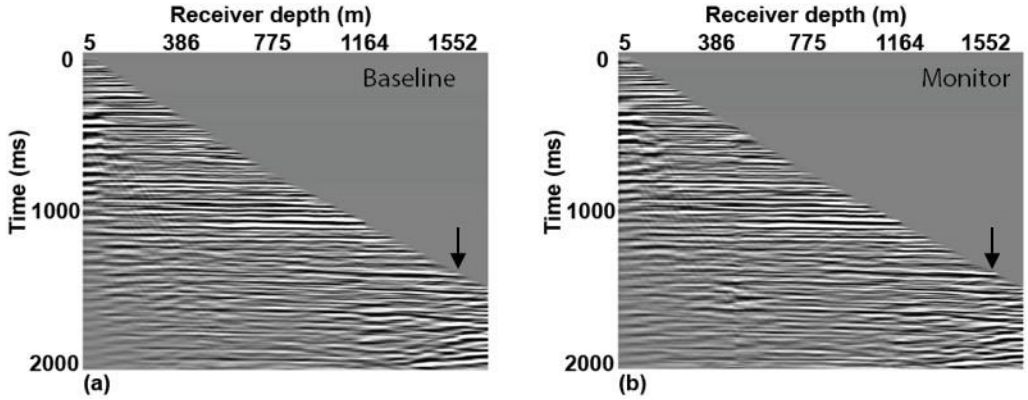

Figure 4-13: Final VSP record after upgoing wavefield enhancement using median filtering for (a) baseline and (b) monitor surveys. The injection interval indicated by the black arrows.

4.2.7 VSP-CDP transform

As an approximation VSP-CDP transform is utilised as described in (Chapter 2, section 2.6.5) in order to understand the respective subsurface location of the recorded reflected signal (i.e., ray-tracing). This is implemented using the interval velocities obtained in the velocity analysis (section 4.2.5). For far-offset shot's this might not be fully accurate as only interval velocities are available (at the well location) and lateral variations of velocity if significant could hinder this routine if applied. However, the VSP-CDP transform results are used to obtain the coverage of the VSP shots only and not for imaging or amplitude analysis, Figure 4-14. we note that for shot 1 and 3, the

VSP-CDP transform is for receivers up to the surface, however, for other shots the shallowest receiver is at depth of 1084m. From the VSP-CDP transform in Figure 4-14 we conclude that for near-offsets (almost zero-offset), that is shots 1,2,4 and 3, VSP migration is not required as the reflected signal originate in the proximity of the injection well (Figure 4-14.).

The results show that for shots 1,2 and 4 the reflections are coming from a lateral distance of less than 100 m from the injection well. Shot 5 and 9 show that we have reflection from about 250 m and 400 m from the injection well, respectively. Due to such small coverage from the injection well, we do not perform migration or VSP-CDP transform for imaging and the reflection data is interpreted after NMO correction directly, hence avoiding introducing unnecessary amplitude changes.

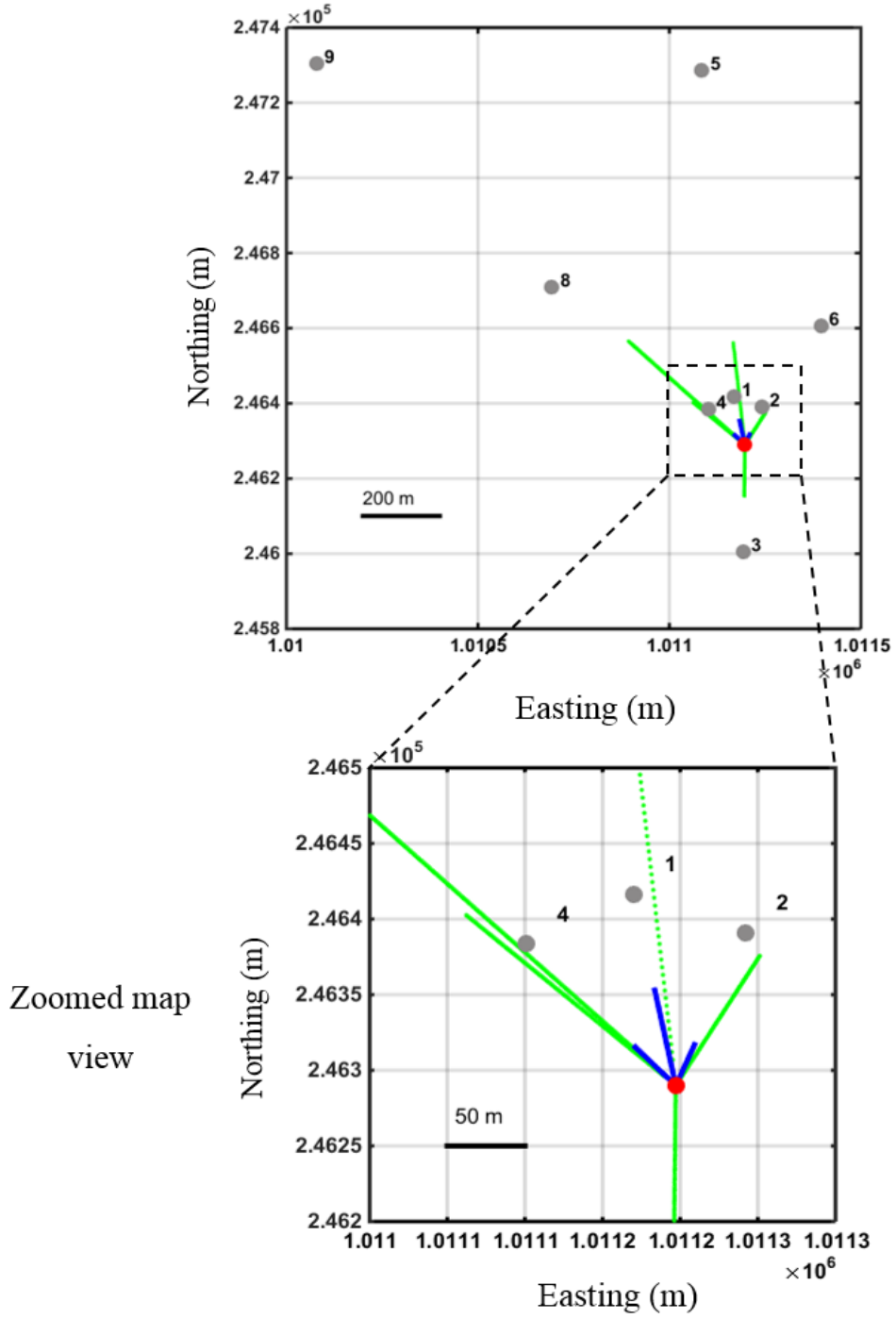

Figure 4-14: Expected reflections locations for each shot-receivers pair using the VSP-CDP transform in a map view for shots 1,2 and 4 (blue) and shots 3,5,6,8 and 9 (green).

4.3 REPEATABILITY ANALYSIS

To understand the repeatability of the data for time-lapse analysis, the final processed sections for shot 1 baseline and monitor surveys and their difference are shown in Figure 4-15. Other shots records and their time-lapse difference are shown in Appendix A. Furthermore, to obtain quantitative results of the repeatability, NRMS repeatability metrics (Kragh and Christie 2002) as described in (Chapter 2, section2.6.6) is used.

It has been reported recently that statics due to near-surface and source signal changes contributed to the low repeatability of the Frio data (Nazari 2014). In my analysis, statics and source wavelet issues have been treated by first applying the field statics and then removing the interleaved receivers which contributed to the static shifts and source signature difference. Furthermore, for the source wavelet, we showed earlier in Figure 4-7 the loss of higher frequencies with depth. This filtration of high frequencies although undesirable (as it reduces the seismic resolution) increased the repeatability of the seismic wavelet - and reflections- at the reservoir depth interval.

The NRMS of the VSP data for the final processed reflections is shown in Figure 4-16 (a,b) for shot 1. The NRMS values vary considerably within the section. However, large values for NRMS are observed as we move to receivers closer to the injection interval indicated by the arrows in Figure 4-16 (a,b). The noise level in the whole section vary strongly but is in the order of 20-160 % NRMS. The results in Figure 4-15 and Figure 4-16 suggest that the amplitude response obtained is a combination of reflection and noise. However, the time-lapse signal still standout for receivers close to the plume top as indicated in the difference section in Figure 4-15 (c) and in the NRMS repeatability for the same receivers in Figure 4-16 (a). The results here show that for receivers at a depth of 1200 m and shallower, the signal from the time-lapse reflection becomes indistinguishable from the variations in the overall section.

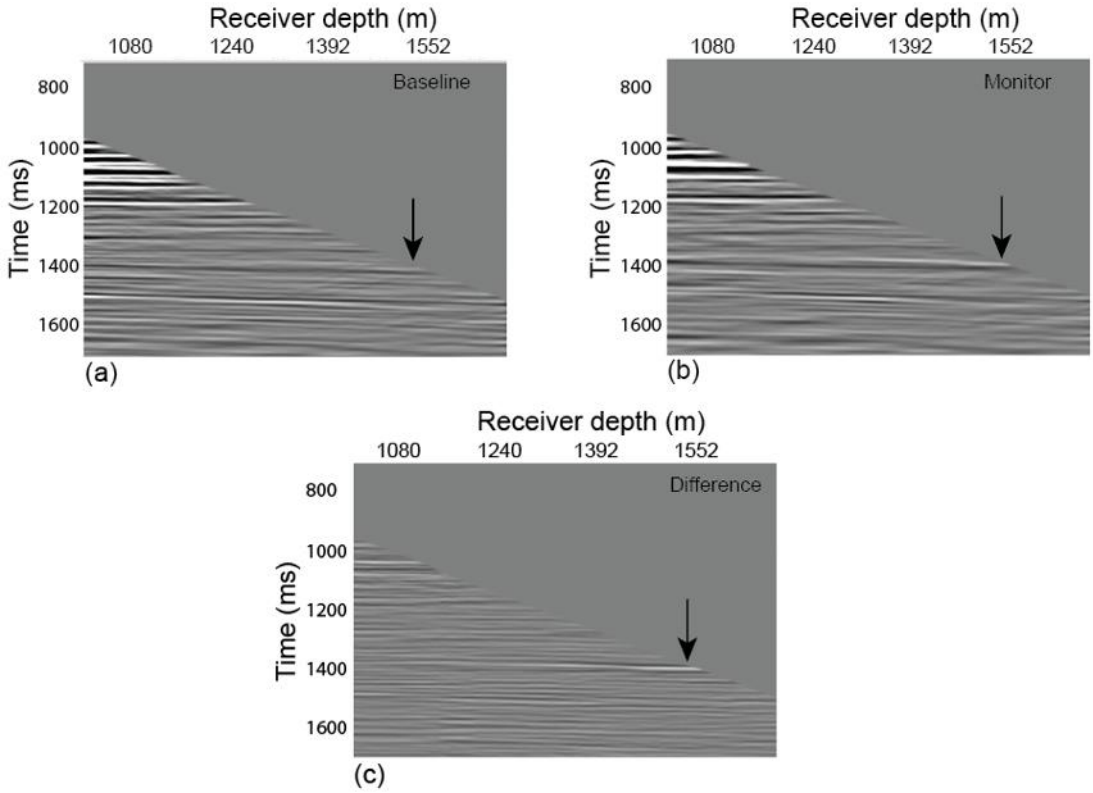

Figure 4-15: A zoomed section for the processed VSP data for shot 1 using the processing flow described earlier for (a) baseline, (b) monitor and (c) difference record. The reservoir reflection is indicated by the arrows.

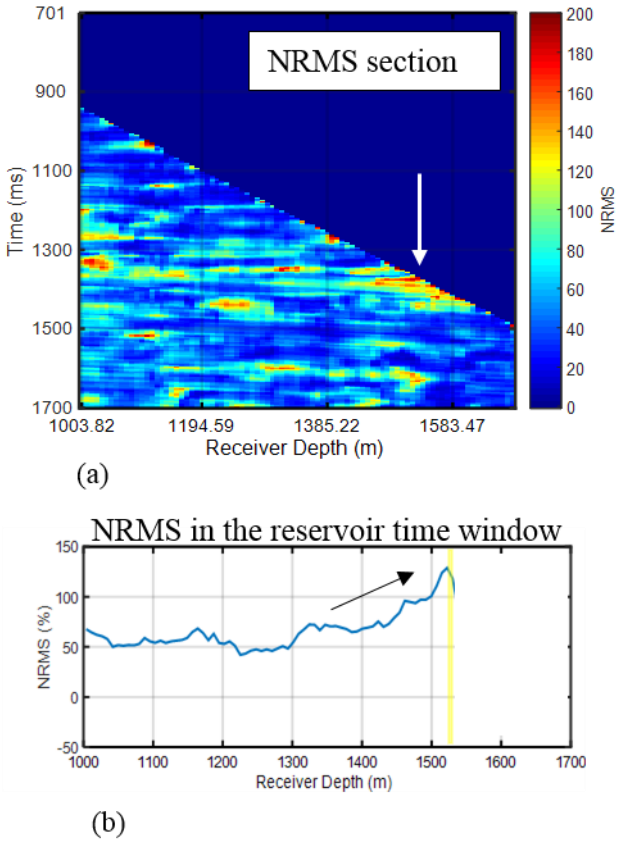

Figure 4-16: (a) NRMS repeatability for shot 1 using 20 ms window. (b) NRMS values over the CO_2 reservoir horizon window (1369 – 1421 ms), the NRMS increases going toward the CO_2 plume (deeper receivers).

4.4 FRIO TIME-LAPSE VSP DATA ANALYSIS

This section presents the analysis for the time-lapse VSP data after the appropriate processing steps are applied as discussed in section 4.2. The goal here is to obtain a quantitative measurement of the elastic changes caused by CO_2 injection at the Frio site in the form of P-wave velocity changes.

4.4.1 Transit time data

For the first arrival analysis a preliminarily processing is performed, which includes the removal of noisy traces, application of field static shifts and resampling of the data (Figure 4-3). These processes do not involve amplitude or phase changing operators such as median filtering and deconvolution. Figure 4-17 shows the first arrivals of the time-lapse VSP data after pre-processing. The first arrival times of the monitor survey are expected to show a time delay associated with a change in the velocity as supercritical CO_2 replaces brine in the pore space. Such a process would cause a velocity decrease in the medium, thus the seismic wavefield of the monitor survey (i.e., rays) travelling through the plume will be delayed in time depending on the magnitude of this velocity change in the medium, Figure 4-17 (b).

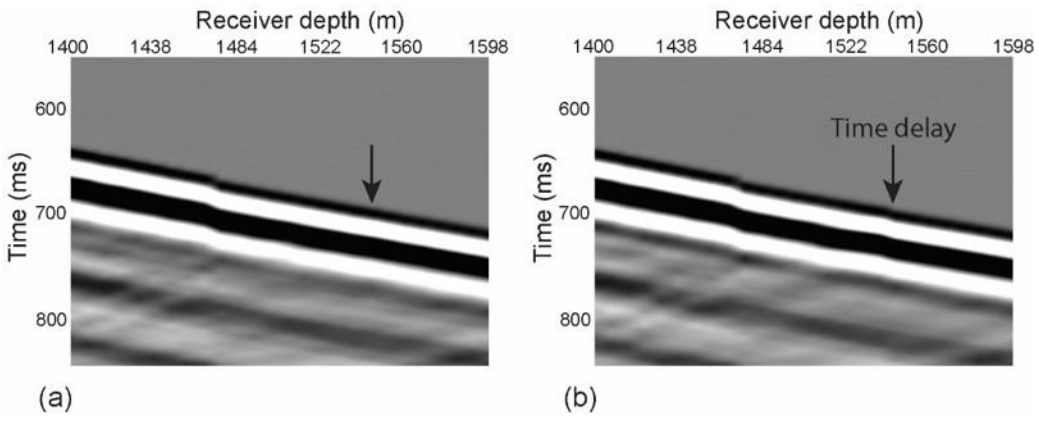

Figure 4-17: A zoomed section from the raw VSP shot 1 after-Pre-processing for receiver interval 1380 – 1600 m for both (a) baseline and (b) monitor surveys. Looking at the first arrivals travel times, a time delay is indicated in the monitor survey.

For shot 1 the largest time delay of 1.3± 0.2 ms is observed for the receiver at a depth of 1545 m (Figure 4-18). This point is approximately 8.8 m below the top of the injection interval. The time delays decrease quickly for deeper receivers and approaches zero for the northwest and northeast azimuths (shots 2 and 4) suggesting

that the zone of significant P-wave velocity changes has a small lateral extent in the immediate vicinity of the injection well. We limit the analysis of the time delays to near-offset shots since we are interested to investigate velocity changes at the vicinity of the injection well. Moreover, for far offset shots, the ray-path distance travelled through the plume is difficult to estimate.

To convert the time delays (Δt) to a change in P-wave velocity ΔV_P we need the post-injection P-wave velocity (V_{P_post}). We use the initial P-wave velocity ($V_{P\_baseline}$) from well logs and the travel distance of the ray-path in the reservoir (d) to calculate the initial transit time (t_0) as

$$t_0 = \frac{d}{V_{\mathrm{P\_baseline}}}. \qquad (4\text{-}1)$$

Then the travel time difference is defined by

$$\Delta t = \frac{d}{V_{\mathrm{P\_post}}} - \frac{d}{V_{\mathrm{P\_baseline}}}, \qquad (4\text{-}2)$$

from which we then obtain V_{P_post} as

$$V_{\mathrm{P\_post}} = \frac{d}{\Delta t + t_0}. \qquad (4\text{-}3)$$

The travel distance (d) is estimated for a maximum possible plume thickness of 8.8 m, assuming a straight ray path and zero-offset geometry, which is considered adequate for receivers close to the CO_2 plume interval. The maximum time delay observed for the depth of about 1545 m corresponds to a velocity reduction of about 750±150 m/s in the immediate vicinity of the injection well as indicated by the peak in the shaded region in Figure 4-18 and about 250±150 m/s for receivers below 1600 m. The uncertainty here is calculated using equation (4-3) with Δt =0.2 ms. It is worth noting that for time-lapse traveltime analysis, the largest errors could be caused by near-surface changes and survey geometry (source and receiver locations), however, these changes will systematic in that they will shift the full traveltime curve, thus, can be corrected by bringing the time delay curve to zero time for the overburden (i. e., above the reservoir). The obtained velocity changes will be utilized to constrain the input parameters for the rock physics model and velocity-saturation relation in the CO_2 velocity-saturation relation in Chapter 5 and Chapter 6.

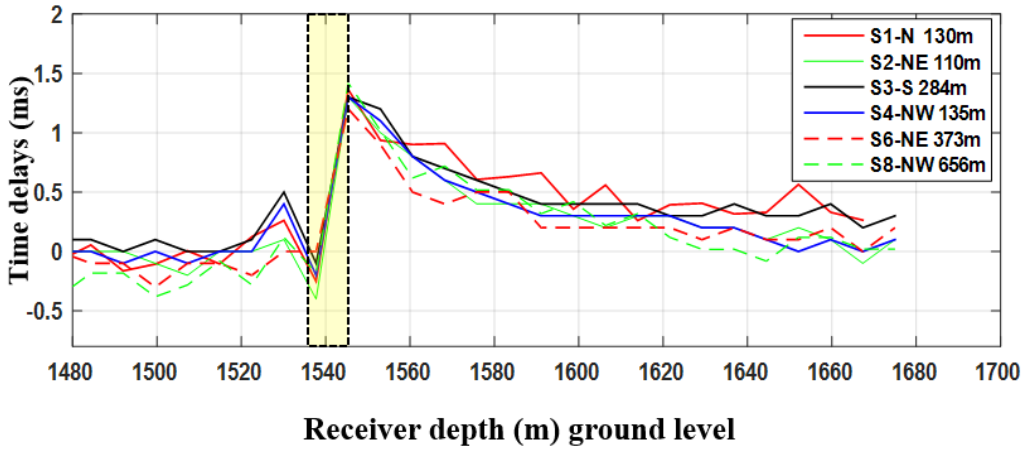

Figure 4-18: VSP first breaks time delays for shots 1-4, 6 and 8 (see Figure 4-1) at different azimuths around the injection well. A maximum delay is observed at receiver depth 1545 m (Ground level), which is approximately 8.8 m below the top of the reservoir. The uncertainty is approximately 0.2 ms estimated from the variation before the reservoir interval from near offset shots 1 to 4.

4.4.2 Transmitted wave amplitudes

The direct arrival amplitude changes are related to the change in the transmission coefficient of the medium. The transmission coefficient defines the decrease of energy for the incident wave given a reflector of infinite lateral extent. However, from the traveltime results in the previous section we know that the CO_2 plume is of a limited lateral extent. Additionally, the plume is expected to spread out less down-dip of the injection well than in the up-dip direction as CO_2 migrates up-dip by gravity. Moreover, the plume thickness is expected to be no more than 8.8 m, which is smaller than the wavelength. Such plume geometry can result in a complex amplitude response comprising diffractions from the plume edges and interference due to tuning.

For the transmitted waves analysis, we pick the maximum amplitudes of the first arrivals shown in Figure 4-4 (yellow line) for the baseline and monitor surveys and normalize each set by its maximum amplitude. Figure 4-19 shows the amplitude difference for the normalized amplitudes of the baseline (A_b) and monitor (A_m) surveys as $(A_m - A_b) \times 100$ versus receiver depth for different shots (where permitted by the data quality). The amplitudes of the direct arrivals have a high signal-to-noise ratio. We correct for any systematic variations for each shot difference which is expected as the source energy differ for the two vintages. This is achieved by bringing the

difference to their appropriate zero line and thus any other variation is either noise or a time-lapse signal caused by the injected CO_2. Variations between the time-lapse surveys above the injection interval are less than 2%, which gives confidence that the observed changes at the top of the reservoir are caused by CO_2 injection.

We obtain an amplitude increase at the reservoir top of 15±2% for shot 1 and up to 18±2% for other near offset shots. Such variations are related to the complexity of the lateral distribution of CO_2 as at different azimuths different CO_2 volumes near the borehole are sampled. Therefore, quantitative interpretation of these observations requires full waveform modelling.

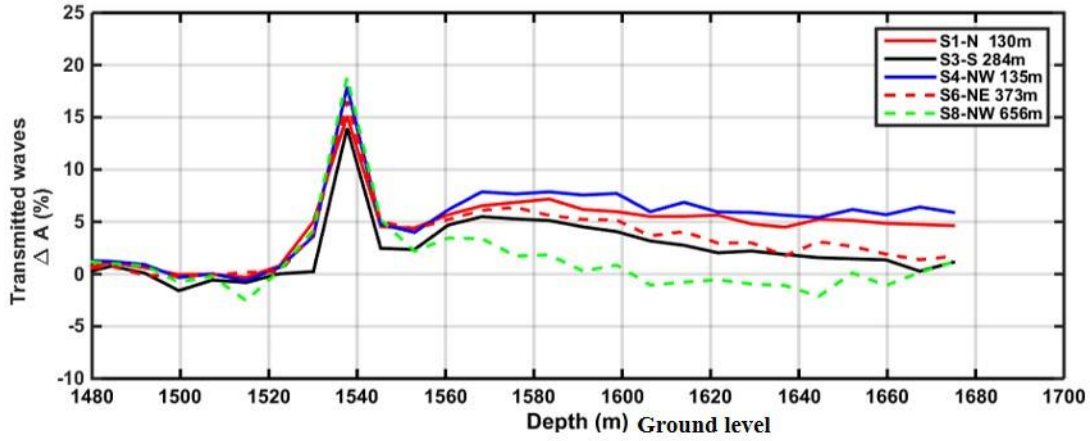

Figure 4-19: Transmitted wave amplitudes difference (i.e., change in the transmission coefficient) for different VSP shots.

4.4.3 Reflection amplitudes

The reflections are obtained after applying the processing sequence described in section 4.2. Seismic waves are reflected from an area in the subsurface rather than a point. Thus, reflection amplitudes are affected by the spatial distribution of CO_2 and the magnitude of the impedance change caused by the injected CO_2 volume. To calculate the amplitude response, we investigate the RMS amplitude (A_{rms}) picked over the same reservoir window for both the baseline and monitor surveys. The change in the RMS amplitude (ΔA_{rms}) response of reflected waves is calculated for the normalized difference in reflection amplitudes as the difference between the post-injection and pre-injection RMS amplitudes (A_{post}) and (A_{pre}) respectively as

$$\Delta A_{\text{rms}} = \frac{(A_{\text{Post}} - A_{\text{Pre}})}{\max(A_{\text{Post}} - A_{\text{Pre}})}. \quad (4\text{-}4)$$

The magnitude of the amplitude changes varies with azimuth, offset and area of investigation. The change in reflected wave amplitude for the near-offset shots is in the range of 0.5 to 0.8 for shot 1 for receivers close to the plume, as shown in Figure 4-20. The uncertainty of the measurement is difficult to determine as it depends on the repeatability of the whole seismic section as we have shown in the repeatability analysis in section 4.3. Thus, fluctuations in the recorded reflection amplitudes are attributed to both noise and the effect of CO_2 plume geometry.

Only shot 1,2,4 and 5 reflection amplitudes are shown in Figure 4-20 as for other shots the records did not show an interpretable time-lapse response due to their low signal-to-noise ratio. Moreover, the time-lapse signal is recognized for receivers up to 1200 m depth, while for shallower receivers the RMS amplitude do not show interpretable time-lapse response. This is attributed to both the level of noise in the data and the limited size of the plume, which is expected to be smaller than the Fresnel zone for shallow receivers. This will be investigated closely later in section 4.5.3.

Similar to the transmitted wave amplitudes, the reflection amplitude changes are difficult to interpret without the support of seismic modelling that can take into account tuning effects and finite lateral extent of the plume. Thus, in the next section we perform finite difference elastic modelling using the velocity changes observed in the field data.

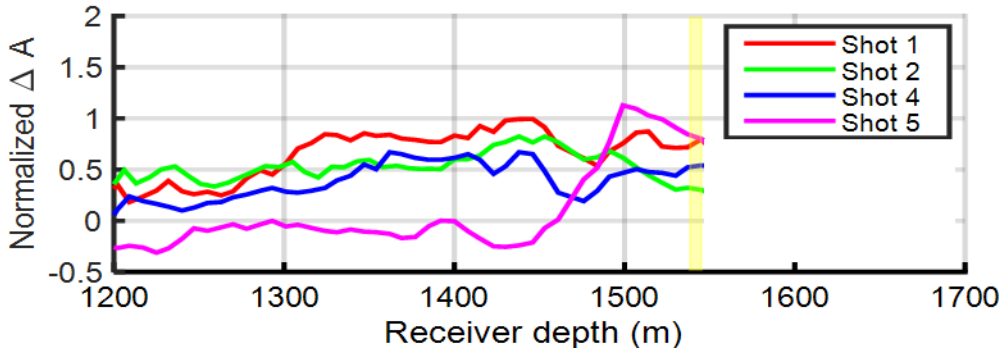

Figure 4-20: Normalized Reflection amplitude difference with reflection enhancement using median filtering. Shot 1,2 and 4 show a similar trend and comparable magnitudes. Shot 5 show large response followed by a rapid reduction indicating that the plume does not extend far from the injection well.

4.5 VSP FORWARD MODELLING TO CONSTRAIN VELOCITY CHANGES

Forward modelling provides a tool to understand the time-lapse (TL) seismic response expected upon fluids injection or production scenarios. After the actual field acquisition of a time-lapse survey, the comparison of the model with the real data could reveal if our predictions are correct or not. If not, then modelling with different parameters for the subsurface elastic model might reveal the cause of the mismatch and help in interpreting field observations. The knowledge gained from forward modelling can refine our understanding of the changes in the reservoir by providing quantitative results that confirm with the real data. An adequate forward modelling scheme would provide the best-case scenario for any seismic experiment if it closely describes the subsurface properties of which the seismic wave will propagate in and the changes in the seismic wavefield caused by the changes in the subsurface properties.

In this section, we use seismic forward modelling to quantify the seismic response for the CO_2 injection using well logs and VSP information to create the subsurface model. Elastic properties changes in the reservoir are set utilizing the obtained velocity changes from the real time-lapse VSP analysis (section 4.4).

4.5.1 Elastic model of the subsurface

We aim to model the time-lapse VSP response near the injection well. Therefore, we assume the reservoir to be about 8.8 m thick, which is inferred from the VSP and log data analysis and comparable to the crosswell results of Doughty, Freifeld, and Trautz (2008). For the elastic parameters, the density log extended to the surface, however, the velocity logs for both V_P and V_S are only available for a depth of 750 m to the total depth of the well. Thus, we use the interval V_P velocities from VSP to complete the model to the surface. Then, V_S is calculated for the same interval by employing the empirical equation of Greenberg and Castagna (1992) with the following:

$$V_S = V_P \times 0.86 - 1.172 \qquad (4\text{-}5)$$

The baseline model we created here will be used for both a preliminary 1.5D and the detailed 2.5D elastic modelling. In the 2.5D modelling, the 1D model will be

extended into 2D space and a CO_2 plume of finite and infinite extent will be inserted in the model while keeping the overburden the same for all cases. Moreover, in the 2D model, for simplicity, we ignore the reservoir dip and perform the modelling for a horizontally layered medium. This means that geometry related uncertainties will be present, but for near-offset shots, we should get an adequate approximation of the seismic response. The post-injection model is similar to the baseline model except for the reservoir that is the 8.8 m interval from 1540.9 m to 1549.7 m. In all modelling cases, the reservoir thickness is kept the same as in this study we are interested in the near injection well area.

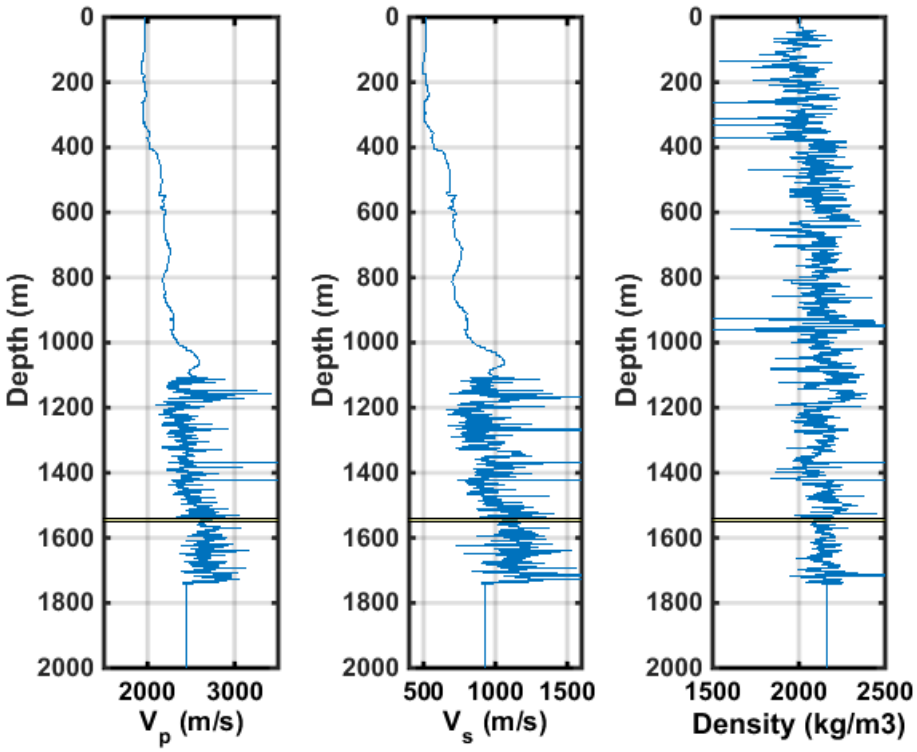

Figure 4-21: Baseline V_P, V_S and density logs used for building the elastic model of the subsurface for both the 1.5D and 2.5D elastic modelling. The interval of interest is shaded.

In the preliminary analysis, we performed a1.5D elastic forward modelling using the OASES software package (Schmidt and Tango 1986). The modelling is run for thin flat intervals with velocities and density taken from the well logs (Figure 4-21) for the interval of interest. However, after investigating the real data response in section 4.4, we concluded that a 2D modelling is required to capture the CO_2 plume

response as it shows a finite lateral extent as evident by the rapid decay of traveltime changes (Figure 4-18) and reflection amplitudes (Figure 4-20).

4.5.2 2.5D Finite-difference modelling

The seismic response is controlled by many factors such as the acoustic impedance as well as the lateral extent and thickness of the reservoir. Thus, to understand the time-lapse seismic response of both traveltime and amplitude changes, we perform a 2.5D finite-difference modelling study which refers to a 3D wave propagation over an extended 2D model of the subsurface (Chapter 2, section 2.5.2). This will aid the quantitative interpretation of the field measurements and later in the velocity-saturation relation.

To this end, we create a baseline 2D elastic model and three post-injection models with various velocity and density changes. The first model assumes a velocity reduction of 750 m/s over the reservoir interval, which is similar in magnitude to the velocity reduction estimated from the field data. The second model assumes a 250 m/s velocity reduction in the same reservoir interval for comparison. In both models, the plume is represented as a flat continuous layer (no plume edges or tapering of the velocity). For the third model we introduce a lateral variable velocity (keeping the reservoir thickness constant) by interpolating from the 750 m/s V_P reduction at the injection well to the baseline model velocity 30 m away from the injection well. In all models, we assume horizontal layering for simplicity. This assumption is adequate for near-offset shots and a limited plume extent. The extent of the 2D elastic model is 2 by 3 km with a grid spacing of 1x1m. A 50 Hz zero-phase Ricker wavelet is used as a source. Table 4-3 contains a summary of the modelling parameters.

Seismic modelling method	Finite-difference, elastic wave equation
Modelling Type	2.5D elastic
Source type	Omnidirectional source
Seismic wavelet	Zero phase Ricker wavelet
Frequency	50 Hz
Grid size (dx, dz)	1 m
Model depth	2000 m

Model length	3000 m

Table 4-3: Parameters of the 2.5D elastic modelling.

4.5.3 Comparison between VSP modelling results and field data

The synthetic data was processed with a similar processing sequence as the field data. However, since we are using a zero-phase Ricker wavelet, we pick the time of the peak amplitude to obtain the first arrivals. Both the variable and constant velocity models give a similar peak value in the traveltime delays of 1.2±0.1 ms near the injection well, which is comparable to the maximum traveltime delay obtained from the field data. However, as we go towards deeper receivers, the variable velocity model best matches with the field data, Figure 4-22 (a).

The first arrival's amplitudes show a peak amplitude change of 19±2 % for both models; that is of the same order as for the field data. Again, the lateral variable model fits the field data better for deeper receivers, Figure 4-22 (b). The reflection RMS amplitudes show a peak response of 0.1, 0.43 and 0.8 for the 250 m/s, 750 m/s and variable velocity model, respectively, Figure 4-22 (c). We note that for the variable velocity model, the recorded reflection amplitude response decreases for shallower receivers. This effect is also observed in field data. These effects are caused by a limited plume extent. We attribute the mismatch between the reflection amplitude and the modelling to the complex geometry of the plume and noise level in the reflection data. Moreover, as the plume spread is small the reflection response decays rapidly for shallower receiver as the Fresnel zone become larger as will be shown next (section 4.6). It can be seen from Figure 4-22 (a,b,c) that a 750 m/s velocity change best matches the peak time-lapse changes of the field data (traveltime delays, transmitted wave amplitudes and reflected wave amplitudes) for receivers in the proximity of the reservoir.

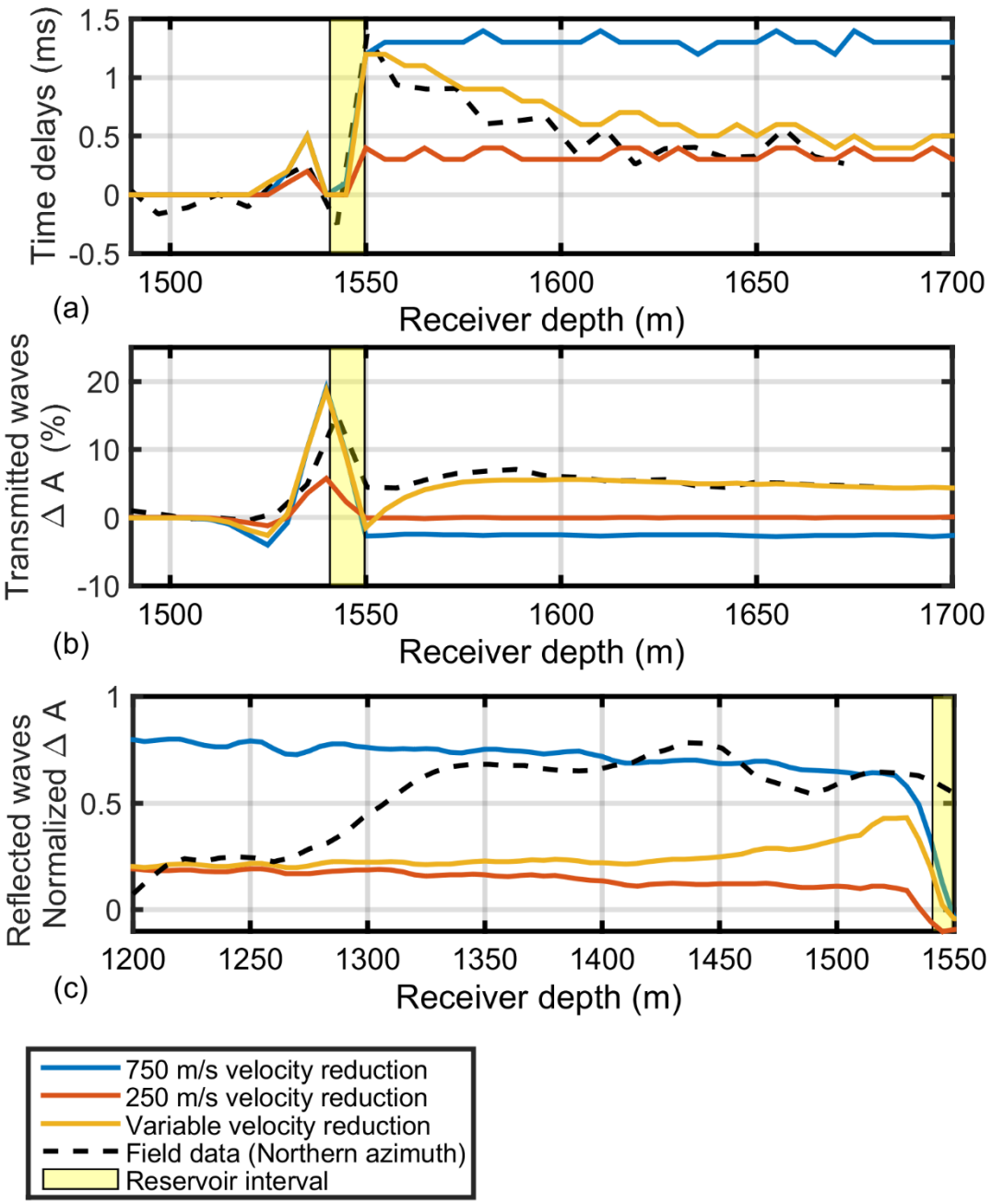

Figure 4-22: Time-lapse VSP for the modelling results and real data for (a) time delays, (b) first arrivals amplitudes difference and (c) reflected wave's amplitudes difference. The velocity changes used in the modelling are as indicated in the legend. The layer thickness is 8.8 m and the injection interval is shaded (yellow). The attributes shown are for an offset of 125 m. The variable velocity change based on the real data is for a CO_2 plume that extends 30 m from the injection well.

4.6 EFFECT OF VSP SEISMIC RESOLUTION ON CO_2 PLUME ANALYSIS: PLUME SIZE AND REFLECTION AMPLITUDES STRENGTH

The Frio data provided an opportunity to use the behaviour of VSP reflection amplitude to determine the approximate CO_2 plume extent. This opportunity arises from one of the advantage of VSP data. We recall here the VSP seismic resolution concepts discussed in Chapter 2, section 2.6.7, showing that although the vertical resolution of VSP here is controlled by the wavelength of the seismic wavefield and velocity, the horizontal resolution in the VSP case has an offset component. From equation (2-49), the horizontal resolution that is the Fresnel radius increases with increasing receiver-to-reflector distance (setting all other parameters constant). As such, if the CO_2 extent is larger than the horizontal resolution for all the receivers, it is expected to get a flat constant reflection response (noise and interference free response). However, if the CO_2 plume lateral extent is small compared to the evolution of the Fresnel radius with receiver-to-reflector distance, then we expect to get a peak amplitude response when the plume size is comparable to the Fresnel zone size followed by a rapid reduction in amplitude. The characteristic of Frio project which allowed this study to be conducted are related to the plume geometry expected and the survey geometry as:

- The CO_2 was predicted to be trapped mainly by capillary forces (Hovorka 2009) due to the small amount of CO_2 injected. This is supported by rapid traveltime delay decay, indicated thinner and/or lower CO_2 saturation away from the injection well.
- The receivers for the time-lapse VSP survey are in the injection well and near-offset shots data is available. Moreover, seismic receivers span the whole interval of the CO_2 plume and all the way to the surface (i.e., shot 1).

In order to compare the real data VSP response with the synthetic, the characteristics of the seismic response for thin and limited lateral extent structures is to be defined for this case study. Understanding if the amplitudes and time delays are affected by the geometry of the CO_2 plume rather than the “velocity” changes caused by fluids saturation is crucial.

The preconception is that first arrivals traveltime are stable and only change if the velocity or path travelled is different. However, as stated earlier in the analysis of the real data, the amplitudes of both transmitted and reflected waves could be affected. Moreover, if the plume extent is small, then we may infer the "size" of the plume by analysing the reflection amplitude response and defining the Fresnel zone in the data.

4.6.1 VSP resolution aspects for time-lapse monitoring

we investigate here the VSP resolution aspects that affect reflection amplitude. These are related to the vertical resolution and horizontal resolution of the VSP method. In general, the detectability of a thin layer which have a high contrast compared to the surroundings (CO_2 plume in this case) is high. However, tuning thickness (vertical resolution) and Fresnel zone (horizontal resolution) could have an effect on the seismic data and must be acknowledged in this study. To this end, seismic modelling is utilized to investigate several scenarios of CO_2 plume thicknesses and extent and analyse the seismic amplitude response.

4.6.1.1 Vertical resolution

The tuning thickness is the parameter which must be identified to understand if the reflection amplitude is caused by a single reflection interface or an interference of two reflections from the top and bottom of the CO_2 plume. Unlike surface seismic, the receivers in VSP are not at the same depth which means that the response could be different for each receiver depth. Thus we create a simple wedge model (with 2D elastic modelling only to minimize computation time) with the receivers set at different depth levels, specifically at 1000 m, 1300 m, 1440 m and 1500 m with the top of the CO_2 wedge at 1540 m. The model is 4x2.5 km with 5 m regular gird and a 50 Hz Ricker wavelet is used as a source, Figure 4-23. The results for a receiver depth of 1000 m and 1500 m are shown in Figure 4-24.

From Figure 4-25 we can observe that the amplitude is constant for each receiver depth for a wedge thickness >20 m approximately, after which we could see the increase in amplitude as the thickness decreases. The amplitudes here are absolute amplitudes picked at the troughs of the top reflection. In the real data this was not possible and the RMS amplitude is estimated instead. The tuning thickness identified is around 10 m evident by the peak in amplitude for that layer thickness, after which the amplitude decrease rapidly. This tuning thickness is comparable for that obtained

using equation (2-48) with V_P = 1900 m and f = 50 Hz which gives a wavelength of 38 m and a tuning thickness of about 9.5 m. For the receiver at 1500 m the amplitude of the reflection is found to be very close to the direct arrivals as shown in Figure 4-24 (b). Thus, we suspect that for receivers very close to the top of the CO_2 plume, interference with direct arrivals could affect our reflection amplitude. Comparing the modelling results behaviour to the real data (Figure 4-20), we conclude that the response of the real data is the result of tuning as the CO_2 plume thickness is about one-fourth of the wavelength of the field VSP data.

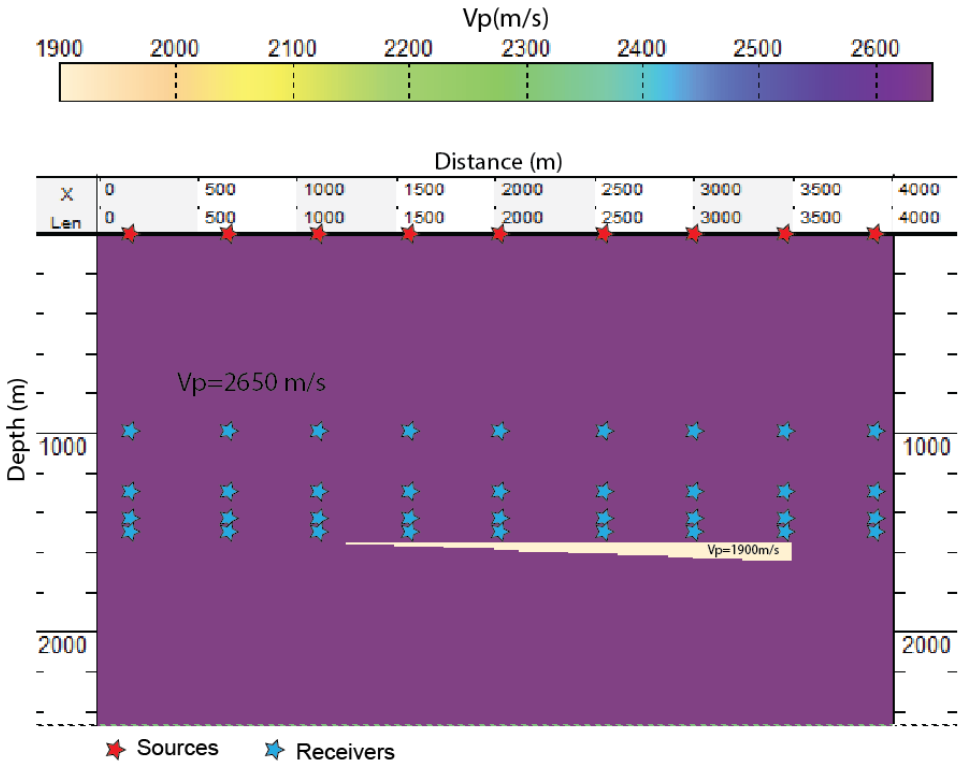

Figure 4-23: wedge model reflection amplitude response for receivers set at different depths (zero-offset VSP geometry).

(a)

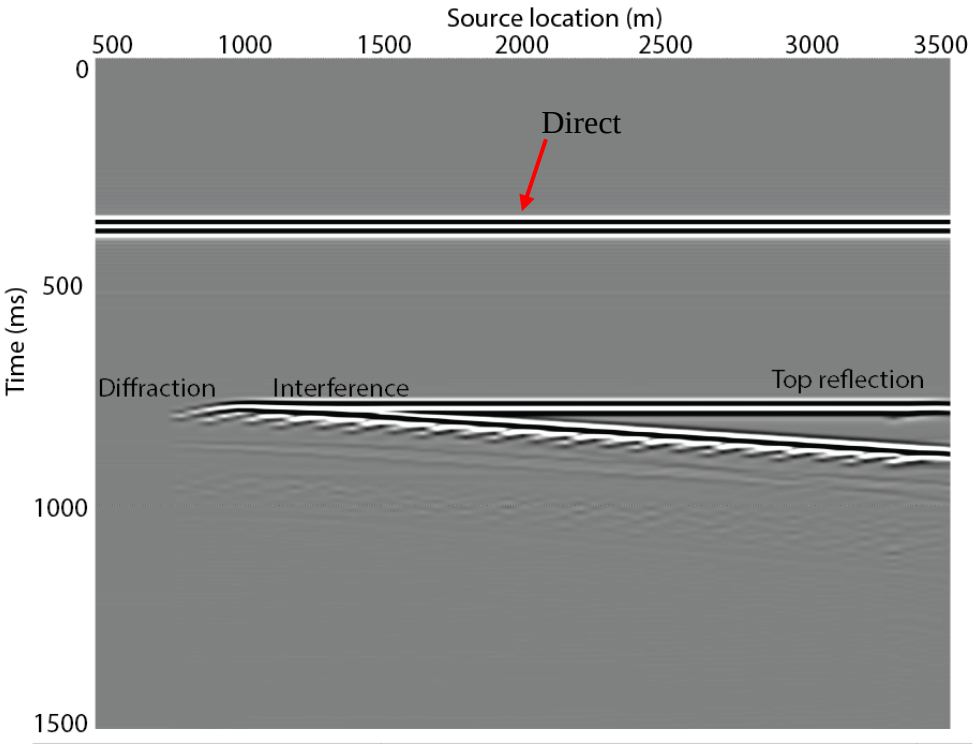

(b)

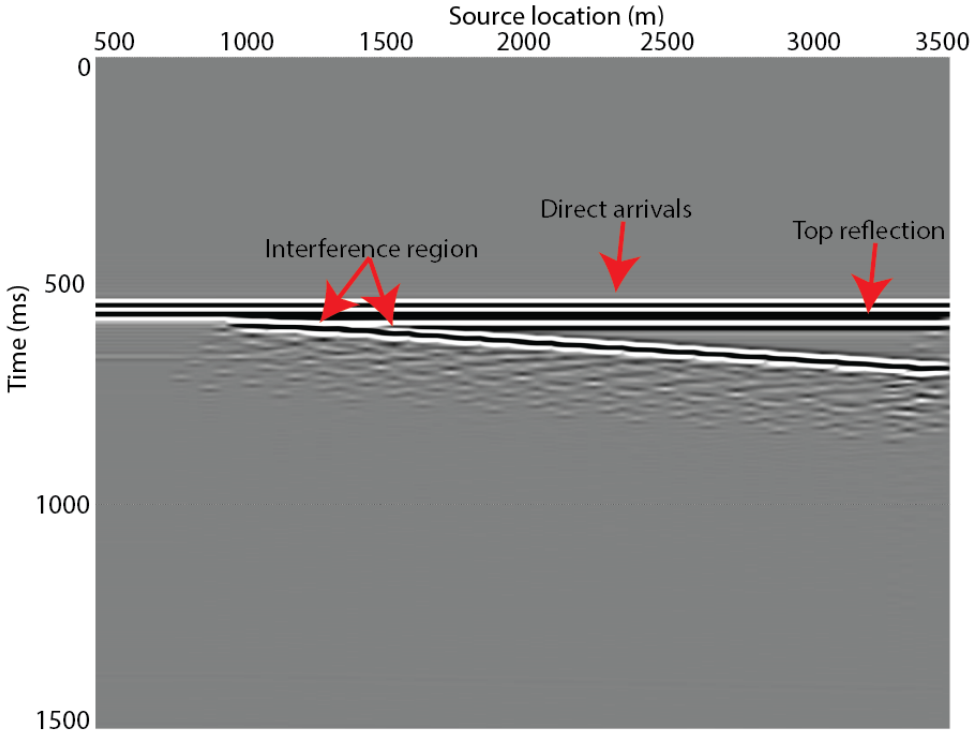

Figure 4-24: The wedge model seismic response for (a) receiver depth of 1000 m and (b) receiver depth of 1500 m.

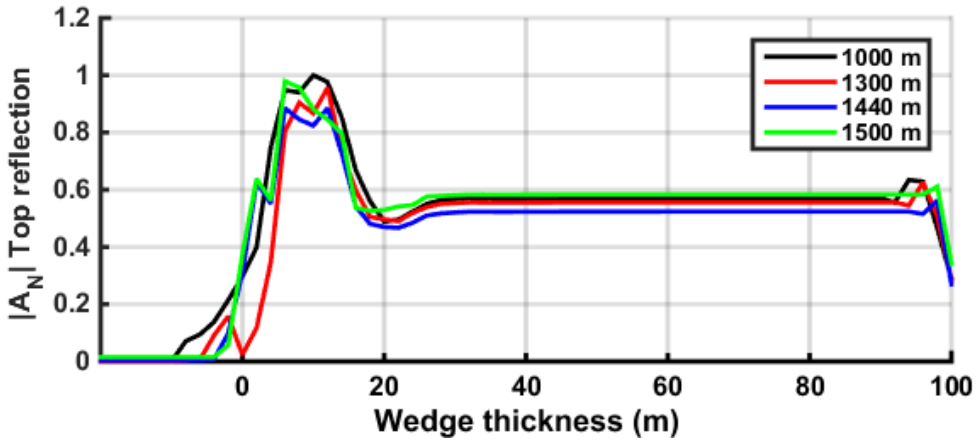

Figure 4-25: Wedge model normalized absolute reflection amplitude $|A_N|$ response for receivers positioned at different depths as stated in for the zero-offset VSP wedge model in Figure 4-23.

4.6.1.2 Horizontal resolution

In zero-offset VSP survey the reflection recorded by a receiver comes from a limited area in the subsurface within the Fresnel zone with its centre at the well (Dillon and Thomson 1984). Moreover, each receiver depth (above the reflector of interest) will have a different Fresnel zone radius as in equation (2-49). However, in the case of offset VSP, the information obtained is for different reflection zones away from the well (Dillon and Thomson 1984). To illustrate this, we carried out a ray tracing study here to complement the VSP-CDP mapping from the real data (section 4.2.7). This is important, as we could define the maximum lateral distance that our first arrivals have penetrated and the reflection points for each receiver depth. The coverage for the first arrivals and illumination of reflections for the synthetic data are shown in Figure 4-26. The maximum coverage of the first arrivals for receivers below the reservoir to a depth of 1700 m illustrate that the information is coming from a limited area around the well. The coverage density is higher for near-offset shots (more rays per distance) for both first arrivals and reflections. Reflected P-waves for 125 m offset show a zone of investigation that is less than 60 m for receivers up to a 1000 m. However, going to further offsets the centre of the Fresnel zone moves away from the receivers well rapidly going toward shallower receivers. We note that in case of dipping reflector the error in the ray tracing – or CDP mapping- is less for receivers near the reflector. We can compare the ray-tracing model in Figure 4-26 to the VSP-CDP transform results

for the real data in Figure 4-14. Both approaches show similar results and suggest that near-offset shots provide an approximate zero-offset case.

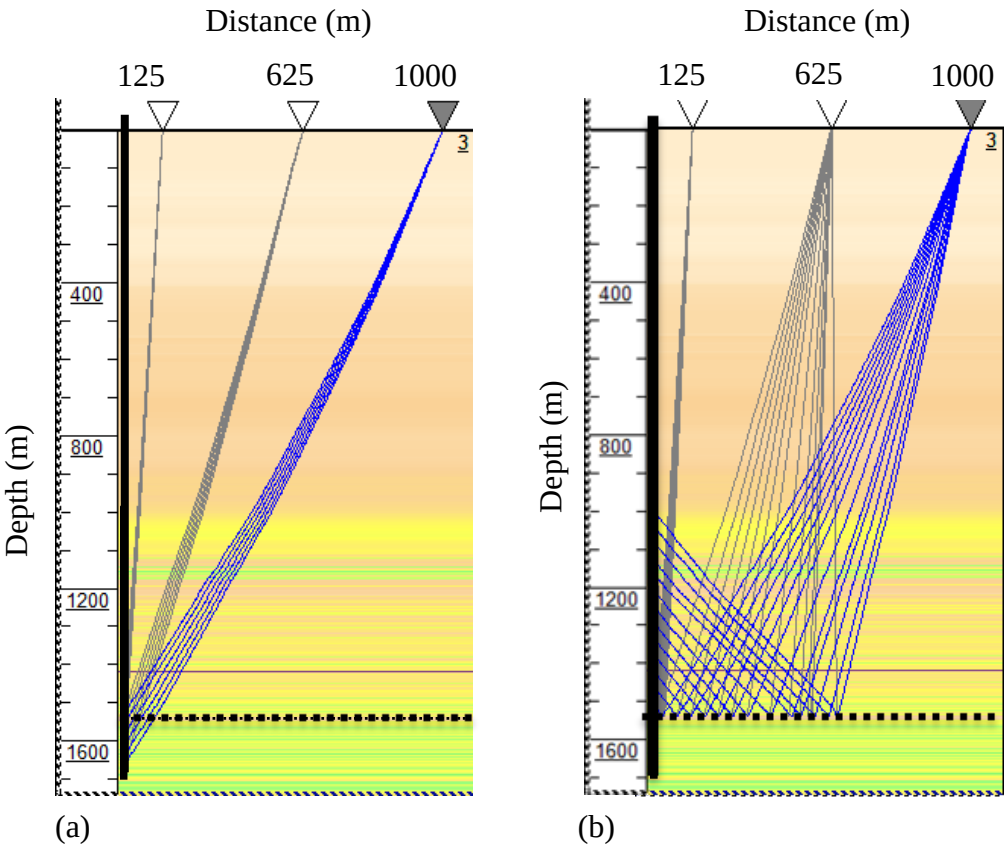

Figure 4-26: VSP ray tracing model using the Frio site subsurface elastic model for (a) Direct arrivals and (b) reflected waves.

To study the Fresnel zone effect of the reflection amplitude we run several 2 layers' case, 2D elastic modelling (to reduce computational time) of the subsurface with CO_2 plume of different lateral extents. These models will have the tuning thickness effect as they used the same thickness of 8.8 m for the reservoir zone of change. The models dimensions are 1x2.5 km with 50 Hz wavelet for the source and a grid spacing of 2x2 m. Two sources are set at the surface for a zero offset and 125 m offset. Receivers are extended from 100 to 1880 m. In all models, the depth of the reflector is 1540 m, an example is shown in Figure 4-27. Theoretically, using equation (2-49) the Fresnel zone diameter (centred at the well for zero-offset VSP) in this case will increase rapidly as the receiver-reflector distance increases. For a 50 Hz frequency and RMS velocity (V_{rms}) of 2305 m/s the Fresnel zone diameter is shown in Figure 4-28. The results of the modelling are summarized as follows:

- In zero-offset and offset VSP the reflection amplitude is largely affected by the lateral extent of the object (reflection interface). If the object lateral extent is wider than the FZ, then the amplitude recorded will build up as the Fresnel zone diameter approaches that of the reflector lateral extent shown in Figure 4-30 and Figure 4-31 for a 100 m reflector.
- A reflector smaller than the Fresnel zone will have a minimum response as its contribution becomes smaller with the increase in the Fresnel zone diameter. However, the response does not vanish to zero.
- The difference in reflection amplitude between zero-offset and 125 m offset is minimum and the overall response behaviour is similar in both cases.
- The size of the reflector has minimum effect on the first arrivals amplitudes as shown in Figure 4-30 (a) and Figure 4-31 (a).

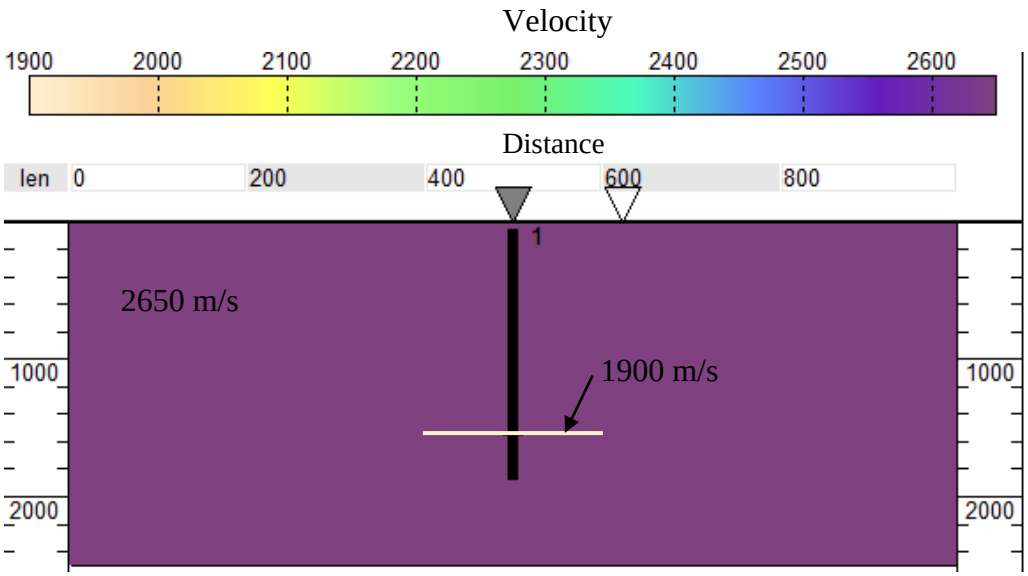

Figure 4-27: Model with a plume thickness of 8.8 m and 100 m extent on both side of the well. Total lateral extent of the plume is 200 m.

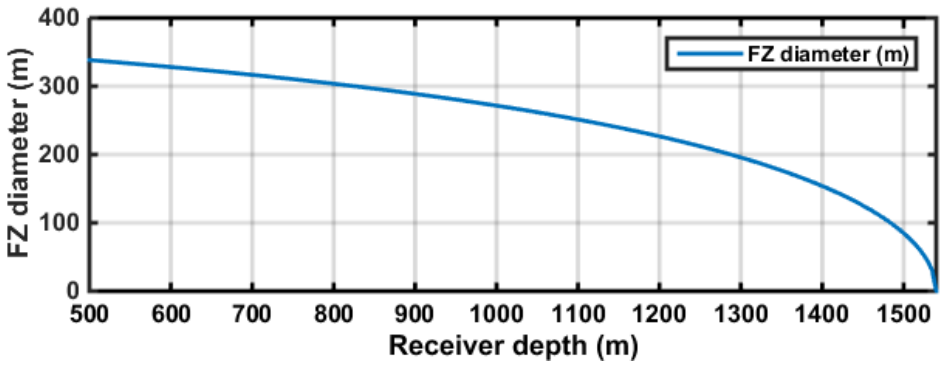

Figure 4-28: Fresnel zone diameter for a 50 Hz dominant frequency and V_{rms}=2305 m/s.

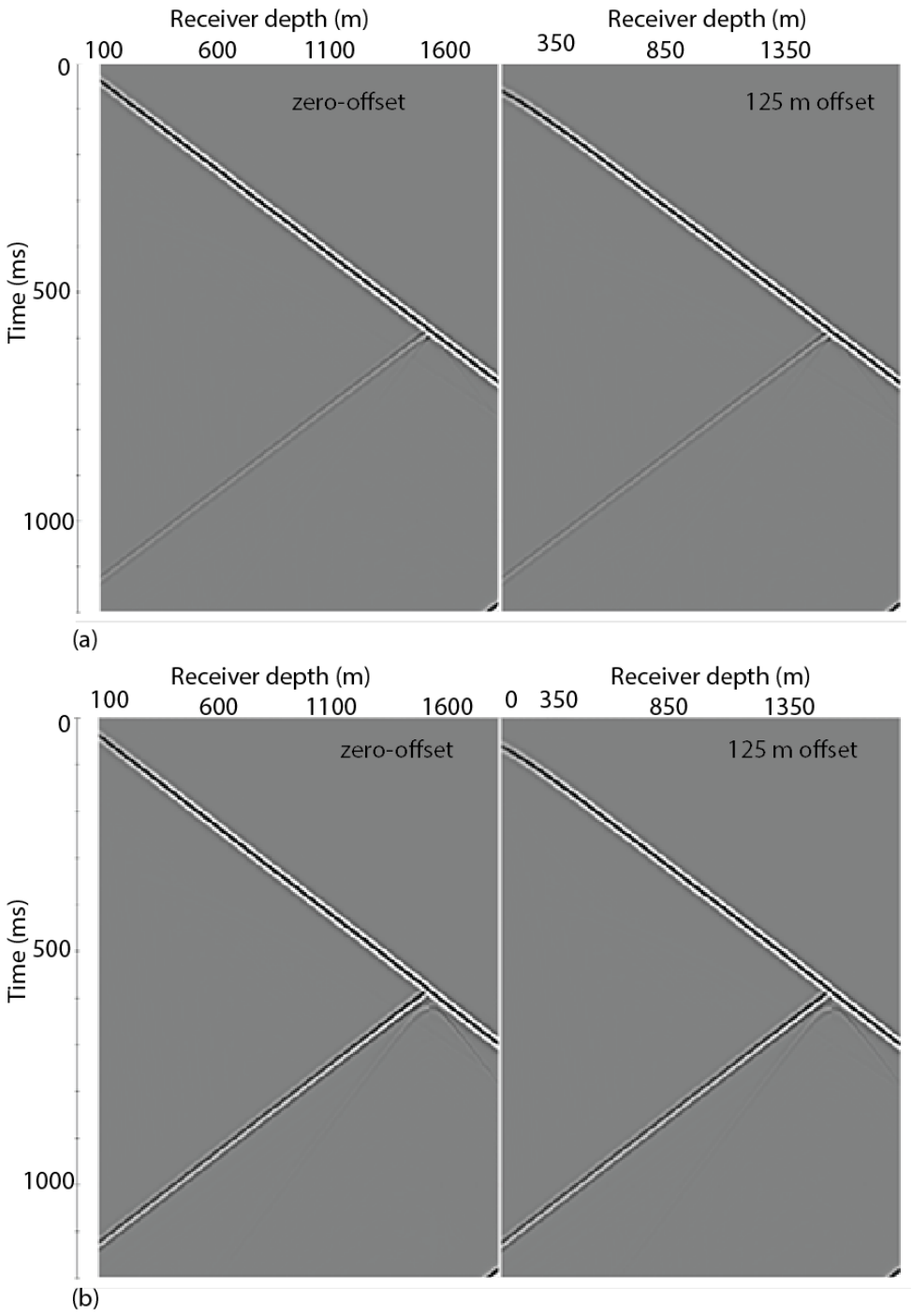

Figure 4-29: Reflection at zero offset (left) and 125 m offset (right) for (a) 20 m CO_2 plume model, (b) 100 m CO_2 plume model.

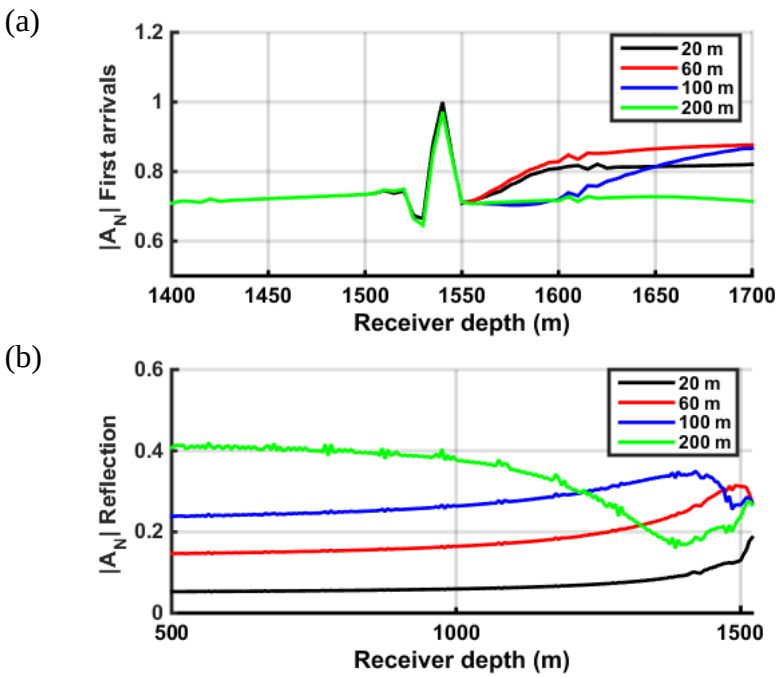

Figure 4-30: Results for different plume lateral extent for zero-offset VSP for (a) normalized first arrivals amplitudes, (b) normalized reflection amplitudes. Note the rapid reduction in reflection amplitude for plume extents of less than 100 m.

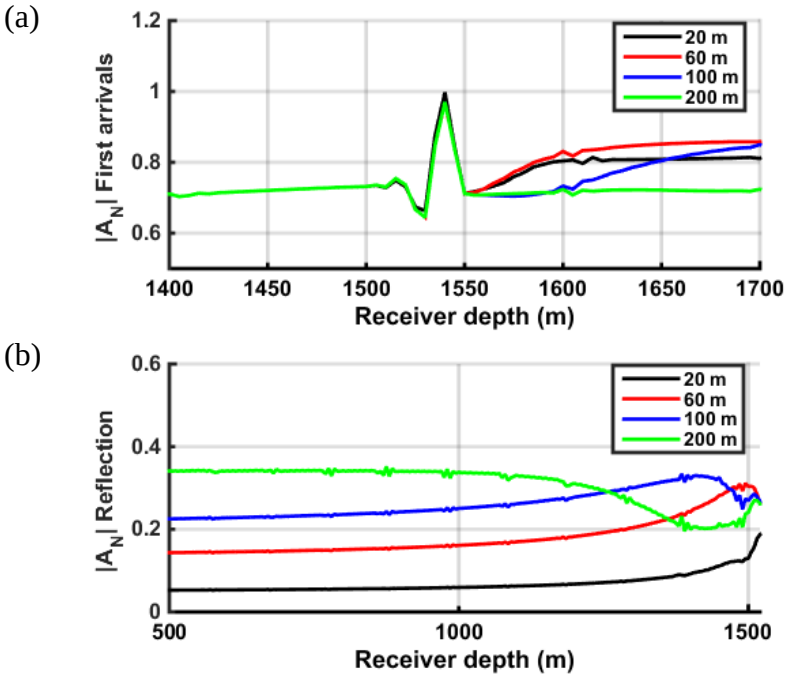

Figure 4-31: Results for different plume lateral extent for 125 m offset VSP for (a) normalized first arrivals amplitudes, (b) normalized reflection amplitudes.

4.6.2 Comparison of 2.5D modelling with real data

we carried out a set of 2.5D forward modelling exercises with a velocity model of the subsurface using the same approach described in section 4.5 for various CO_2 plume radius (centred at the injection well). The aim here is investigate if using the VSP data we could infer the approximate plume size in the subsurface. The initial simple modelling results described earlier in sections show that indeed the aspects of resolution have large effects on the magnitude of reflections. Moreover, we have shown that using the Fresnel zone concept, we could be able to infer the approximate CO_2 plume size.

This is illustrated in Figure 4-32 with the Fresnel zone radius plotted as a function of receiver depth and the response of the raw VSP data for shot 1 (Northern azimuth) is shown with the amplitude response for the modelling. The shaded area in Figure 4-32 for the deep receivers are those for which the assumptions of equation (2-49) might be invalid and interference of first arrivals with reflections could be affecting the amplitudes. While the red shaded area for receivers shallower than 1200 m are those of which the real data have low signal-to-noise ratio. Thus, for comparison we focus in the area in between. Observed reflection amplitudes show best match for a CO_2 plume in the modelling that have a 60 m to 100 m radius. This can be seen also in the Fresnel zone radius calculated using equation (2-49), which suggest a Fresnel zone of about 85 m radius.

The results are in agreement with comprehensive reservoir simulation and reactive transport modelling from previous studies which suggested that the CO_2 plume will be trapped by capillary and residual trapping mechanisms and its extent is small due to the small volume of the injected CO_2 of 1600 tons (Daley et al. 2008). Reactive transport modelling have shown that the CO_2 plume will extend no more than 90 m radially from the injection well after about 0.5 year (Xu et al. 2010, Ghomian, Pope, and Sepehrnoori 2008). The monitor seismic survey was conducted about 6 weeks after the injection was halted. Thus, we expect that the CO_2 plume extent will be less than 90 m radially. Moreover, first arrivals traveltime for receivers below the plume show that we have almost no time-lapse signature (no time delays of first arrivals) other than that for the Northern azimuth for receivers at depth of 1650 m for shots 4,6 and 8, Figure 4-18. The ray tracing study suggests that these first arrivals time-delays do not extend more than 40 m from the well. This indicates that the plume

does not extend far from the injection well other than the northern azimuth (i.e. plume is elongated toward the northern azimuth, updip). The results here show that the reflection data could be used to infer small scale fluids accumulations using VSP data. This might be of use in CO_2 leakage scenarios and monitoring in the early injection stages of CO_2 sequestration projects.

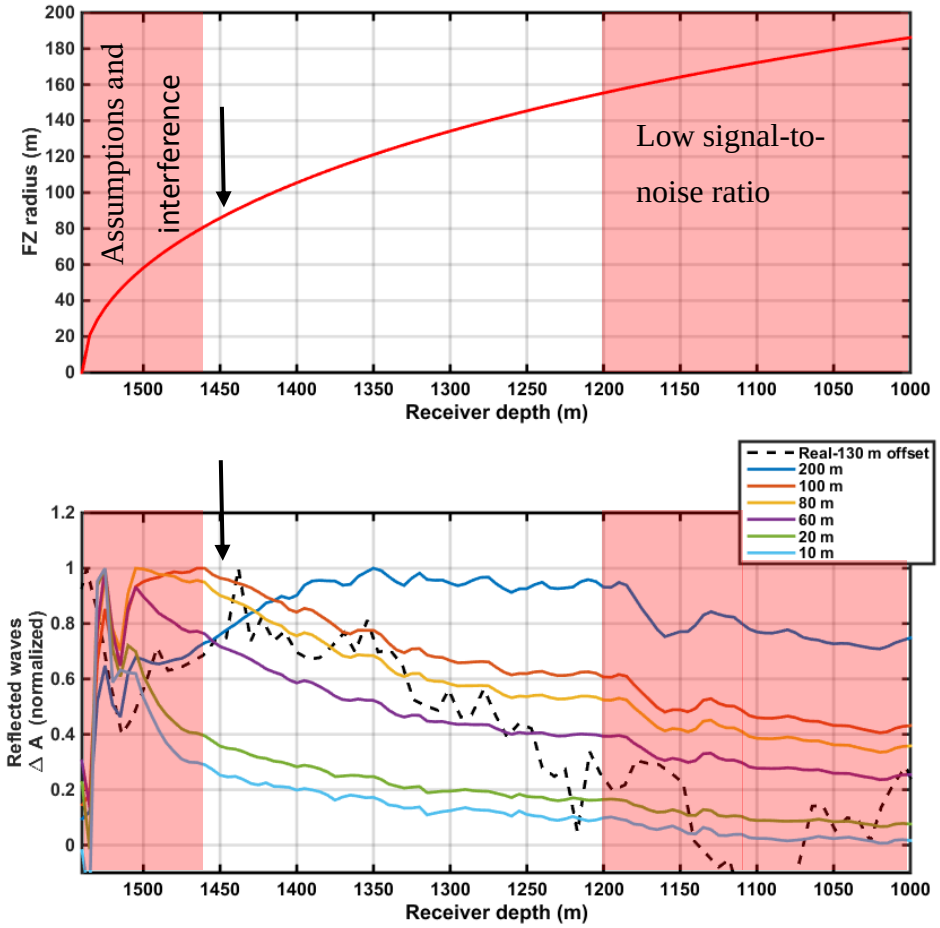

Figure 4-32: Results for different plume lateral extent modelling for 125 m offset. VSP. Raw shot 1 reflection response is shown (No median filtering).

4.7 FRIO CROSSWELL DATA

At the Frio CO_2 injection site, two high-resolution crosswell surveys were conducted between the injection well and observation well. The 3-component receivers used to extract first arrivals span between 1377 to 1680 m (4517 – 5512 ft). The sources span an interval between 1501 to 1577 m (4925 – 5175 ft). This resulted in 303 m receivers span and 75 m sources span covering the injection interval between the wells, Figure 4-33. The receivers and sources spacing was about 1.52 m (5 ft), see Figure 4-33 . The waves were generated using an orbital vibrator source with two orthogonal horizontal polarizations (2-component) , providing high signal-to-noise ratio P- and S-wave records with frequency range of 70 – 350 Hz, see Figure 4-34 and Figure 4-35 (Daley, Myer, and Majer 2005, Daley et al. 2008, Daley and Cox 2001). The crosswell data were supplied by LBNL both as raw data and as time picks of the P-wave and S-wave first arrivals.

The sources and receivers used provided a set of 6-component crosswell records. This allowed the picking of both P-wave and S-wave as it was possible to separate the two events. The time-picks provided used the inline source for the P-wave, while the crossline sources were used to pick the S-wave (Daley, Myer, and Majer 2005).

4.7.1 Crosswell tomography

Seismic traveltime tomography is a method of using first break traveltimes of various recorded traces to create a velocity map in the area of the subsurface travelled by the seismic raypaths (wavefield) (Zhou 2003). Crosswell tomography results accuracy and resolving power depends on the raypath coverage, inversion method, signal-to-noise ratio and how the noise propagate in the inversion routine (Zhou et al. 1993).

The traveltimes for both V_P and V_S were already picked with the number of rays available for the inversion process and mean V_P presented in Table 4-4. The data provided were the coordinate of sources and receivers and traveltimes. The tomography processing is performed using a commercial software package (ReflexW version 7.0.0). The tomography algorithm is based on the simultaneous iterative reconstruction technique (SIRT). The program only allows for 2D processing if one want to obtain a 2D section of the velocity profile. However, the wells are not vertical (Figure 4-33). Thus, the data is converted from 3D coordinate to 2D coordinates by a

projection of any out of plane points to a common plane. This process is bound to introduce some geometrical changes to the source-receiver offset and hence traveltime changes. After applying the projection, the maximum change in any source-receiver pair distance from this projection is found to be less than 1.1 m. we applied this geometry change to both vintages. We note here that geometrical effects are expected even if this projection is not performed as the sources and receiver's location in both wells were not well known -absolute distances - due to various operational limitations. To reduce or eliminate errors caused by such uncertainty in the geometry we mainly look at the time-lapse change (difference only) rather than a single vintage traveltimes (or velocities). we use a grid size of 2 m both vertically and laterally in the inversion; however, the results are interpolated to 1 m (Figure 4-36). In general, the uncertainty would be high at the edges of the model where there are less number of rays and where the velocity changes fluctuate in a very short interval due to the lack of resolution.

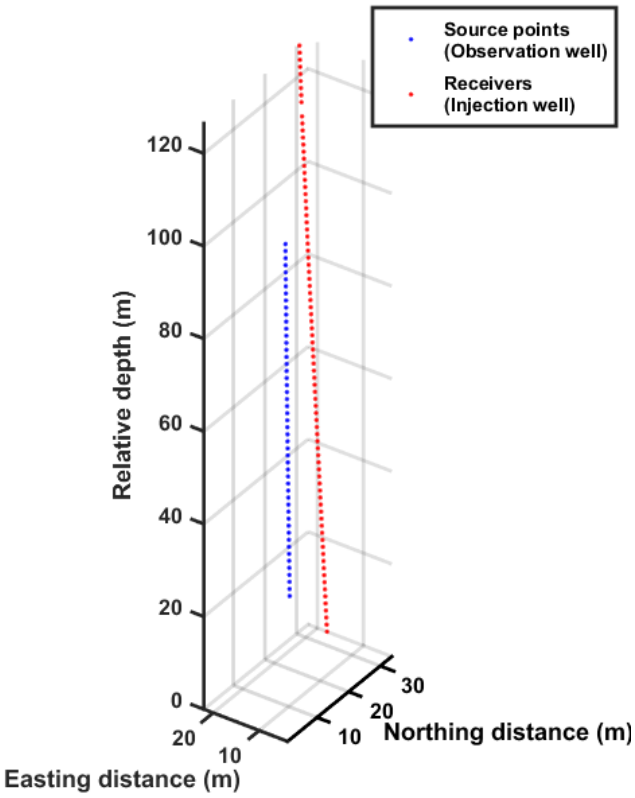

Figure 4-33: Geometry of the wells used for the crosswell survey in 3D space (relative distances). Only shots and receivers used in the tomography are shown. Note that the wells are not in a common plane and a projection of the points into a 2D plane is required to process the data in a 2D space.

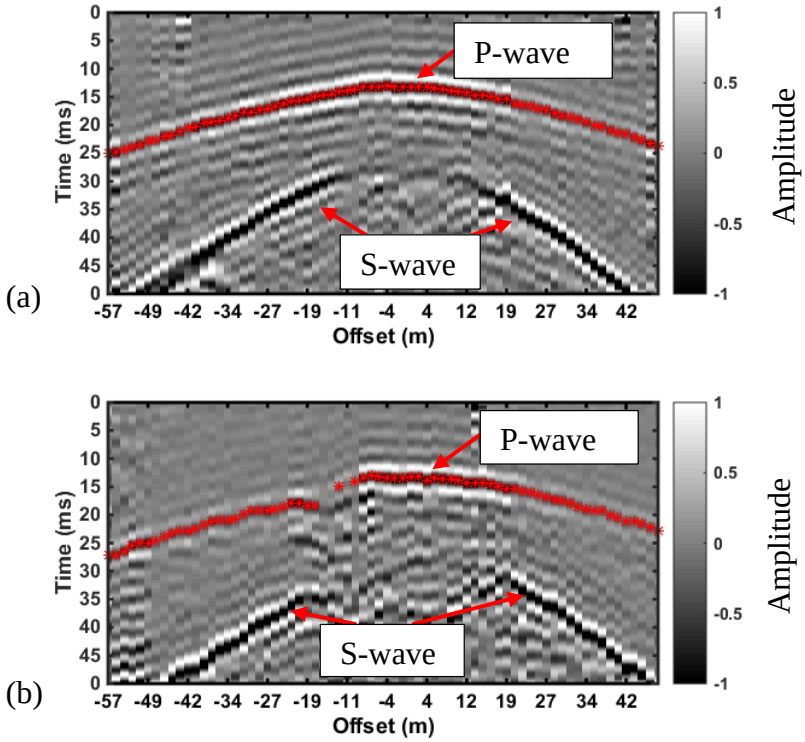

Figure 4-34: An example of a shot record for the crosswell survey for (a) pre-injection, (b) post-injection. Note the good separation between the P-wave and S-wave and the time delay in the arrivals of the P- and S-waves.

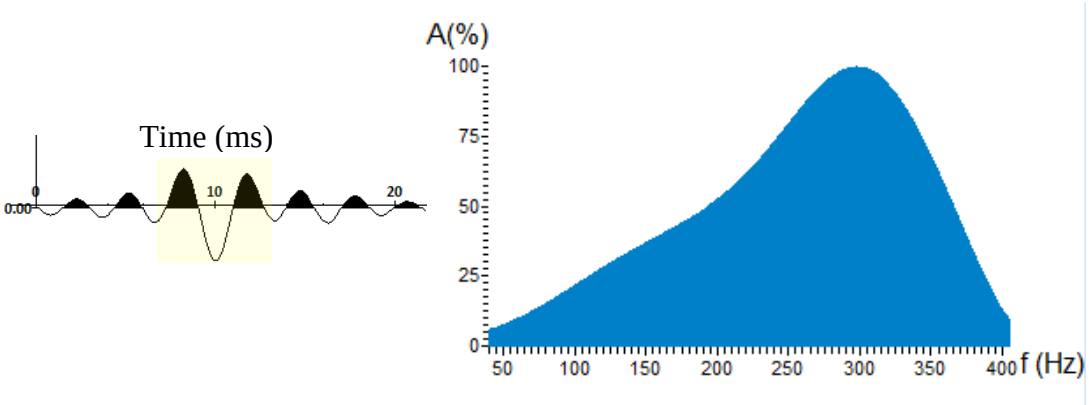

Figure 4-35: An ensemble wavelet (left) and its amplitude spectrum from the crosswell data (right).

Crosswell Survey	*Baseline*	*Monitor*
Number of Rays	**4151**	**3301**
Mean V_P velocity (m/s)	**2572**	**2489**

Table 4-4: Number of rays (source-receiver paths) for the crosswell experiment for the baseline and monitor surveys.

4.7.2 Crosswell tomography results

Looking at the final differential tomograms in Figure 4-36 the following observations could be made:

- The largest P-wave velocity reduction in the crosswell is about -750 m/s and -350 m/s at the injection well and observation well, respectively.
- S-wave reduction of about -250 m/s is observed at the injection well. However, at the observation well the S-wave velocity change is negligible.
- We can see that the large V_P change in velocity (reduction) is in the same area of the large V_S reduction.
- Good match between the saturation profile from saturation logs and the velocity reduction qualitatively (largest velocity reduction at the highest CO_2 saturation). The results of the tomography are similar in magnitude to those obtained by Daley et al. (2008) and comparable to those obtained by Ajo-Franklin, Minsley, and Daley (2007) using compactness constraints. This further confirmed our tomography results.

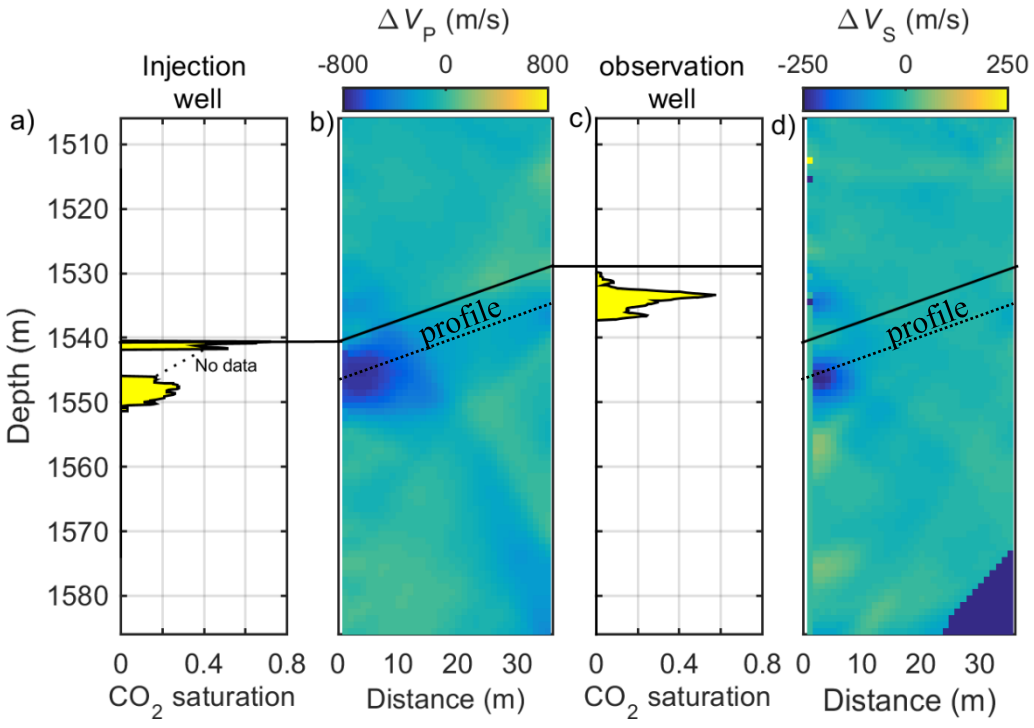

Figure 4-36: Crosswell velocity differential tomograms (b) ΔV_P and (c) ΔV_S and RST saturation logs for the injection and observation wells taken after the monitor crosswell survey (see Figure 3-12).

4.8 SUMMARY

This chapter dealt with the processing and analysis of the time-lapse VSP and crosswell data of the Frio project. Focusing of the VSP data, we implemented a processing flow with the objective of obtaining quantitative time-lapse geophysical parameters. We have confirmed the magnitude of P-wave velocity changes obtained from the real data using 2.5D finite-difference modelling. The velocity reduction confirmed at the injection well is estimated to be about 750 ±150 m/s which is confirmed using three independent measurements, that is traveltime delays, transmitted waves amplitude and reflections.

We have shown using seismic modelling the effect of horizontal and vertical resolution of VSP seismic on the analysis of reflection and transmission amplitudes. We have found that reflection seismic is highly affected by the resolution and the geometry of the plume. The Frio project CO_2 plume geometry have been confirmed by looking at the reflection behaviour with receiver depth for the VSP data.

Interestingly, the reflection behaviour and the Fresnel zone calculated both suggest a CO_2 plume between approximately 60 m to less than 100 m radius around the injection well. These results conform with previous reservoir modelling results and with the obtained time-lapse responses which all indicate a limited plume extent around the injection well.

The crosswell data offered a high-resolution information of the reservoir velocity change for both V_P and V_S. However, single vintage velocities were not usable. The V_P velocity changes obtained confirm with those obtained from the VSP data at the injection well. The results show anomalous reduction is S-wave velocity which is not expected in fluid substitution scenarios as we will discuss in Chapter 6.

These results from this work will be utilized in Chapter 5 and Chapter 6 for rock physics modelling. Moreover, the learnings from the time-lapse VSP for the Frio case study conducted here will be utilized later in Chapter 7 in the study of the Otway 2C project.

CHAPTER 5. ROCK PHYSICS MODEL OF FRIO "C" SANDSTONE-PART 1: USING GASSMANN'S POROELASTICITY THEORY

The seismic related parameters in the Frio project and their resolution have been discussed in Chapter 4. However, for quantitative interpretation, the observed time-lapse seismic changes must be linked to reservoir properties using a rock physics model that predicts the changes in the elastic properties corresponding to the changes in the reservoir properties (Johansen et al. 2013). A conventional way is to use Gassmann poroelasticity theory (Gassmann 1951). Gassmann's theory assumes that the medium is homogeneous on both microscopic and macroscopic scale, and also isotropic on the micro-scale. As noted by Brown and Korringa (1975), "Sedimentary materials, to which his theory is most often applied, do not even approximately satisfy the conditions of microhomogeneity and microisotropy". In particular, in the context of time-lapse VSP, both direct and reflected waves sample large volumes of subsurface rocks, which might not satisfy this assumption. Therefore, in order to use Gassmann theory at the seismic scale, it is essential to test its applicability at this scale using field data. This problem arises in many time-lapse monitoring projects such as enhanced oil recovery (EOR), production monitoring (Yang et al. 2014, Lumley 2001) and more recently CO_2 sequestration monitoring (Arts et al. 2004, Ivanova et al. 2012, Daley et al. 2008). Geophysical data acquired during CO_2 sequestration in saline aquifers such as Ketzin, Nagaoka, Otway and Frio (Michael et al. 2010) provide high-resolution *in situ* data for calibration with theoretical rock physics. Thus, the Frio-I project present an attractive opportunity to investigate the applicability of theoretical models at the seismic scale.

This chapter contains a case study conducted to assess the applicability of Gassmann poroelasticity theory (Gassmann 1951, Biot 1956) for the Frio "C" and our ability to constrain the velocity-saturation relation at the Frio CO_2 injection site using time-lapse VSP data and baseline well logs with the goal to be able to predict the time-lapse velocity changes obtained in the field.

Part of the results of this work are published in a conference paper (Al Hosni, Caspari, et al. 2015) ©ASEG 2015 and a journal paper (Al Hosni et al. 2016). These references will not be cited in this chapter anymore.

5.1 METHODOLOGY

The need for a rock physics model that can predicts the elastic changes of the reservoir upon CO_2 injection is crucial for estimating CO_2 saturation in the subsurface and facilitate the use of the time-lapse seismic data to monitor the CO_2 plume saturation distribution through seismic modelling and seismic inversion. One of the missing components for the Frio pilot data analysis is a site-specific rock physics model that describes the Frio "C" sandstone at the injection interval. Yet, when looking at the various data available for the Frio project now, it becomes feasible to create such a model using the baseline logs and core measurements. High uncertainties associated with well log measurements (V_P and V_S) affected by borehole conditions can affect our ability to constrain a rock physics model for the Frio reservoir. However, the time-lapse Vertical Seismic Profile (VSP) data presented in Chapter 4 span both the near-well region and far beyond the borehole and can provide a good control for correcting these measurements and reducing the uncertainties thereafter.

A good rock physics model starts with an accurate representation of the rock constituents; namely grains and matrix properties followed by fluids properties. In the literature, sandstones grain elastic properties have been modelled with reasonable accuracy using simple minerals composite mixtures such as quartz, feldspar and shale applying either contact models, simple bounds such as the Hashin-Shtrikman bounds and the use of inverse Gassmann. In our case Gassmann poroelasticity theory (Gassmann 1951) is considered an attractive option to use with the presence of well logs that are verified by VSP measurements.

The methodology we use to constrain the velocity-saturation relation at the Frio project is based on data integration and seismic modelling. The starting point is the raw field data, that is well logs and core presented in Chapter 3 and time-lapse VSP data presented in Chapter 4. Both data sets complement each other as they could provide information about the elastic properties of the subsurface and help filling any missing components for the rock physics modelling. However, they are at different

scales. For example, although well logs data could provide CO_2 saturation and velocities at a resolution of 10's of centimetres, the VSP method resolution is at 10's of meters. This necessitate some scaling, usually from the smallest scale to the largest scale if a relationship is to be established between the two measurements. The second step is to use rock physics theories. For this we use Gassmann's poroelasticity theory (discussed in Chapter 2, section 2.4.1) as all the pre-requests for the model are available. We investigate each input parameter for the rock physics model separately and assess their sensitivity when applicable. The output from this model is then used as input for the modelling. We compare the magnitude of the elastic changes predicted by the rock physics model to those obtained from the real data. Figure 5-1 shows a workflow for the methodology.

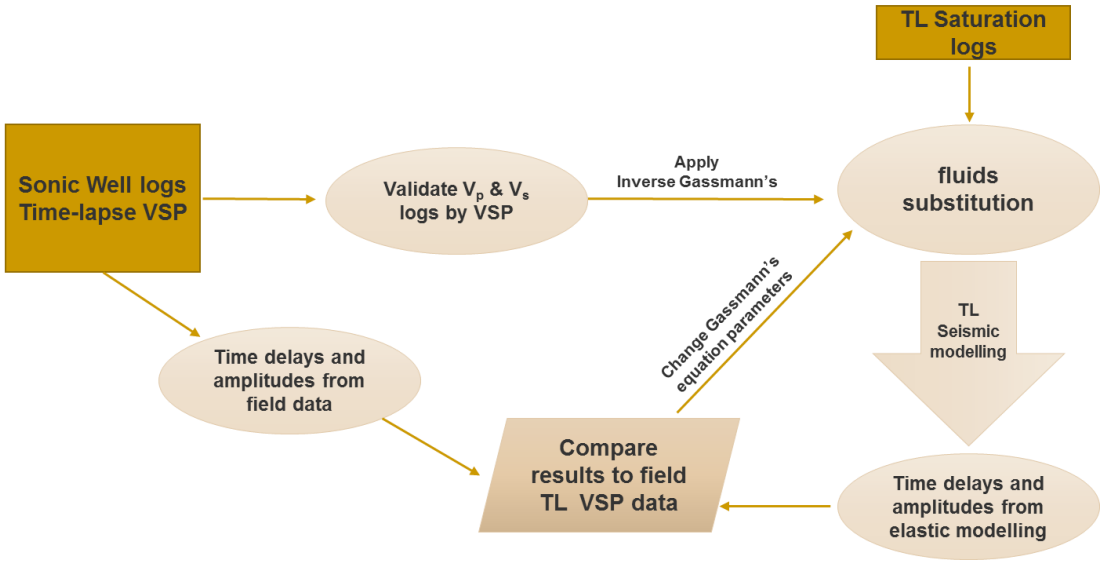

Figure 5-1: A flow chart of the methodology used in the investigation of the velocity-saturation relation at the Frio site using time-lapse (TL) VSP (Chapter 4) and rock physics analysis.

5.2 ELASTIC PROPERTIES OF THE FRIO "C" USING GASSMANN'S PORELASTISITY THEORY

The injection unit in the Frio "C" formation is a relatively homogenous sandstone with high porosity; thus, an attractive option is to use Gassmann's equation (Gassmann 1951) to model it. However, one must obtain all the input parameters for the model preferably from field measurements. Assumptions and validity of

Gassmann's fluid substitution have been summarised in (Chapter 2, section 2.4.1) and a comprehensive treatment of these assumption is widely discussed in the literature (e.g., Han and Batzle 2004, Nolen-Hoeksema 2000, Berryman 1999, Smith, Sondergeld, and Rai 2003, Grochau and Gurevich 2009). Input parameters for Gassmann's equation (Gassmann 1951) can be obtained from laboratory measurements or field data such as well logs. Quality control of these input parameters is essential to reduce the uncertainty in applying the fluid replacement equation. In the following, we provide a description of how we obtain these input parameters from the available data and evaluate their uncertainty. In the case of high uncertainty for a parameter, we perturb the model over a range of values to assess the sensitivity of the result to the input values.

5.2.1 Fluids mixture properties at reservoir conditions and CO_2 saturation

The fluids properties used in the rock physics model are based on both lab measurements and fluids properties equations with known pressure and temperature conditions reported in the literature (Batzle and Wang 1992). The brine properties are calculated easily, as both temperature, pressure and salinity are well known. However, for CO_2 the calculations are not as robust and require some analysis. Figure 5-2 shows the CO_2 properties for different pressure at Frio reservoir temperature of 55 C. Here, we confirm the values provided in the previous work of Daley et al. (2008). Table 5-1 shows the fluid properties of the *in-situ* brine and injected CO_2 at reservoir conditions of 55° C and a pressure of 15 MPa.

	K	μ	V_P (m/s)	V_s (m/s)	Density (Kg/m_3)	Viscosity (Pa.s)
Brine	2.75e9	0	1634	0	1030	7.06e-3
CO_2	73.2e6	0	335	0	653	5.12e-05

Table 5-1: Brine and CO_2 properties for the Frio experiment at reservoir condition. From (Daley et al. 2008).

The fluid mixture of two immiscible fluids could be uniform or patchy (Masson and Pride 2011). Hence, the choice of a mixing law of the fluids determines the magnitude of the P-wave velocity change predicted by the fluid replacement scheme.

Assuming a uniform homogenous mixture of fluid phases, Wood's equation (Mavko, Mukerji, and Dvorkin 2009) can be used to calculate the effective bulk modulus of the fluids (K_{fl}),

$$K_{fl} = \left[\frac{S_{brine}}{K_{brine}} + \frac{S_{CO2}}{K_{CO2}}\right]^{-1} \tag{5-1}$$

where K_{brine} is the bulk moduli of brine, S_{brine} is the saturation of brine, K_{CO2} is the bulk moduli of CO_2 and S_{CO2} is the saturation of CO_2. This mixing law predicts the maximum velocity change due to saturation. If the saturation is patchy, then for a given mixture of CO_2 and brine the maximum P-wave velocity change will be lower than or equal that predicted by Wood's equation. However, given that the observed velocity changes in the time-lapse VSP data are large we use the uniform fluid mixture to model for the maximum velocity change due to CO_2 saturation. The density of the CO_2 and brine fluid mixture is given by

$$\rho_{fl} = \rho_{brine} S_{brine} + (1 - S_{brine})\rho_{CO2} \tag{5-2}$$

where ρ_{brine} and ρ_{CO2} are the brine and CO_2 densities at reservoir conditions. The fluid mixture (CO_2 and brine) properties for the Frio reservoir conditions are shown in Figure 5-3.

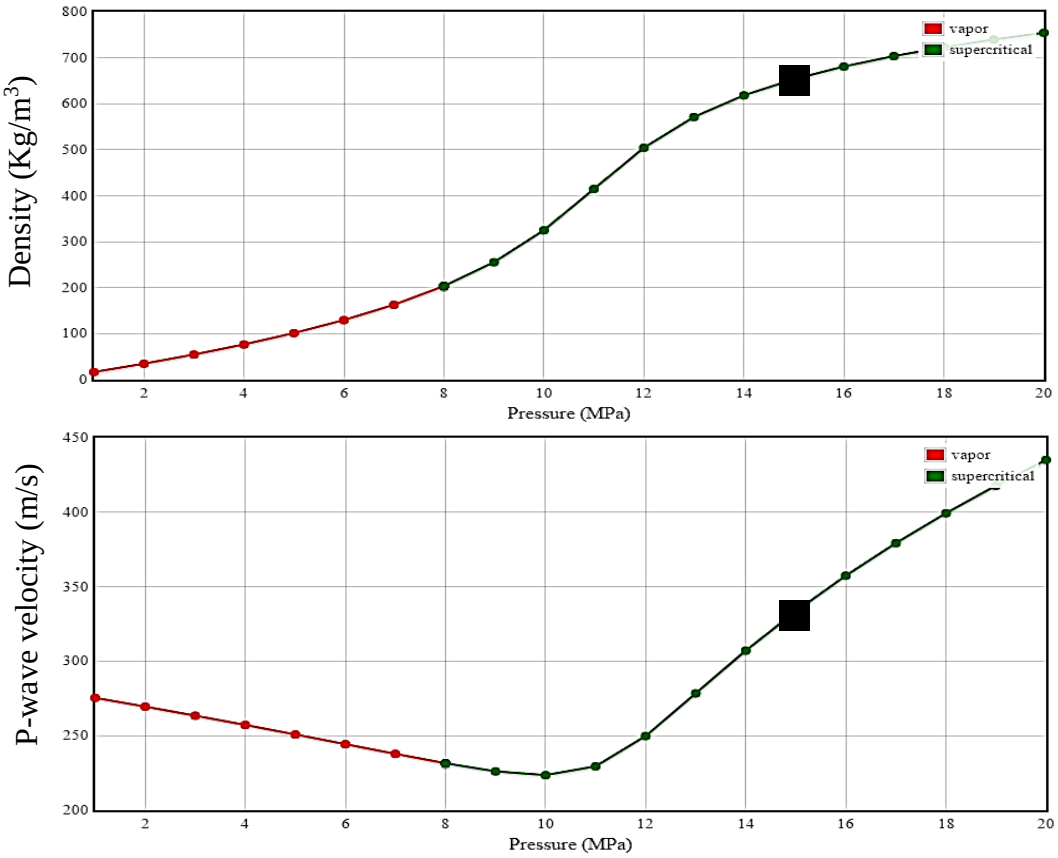

Figure 5-2: CO_2 properties, density (top), P-wave velocity (bottom) at a reservoir temperature of 55° C. Frio reservoir conditions are shown by the black square. Modified from The National Institute of Standards and Technology (2014).

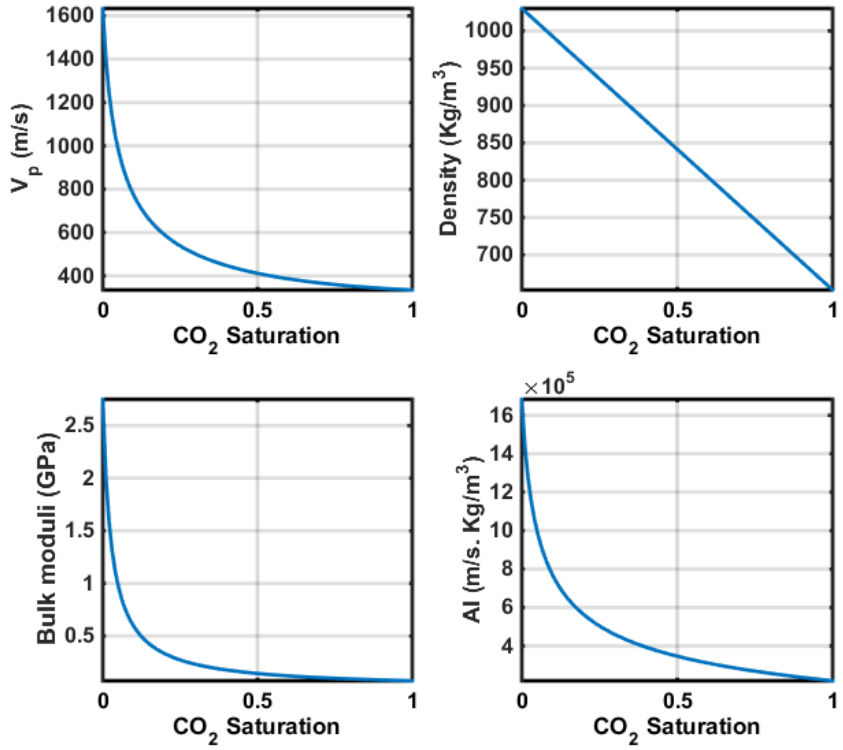

Figure 5-3: Brine and CO_2 fluid mixture elastic properties and acoustic impedance (AI) using Wood's equation for the Frio project.

Fluid saturation is a common unknown in many time-lapse studies. In the Frio project CO_2 saturations were inferred using the Schlumberger reservoir saturation tool (RST) (Hovorka, Benson, et al. 2006, Sakurai et al. 2006, Doughty, Freifeld, and Trautz 2008). However, there was no reliable saturation estimation for some parts of the injection reservoir interval after the monitor seismic survey as was shown in (Chapter 3, Figure 3-12) due to wellbore issues related to the casing deployment (Hovorka, Benson, et al. 2006). Thus, we consider CO_2 saturation in the range of 0.18 to 0.62 after injection at the injection well based on the available data (Hovorka, Benson, et al. 2006, Sakurai et al. 2006).

5.2.2 Porosity

Another parameter needed in order to use Gassmann's equation is the porosity of the rock frame. An average porosity of 32% was obtained from core measurements for the injection interval (Sakurai et al. 2006). The porosity in the upper 5 m of the formation interval is around 34% while for the lower shaley interval the porosity decreases to about 28%. We used these core values to calibrate our porosity log

calculated from density as discussed previously in Chapter 3, section 3.3 with an overall good agreement for the injection interval obtained.

5.2.3 Grain properties

The grains elastic moduli K_g is an important input to create an accurate rock physics model of the rock. This parameter is usually difficult to measure, even with the availability of core measurements. However, in most situations simple approximations of K_g can be used and still produce acceptable results (Hashin and Shtrikman 1963, Nolen-Hoeksema 2000, Smith, Sondergeld, and Rai 2003).

In the case of Frio project, it has been decided to use a simple mineralogy by taking the shale volume interpreted from the Gamma Ray log with quartz as the major constituent. In Figure 5-4, looking at the gamma ray logs at the interval of interest that covers about 9 m with the injection perforations at the top 5 m interval it is seen that clean sand is present with minimum shale as interpreted from the logs. For the lower interval, the shale volume is averaging about 20%. In addition we assume a constant percentage of 20% feldspar (orthoclase and plagioclase) which has been recorded in the limited core analysis by Hovorka, Sakurai, et al. (2006) and reported also by Sakurai et al. (2006), see Figure 5-4. This approach is used as there are no available site-specific data that accurately define the mineralogy of the Frio "C" sandstone. The elastic properties of these mineral constitutes are obtain from literature and presented in Table 5-2.

Here we use the arithmetic average of Hashin–Shtrikman bounds (Hashin and Shtrikman 1963) as defined in Chapter 2, section 2.2.1.2. The simplicity of the Hashin-Shtrikman bounds is that we only need the minerals constitutes of the rock in order to predict the minimum and maximum bound for which our data would fall in if the assumptions of these bounds are satisfied. As such, this average does not take into account the complex geometrical factors involved in grain mixtures but it provides a reasonable first-order approximation especially when the lower and upper bounds are not too far apart, Figure 5-5 (a,b).

Constitute	Density(kg/m3)	K (GPa)	μ (GPa)	Poisson ratio
Quartz	2650	36.6	45	0.08
Feldspar Plagioclase* (average Feldspar)	2630 (2620)	75.6 (37.5)	25.6 (15)	0.35 (0.32)
Shale (variable-average)	2260	13.1	4.43	0.348

Table 5-2: Density, moduli and Poisson ratio of minerals and constitutes used in the Frio "C" rock physics modelling, from (Mavko, Mukerji, and Dvorkin 2009) . *value used in the model.

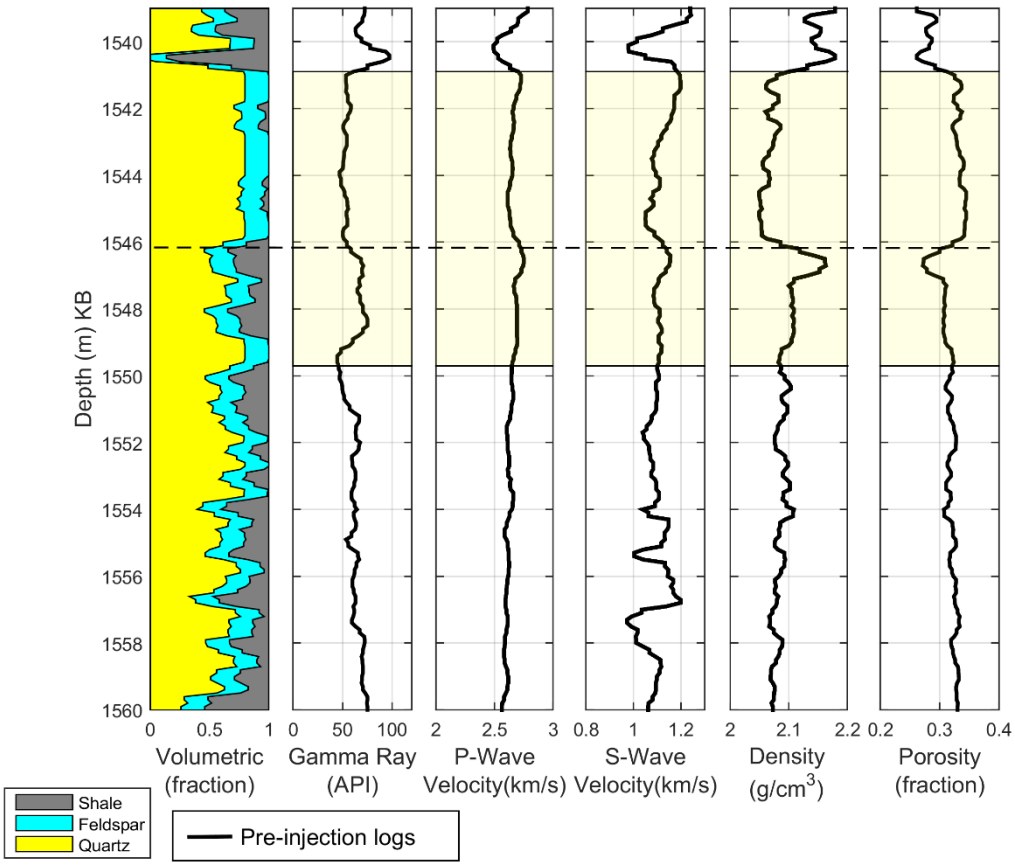

Figure 5-4: Frio formation mineralogical composition from GR log and literature, V_P, V_S, density and porosity logs used in Gassmann's equation. The reservoir interval is shaded. Dashed line indicate the boundary between the upper clean sandstone and lower shaley sandstone.

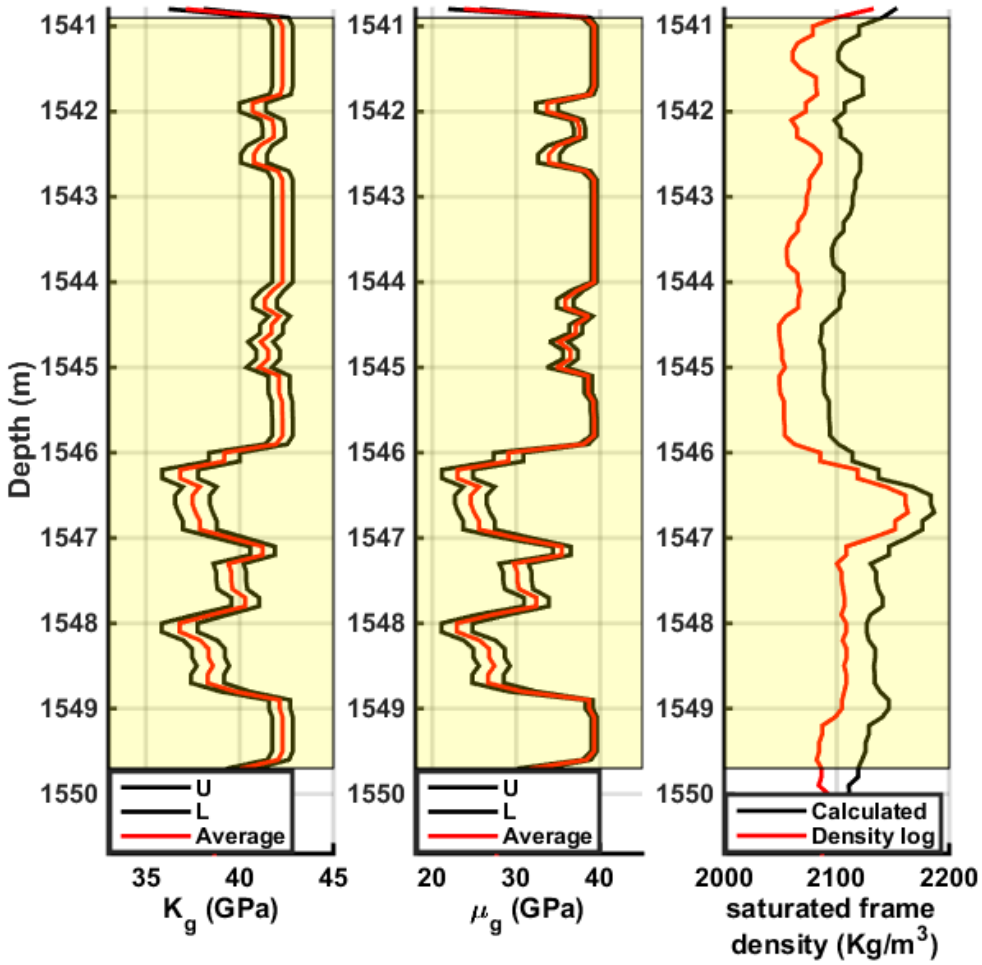

Figure 5-5: Elastic bounds for the frame forming grain (a) bulk moduli and (b) shear modulus. The Upper (U) and lower (L) Hashin–Shtrikman bounds are the black lines and their arithmetic average is in red. (c) The density for the saturated Frio-C interval calculated using the grains properties and porosity and from density log.

5.2.4 Drained frame properties

The dry-frame (or drained) bulk modulus is the most important variable in the fluid substitution scheme. Often the dry-frame bulk modulus K_{dry} is unknown and is obtained by rewriting Gassmann's equation assuming the knowledge of K_{sat} as we have shown in Chapter 2, section 2.4.1 (Smith, Sondergeld, and Rai 2003, Zhu and McMechan 1990, Engelmark 2002).

A common approach in the oil and gas industry is to utilize wireline measurements of the brine-saturated intervals of the reservoir of interest (Engelmark 2002). However, this approach requires a careful check of the input parameters from

well logs, especially: P-wave velocity (V_P), S-wave velocity (V_s) and the density of the saturated rock frame (ρ_b). Inputting wrong values can result in large errors or even unphysical values of K_{dry} (Kazemeini, Juhlin, and Fomel 2010). This has been investigated earlier in (Chapter 3, section 3.3.3) were the upscaled log velocities and VSP interval velocities showed a good agreement.

After ensuring the quality of the input log velocities we first calculate the bulk (K_{sat}) and shear moduli (μ_{sat}) of the in-suite brine saturated rock from the baseline V_P, V_S and ρ_b logs:

$$K_{sat} = \rho_b \left(V_p^2 - \frac{4}{3} V_s^2 \right), \tag{5-3}$$

$$\mu_{sat} = \rho_b V_s^2. \tag{5-4}$$

Second, the drained frame bulk ($K_{drained}$) and shear moduli ($\mu_{drained}$) are calculated using the inverse Gassmann equation's (Zhu and McMechan 1990)

$$K_{drained} = \frac{K_{sat} \left(\frac{\phi K_g}{K_{fl}} + 1 - \phi \right) - K_g}{\frac{\phi K_g}{K_{fl}} + \frac{K_{sat}}{K_g} - 1 - \phi}, \tag{5-5}$$

$$\mu_{drained} = \mu_{sat} \tag{5-6}$$

The density of the frame can be either calculated using the porosity and density of the constituents or by using the well log density. The exact mineralogy used in creating the density log (as provided) is not known. Yet, we found that both approaches give good agreement (Figure 5-5), hence, the density of the drained frame ($\rho_{drained}$) is calculated from the brine saturated density log (ρ_b) with the following equation

$$\rho_{drained} = \rho_b - \rho_{brine} \phi. \tag{5-7}$$

The calculated drained frame bulk and shear moduli are held constant during subsequent fluids substitution. Such an assumption may be invalid if the drained frame

properties changed during fluid replacement, e.g. as the case with formation damage by pressure or geochemical interactions of the fluids with the frame forming minerals. If a change is observed in the bulk and shear moduli of the drained frame, then its properties should be updated.

5.3 FLUID SUBSTITUTION AND CONSTRAINING THE VELOCITY-SATURATION RELATION USING TIME-LAPSE VSP

Fluid substitution is the last step in many rock physics routines after obtaining the required parameters for Gassmann's fluid substitution. At this stage, the results can be very informative for predicting elastic parameters of interest when fluids are introduced in the porous rock frame. In many cases, the goal is to see how the elastic properties -in this case study mainly V_P changes with changing fluid saturation- given a combination of fluids. In the case of the Frio project the fluids combination is brine and supercritical CO_2. We recall here the time-lapse changes in the elastic properties caused by CO_2 injection that were obtained from the TL VSP data and confirmed by forward modelling. Here we use the quantitative values obtained (from field VSP and modelling) as summarised in Table 5-3 to investigate if our site-specific rock physics model could explain the field observations.

Parameters	ΔV_P	ΔT_P	ΔA_{rms} *(Normalized Reflections)*
Real data (maximum change observed)	-750±150 m/s	15±2% to 18±2%	0.8
Best modelling (matching obtained)	-750±75 m/s	19±2%	0.8

Table 5-3: Summary of time-lapse changes obtained using real VSP and the matching maximum change parameters from modelling obtained as presented in Chapter 4. Best results suggest a -750 m/s velocity change at the injection well.

For porous rocks saturated with two or more immiscible fluids, Gassmann-wood (GW) provides the relaxed-low frequency limit. This means the brine and the CO_2 are mixed to the finest scale and no wave-induced fluid flow occur. In the case of the Frio project, however, this might not be the case. Because possible fluid patches at larger scale may exist. To examine this, we show the relation between the characteristic length scale (L_c) and the frequency calculated using equation (2-29) at each data point in the zone of interest using well logs data (Figure 5-6). It can be seen that on average - at VSP frequencies- to be in the patchy saturation regime patches with L_c of more than or comparable to 0.15 cm approximately should be present. However, given the available data, we cannot confirm nor exclude patchy saturation effects. Thus, to incorporate such a possibility we will investigate both the lower and upper bounds of the velocity-saturation relation, those are the Gassmann-wood (GW) and the Gassmann-Hill (GH) equations. To start with, we evaluate the P-wave velocity difference between the two limiting cases for the average reservoir properties. This is shown in Figure 5-7 (a,b). It is obvious that the velocity difference between the homogenous fluid-mixing and the heterogeneous fluid-mixing is pronounced particularly for low CO_2 saturation.

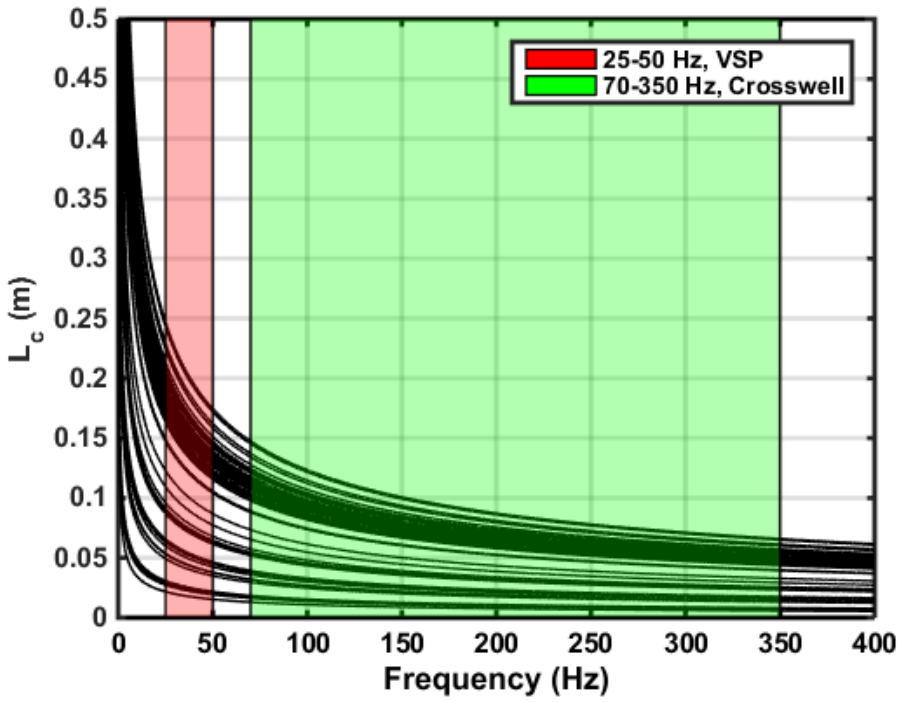

Figure 5-6: Characteristic length (L_c) versus frequency (f) for each data point in the Frio reservoir from the well logs. The shaded regions are for the frequency range of

the field VSP and crosswell seismic data. A patchy saturation response is expected in the region above the curves.

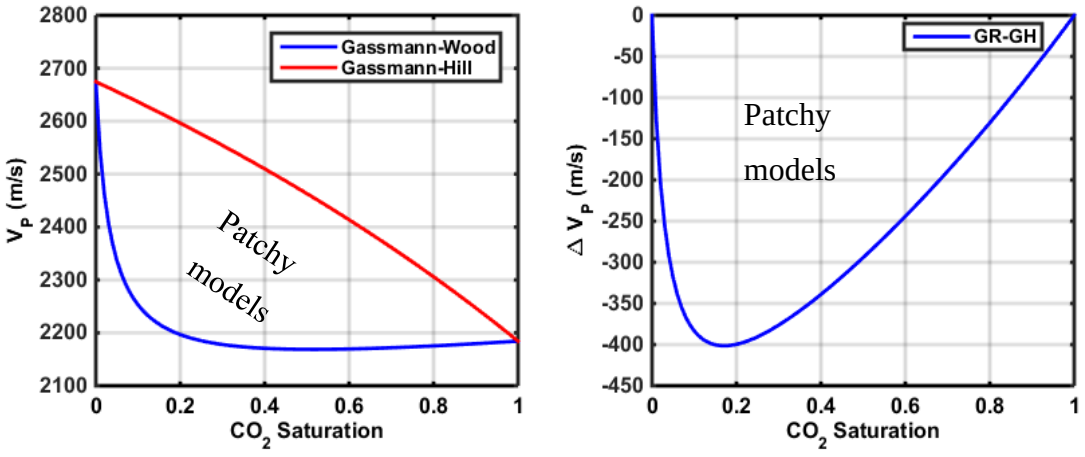

Figure 5-7 (a) Gassmann's fluids substitution using Wood's and Hill average. (b) The velocity difference between GW and GH. The velocity difference is large particularly at low CO_2 saturation.

To investigate the elastic properties changes at the Frio project, in Figure 5-8 (a) we plot the variations of the Gassmann-Wood and Gassmann-Hill using the well log data. While in Figure 5-8 (b) we plot the change in the transmission coefficient using equation (2-42). The reservoir acoustic impedance associated with the baseline is calculated by assuming the reservoir is fully brine-saturated. Then, for the post-injection case, we introduce the change in impedance due to CO_2 saturation. In both graphs we plot the calculated values of the velocity change and the transmission coefficient change based on the TL VSP data with their uncertainty (vertical bars), while the saturation is plotted for the range of values as we discussed earlier in section 5.2.1. It is clear here that even when taking the variations (with respect to depth for each data point in the well logs) in the reservoir interval, the rock physics model cannot predict such a large velocity decrease. Moreover, if the VSR is patchy, then this would entail a larger discrepancy between the rock physics model predictions and field data. Thus, we do not investigate the patchy saturation effect as a possible cause of this discrepancy in the sensitivity analysis section coming next.

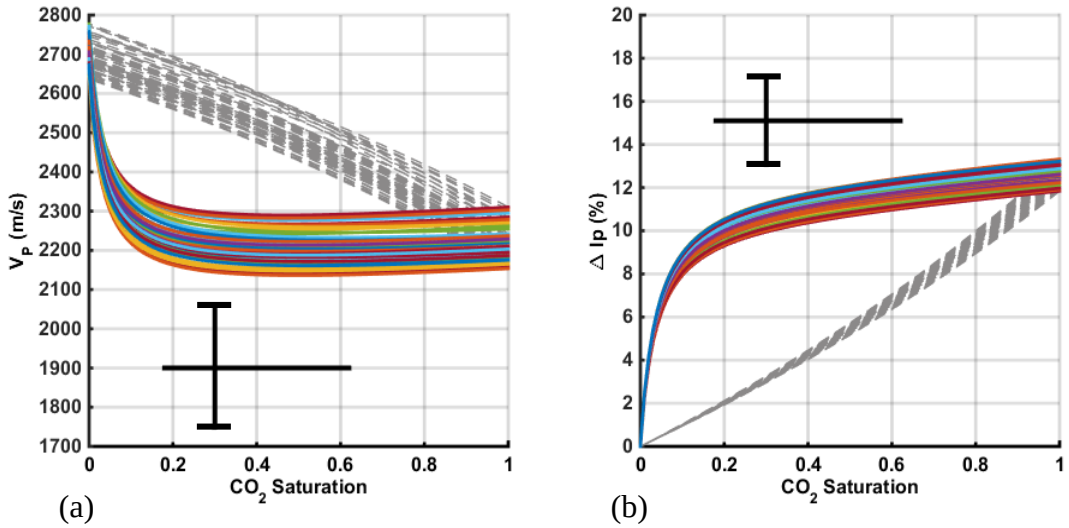

Figure 5-8: (a) Velocity-saturation relation for the Frio "C" injection interval at each point. (b) The change in transmission coefficient with CO_2 saturation for the Frio-C injection interval at each point. Taking the possible variations in the interval and accounting for the uncertainty in the TL VSP field data results (vertical error bar) still the model could not predict the field results. Solid lines (GW), Dashed grey lines (GH). The control on CO_2 saturation (horizontal bar) is from the saturation logs range at the injection well from Doughty, Freifeld, and Trautz (2008).

5.3.1 Sensitivity and uncertainty analysis of the input parameters of the Gassmann's equation

It is well known that "errors are not created equal" and that for geophysical data collected in the field, uncertainties are there although they are difficult to assign (Engelmark 2002). Could these uncertainties, in the form of errors, be the cause of the discrepancy obtained earlier? To investigate this, we assign some uncertainties in the input parameters for the rock physics model for the Frio "C" interval based on the analysis performed earlier and our quality control of the data performed in Chapter 3. This uncertainty will be introduced as a change in each parameter (*Par*), as

$$Change = par + (Uncertainty \times par) \qquad (5\text{-}8)$$

In the sensitivity analysis only one key parameter is allowed to change at a time. Moreover, in order to compare the results in a quantitative and interpretable way to this case study, we present the final VSR that would result for each parameter

uncertainty. The nominal model which will be used for the average Frio "C" formation properties is presented in Table 5-4.

The properties of the fluids (section 5.2.1), temperature and pressure conditions (Chapter 3, section 3.3.1) are well understood and measured with good accuracy, thus we do not investigate them here. Finally, the Frio "C" sandstone mineral constitutes are not well constrained by a lab measurement, thus it might be a source of uncertainty. Moreover, the geometrical arrangement of the grains might add a further uncertainty. Thus, we will investigate their effects separately.

	Parameter	Values
Grains	Bulk modulus, K_g (GPa)	42.2
	Shear Modulus, μ_g (GPa)	39.3
Logs measurements	V_P (m/s)	2648
	V_S (m/s)	1117
	Density, ρ_{log} (Kg/m^3)	2075
	Porosity, ϕ (fraction)	0.33

Table 5-4: Nominal model properties for the Frio "C" sandstone used as input for calculating the sensitivity analysis.

5.3.1.1 well logs (V_P, V_s, density, porosity*)*

The well-log data although considered as hard data, they can have some uncertainties that are not usually taken into account when used in calculations of the petrophysical properties. Fortunately, interval VSP velocities have verified the well-log-derived V_P and V_S, thus we only assign a 4% uncertainty for these velocities. Applying these values of V_P and V_S in the Gassmann's equation and the fluid substitution we obtain a velocity-saturation relation as shown in Figure 5-9. The results show that the velocity-saturation relation and change of transmission is very sensitive to V_P with a velocity discrepancy from the nominal model by about ±200 m/s and transmission coefficient change of about ±2.5%, while for V_s a small change is observed.

Similar to V_P and V_S, the density from the logs and that computed by the mineralogy showed good agreement (Figure 5-5). Moreover, the porosity log is well constrained by core measurements as presented in Chapter 3, section 3.3.2. Here, we assign ±5% uncertainty to the porosity and the density and investigate their effects.

The results show that in that V_P is more sensitive to the porosity than the density, while for the transmission coefficient change, it appears to be more sensitive to the density variations.

From Figure 5-9 and Figure 5-10, the sensitivity analysis shows that we are always underestimating the velocity changes obtained from the field data. Although the V_P sensitivity shows that a 4% error in V_P may be able to explain the observed changes, an over estimated velocity is needed to match exactly with the VSP data obtained. This is unlikely given that the interval VSP velocities matches well with the V_P well logs using several VSP shots (Figure 3-8).

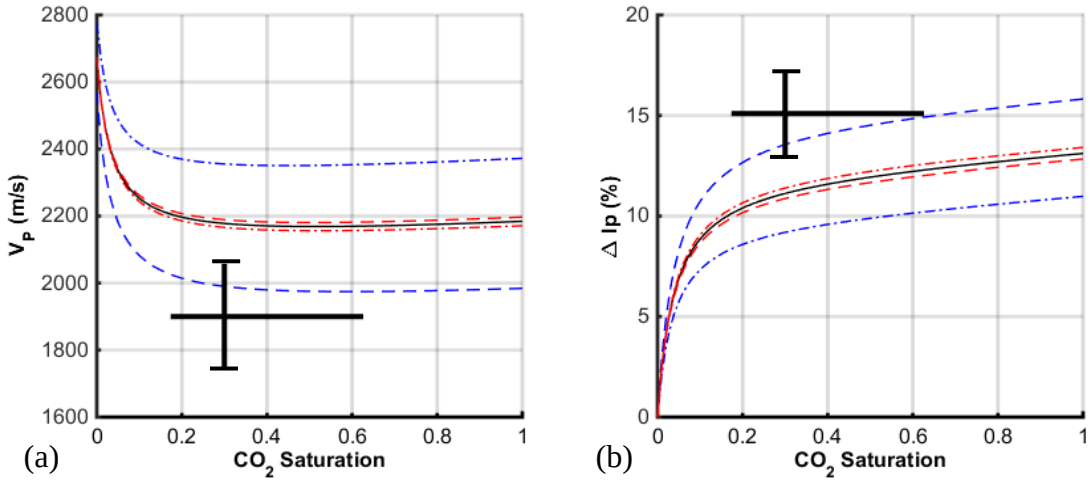

Figure 5-9: Sensitivity analysis for the nominal model VSR and transmission coefficient change (black lines) to V_P (blue) and V_s (red) using GW. The dash-dotted lines indicate an overestimation of a parameter (+) and the dashed lines indicate an underestimation (-).

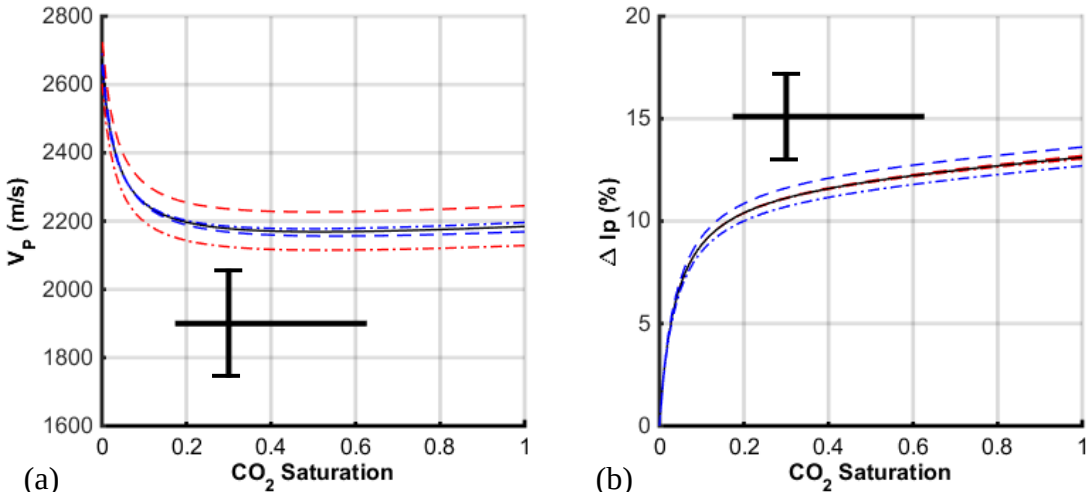

Figure 5-10: Sensitivity analysis for the nominal model VSR and transmission coefficient change (black lines) to *porosity* (blue) and *density* (red) using GW. The dash-dotted lines indicate an overestimation of a parameter (+) and the dashed lines indicate an underestimation (-).

5.3.1.2 Grain properties

A way to evaluate the sensitivity of our model to K_g is by perturbing the input values of K_g for the calculation of the drained frame properties (inverse Gassmann) and then for the saturated frame properties. We keep the model parameters in Table 5-4 constant except for K_g, which is changed from the initial value by an increment of 10 GPa up to 82 GPa. The velocity-saturation relations with changing K_g are shown in Figure 5-11 (a); we see that we need a K_g over 70 GPa to match the observations. Similarly, to explain the transmission coefficient change ΔI_p observed in the field (shown in Figure 5-11 (b)), a K_g value of more than 52 GPa is required. Such large value of the grain modulus is inconsistent with the predominant quartz mineralogy of the formation. Thus, we do not expect the discrepancy is a result of uncertainty in the grains elastic properties inputted into Gassmann's equation.

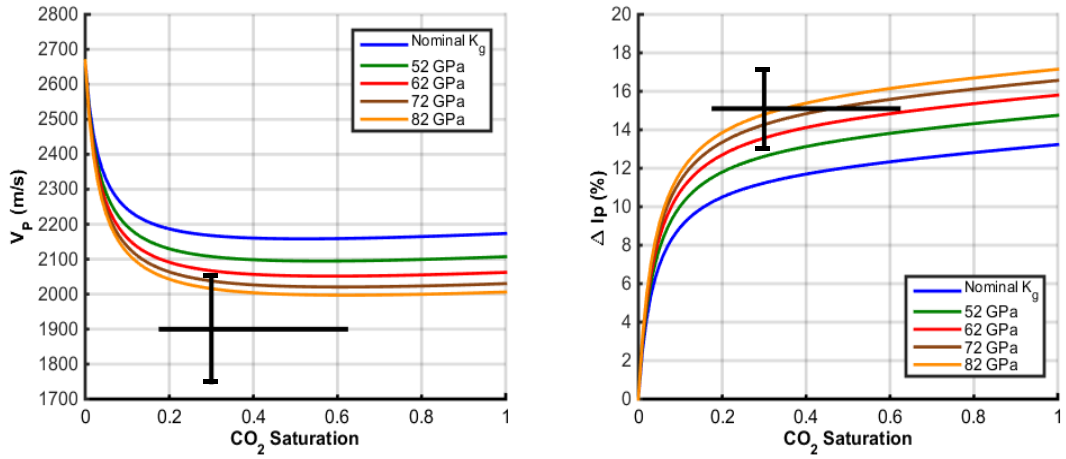

(a) (b)

Figure 5-11: (a) The velocity-saturation relation for the Frio "C" sandstone with changing grain bulk moduli. (b) The transmission coefficient change as a function of CO_2 saturation. The vertical bar in (a) is velocity reduction estimated from the time-lapse VSP with the uncertainty, while in (b) is that obtained from the real VSP first arrivals peak amplitude change with their uncertainty. The control on CO_2 saturation (horizontal bar) in (a,b) is from the saturation logs range at the injection well (Figure 3-12).

5.4 DISCUSSION

We have shown that neither the time-lapse VSP anomalies for first arrivals nor reflection amplitudes could be explained by the Gassmann fluid substitution even when the uncertainties of the field measurements have been taken into account. Time-lapse VSP has provided three independent attributes: direct arrival traveltimes, first arrival amplitudes and reflection amplitudes. The most robust quantitative measure here is the traveltime delay, which has a smaller uncertainty in comparison with the amplitudes. For the direct arrivals, we observe a maximum time delay of about 1.3±0.2 ms that corresponds to a P-wave velocity reduction of about 750±150 m/s. The constrained rock physics model for the Frio "C" reservoir is not capable of predicting such large reduction in V_P.

What could be the reason for this discrepancy? Since the effect of injected CO_2 on elastic properties was estimated using Gassmann's equations, it might be possible that one or more of the assumptions of Gassmann's theory are violated. The main assumptions of the Gassmann's equations are:

- The rock frame is isotropic on both micro-scale and macro-scale (Brown and Korringa 1975). Since nearly all minerals are anisotropic, the assumption of isotropy on the micro-scale is never satisfied exactly. However, an assumption is usually made that anisotropic mineral grains with random (isotropic) distribution of orientations mixed on a fine scale result in a medium nearly isotropic on the grain scale. Furthermore, sandstones are commonly assumed to be relatively isotropic on a macro-scale. This suggests that the effect of any anisotropy on the fluid substitution is likely to be small.
- The rock frame is homogeneous on the micro-scale (Mavko, Mukerji, and Dvorkin 2009), that is, it is made of a single mineral. Since the Frio "C" sandstone consists mainly of quartz, this assumption is approximately valid, and any micro-heterogeneity is unlikely to cause significant deviations from the predictions of Gassmann's theory.
- Both the rock frame and the fluid are also homogeneous on the macro-scale (Mavko, Mukerji, and Dvorkin 2009), that is on a scale of a representative volume. The injection interval in Frio is fairly homogeneous, but the fluid distribution might not be uniform. Yet any deviation from uniform distribution would result in even higher saturated bulk modulus, and hence even larger discrepancy, than for uniform saturation, and hence cannot explain our discrepancy.
- The fluid pressure is uniform throughout the pore space in a representative volume of the rock (relaxed regime). This assumption is satisfied when the frequency is sufficient time to equilibrate within one half-cycle of the wave, that is, when the wave frequency is much lower than the squirt frequency (Mavko, Mukerji, and Dvorkin 2009). This assumption is always assumed to be satisfied at seismic frequencies, at least for the high-porosity and high-permeability rocks such as Frio sandstone.
- Finally, Gassmann's theory assumes the rock frame properties do not change with the change of the pore fluid (Mavko, Mukerji, and Dvorkin 2009). This appears to be the only assumption that can be violated. That is, it is possible that injection of CO_2 into the pore space could have caused some physical or geochemical processes that can result in the weakening of the rock frame.

Previous studies of crosswell traveltime tomography at the Frio site have reported that the large P-wave reduction at the injection well is accompanied by a reduction in S-wave velocities of more than 220 m/s (Daley et al. 2008). Such a large change in S-wave velocity is not predicted by the Gassmann fluid substitution as the shear moduli is assumed to be constant according to equation (5-4). Moreover, according to same equation, any density change by injecting a lower density fluid (CO_2 in this case) would cause an S-wave velocity increase rather than a decrease. Rock frame changes during fluid injection could be caused by many factors including pressure effects by fluid injection (Saul and Lumley 2015) or in the case of injecting reactive fluid such as CO_2 by geochemical interactions that alter the rock frame forming mineral (Marbler et al. 2013).

Let's first discuss the pressure changes associated with CO_2 injection as a possible cause of frame weakening. In the Frio site the maximum effective pressure decrease was less than 0.5 MPa (Sakurai et al. 2006); such a small pressure decrease is not expected to cause significant velocity changes for an initial reservoir effective pressure above 15 MPa (Makse et al. 1999). Indeed, according to Eberhart-Phillips, Han, and Zoback (1989) at such reservoir conditions, P-wave and S-wave velocity changes due to such pore pressure increase are less than 30 m/s, which is much smaller than the magnitude of the velocity changes observed in the VSP data.

On the other hand, geochemical analysis have suggested that CO_2 can lead to the dissolution of rock-forming minerals (Kharaka et al. 2006). Rock frame changes, if induced by geochemical processes are difficult to quantify without independent measurement. The frame shear moduli are not affected by saturation changes (Gassmann fluid replacement assuming no geochemical effect) and thus may encode the information about the changes in the rock frame. In other words, S-waves could be a source of such information. Unfortunately, we were unable to obtain the time-lapse changes for the S-wave interval velocities from the VSP data due to the insufficient signal-to-noise ratio for S-wave arrivals.

The rock physics model based on the Gassmann fluid substitution (Gassmann 1951) can only handle mechanical changes caused by replacement of the pore fluids. Thus, we suggest that an alternative model is required to handle possible reservoir rock frame weakening effect due to fluid injection. Such a model should take into account the variation of the drained frame shear and bulk moduli based on field observations.

This will be investigated in the next chapter. By using rock microstructure diagnostics, we introduce a new fluid substitution strategy (model) which incorporates parameters that could be updated and therefore, accounting the rock frame weakening effect. Moreover, we will integrate the crosswell data into the rock physics modelling as the crosswell data provide better resolution for both ΔV_P and ΔV_S in the reservoir.

CHAPTER 6. ROCK PHYSICS MODEL OF FRIO "C" SANDSTONE-PART 2: ESTIMATION OF ROCK FRAME WEAKENING USING TIME-LAPSE CROSSWELL

So far, only changes of fluids saturation effects on the porous rock frame has been considered in the velocity-saturation relation for the Frio CO_2 injection project. However, in the case of injection of reactive fluids, such as CO_2, chemical interactions with the host rock could occur. These interactions can change the dry frame elastic properties either by dissolution of frame-forming minerals, precipitation of new minerals or changing the surface properties of minerals, such as minerals dehydration (e.g., Vanorio, Nur, and Ebert 2011, Marbler et al. 2013, Le Guen et al. 2007, Hangx, Spiers, and Peach 2010, Ilgen and Cygan 2016). A review on some of the possible geochemical reactions has been introduced in section 2.1.3.

We recall in this chapter the results obtained in Chapter 4 and Chapter 5. Analysis of time-lapse VSP data in the Frio CO_2 injection project shows that the reduction in V_P after CO_2 injection far exceeds that predicted by Gassmann equations. We have stated in the discussion of Chapter 5, that geochemical changes in the rock frame are not accounted for in Gassmann poroelasticity theory (Gassmann 1951) as the dry frame properties are kept constant during fluid substitution. After investigating some of the possible causes of discrepancy between the field data and rock physics model as per Chapter 5 discussion, we concluded that geochemical interaction of CO_2 with rock-frame forming minerals is the most likely reason of such discrepancy. If this is true, then we expect to see a comparable change in shear wave velocity. To check this, the crosswell data presented a good opportunity as both ΔV_P and ΔV_S are available with a high resolution, compared to the VSP data for which the S-wave velocity change could not be obtained within the resolution needed for such a study due to their low signal-to-noise ratio.

The objective of this chapter is to "quantify" rock frame weakening effect caused by possible geochemical interaction of CO_2 with the rock frame forming mineral using

the S-wave velocity change observed from the crosswell traveltime tomography. This frame weakening is thus not purely mechanical and might involve the removal of frame forming minerals, change of minerals volume or precipitation of new minerals. This quantification at a field scale is challenging as there are several mechanisms possible and their effect on the elastic moduli is still not well understood. Identifying and quantifying this frame weakening is crucial for velocity-saturation relation and prediction of the time-lapse seismic response. Not incorporating these changes in the rock physics model could result in large errors in estimating CO_2 saturation distribution in the reservoir.

This chapter contains some of the work published in two conference papers (Al Hosni, Gurevich, et al. 2015, Al Hosni, Gurevich, and Daley 2015). And one submitted peer-reviewed paper (Al Hosni, et.al 2016). These references will not be cited anymore in this thesis.

6.1 EFFECTS OF CO_2 INJECTION ON ROCK PROPERTIES

Broadly, in a fluid injection scenario, we assume that changes in the rock frame could be induced by either the injection pressure (independent of the fluid type) or geochemical changes by fluid-rock-interaction (in the case of reactive fluid). For the former, if the injection pressure (of any fluid) is higher than the formation fracturing pressure, this could cause mechanical weakening of the reservoir rock frame (Saul and Lumley 2015) by either breaking grain contact or fines migration. Pressure sensitivity of rocks have been long known in the rock physics community (Avseth and Skji 2011). On the other hand, geochemical effects on the rock frame elastic properties is a topic of current investigation especially in the case of injection reactive fluids such CO_2 (e.g., Vialle and Vanorio 2011, Vialle, Dvorkin, and Mavko 2013).

Marini (2006) provided an extensive treatment of the reactivity of CO_2 with reservoir fluids and rock minerals in the case of geological sequestration. Initial factors which affect the geochemical reactivity of CO_2-brine mixtures in the subsurface is the pressure and temperature, followed by the salinity of the brine. As such, injecting CO_2 into brine formations causes the reduction of pH of the fluids and create an acidic condition that can cause the dissolution of carbonate and silicate minerals and many other rock forming minerals, thus triggering the CO_2-brine-rock interaction (Wellman

et al. 2003). The instantaneous reaction that occur when injecting aqueous $CO_{2(aq)}$ into brine (or water) can be given as:

$$CO_{2(aq)} + H_2O \leftrightarrow H^+ + HCO_3^-. \quad (6\text{-}1)$$

As an example, given a mineral assembly such as solid calcite $CaCO_{3(s)}$ with the presence of H^+ the following simple reaction could be triggered,

$$CaCO_{3\,(s)} + H^+ \leftrightarrow Ca^{2+} + HCO_3^-. \quad (6\text{-}2)$$

This reaction means that the solid calcite would be dissolved. Consequently, if the calcite involved in such a reaction is acting as a contact cement, then the rock frame strength could be affected by its removal. Moreover, such a reaction could trigger the migration of fine particles which are attached by carbonate cement.

It has been demonstrated in an experimental study that the reactivity of CO_2-brine fluid mixture in subsurface reservoirs is controlled first by the type of lithology, that is the mineral constituent and microstructure of the rock and second by the magnitude of reactive fluid flushed through the rock for a given surface area (Wellman et al. 2003). Moreover, as outlined by Luquot et al. (2012) and Vialle, Dvorkin, and Mavko (2013), rock frame changes caused by fluids injection could have a distribution in the reservoir that is not homogenous (i.e., varies in space). Figure 6-2 shows a schematic of the possible scenarios of rock frame weakening which may be triggered by dissolution of frame forming mineral. We emphasize here that these processes could occur individually or in a combination, and that other mechanisms could be involved.

Although most of the CO_2-rock-water interaction studies are conducted for carbonate rocks, similar effects could be present in clastic rocks, especially in carbonate cemented sandstone, or with the presence of carbonate in the sandstone cement. In an experimental study the injection of CO_2 saturated brine into the Tuscaloosa sandstone have caused large changes in the dry frame interpreted to be caused by the alteration of iron-bearing minerals and calcite (Joy, Vanorio, and Sen 2011). Joy, Vanorio, and Sen (2011) have reported more than 9% and 6.5% decrease in the bulk and shear moduli of the rock upon CO_2 rich brine injection. While the bulk moduli of the saturated sample is expected to change due to fluid replacement, the shear moduli is expected to be constant, which was not the case. SEM Images from

the same study have shown this rock frame weakening as alteration of frame forming minerals, mainly cement (contact and non-contact), Figure 6-1.

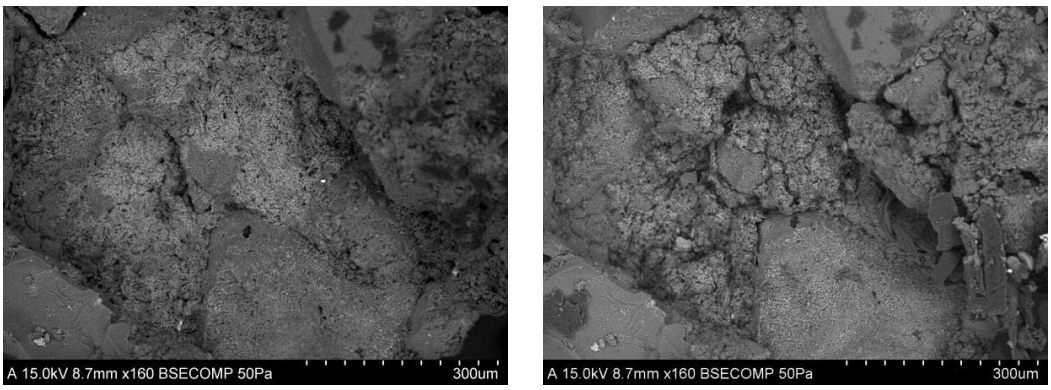

(a) (b)

Figure 6-1: SEM image of the core plug (a) before and (b) after injecting CO_2 rich brine. Note the change in the microstructure of the cement from (a) to (b). From (Joy, Vanorio, and Sen 2011).

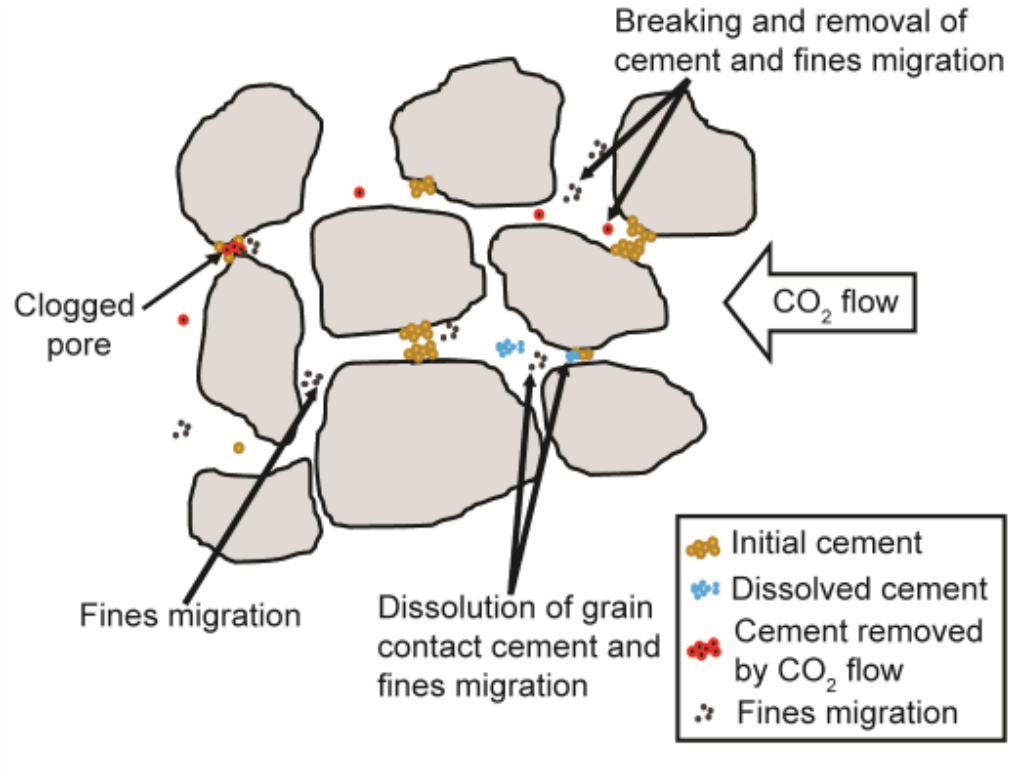

Figure 6-2: A simple schematic of possible scenarios that could cause contact cement reduction due to CO_2 injection.

In general, changes in the rock frame due to CO_2-brine-rock interactions causing mechanical weakening and/or changes in P- and S-wave velocities have been experimentally observed and discussed in several studies, for carbonates (Le Guen et al. 2007, Vialle and Vanorio 2011, Nguyen, Bemer, and Dormieux 2011, Bemer and Lombard 2010, Lebedev, Wilson, and Mikhaltsevitch 2014, Espinoza, Kim, and Santamarina 2011) and for sandstones containing reactive minerals such as calcite (Adam et al. 2015, Ross et al. 1982). On the opposite, shale and mudstones (Gaus, Azaroual, and Czernichowski-Lauriol 2005, Fleury et al. 2010, Hangx, Spiers, and Peach 2010, Bildstein et al. 2010) and low- to moderate-porosity quartz-cemented sandstones (Hangx et al. 2013, Le Guen et al. 2007, Canal et al. 2014) did not show any CO_2-induced mechanical changes.

We relate here to the Frio case study which may be affected by such CO_2-brine rock interactions and we state part of the field observations and geochemical studies which support this research. Several geochemical studies were conducted using the Frio project brine chemistry changes obtained after the breakthrough of CO_2 at the observation well (Ilgen and Cygan 2016, Kharaka et al. 2009, Xu et al. 2010, Kharaka

et al. 2006, Kampman et al. 2014). We summarise here some of the results obtained from these studies:

- Field brine samples have shown strong drop of pH accompanied with large increase in $HCO3^-$ ions, aqueous iron Xu *et al.* 2010. These are attributed to the dissolution of carbonate by the reactions in (6-1) and (6-2) and iron oxyhydroxides as depicted in the redox reaction:

$$8Fe(OH)_3\ (s) + CH_3COOH^0 + 14H^+ \leftrightarrow 8Fe_2 + 2HCO_3^- + 20H_2O. \quad (6\text{-}3)$$

- The time scale for the mentioned reaction (calcite and iron- oxyhydroxides) is fast (Klein et al. 2013) and is within the time-lapse seismic study time scale (with the monitor surveys taken about 6 weeks after the end of injection).
- Recently an independent geochemical modelling study have shown that about 0.02% by weight of the considered rock mass is dissolved from calcite and iron oxides (Ilgen and Cygan 2016). Even though this amount is small, from an elastic viewpoint where the minerals amount change occurs (e.g., at grain contact compared to around a pore) is more important than how much has been dissolved.

Therefore, invoking rock frame weakening parameters in purely elastic rock physics models appears to be essential to accurately and effectively interpret time-lapse seismic in the case of CO_2 injection in such cases as the Frio. If such factors are ignored, then large discrepancy may be observed between the theory and field data or worse, the quantitative interpretation (e.g., saturation) will be erroneous throughout the field if applied. In the next section, we present a methodology of quantifying and modelling this possible rock frame weakening using rock microstructure diagnostics and the crosswell data for the Frio case study.

6.2 METHODOLOGY

At the lab scale, the elastic properties of the rock frame can be monitored and fluids saturation change can be accounted for more accurately than in the field. Moreover, it is possible to re-measure the frame elastic properties of the rock frame by draining the sample after injecting reactive fluids such as $scCO_2$. Such an approach is not viable in the field and fluids saturation changes will always be present. For this

reason, quantification of these possible rock frame changes using P-wave velocity in the field is challenging because fluids substitution causes elastic changes in the rock frame which cannot be separated from the dry rock frame changes caused by other mechanisms (e.g., chemical dissolution, pressure effect, fines migration). However, S-waves have an advantage that they are least affected by fluid substitution. Assuming that the frame shear moduli is constant during fluid substitution we only need to compensate for density change in order to predict the S-wave velocity change after CO_2 injection. Thus, S-waves velocity change can be used as a tool to estimate the change in the frame shear moduli (which is thought to be constant if no dry-frame changes occurred).

After estimating the "change in the shear moduli", the question is, what is the parameter in a rock physics model which can be calibrated for this change to obtain the possible change in the frame bulk moduli? Several studies have shown that the changes in the rock frame due to chemical interactions depend on the microstructure of the rock (Vialle, Dvorkin, and Mavko 2013, Steefel and Maher 2009, Molins et al. 2012). Therefore, to quantify these changes, we need to understand the microstructure of the rock and its elastic properties before CO_2 injection. Thus, we investigate the use of an appropriate rock physics model according to the microstructure, lithology and porosity of the Frio "C" sandstone.

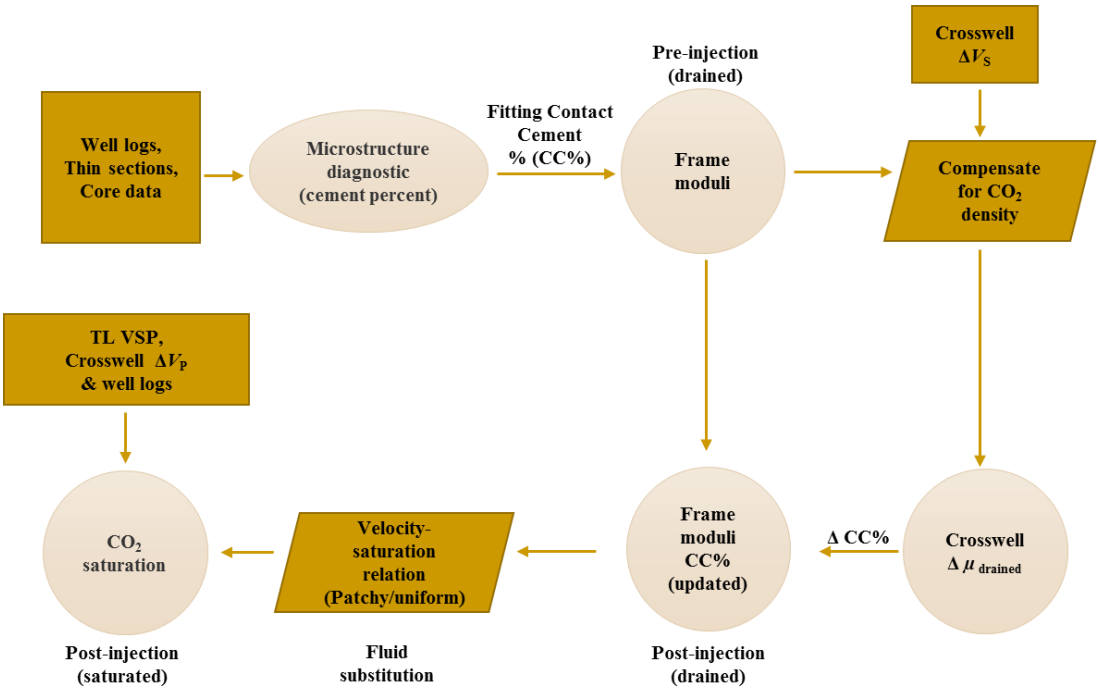

Figure 6-3: Workflow used to estimate the frame weakening as change in the grain contact-cement percent using rock microstructure diagnostic.

6.3 DISCREPANCY OF RESULTS USING GASSMANN

Previously in Chapter 5 we obtained the rock frame properties using inverse Gassmann and the corresponding velocity-saturation relation assuming a uniform saturation. This model although based on site-specific formation properties could not explain the time-lapse VSP travel time and amplitude changes. We show here that this discrepancy is also observed in the crosswell data. The crosswell tomography of the Frio brine pilot project show a large decrease in both P and S-waves velocities (Chapter 4, Figure 4-36). This decrease is more pronounced around the injection well, where P-wave velocities decreases by more than 750 m/s that is about 20% reduction and shear waves velocities by more than 200 m/s which is about 16% reduction from the baseline values. A profile is taken from the crosswell tomography results at the centre of the injection interval (Chapter 4, Figure 4-36) for both ΔV_P and ΔV_S. The discrepancy between the maximum ΔV_P expected using Gassmann's equation approach and that obtained using the crosswell tomography is shown in Figure 6-4. The V_S change allowed is set based on the background velocity change observed away from the injection well, however, theoretically, V_S should increase upon injection of lower

density fluid as equation (2-40) dictates. Thus, it is clear here that V_S do not follow this which further support the assumption that the frame moduli changed after CO_2 injection. Furthermore, it is clear here that both ΔV_P and ΔV_S show a similar trend from the observation well to the injection well. We note here that several studies have suggested that the vicinity of a CO_2 injection well will be the most affected by chemical interactions if any and thus show the largest induced mechanical deformation (Le Guen et al. 2007).

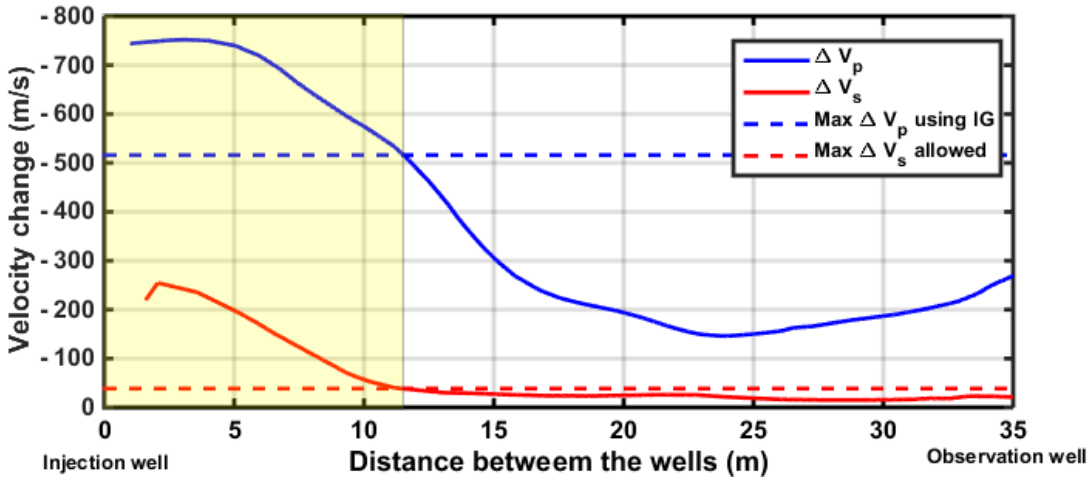

Figure 6-4: Velocity change profile from Frio Crosswell tomography results from Chapter 4, Figure 4-36 (solid lines) and the maximum ΔV_P predicted by the Gassmann's consistent rock physics model (dashed blue). The shaded area cannot be predicted using the Gassmann consistent rock physics model obtained in Chapter 5.

6.4 ROCK PHYSICS DIAGNOSTICS OF FRIO SANDSTONE

Rock physics diagnostics comprises finding a rock physics model (i.e., a relationship between some elastic properties derived from seismic data and reservoir properties) that fits the elastic data. Each rock physics model is only applicable to a certain rock type and a range of porosity. The Frio "C" reservoir interval is characterized as a reworked fluvial, poorly consolidated sandstone. The mineral volume abundance for the reservoir is not well constrained but is reported to be of similar composition to that of the US Gulf Coast sandstone formations which have an average mineral volume of 58% quartz, 28% orthoclase and plagioclase feldspar, 4.5% chlorite, 3.8% Na-smectite, 2% kaolinite, 1.9% calcite and many other minor minerals (Hovorka, Sakurai, et al. 2006, Xu et al. 2010). The injection interval is highly porous

with more than 34% porosity in the upper 5 meters (Figure 6-5) and an average of 32% porosity in the overall top 10 m below the seal (Figure 6-5). The V_P and V_S velocity values of the formation imply a high V_P/V_S ratio (average of about 2.4 in the shaded interval of Figure 6-5) typically associated with high porosity, poorly consolidated sandstones (Avseth, Mukerji, and Mavko 2010).

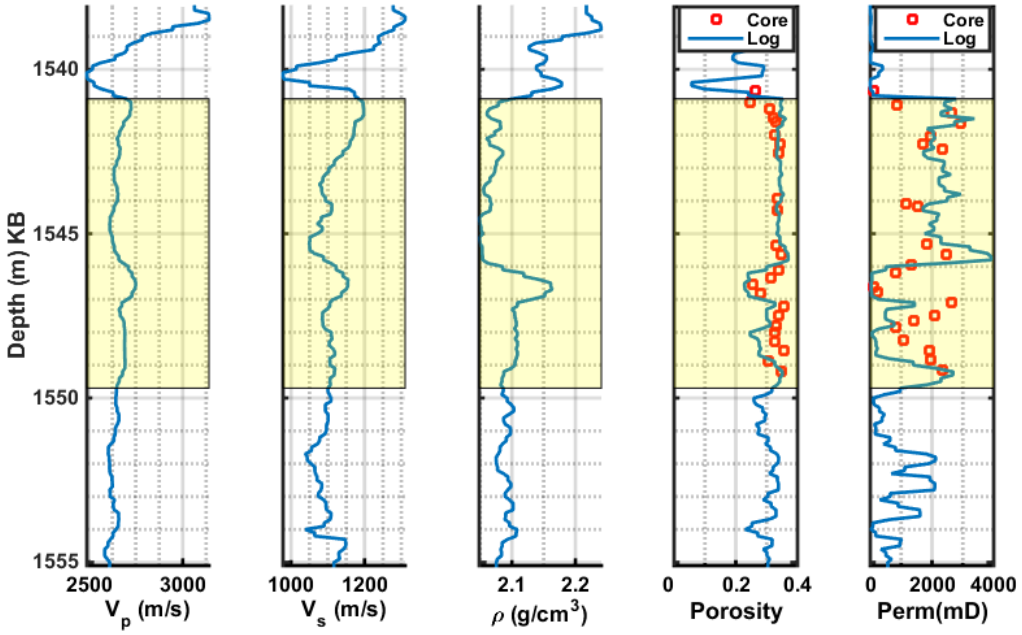

Figure 6-5. Well logs and core data of the injection interval. Core data from Doughty, Freifeld, and Trautz (2008).

Previous studies of rock texture of high porosity sandstones have shown that mineralogically similar samples could have a very different elastic behaviour based on their grain and pore-filling material arrangement, that can be described using grain contact theories (Dvorkin and Nur 2002, Dvorkin, Nur, and Yin 1994). Two well-known theories are the contact-cement theory (i.e., cementation theory) and the friable-sand model (Dvorkin and Nur 1996) which describe the behaviour of the bulk and shear moduli with loss of porosity from the critical porosity (ϕ_c): in the former, the material is added on the grain surface, acting as cement, whereas in the latter, the material is added away from the grain contact, as a deteriorating sorting. The cementation model predicts a sharp increase in the elastic moduli as porosity departs from ϕ_c, (upper curve Figure 4); the friable sand model on the opposite predicts very small changes in the moduli with decreasing porosity (lower curve Figure 6-6). The

cementation theory shows that the volume of cement at grain contact is the main factor controlling the effective elastic properties of cemented grains near the critical porosity. Thus, if the cement is deposited at the inter-granular grain contact, then even a very small amount of cement could greatly increase the frame stiffness (Dvorkin and Nur 1996, Dvorkin, Mavko, and Nur 1991, Dvorkin, Nur, and Yin 1994). In an opposite way, the removal or breaking of this intergranular cement by dissolution or any other mechanism would cause large weakening in the rock frame. The friable sand model and the two cementation schemes of the contact-cement model (Dvorkin and Nur 1996), whether the cement is deposited at grain contact as in scheme 1 or distributed evenly as a ring (i.e., grain coating cement, scheme 2), are summarized in Figure 6-6.

The constant cement model (Avseth et al. 2000) is a combination of the sorting trend given by the friable-sand model and the diagenetic trend given by the contact-cement model. The initial loss of porosity at (ϕ_b), from the critical porosity ϕ_c, is assumed to be due to deposition of cement at grain contact using the contact-cement model. Then, subsequent porosity reduction is caused by deteriorating sorting as in the friable-sand model (see schematic in Figure 6-6). Thus, the constant cement model predicts a large increase in the elastic moduli with the deposition of small amount of cement (typically less than 1%) at grain contact (i.e., initial porosity loss), and then any subsequent material is an added pore filling away from grain contact with little effect on the elastic moduli of the rock frame (Figure 6-6).

The elastic moduli for the constant-cement model are written as:

$$K_{dry} = \left(\frac{\phi/\phi_b}{K_b + \frac{4\mu_b}{3}} + \frac{1-\phi/\phi_b}{K_s + \frac{4\mu_b}{3}} \right)^{-1} - \frac{4\mu_b}{3}, \qquad (6\text{-}4)$$

$$\mu_{dry} = \left(\frac{\phi/\phi_b}{\mu_b + z} + \frac{1-\phi/\phi_b}{\mu_b + z} \right)^{-1} - z, \; z = \frac{\mu_b}{6} \frac{9K_b + 8\mu_b}{K_b + 2\mu_b}, \qquad (6\text{-}5)$$

with K_s and μ_s as the mineral phase bulk and shear moduli, respectively; K_b and μ_b are the bulk and shear moduli for the cemented sand calculated from the contact-cement model equations in Dvorkin and Nur (1996) using scheme 1.

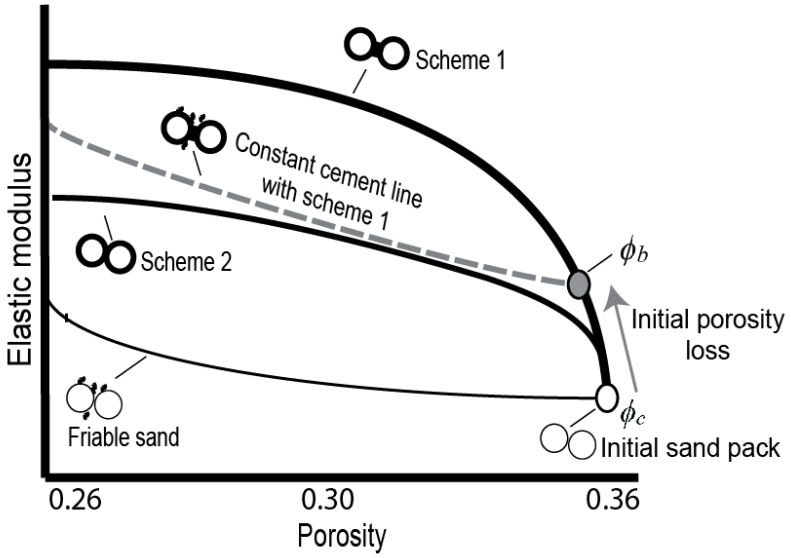

Figure 6-6: Schematic representation of the three theoretical models for high porosity sands. The thickening of the circles represents the addition of cement from the initial sand pack. The slope of the contact cement line depends on the type of cementation. Reproduced from Avseth, Mukerji, and Mavko (2010).

We apply the constant-cement model to the Frio "C" reservoir interval. This model is chosen based on initial analysis of V_P and V_S trends with porosity that show a sorting trend (slight decrease in the drained frame moduli with decreasing porosity) and a diagenetic trend as the drained frame moduli fall above the friable-sand model line as shown in Figure 6-8. The initial parameters for the contact-cement model (scheme 1) we choose a critical porosity of 36% which is that of a fundamental grain pack of random spheres (Nur et al. 1998) and a coordination number of 9 based on the work of Murphy (1982) for the typical Frio "C" formation porosity range. This rock physics diagnostic of the Frio "C" reservoir described above is also supported by the examination of sample thin sections shown in Figure 6-7 with the contact cement and pore-filling material indicated. The thin sections suggest that cement content is minimum and present at some of the grain contacts.

The underlying friable-sand model and the contact-cement model of which the constant-cement model is built on are known to overpredict the frame shear moduli due to the assumption that no slip occurs at grains boundaries; however in case of uncemented or poorly cemented sandstone this assumption can be invalid (Bachrach, Dvorkin, and Nur 2000, Avseth and Bachrach 2005, Mavko, Mukerji, and Dvorkin

2009). Thus, assuming a slip at grain contact reduces the shear moduli and increases the V_P/V_S ratio (Bachrach, Dvorkin, and Nur 2000, Avseth and Bachrach 2005). Accordingly, in our analysis we introduce the slip at grain contact in the form of a reduction factor to the shear moduli calculated from the grain contact theories. This shear reduction factor is obtained by matching the constant cement line with the drained frame moduli solved from Gassmann equation (Smith, Sondergeld, and Rai 2003) using well logs data. A shear reduction factor of 0.38 is obtained and thus, the shear moduli from the grain contact theory models are multiplied by this value. Taking the parameters mentioned above, we obtain the constant-cement lines shown in Figure 6-8. An initial cement percentage of 0.1% for the Frio "C" is inferred by plotting the baseline drained frame properties from inverse Gassmann into the model template as Figure 6-8 shows. This gives an initial porosity loss of 0.1% and thus a value of 35.9% for ϕ_b. Such a small amount of contact cement explains the high friability of the formation reported during core recovery (Sakurai et al. 2006). The template also shows that less than 0.1% change in the grain contact cement percentage would result in large frame moduli change. The data points in Figure 6-8 with shale volume larger than 0.25 and porosities lower than 29% are interpreted to be part of the shaly interval and are of different microstructure than the high porosity sandstone as we have shown previously in Chapter 3, Figure 3-13.

We highlight here that the anomalously large velocity reduction in both compressional and shear velocities from the crosswell data in Chapter 4, Figure 4-36 are mainly present at the injection well. This is where we do expect that any chemical dissolution or mechanical changes in the rock matrix will be strongest due to injection pressure and CO_2 influx into the reservoir. We discuss in the next section how we can use the constant-cement model template presented in Figure 6-8 to quantify the changes in the rock frame expected to be caused by CO_2 injection.

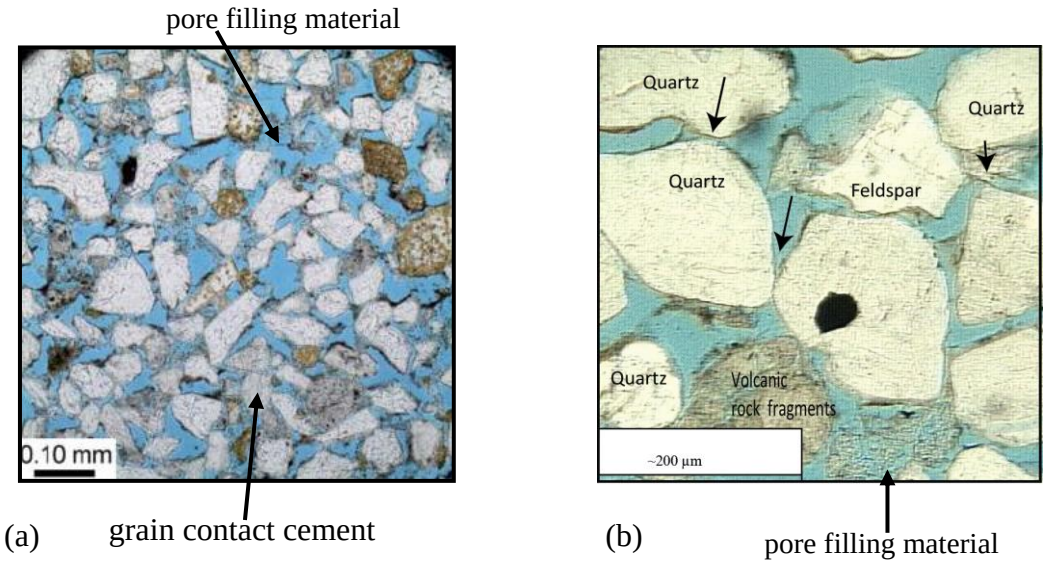

Figure 6-7: Thin sections of the high porosity and permeability Frio "C" sandstone, pore space indicated in blue. The mineralogical constituents are indicated on the thin section in the right. (a) From Sakurai et al. (2006) and (b) from McGuire (2009).

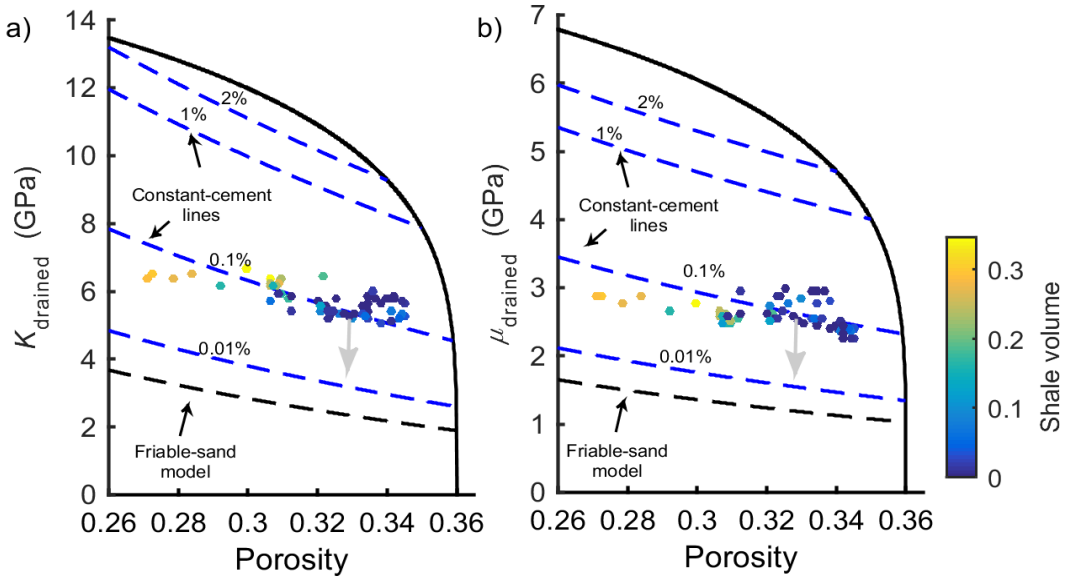

Figure 6-8: Drained-frame (a) bulk moduli and (b) shear moduli versus porosity from Frio-C injection interval. The friable-sand model and contact-cement model are calibrated using well logs data and core measurements. The pre-injection data points are calculated using Gassmann equation and fit the 0.1% constant-cement curve. The post-injection drained-frame shear moduli (and consequently post-injection drained-

frame bulk moduli) for the maximum change is shown by the grey arrow to be at about 0.01 % contact cement.

6.5 TIME AND SPACE VARIATION IN CONTACT-CEMENT BASED ON CROSSWELL SHEARWAVE VELOCITIES

We apply a simple theoretical approach to derive the variation in time in the drained frame bulk and shear moduli due to potential rock frame weakening for the post CO_2 injection reservoir rock matrix. In a time-lapse sense assuming no dry frame properties change, S-wave velocity is only affected by fluid density changes. Thus, if we compensate for this density change, the drained frame shear moduli should be constant. Consequently, any deviation from the pre-injection drained frame shear moduli is assumed to be caused by rock frame weakening and can be related to this contact cement reduction. This approach allows us to vary the contact cement percentage based on the magnitude of change in the shear moduli and move to different constant cement lines. We stress here that as a simplification and due to the availability of differential tomograms only we use an average value for each parameter for the pre-injection reservoir parameters (porosity, grains moduli, density, V_S, V_P and permeability) from well logs to represent the entire reservoir (the same as used in Chapter 5, Table 5-4). Then for the post-injection elastic properties (V_P and V_S) we subtract the differential values of the tomograms from the average log values in the reservoir to obtain the post-injection V_P and V_S velocities.

Accordingly, based on the crosswell S-wave velocity tomograms we calculate the drained frame shear moduli change. We start by calculating the density change for the post-injection case which is assumed to be caused by introducing 60% CO_2 into the reservoir. This represents the maximum observed value of CO_2 saturation for both wells after the monitoring survey. Brine density (ρ_{brine}) of 1030 Kg/m^3 and supercritical CO_2 density (ρ_{CO_2}) of 653 Kg/m^3 are reported for the reservoir (Daley et al. 2008). This means that CO_2 injection would cause a density reduction in the reservoir when replacing brine. We note here that a density reduction should cause an S-wave velocity increase rather than a decrease, contrary to the observed change in the crosswell tomography (Figure 4-36). Moreover, using the highest expected CO_2 saturation means that any effect of density change by saturation change on S-wave velocity is

either compensated for or overestimated. Measured S-wave velocity is related to the saturated frame shear moduli μ and the fluid saturated rock frame density ρ_B as

$$V_{\mathrm{S}} = \sqrt{\frac{\mu}{\rho_{\mathrm{B}}}}. \tag{6-6}$$

The post-injection density, ρ_{f} of the CO_2-brine mixture, can be calculated simply as

$$\rho_{\mathrm{f}} = S_{\mathrm{brine}}\rho_{\mathrm{brine}} + S_{\mathrm{CO_2}}\rho_{\mathrm{CO_2}}, \tag{6-7}$$

with S_{brine} and $S_{\mathrm{CO_2}}$ being brine saturation and CO_2 saturation, respectively, and ρ_{brine} and $\rho_{\mathrm{CO_2}}$ being brine and CO_2 density, respectively. For a given reservoir porosity (ϕ) and grains density (ρ_{g}) the density for the fluid saturated rock frame is given by:

$$\rho_{\mathrm{B}} = \rho_{\mathrm{g}}(1-\phi)+\rho_{\mathrm{f}}\phi. \tag{6-8}$$

Figure 6-9 shows a sensitivity analysis of the saturated rock frame density change caused by changing CO_2 saturation. From Figure 6-9 we conclude that fluid replacement effect on the drained frame shear moduli for fixed *V*s and any given CO_2 saturation should result in an increase in the rock frame shear moduli rather than a decrease as the bulk density decreases with increasing CO_2 saturation.

The pre-injection drained-frame shear moduli is calculated for the averaged pre-injection S-wave velocities from log data ($V_{\mathrm{S\_log}}$) for a fully brine saturated rock frame, as

$$\mu_{\mathrm{drained\_pre}} = V_{\mathrm{S\_log}}^2\rho_{\mathrm{B}}. \tag{6-9}$$

The post-injection drained shear modulus is calculated from the change in S-wave velocity from the crosswell data ($\Delta V_{\mathrm{S\_CW}}$) as shown in Figure 4-36. with ρ_B of the reservoir calculated assuming a 60% CO_2 saturation in equation (6-7) as

$$\mu_{\mathrm{drained\_post}} = \left(V_{\mathrm{S\_log}} + \Delta V_{\mathrm{S\_CW}}\right)^2. \tag{6-10}$$

The drained-frame shear modulus difference, $\Delta\mu_{\mathrm{drained}}$, is thus

$$\Delta\mu_{\mathrm{drained}} = \mu_{\mathrm{drained\_pre}} - \mu_{\mathrm{drained\_post}}. \tag{6-11}$$

The change in shear modulus values computed from this workflow is plotted in Figure 6-10. A zone of shear moduli reduction is observed at the injection well (that is a shear moduli reduction in the post-injection survey). This reduction is clearly a

function of the distance from the injection well. Moreover, at some distance away from the injection well the difference is essentially zero and no shear moduli weakening is observed.

We now estimate the cement percentage at grain contact that would be consistent with the post-injection drained frame shear modulus values computed from equations 4-8. Given that the initial reservoir contact cement is about 0.1% (Figure 6-8), then any $\Delta\mu_{\text{drained}}$ estimated can be used to calculate for a new ϕ_b by solving equation (2-24) iteratively. Figure 6-11 shows the sensitivity of the changes in drained frame shear moduli as a function of grain contact cement for varying reservoir porosities. The results show that frame weakening is not very sensitive to porosities; moreover, they predict a shear moduli reduction of more than 1.2 GPa as a results of removal or breakup of all the initial 0.1% grain contact cement. The yellow ellipse in Figure 6-8b shows that for the maximum observed reduction in μ_{drained} (about 250 m/s reduction in V_S measured from crosswell tomograms) the contact cement percentage must be reduced down to 0.01% from its initial 0.1%. Thus, based on the drained-frame shear moduli map in Figure 6-10 and applying a similar relationship to sensitivity study in Figure 6-11 for the average reservoir porosity of 0.33 taking a 0.1% contact cement for the pre-injection case, we calculate the post-injection contact cement percent change map for the reservoir in Figure 6-12. Once a value for ϕ_b is computed for each point in the reservoir for the post-injection case, we use equation (2-23) to calculate the corresponding time variant drained frame bulk moduli. Thus, we are able to quantify the weakening in the drained rock frame bulk moduli as a function of grain contact cement change guided by the shear moduli changes using the constant-cement model.

The resulting map of the contact cement percentage change displayed in Figure 6-12 shows that for the Frio "C" reservoir the grain contact cement reduction is maximum at the injection well. The sensitivity analysis results in Figure 6-9 suggest that the maximum density change for a critical porosity of 0.36 is less than 7% (compared to a full brine saturated rock frame), as such even if the density (i. e., CO_2 saturation) changes were underestimated or overestimated the error in the formation drained frame shear moduli according to equation (6-11) would be no more than ±0.21 GPa. This is only 18% of the observed 1.2 GPa weakening in the shear moduli of the reservoir at the injection well. Hence, in our workflow uncertainties in some of the

input parameters (e.g., density, CO_2 saturation, porosity) are second-order effects compared to the effect of grain contact cement percent change. Using this new interpretation of the Frio "C" reservoir drained frame properties and their change in a time-lapse sense, we discuss in the next section its use to derive the velocity-saturation relation between the wells using the crosswell data.

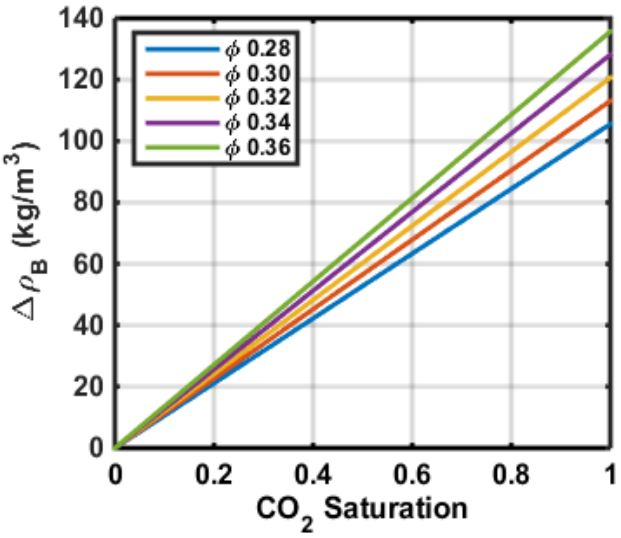

Figure 6-9: Density change of the saturated rock frame due to CO_2 replacing brine for different porosities.

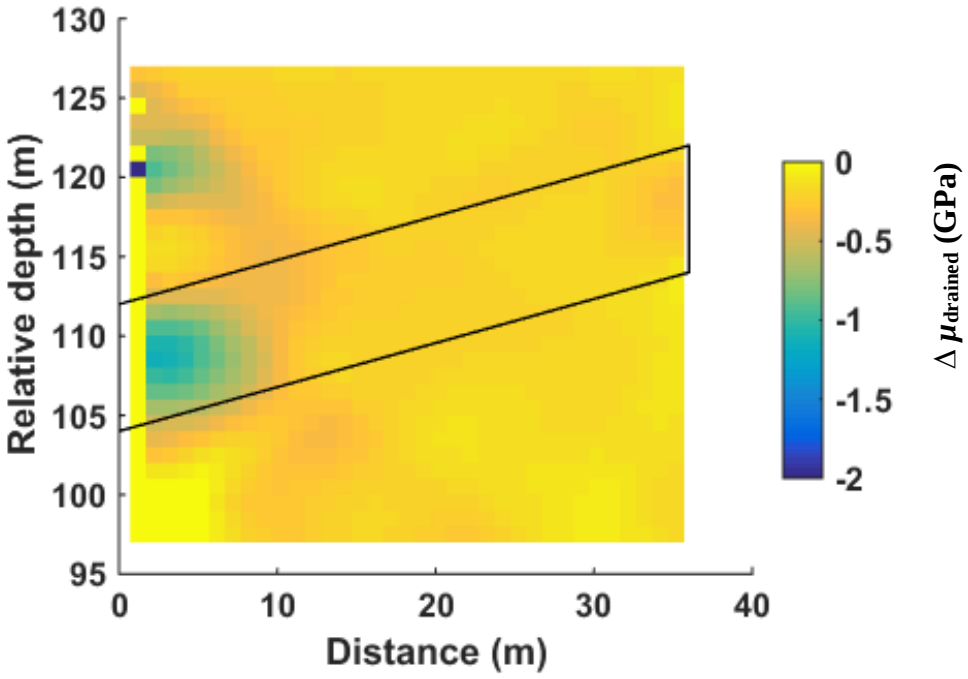

Figure 6-10: Map of $\Delta\mu_{\text{drained}}$ calculated for a 33% porosity and 60% CO_2 saturation. The area of interest boarded in black.

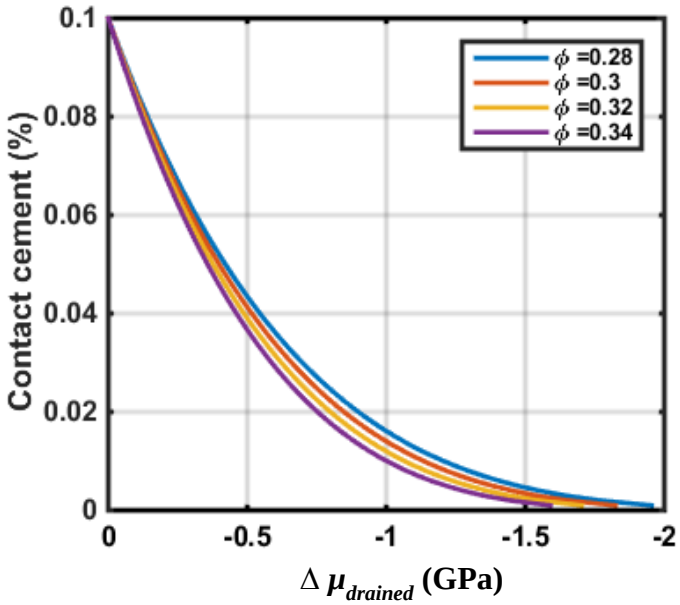

Figure 6-11: Drained-frame shear moduli change as function of contact cement for an initial 0.1 percent contact cement and 28% to 34% porosity.

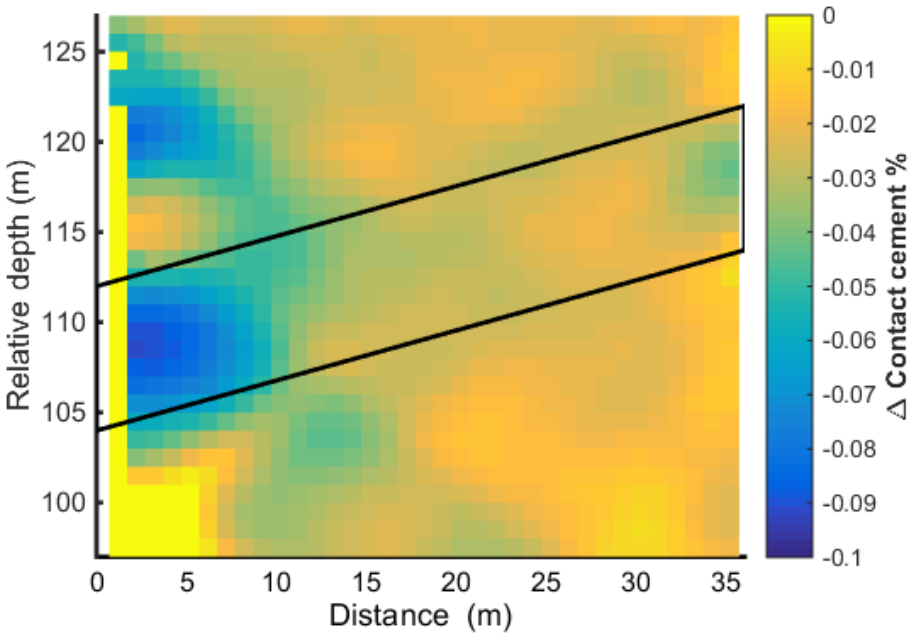

Figure 6-12: Time- and space variation in the contact-cement percent based on the drained-frame shear moduli change from the crosswell tomography assuming a 0.1% initial contact cement. The area of interest boarded in black.

6.6 VELOCITY-SATURATION RELATION

The assumed 60% CO_2 saturation earlier was used to quantify the magnitude of the change in the drained rock frame shear moduli by first compensating the density change associated with CO_2 replacing brine in the reservoir. Sensitivity analysis of P-wave velocity to density changes shows that the effect of the density reduction (which is 80 kg/m^3) associated with 60% CO_2 saturation change is less than 2% on the observed velocity change. Thus, we conclude that the density change effect on V_P is negligible. The methodology to construct the VSR here is to first investigate the possibility of a patchy saturation response by investigating the Frio "C" average reservoir properties. Then, using the time- and space-variant drained rock frame

properties obtained from the previous section we investigate several saturation scenarios using the crosswell ΔV_P tomograms.

To start with, knowing the type of velocity-saturation relation (VSR) is an important aspect to derive saturations from P-waves velocity changes. The different geometrical distribution of the fluids phases (e.g., brine and supercritical CO_2), that is whether the fluids are finely mixed or if CO_2 form patches, can result in a different seismic velocity response depending on the size of these fluid patches in the reservoir (Cairns et al. 2010).

The 'uniform' and 'patchy' saturation regions for the Frio site were presented earlier in Figure 5-6 for both the VSP and crosswell frequency range. For the crosswell range of frequencies, the length scale varies on average between 1 cm for 70 Hz frequency to less than 0.5 cm at 350 Hz to be in the patchy saturation region. For the patchy saturation distribution, we use the 3D continuous random medium model (Toms, Müller, and Gurevich 2005) with a patch size of 0.2 m and a dominant frequency of 300 Hz based on the crosswell data. This patch size is deduced from the data (best fit for both the VSP and crosswell data). For the wood's (also known as the Reuss average) and Hill averages, we make use of Gassmann's fluids substitution theory (Gassmann 1951) to account for the fluids effect on the rock elastic properties. The results are given by Gassmann-Wood (GW) and Gassmann-Hill (GH) bounds.

We recognize that due to the effect of irreducible water saturation (S_{wirr}) CO_2 cannot replace all the brine in the pore space (Azuma, Konishi, and Xue 2013). The presence of residual fluids saturation is well-known and needs to be taken into account in the fluid substitution flow. We employ the modified patchy saturation model (Azuma, Konishi, and Xue 2013) which take into account the effect of irreducible water saturation S_{wirr}. In our case the reservoir is initially saturated with brine, thus our starting point in the VSR is at 100% brine saturation and no residual gas saturation is present. However, we do not expect CO_2 saturation to reach 100% as CO_2 is injected into the formation. An average S_{wirr}=0.15 for the formation is reported by Ghomian, Pope, and Sepehrnoori (2008) which is calculated using Holtz's correlations (Holtz 2002), thus the maximum gas saturation (S_{gmax}) assumed in the VSR is 0.85.

Figure 6-13 shows the VSR obtained for these three CO_2 brine distributions discussed above for the 0.1% contact cement model (pre-injection; no-shear moduli weakening) and the 0.01% contact cement model (post-injection; maximum shear

moduli weakening observed). We see that the data points from the saturation logs and crosswell P-wave velocity reduction at the injection and observation wells show a separate VSR. This separation is because of the time-variant rock frame changes. Moreover, we observe that the data points fall in between the (GW) and (GH) bounds which is in the patchy region. We note that some of the points do fall off the VSR bounds for each well and we attribute this to the scale and resolution difference between the saturation logs (high resolution in depth and low lateral penetration) and the crosswell traveltime tomography velocities (2 m resolution laterally and vertically). This effect is largest at plume edges and where CO_2 saturation changes dramatically within a small depth interval as we can only see an average smoothed response in the crosswell velocity tomograms.

We now derive the saturation map using the crosswell P-wave velocity change. We compared several scenarios: in the first one (top row in Figure 6-14) the amount of cement inferred from the constant cement model (of 0.1%) is kept constant. In the second scenario (middle row in Figure 6-14) the constant cement percent is time-variant only (from 0.1% for the pre-injection down to 0.01% for the post-injection case in the entire reservoir) and in the third scenario (bottom row) the constant cement percent is both time- and space- variant based on the contact-cement percent map in (b). For each scenario, we present a patchy saturation model (last column) and the two limit cases of homogeneous mixing (GW) and no mixing (GH).

The results from Figure 6-14 show that if we use the drained-frame properties without the time-variant changes (0.1% contact-cement) we cannot predict the velocity changes at the injection well using any of the VSR curves. In the other hand, if we consider that the cement at grain contact decreases uniformly from 0.1% to 0.01% in the entire reservoir, the saturation at the observation well is largely underestimated (Figure 6-14, middle row) if compared to that measured by the saturation logs shown in Figure (4-36). Finally, if we apply a time- and –space variant contact-cement model in conjunction with the patchy saturation theory as shown in Figure 6-14 (bottom row) the resulted saturation maps provide the best match with the saturation logs at both the injection well and observation well.

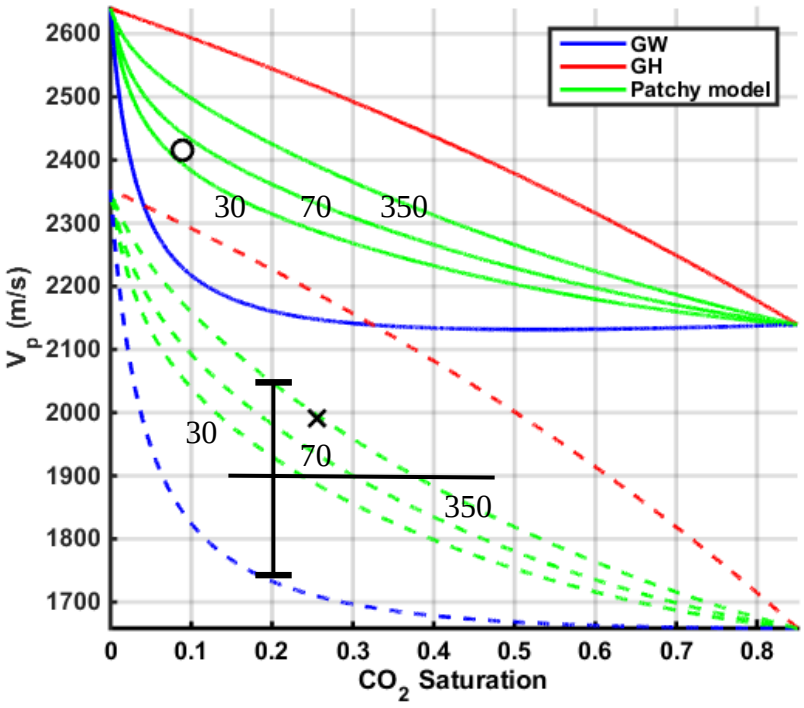

Figure 6-13: VSR for the average reservoir properties for the 0.1% contact cement (solid lines) and a time-variant model with 0.01% contact cement (Dashed lines). The patchy saturation lines using the 3D CRM for frequencies of 30, 70 and 350 Hz are indicted. The data points are from the saturation logs and crosswell P-wave velocity change. Note the separation of the two models and the data points for the injection well (stars) and observation well (circles).

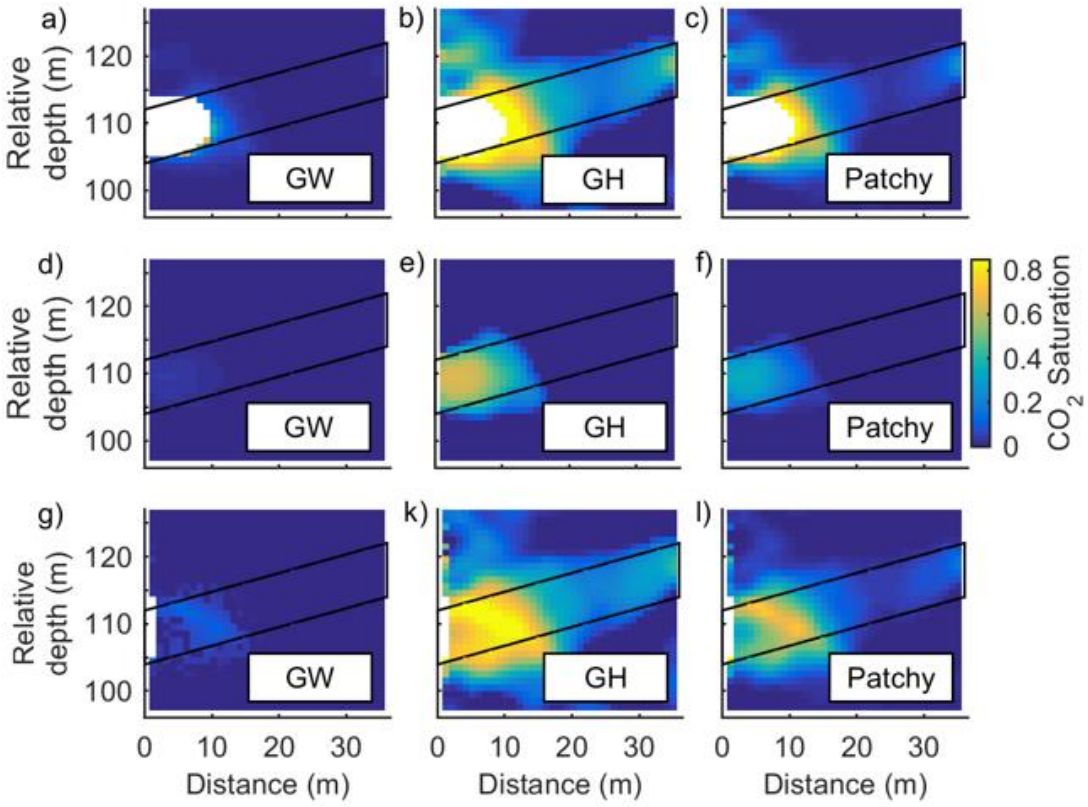

Figure 6-14: Saturation maps for various VSR type and different frame properties. Using the 0.1% constant-cement (top row), the time variant 0.01% constant cement (middle row) and a time – and space- variant model using the contact-cement percent map from Figure 6-12 (bottom row). For the patchy case the 3D CRM model with 0.2 m patch size and f = 300 Hz is used. The uncoloured areas in (a), (b) and (c) indicate that the velocity reduction is greater than what could be predicted using 0.1% contact-cement model.

6.7 DISCUSSION

we have shown that the post-injection crosswell seismic data are consistent with frame weakening due to removal of cement at grain contacts. The average amount of cement at grain contact (before CO_2 injection) that has been estimated from the rock physics diagnostic is about 0.1% only, which is consistent with the poorly consolidated nature of the Frio "C" interval. For these high porosity sandstones (close to the critical porosity, above which the rock can be seen as a suspension) it has been shown that small changes in the amount of cement at grain contacts will lead to large changes in the stiffness of the rock (Dvorkin and Nur 1996). This can be clearly observed in

Figure 6-8 were adding the initial 1% grain contact cement increased the dry frame bulk moduli by 400% and the shear moduli by more than 200% compared to the initially uncemented sand pack presented by the friable-sand model. Hence, our rock physics diagnostic was able to explain the velocity changes observed in the crosswell seismic data by considering only a small change of cement content (less than 0.1%) at grain contact. This behaviour is consistent with the geochemical field data (Kharaka et al. 2006) and the reactive transport modelling (Ilgen and Cygan 2016) which both conclude that the dissolution of the present minerals is volumetrically insignificant. In our analysis, we obtained an average contact cement percent for the reservoir after injection of 0.06% (average over the area of interest). This corresponds to an average decrease of 0.04% of the initial rock volume. Hence, the changes in the rock frame stiffness are not due to changes in porosity, as classically predicted by simple rock physics models, but arise from small changes at grain contacts.

Nevertheless, the exact mechanism of this inferred cement weakening at grain contacts cannot be determined at this stage, due to the lack of any detailed microstructural analysis or any laboratory experiment, performed on the Frio "C" sandstone itself or any other rock of similar mineralogy and texture. Hence, other mechanisms than cement dissolution, such as fines migrations or breakup of cement, cannot be excluded. Indeed, fluid injection (fluid flow) pressure, causing the breakup of grain contact and/or removal of cement supporting matrix mechanically, has been able to explain 4D seismic data of offshore Australia poorly consolidated sandstones (Saul and Lumley 2015). In this case, as observed for the Frio data, we expect to observe the largest contact cement reduction at the injection well where the pore pressure increase due to CO_2 injection is the largest. However, for the Frio Brine Pilot site, it has been reported that reservoir pressure change was less than 0.5 MPa (Daley et al. 2008) and could not be responsible for the large reduction of velocity observed. The velocity change expected for this case as previously presented in the discussed of Chapter 5 is found to be less than 30 m/s for both V_P and V_S.

A second possible mechanism is migration of fines (i.e., cement that has been mechanically removed). In such case, we expect the small particles to be deposited somewhere away from the borehole causing a permeability and porosity reduction. C. DellePiane, (personal communication, 2016) experimentally observed that the injection of pure CO_2 at supercritical conditions in Berea sandstone results in a loss of

stiffness of the rock with respect to the dry and saturated conditions. This effect was attributed to CO_2 adsorption on kaolinite (present at 3% in weight) based on microstructural analysis coupled with stress dependency considerations. We recognize from previous work of Daley et al. (2008) that the velocity reduction distribution in the crosswell traveltime tomography showed some heterogeneity that have been interpreted to be a possible low permeability zone in the middle and top sections between the wells. However, as baseline crosswell data are not suitable for analysis, we could not conclude if this zone was also present before CO_2 injection or not.

Another probable mechanism is that CO_2 dissolved the cement forming minerals such as carbonate and other minerals. This is supported by previous fluids chemical analysis which indicated a rapid increase of calcium, alkalinity, iron and other metals along with a decrease in pH at the monitoring well, reaching a maximum change in chemistry about 52h after injection of CO_2 (Kharaka et al. 2006). This mineral dissolution is expected to be strongest close to the injection well where the influx of CO_2 is highest. Recent reactive transport modelling performed based on the geochemical data measured at the monitoring well found that 0.023% of the total rock mass (calcite and iron hydroxides) have dissolved due to injection of CO_2 (Ilgen and Cygan 2016). Given the uncertainty of both methods, rock physics interpretation for this study and reactive transport modelling for the geochemical study, the two independent results (0.04% of cement loss for the former and 0.02% of rock mass loss due to dissolution for the latter) are comparable. The smaller value given by the reactive transport modelling might indicate that other mechanisms than mineral dissolution are present, as this modelling does not take into account any fines migration, clay shrinkage or any other weakening of the rock frame such as breakup of cement due to pressure increase in the reservoir, change in free surface energy etc.

We have highlighted the importance of taking the type of velocity-saturation relation into account when estimating fluids saturation. Field result matched the model within the patchy saturation regime for both wells as they both fall between the Gassmann-wood and Gassmann-hill bounds and a patch size of about 0.2 m is estimated from the data. The uncertainties in these measurements are difficult to assess due to lack of high-resolution data such as time-lapse sonic logs. However, these results do not contradict with field measurements and fit well the time-lapse VSP results at the injection well as Figure 6-13 (b) showed earlier.

We finally point out that this study shows the importance of obtaining high-resolution geophysical data for monitoring injections involving reactive fluids such as CO_2. A fluid independent measurement with a high resolution such as the shear moduli obtained from crosswell S-waves velocities showed to be of great benefit in interpreting the seismic time-lapse response. The use of borehole source generating both P- and S-waves was thus key to the utility of the crosswell survey.

6.8 CONCLUSION

The ability to explain time-lapse seismic attributes in terms of fluid saturation depends on the chosen rock physics model of the reservoir. The P- and S-wave velocity changes observed from the Frio CO_2 time-lapse crosswell study could not be explained by purely mechanical models (i.e., models that assume that changes are only due to saturation and pressure changes). The rock physics diagnostic we have performed here showed that when injecting reactive fluids such as CO_2 into poorly consolidated sandstones a change in the rock frame may be in play. We used S-waves velocity from crosswell traveltime tomography to quantify this change and interpreted it as a contact-cement percent change. The results are consistent with frame weakening resulting from 0.04% change in the contact-cement percent that cause a large reduction in the frame elastic moduli as predicted by the cementation theory of high porosity sandstone. This small decrease in cement percent is furthermore consistent with geochemical field data acquired during the CO_2 injection that show that even though some mineral dissolution was present, it was not volumetrically significant. The velocity-saturation relation shows best match with the saturation logs for a patchy saturation case at both the injection well and observation well. This approach could be applied to similar situations and may provide a better understanding of the time-lapse response of poorly consolidated sandstones in case of fluid injection.

CHAPTER 7. OTWAY 2C SENSITIVITY ANALYSIS USING SYNTHETIC TIME-LAPSE VSP DATA

The use of VSP as a tool for monitoring CO_2 injection in the subsurface has been discussed in Chapter 4. VSP application in constraining theoretical rock physics models has been shown using real data in Chapter 5. In this chapter, we evaluate the use of VSP in the monitoring of a small scale gas injection (15,000 tons of gas) using a full-waveform time-lapse synthetic modelling (3D modelling) seismic data set.

The first objective of this study is to determine qualitatively and quantitatively the time-lapse signal that could be obtained using sparse offset-VSP shots for the CO2CRC Otway Project (Stage 2C). Such objective is vital as deploying full-scale surface seismic or 3D VSP for permanent or long term monitoring would be expensive and logistically difficult due to land access permits. Moreover, few locations around the injection well are planned to have permanent seismic sources and the wells to have permanent seismic receivers. Thus, a study to understand the time-lapse that could be obtained from such a monitoring plan is in order.

The second objective is to utilize the methodology developed for the Frio case study (Chapter 4Chapter 5) to investigate if the rock physics model prediction of velocity changes and reservoir modelling results for the Otway 2C (Paaratte Formation) used in a synthetic modelling study could be recovered using the offset VSP shots proposed for monitoring.

Previous studies on time-lapse VSP and repeatability for the CO2CRC Otway Project have shown that it is possible to obtain high signal-to-noise ratio zero-offset and offset VSP seismic at the Otway site (Pevzner, Urosevic, and Nakanishi 2010). However, a time-lapse VSP feasibility study on regard to the time-lapse signature caused by CO_2 injection, its ability to monitor the gas plume and use for quantitative interpretation was not performed before. This work is an extension of previous work on the feasibility of CO_2 plume detection using 4D seismic at CO2CRC Otway site (Stage 2C) by Pevzner et al. (2015) and Caspari et al. (2015).

7.1 CO2CRC OTWAY CO_2 INJECTION PROJECT STAGE 2C

7.1.1 Overview

The CO2CRC Otway Project is the first CO_2 storage demonstration project in Australia. In Stage 1 of this project, 66,000 tons of CO2/CH4 gas mixture was injected in the Waarre Formation, which is a depleted gas field (Pevzner, Urosevic, and Gurevich 2015, Jenkins et al. 2012, Cook 2014).

In stage 2C (currently underway) the objective is to study the stabilization of about 15,000 tons of gas injection into a saline aquifer (Paaratte Formation) at a depth of about 1.5 km. The injection is to take place using CRC-2 well, while CRC-1 well will be utilized for the monitoring. This small injection can be considered a simulation of CO_2 leakage from a hypothetical commercial-scale injection into aquifers above the injection zone. Figure 7-1 shows a schematic diagram of the Otway 2C project. In this project, for a successful achievement of the objectives described, the seismic monitoring methods should provide high-resolution images of the gas plume as it migrates in the subsurface. For this, both 3D VSP and offset VSP seismic is planned to be acquired after the injection of predefined volume of CO_2/CH_4 mixture. The advantage of the VSP data here is that the seismic receivers are planned to cover large interval in the well and intersect the injection zone. Thus, high-resolution data could be extracted to analyse the effect of the gas injection of the formation elastic properties. Moreover, as an assurance, such high resolution data is expected to be able to detect the gas plume in the subsurface.

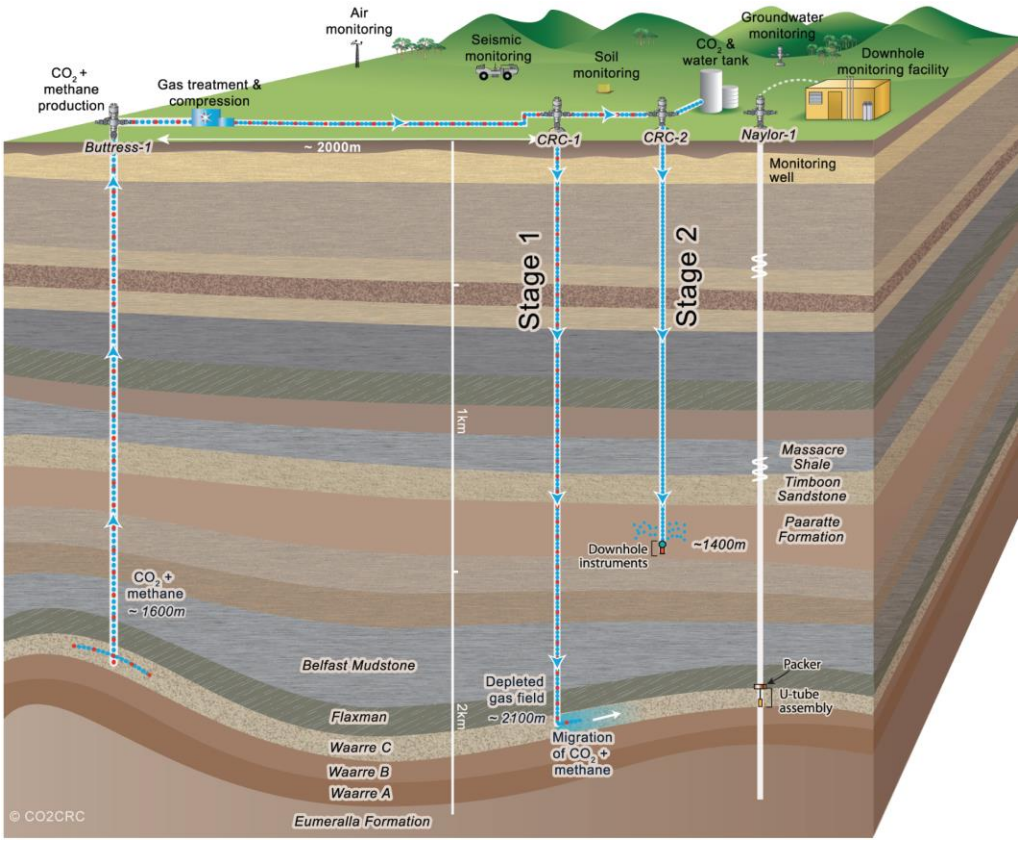

Figure 7-1: A schematic diagram the Otway project site. Stage 2C is aimed at injection of gas into a brine saturated interval. From (CO2CRC 2015).

7.1.2 Rock physics model

The Paaratte Formation contains intervals of clean sandstone and shaley sandstone with the proposed injection zone dominated by clean quartz-rich sand (Gurevich et al. 2014), see Figure 7-2. The porosity of the injection interval is in the range of 22%-34% and permeability of the range of 0.1-1 D (Caspari et al. 2015). A comprehensive rock physics study for the injection interval elastic properties and velocity-saturation relation was conducted recently by Caspari et al. (2015). The study highlighted that the rock physics model must take the variability in the sandstone and shaley sandstone sequences to predict the elastic changes induced by fluid replacement. For this, Caspari et al. (2015) used the shaley sediment model developed by Dvorkin, Mavko, and Gurevich (2007), which utilizes the effective porosity for the fluid substitution scheme. The frame effective properties are calculated for the wet-shale and sand mixture as a new solid composite. The grain contact cement model parameters are: a shear reduction factor of 0.7, critical porosity of 0.38 and a coordination number of 5.6. The rock properties used for the modelling are those

presented in Table 7-3. The volume of clay (f_{clay}) is assumed to an intrinsic porosity of 0.2 and is calculated from the total porosity (ϕ) as

$$f_{clay} = -2.14\phi + 0.78.$$

Furthermore, Caspari et al. (2015) found that at seismic frequencies Gassmann-Wood (uniform saturation case) is appropriate for the Paaratte formation. They also present the full treatment of the rock physics model and its application on the Paaratte formation. The Gassmann-Wood velocity-saturation relation is characterized with a rapid decrease in V_P as saturation of CO_2/CH_4 mixture increases from 0% to about 20%. This is shown in the velocity-saturation relation curves in Figure 7-3 for each point in the reservoir interval. Thus, if such an assumption is correct, it would be quite difficult to estimate the exact saturation above 5% in such cases as the velocity-saturation relation curve exhibits negligible variations in V_P with changing CO_2/CH_4 saturation. However, the presence of some gas should be detectable. In this study, we will employ the same model to invert for the petrophysical properties from the changes induced by the injection of $CO_2/CH4$ mixture in the sensitivity analysis using a synthetic data set.

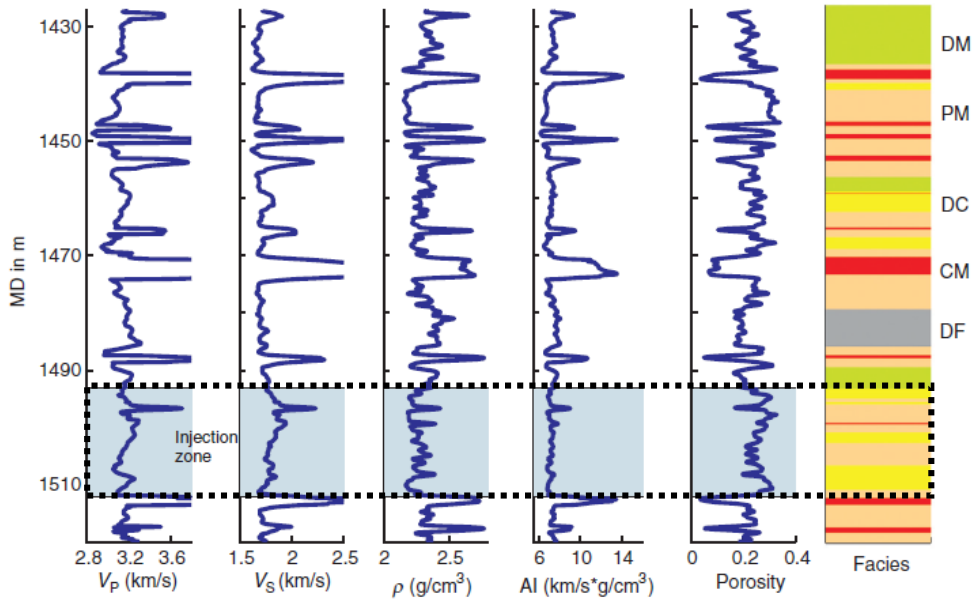

DM: Distal mouthbar DF: Delta front PM: Proximal mouthbar

DC: Distributary channel CM: Cements

Figure 7-2: The Paaratte formation facies units for CRC-2 well as given by Caspari et al. (2015).

Property	K_g (GPa)	μ_g (GPa)
Quartz	37	44
Clay	11.4	5.32

Table 7-1: Mineral grain properties used in the model. From Caspari et al. (2015).

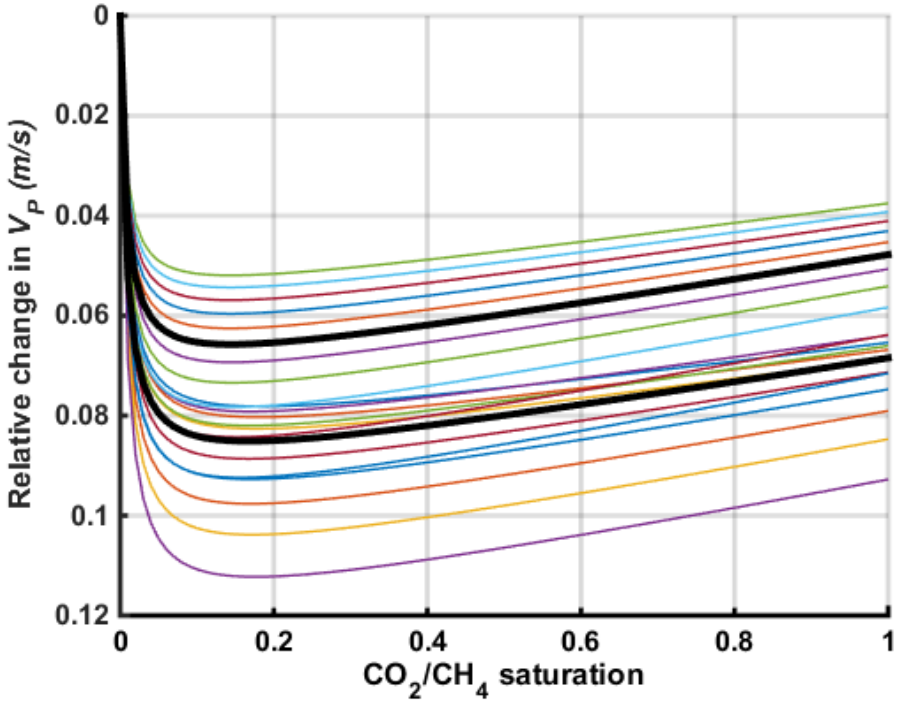

Figure 7-3: Velocity-saturation relation for the Paaratte formation (CRC-2 well) using the rock physics model proposed by Caspari et al. (2015). The average lines (black lines) are presented as an average due to the variable nature of the formation lithology for the DC and PM prominent in the proposed injection interval as shown in CRC-2 well logs (Figure 7-2). A 5% gas saturation approximately corresponds to 6-8% drop in V_P (taking reservoir interval variations).

7.2 METHODOLOGY

In the first part of this study, we focus on the analysis of the time-lapse signal that could be obtained from the sparse synthetic time-lapse VSP data. First, for the reflection amplitude signal we utilize the NRMS difference between the two surveys,

which would reveal the highest time-lapse signal difference in an NRMS sense for each shot-well pair. Second, we extract first arrivals time delays, first arrivals amplitude and reflection amplitudes for each shot-well pair.

We then analyse the use of the time-lapse signal obtained to recover the rock physics model which was initially used in creating the reservoir model. As we have seen in Chapter 4, reflection amplitude is the most challenging attribute to use for saturation evaluation. However, it could be used to estimate gas plume geometry as was shown in Chapter 4 for the Frio case study. Thus, here, we will utilize the reflection amplitude to map the extent of the plume. This is achieved by applying VSP-CDP transform and VSP depth migration to provide the approximate subsurface location of reflections depth points. Figure 7-4 shows a summary of the proposed workflow to accomplish the objectives of this chapter.

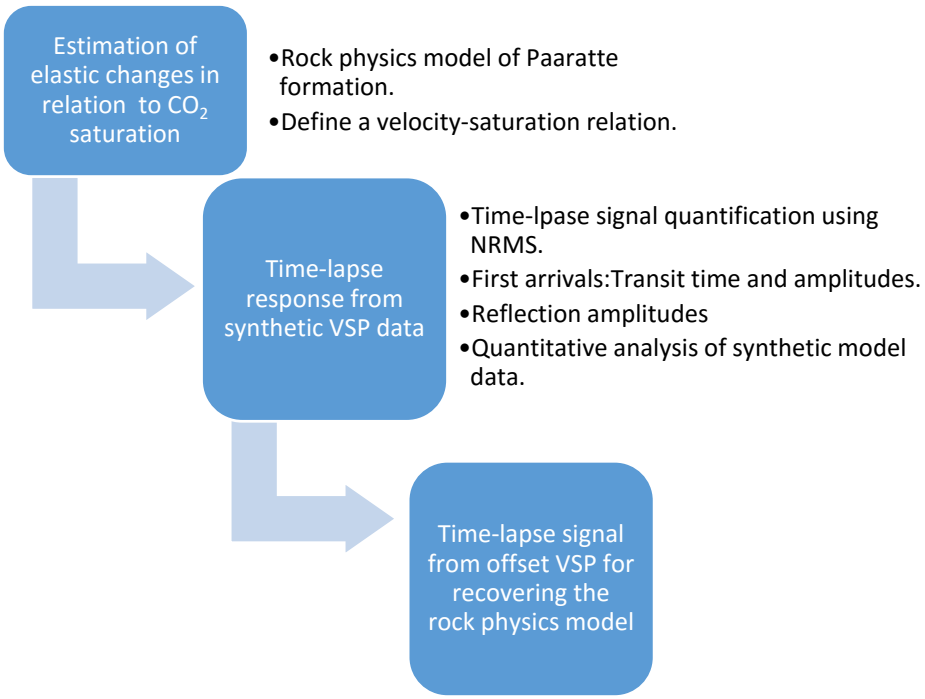

Figure 7-4: Workflow for the Otway 2C synthetic analysis for time-lapse offset VSP and their use to constrain the rock physics model initially used in the model.

7.3 SYNTHETIC TIME-LAPSE VSP DATA

The noise free synthetic VSP data we use in this study is part of a large realistic 3D time-lapse surface seismic data set simulated for the Otway 2C project (Glubokovskikh et al. 2016, Pevzner et al. 2015). This model is produced after a comprehensive rock physics modelling, 1.5D modelling, 2D FDTD synthetics were investigated (Gurevich et al. 2014, Caspari et al. 2015, Pevzner et al. 2015, Pevzner et al. 2013). A log of the elastic properties along the CRC-2 well is shown in Figure 7-6. The model was created for a realistic 3D geometry of the field and rock properties of the reservoir based on interpretation of previous 3D seismic volumes, VSP data, well logs and core data (Pevzner et al. 2015, Caspari et al. 2015, Glubokovskikh et al. 2016). This is important for the design of the optimal processing flow and quantitative analysis of the data as the seismic waves are affected by the overburden geometry. The model with the CO2/CH4 gas injection is run by simulating the injection of 15,000 tons of gas into the reservoir. The thickness of the gas plume at the end of the injection for which the monitor synthetic seismic is modelled is shown in (Figure 7-5). The model uses a 5% constant gas saturation; however, the thickness varies based on the reservoir simulations. The use of a constant saturation at 5% is a first order approximation and can be justified by previous analysis as we shown for the rock physics model (Figure 7-3). Because the velocity-saturation relation is expected to follow Gassmann-Wood (uniform saturation), the velocity changes for 5% saturation is similar in magnitude to that for higher saturation values.

In this study, we will employ only some shot locations in this time-lapse VSP study based on previous considerations optimized for CO_2 plume monitoring given the field layout, access permits, previous vintages of VSP shots and time-lapse response expected as will be shown next. Furthermore, to avoid redundancy, we will only present some of the synthetic data, which are expected to have corresponding real data acquired. It is worth noting that the processing and analysis of the synthetic data took place before acquiring the real data and updated based on initial real data acquisition geometry obtained later.

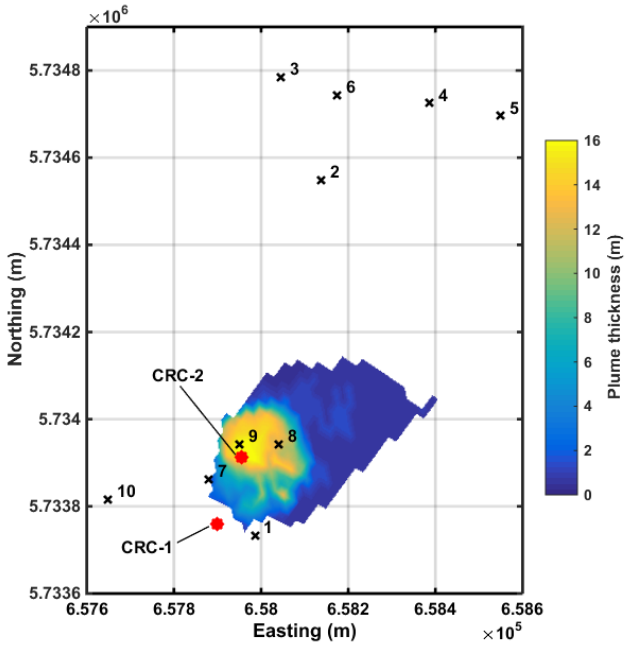

Figure 7-5: Map view of gas plume thickness in the model for 15,000 tons of gas. The saturation of gas is a constant 5%.

7.3.1 Geometry of synthetic VSP data

The offset VSP shots locations were optimised based on a 3D full-waveform synthetic study using a flat earth model by Pevzner, Urosevic, and Gurevich (2015). The time-lapse seismic signal obtained from the study are used to optimise the location of the shots and provide the best coverage. We choose the shot locations in Table 7-2 based on this study, the presence of previous VSP data at some locations and proposed location of permanent sources. Both CRC-1 and CRC-2 will be utilized as monitoring wells (in the synthetic data only). The receivers are set with 2 m spacing in both wells from the surface to the total depth in the synthetic model. All shot points are set at a plane surface that is 50 m above sea level, which is the average relief in the Otway site.

Figure 7-7 shows a map view of the wells and shots location for the model. In this study, we divide the shots locations to far- and near-offset. Near-offset VSP Shots are those less than 400 m away from the receivers well, while those more than 400 m offset are considered far-offset shots.

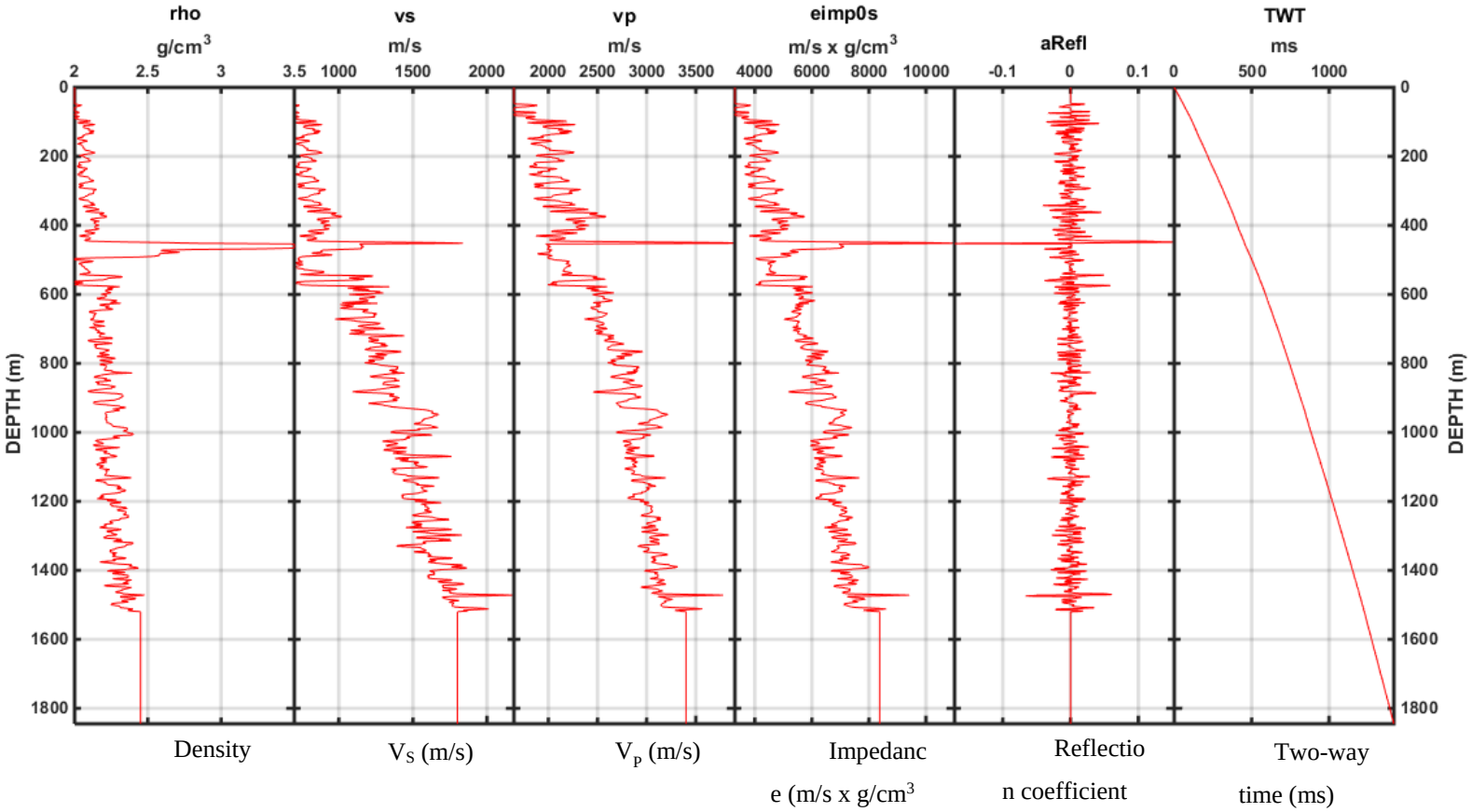

Figure 7-6: Elastic parameters extracted along the CRC-2 well and derived seismic impedance, reflectivity and two-way time (TWT). The injection interval is between 1490-1510 m approximately.

Shot #	Well/Shot description	X (m) Easting	Y (m) Northing	Offset CRC_1 (m)	Offset CRC_2 (m)
Well	CRC-1 (1847 TD)	657899	5733759	0	163
Well	CRC-2 (1525 TD)	657954	5733913	163	0
1	CRC1_ZVSP_2010	657986	5733733	91	183
2	CRC1_OVSP_1_2015	658138	5734549	825	662
3	CRC1_OVSP_2_2015	658046	5734784	1035	876
4	CRC1_OVSP_3_2015	658386	5734725	1082	920
5	CRC1_OVSP_4_2015	658549	5734696	1141	984
6	Shot 6	658174	5734744	1023	860
7	CRC2_ZVSP_2010	657880	5733862	105	89
8	CRC2_DAS_ZVSP	658040	5733942	231	91
9	PS1	657951	5733943	191	30
10	PS2	657648	5733815	257	321

Table 7-2: Wells, shots numbers, shots locations and offsets for the Otway time-lapse VSP synthetic study. Proposed Permanent source (PS). Total depth (TD) is for the true well geometry. The synthetic model utilizes CRC-1 and CRC-2 wells to a depth of 2000 m.

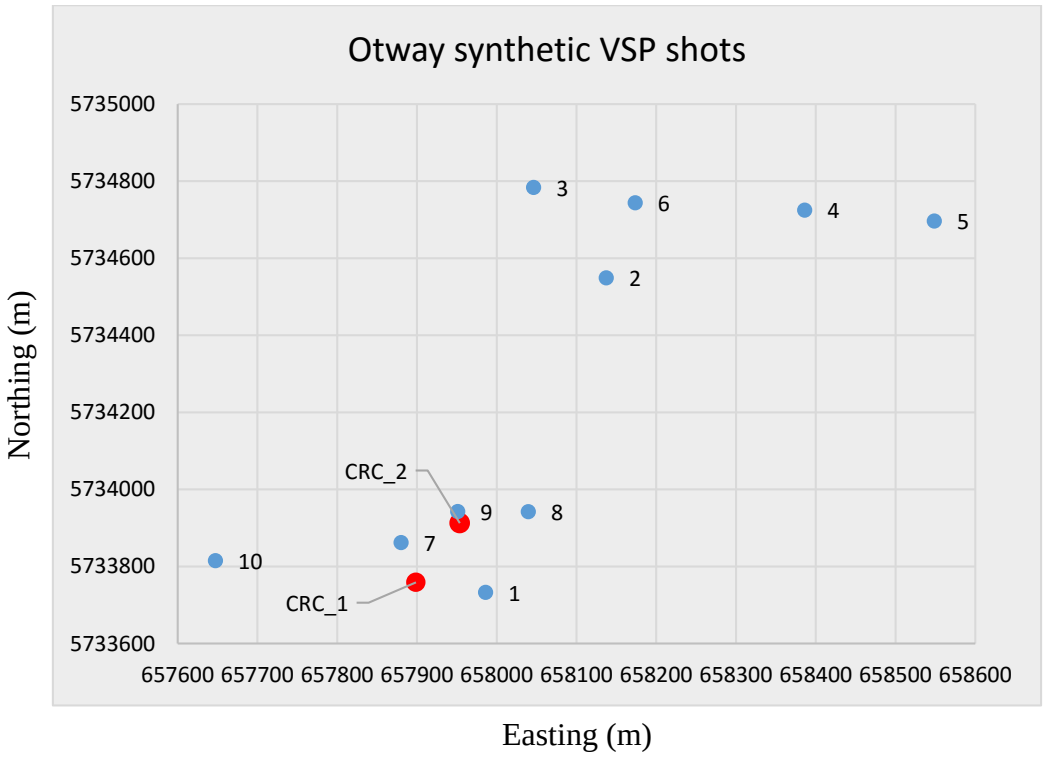

Figure 7-7: Map view of wells (red) and shot location (blue) in the synthetic time-lapse VSP study.

7.3.2 Synthetic data processing

The synthetic VSP data is noise free. Thus, minimum processing steps are required to extract the first arrivals traveltime and amplitude and reflection amplitudes. The processing steps and data extraction are summarized in Figure 7-8. These processing steps are described in details in Chapter 2, section 2.6 and their application to real and synthetic data was shown in Chapter 4 using the Frio VSP data. We present here the final processed sections for two shots from the synthetic data; that is one near-offset (shot 1) and one far-offset (shot 2) for CRC-1 and CRC-2 wells. However, the analysis in section 7.3.5 is shown for all the shots a similar manner to that presented here.

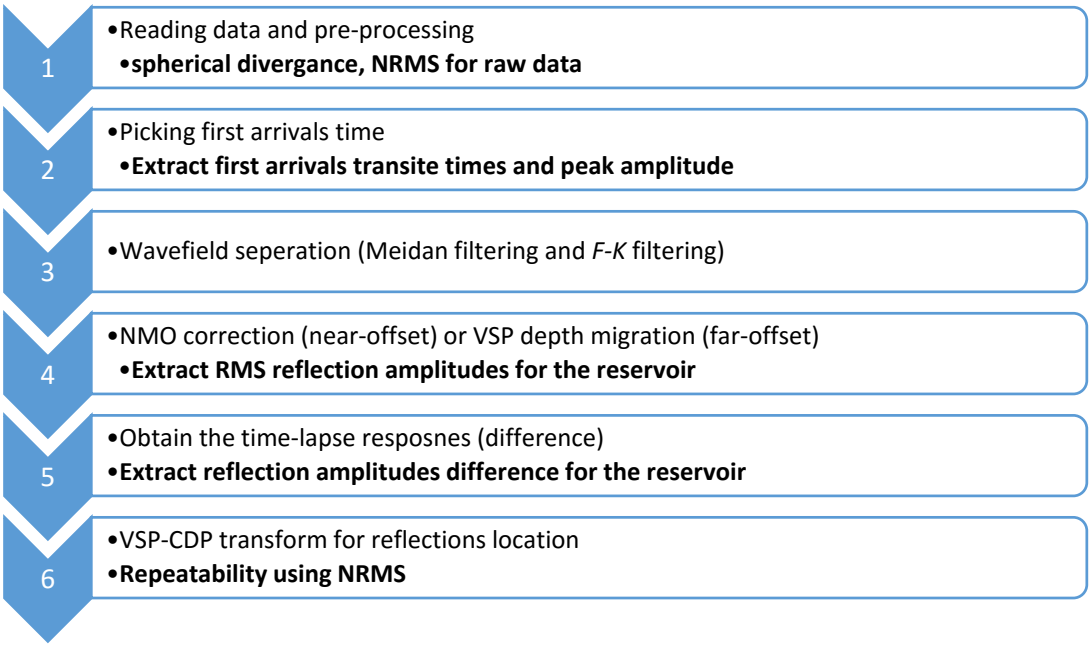

Figure 7-8: Synthetic VSP data processing flow and extraction of data for analysis.

Figure 7-9 shows the final processed sections for the baseline and monitor sections and their difference sections for shot 1 (CRC-1). It can be seen that the time-lapse signal is weak for all the receivers. This is expected as in the model the gas plume does not intersect CRC-1 well. Figure 7-10 shows the final processed sections for the baseline and monitor sections and their difference sections for shot 1 (CRC-2). We note that the reflection amplitude difference in Figure 7-10 (c) is strongest for receivers above the plume, then the response decreases moving toward shallower receivers. This is attributed to both the increase of Fresnel zone and the reflection depth-point moving away from the thickest part of the plume toward the edges as we have observed previously for the Frio project in section 4.6.

Figure 7-11 shows the final processed sections for shot 2; that is about 825 m from CRC-1 well. A depth migration is performed to obtain the spatial location of the reflection and their magnitude. We note from the difference section in Figure 7-11 (c) that the time-lapse amplitude difference is strongest where the supposed location of the reflection is at the thickest part of the plume and closer to CRC-2 well (see CDP locations in Figure 7-14). Figure 7-12 shows the migrated section of shot 2 for CRC-2 well. A similar behaviour is observed for the reflection amplitudes from CRC-1 with a strong signal close to CRC-2 well, where the plume is thickest in the model.

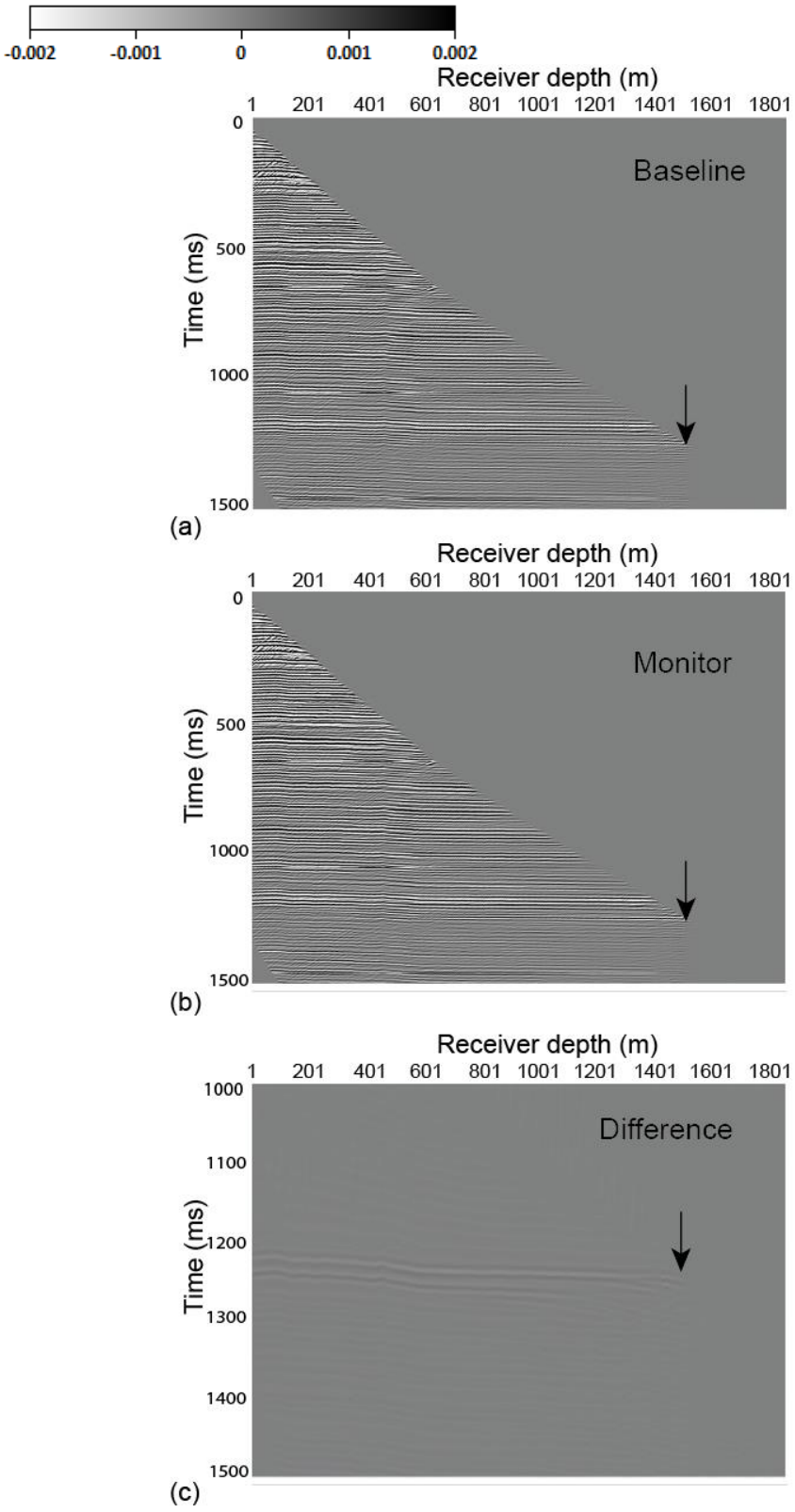

Figure 7-9: Final processed near-offset VSP shot record for Shot 1, CRC-1 well with NMO correction applied for (a) baseline, (b) monitor and (c) zoomed difference section.

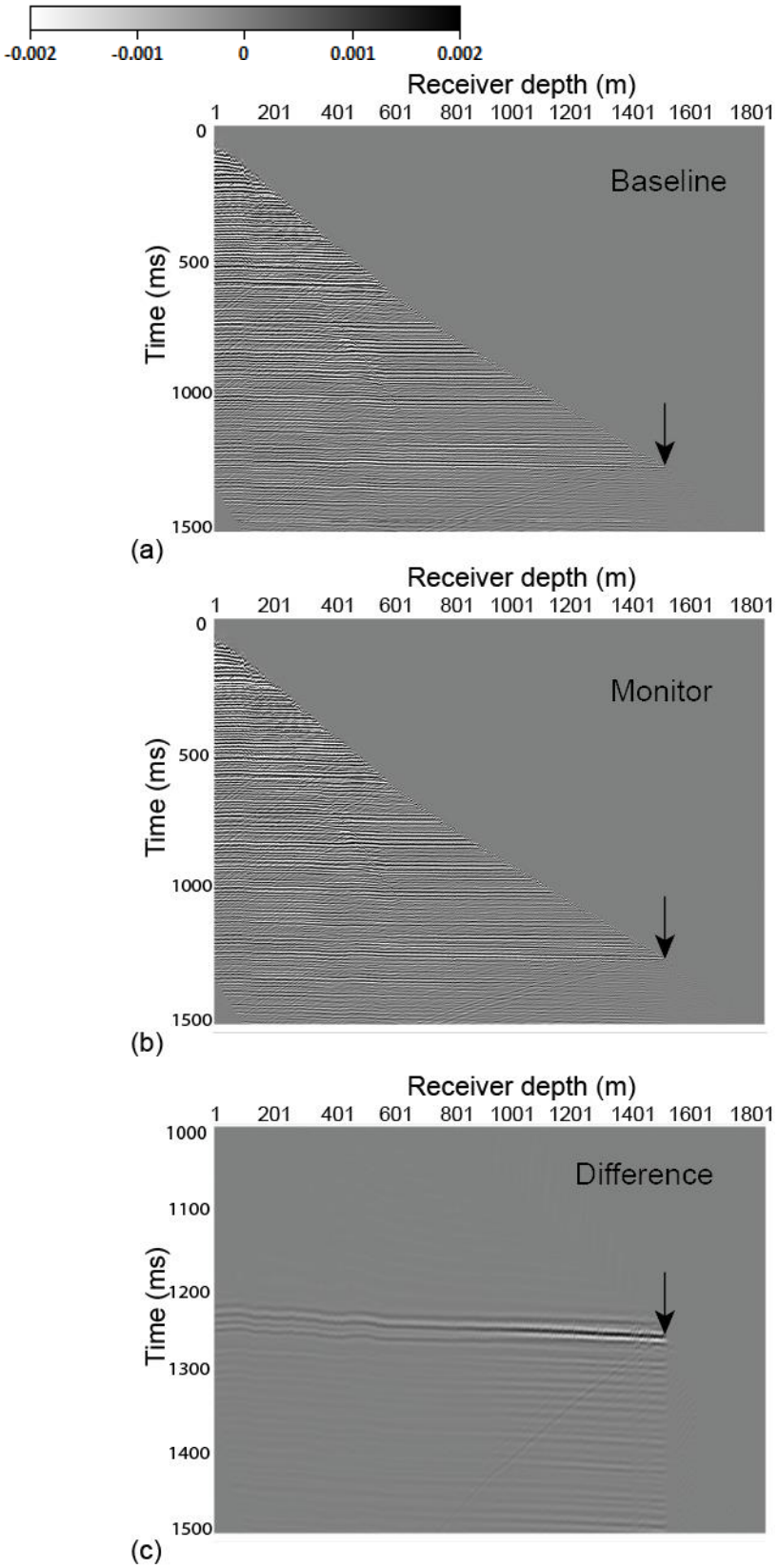

Figure 7-10: Final processed near-offset VSP shot record for Shot 1, CRC-2 well with NMO correction applied for (a) baseline, (b) monitor and (c) zoomed difference section.

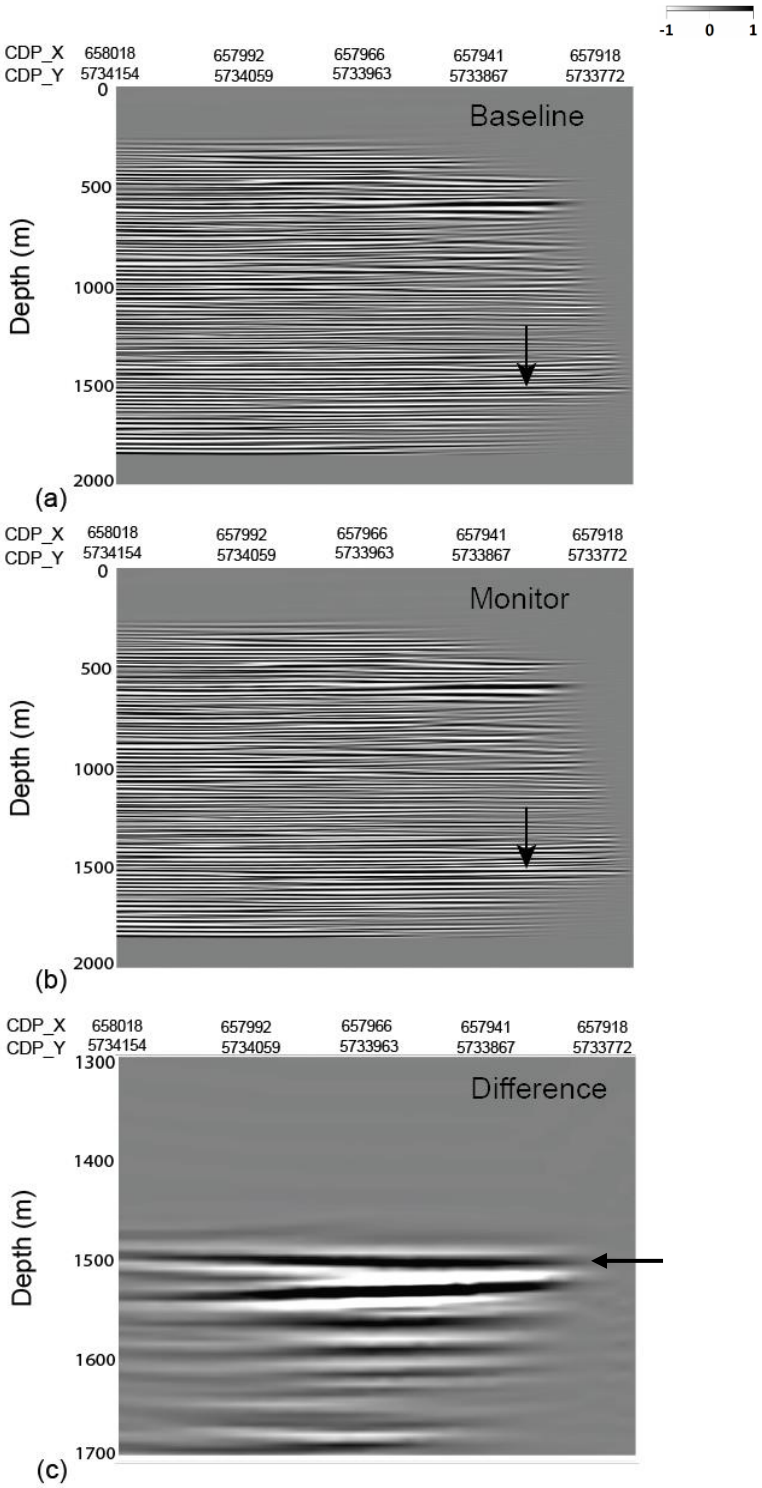

Figure 7-11: Final processed far-offset VSP shot record for Shot 2, CRC-1 well with VSP depth migration performed for (a) baseline, (b) monitor and (c) zoomed difference section. CDP_X (Easting), CDP_Y (Northing).

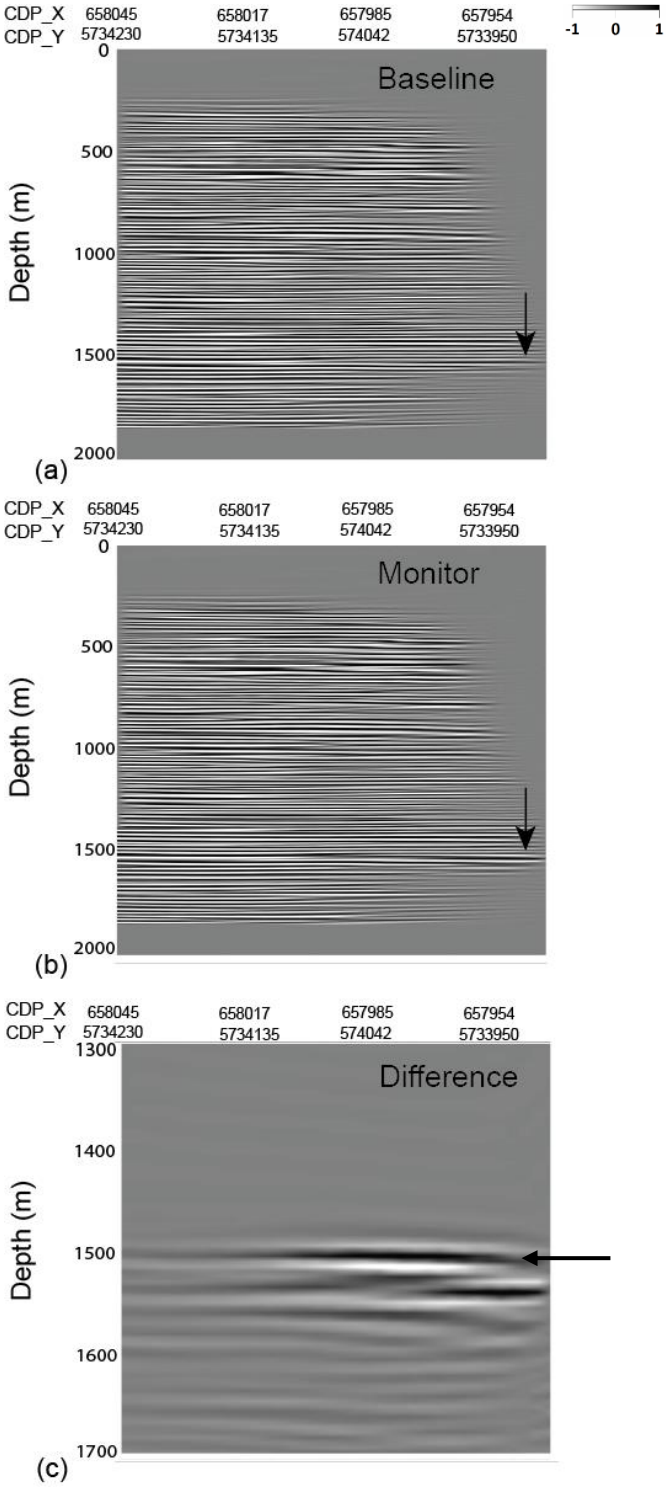

Figure 7-12: Final processed far-offset VSP shot record for Shot 2, CRC-2 well with VSP depth migration performed for (a) baseline, (b) monitor and (c) zoomed difference section. CDP_X (Easting), CDP_Y (Northing).

7.3.3 VSP-CDP transform and VSP-migration for CDP locations

Understanding the expected lateral coverage of the VSP shots used in this study is of main importance. As we have discussed in Chapter 2, VSP-CDP transform and VSP migration provide an approximate and true lateral position of the reflections (depth-points) in the subsurface (for an accurate velocity model), respectively. For near-offset shots VSP-CDP transform is applied to get the reflections position and not for amplitude interpretation, Figure 7-13. As a first order approximation, the results show that reflections are less than 150 m away from the wells except for shot 10 which is in the medium offset range.

VSP depth migration is performed on the far-offset shots as we have shown earlier. The location of the depth points for the migrated shots are shown in Figure 7-14 (a) and Figure 7-14 (b) for CRC-1 and CRC-2 wells, respectively. The CDP locations show that with the given VSP shots we will be imaging only part of the plume, which is about 50% of the total areal extent of the plume in the subsurface. The far offset shots provided the best coverage away from the wells in comparison to the near-offset shots.

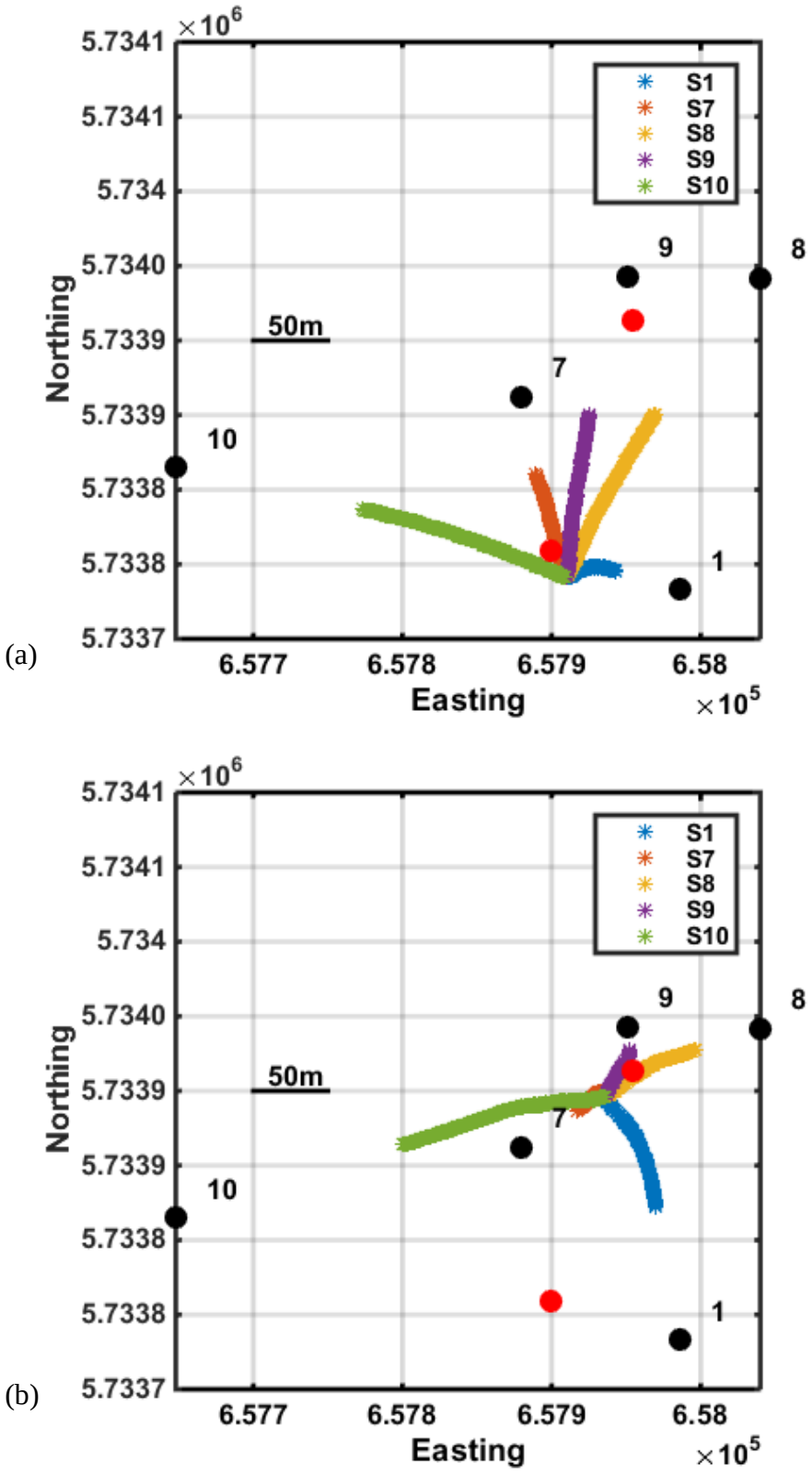

Figure 7-13: Approximate CDP locations using VSP-CDP transform for near-offset shots for (a) CRC-1 and (b) CRC-2. Shots location (black), wells locations (red).

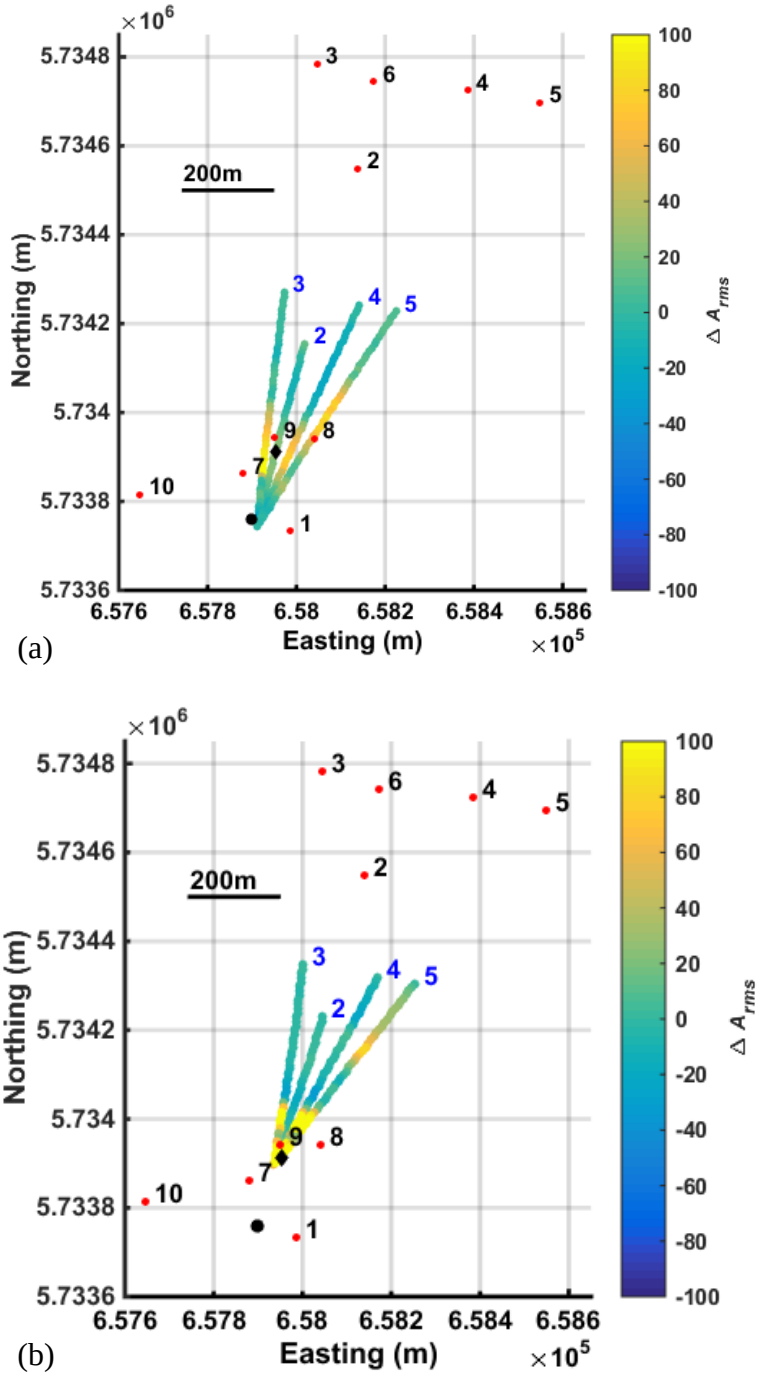

Figure 7-14: Approximate CDP locations for far-offset shots (2,3,4 and 5) after migration for (a) CRC-1 (black circle) and (b) CRC-2 (black diamond). The colour scale is for the normalized RMS amplitude difference calculate in the reservoir window using equation (7-1). Shots locations are numbered (red circles).

7.3.4 Analysis of time-lapse signal strength using NRMS

One way to measure time-lapse changes in the reflected waves is to look at the NRMS (Kragh and Christie 2002) difference between the two surveys (baseline and monitor) using equation (2-45) . The results are informative in case of real data about the noise level and repeatability, and in this case NRMS gives an indication of the strength of the time-lapse signal without noise. This could be done either with the raw data sets or the final processed sections. In the case of real data, processing the data by removing unwanted noise and downgoing waves is essential. However, in the case of synthetic with no noise, the results of the NRMS should provide a measure of the signal which is caused by the gas plume in this case. Thus, we calculate here the NRMS value for both CRC-1 and CRC-2 shots in panels to assess their sensitivity to the final plume geometry in the modelling.

The raw data NRMS signal for CRC-1 VSP shots show that only few shots have a strong NRMS response, that is, the far-offset shots 2 to 6, while for other shots the NRMS signal is weak with values less than 30% as Figure 7-15 shows. Moreover, for far-offset shots that do show an NRMS signal, the signal is strongest for the receivers just above the CO_2 plume in the model. As we move toward shallower receivers the NRMS signal diminishes for receivers near the surface. For the model plume geometry, this indicates that, for CRC-1 receivers far offset shots reflections have the best monitoring capability if the receivers are set close to the top of the injection zone.

For CRC-2 raw data the near-offset, shots 1,7,8 and 9 show a strong NRMS signal for all the receivers up to the surface as Figure 7-16 shows. For far-offset shots, similar to the CRC-1, only receivers close to the injection zone show a strong NRMS signal. The time-lapse signal decay for shallower receivers for far-offset shots is either due to increase of Fresnel zone size (for approximate zero-offset shots) or as the reflection depth-point is moving away from the well, for both cases the reflected seismic wavefield images a smaller part of the CO_2 plume or a thinner gas plume. This interpretation is supported by the VSP-CDP transform and migrated sections reflection locations presented in Figure 7-13 and Figure 7-14. The results of the NRMS are expected as the model have the CO_2 plume thickest at CRC-2 (Figure 7-5) which shows the strongest response for the near-offset shots.

The time-lapse NRMS signals for the processed near-offset VSP shots for the CRC-1 and CRC-2 are shown in Figure 7-17. Both CRC-1 and CRC-2 processed shots

show a stronger NRMS signal compare to the raw data in Figure 7-13. Thus, processing the data enhanced the time-lapse signal.

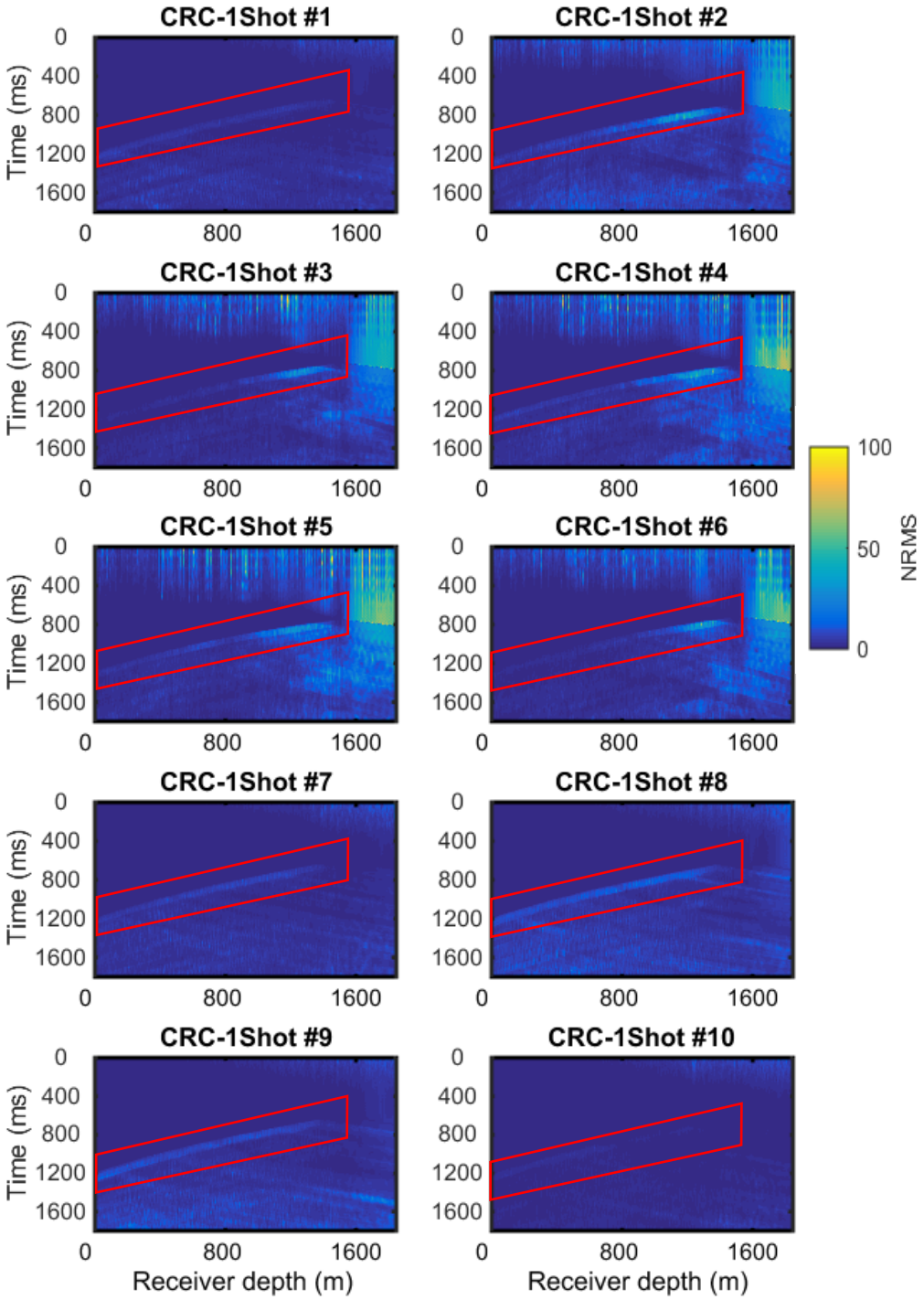

Figure 7-15: NRMS sections for CRC-1 VSP shots before processing in a 60-ms window. The injection interval reflection zone is within the red bordered area.

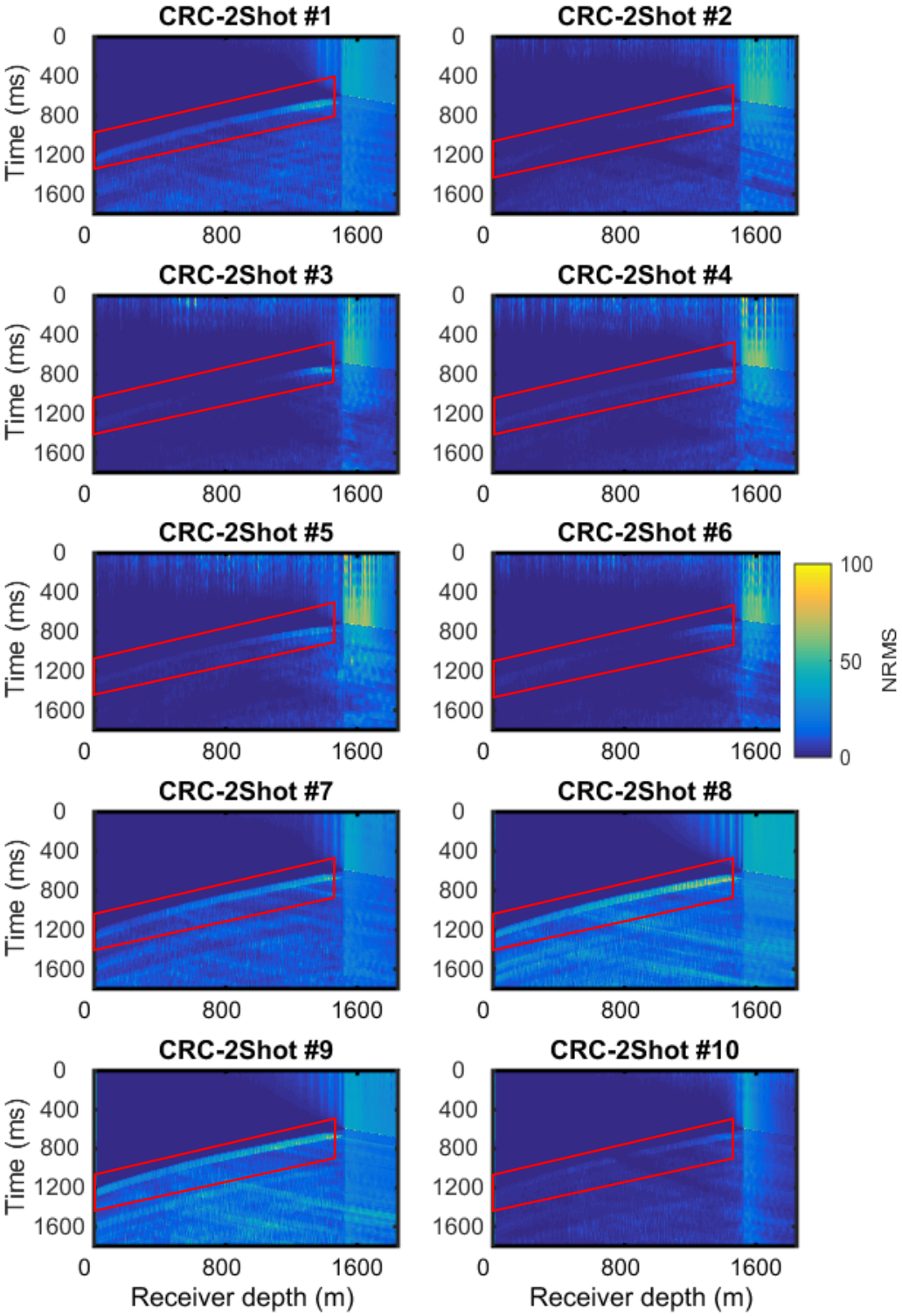

Figure 7-16: NRMS sections for CRC-2 VSP shots before processing in a 60-ms window. The injection interval reflection zone is within the red bordered area.

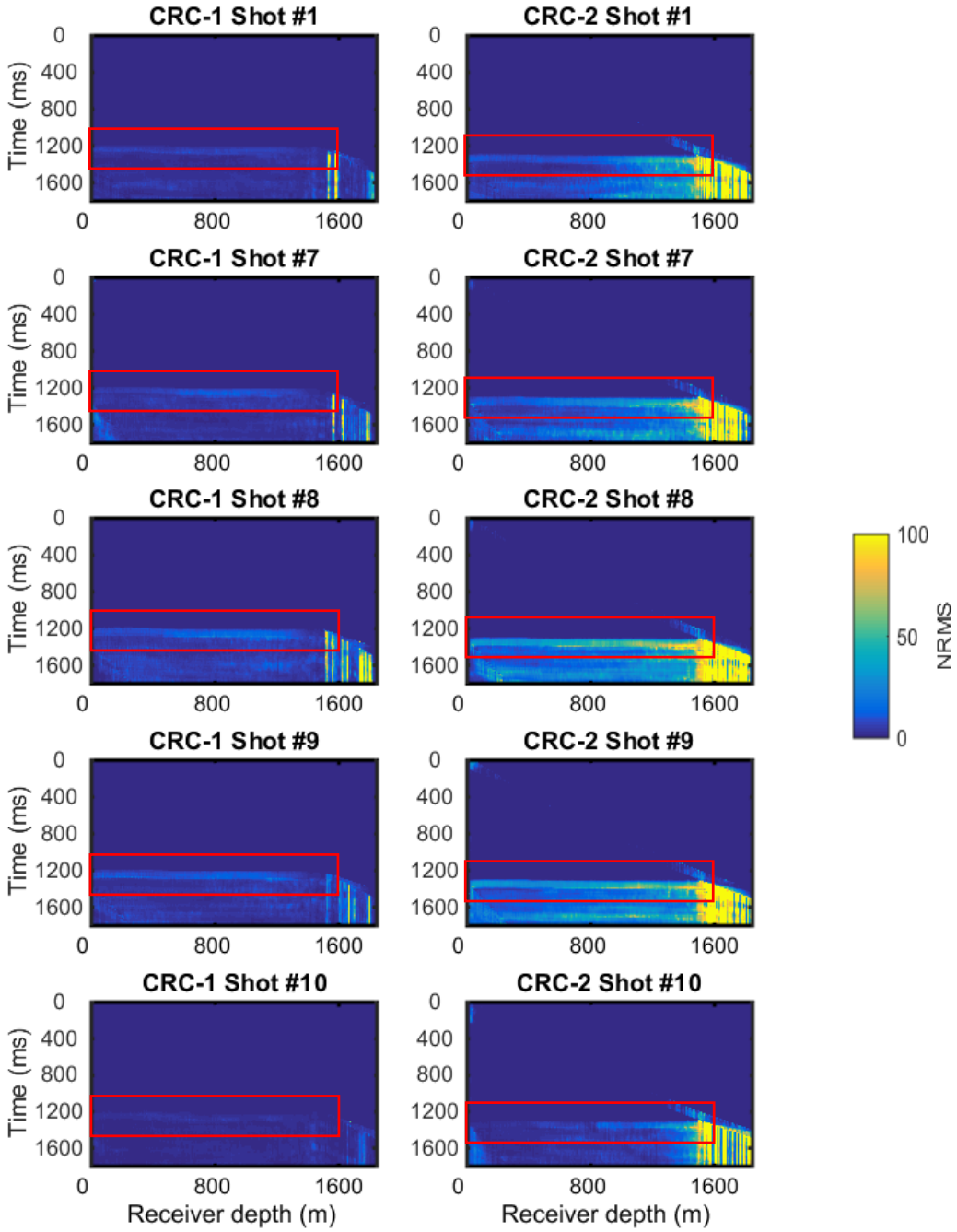

Figure 7-17: Near-offset shots (1,7,8,9 and 10) NRMS sections for CRC-1 (left) and CRC-2 (right) after processing in a 60-ms window. The injection interval zone is within the red bordered area.

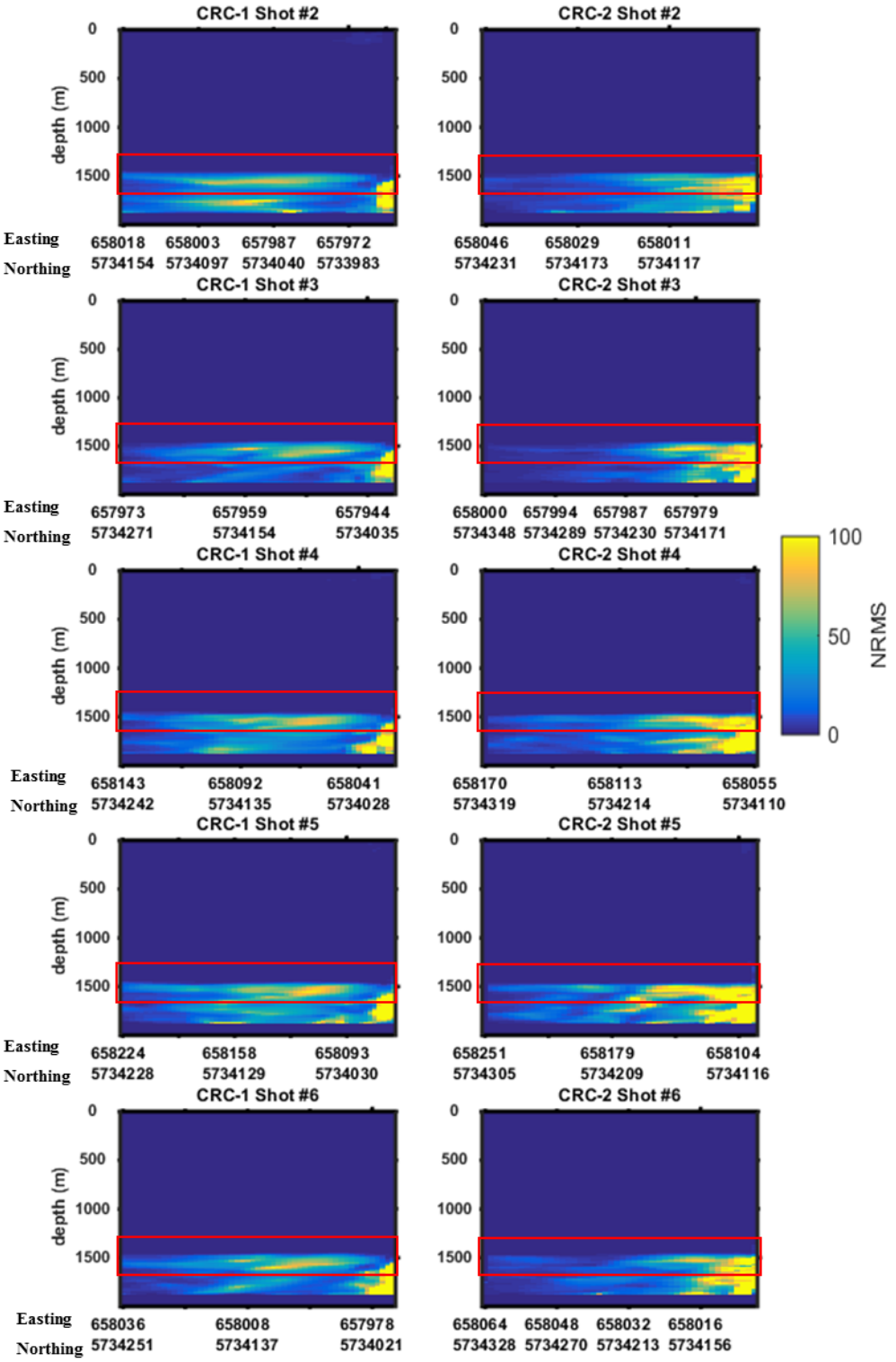

Figure 7-18: Far-offset shots (2,3,4,5 and 6) NRMS sections for CRC-1 (left) and CRC-2 (right) after depth migration in a 60-ms window.

7.3.5 Otway 2C synthetic data analysis

Here we extract the information required to obtain quantitative measurements of time-lapse response caused by the CO_2 plume in the model. A similar flow to that applied on the Frio field data (Chapter 4, section 4.4) is implemented here.

7.3.5.1 Transit time delays

The transit time delays have an uncertainty of ±0.1 ms which is the time sampling of the synthetic data during the picking routine. This appears clearly in the data for both the near- and far offset in Figure 7-19 (a) and Figure 7-20 (a). It can be seen from Figure 7-19 (a) and Figure 7-20 (a) that there is no transit time delay for most of the CRC-1 well shots locations for the near offset shots. However, for far-offset shots, no change is observed for receivers just below the gas plume model until the depth of 1540m, then the time delays increase as we move toward deeper receivers indicating that the seismic wavefield passes through the gas plume away from the well. An opposite response is recorded for the CRC-2 well, as the time delays decrease as we move toward deeper receivers, indicating that the passing seismic wavefield is probably going toward the plume edges where the gas plume is thinner. In Figure 7-19 (a) we see that for shot 10, the time delay diminishes for deep receivers indicating that the gas plume extent toward shot 10 is small, which is in agreement with the model.

The transit time delays can also provide an estimate of plume thickness. This can be achieved by either knowing the receiver locations and top sealing layer or by the behaviour of the first arrivals in an approximate zero-offset shots given a dense receiver spacing. In the Otway project a possible sealing thin bed in the CRC-2 well is located at depth of about 1490 m. Therefore, given that the maximum time delay for the near-offset shots (approximate zero offset) stabilizes or reaches a maximum for a receiver at depth 1511 m and lower, this means that the gas plume is no more than 21 m thick approximately at the CRC-2 well. The use of far-offset shots for a similar objective is more challenging and susceptible to large uncertainties as the distance travelled by the seismic wave in the gas plume can only be approximated using ray tracing which is not a trivial task as the plume thickness is also unknown. To obtain the velocity changes from the time delays equation (4-3) is used. The initial velocity could either be approximated from the VSP interval velocity or calculated using the sonic-log P-wave velocity for the same interval. Here, for comparison we utilize both methods and the results are shown in Table 7-3.

Although CRC-2 is probably the best VSP location to monitor traveltime delays, it has a very limited depth below the proposed injection interval. On the other hand, for CRC-1 the synthetic study results suggest that most rays do not travel through the gas plume which is in agreement to that shown previously for a flat earth model synthetic data (Pevzner, Urosevic, and Gurevich 2015).

	Transit time (ms)	**Average pre-injection velocity (m/s)**	**Average Post-injection velocity**	**ΔV_P (relative change)**
VSP	6.50	3252	3062	0.063
Well logs	6.56	3198	3014	0.061

Table 7-3: Table of average post-injection velocity with the baseline V_P calculated using VSP interval velocities and well logs. The traveltime delay is set at 0.4 ms as observed for the near offset shots in CRC-2 well. The layer thickness is set to be 21 m in the depth range of 1490 m to 1511 m.

7.3.5.2 Transmitted waves amplitudes

Figure 7-19 (b) shows the first arrivals amplitude change. We see that the uncertainty in the transmitted waves amplitude is about ±2%. This is considered large, given that the maximum change obtained for the near-offset shots is 4±2%. Looking at the results in Figure 7-19 (a,b) for the near-offset shots for CRC-1 reveals that although no traveltime delays are associated with first arrivals, their amplitudes do change, indicating that the seismic wavefield is affected by the gas plume. However, we could not interpret these results quantitatively, but qualitatively they indicate the presence of the gas plume. In Figure 7-20 (b) ΔI_p (change in impedance) in the far-offset shots is about 9±2%. Interpretation of these changes requires taking the offset effect (angle dependency) of the transmitted waves which is not treated in the research.

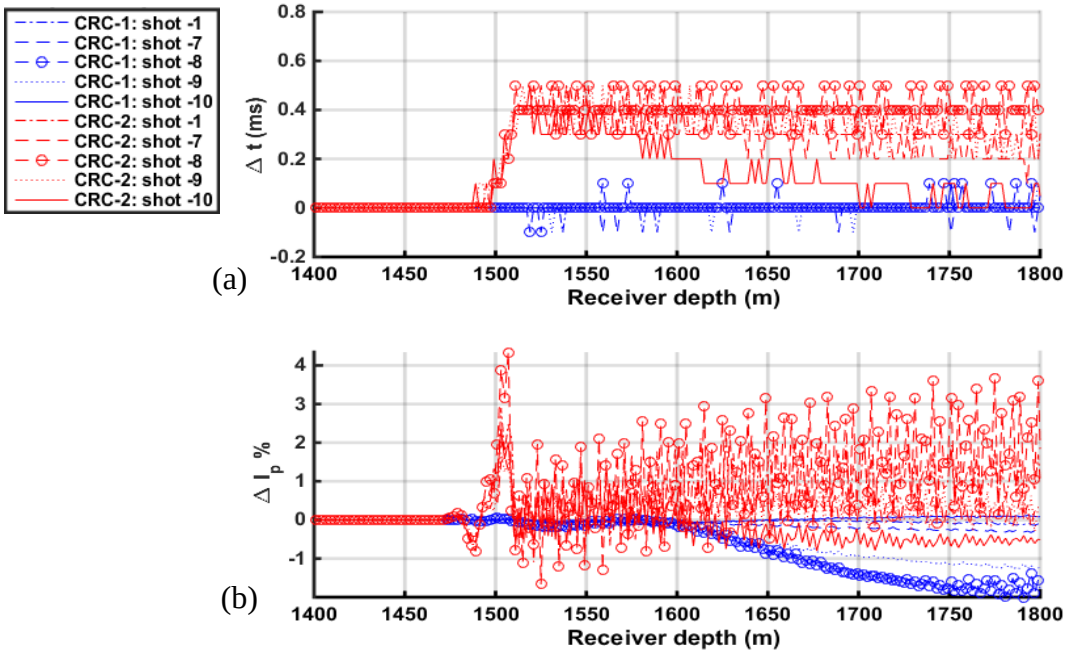

Figure 7-19: Near-offset shots (a) transit time delays and (b) transmission coefficient change for CRC-1 and CRC-2 wells.

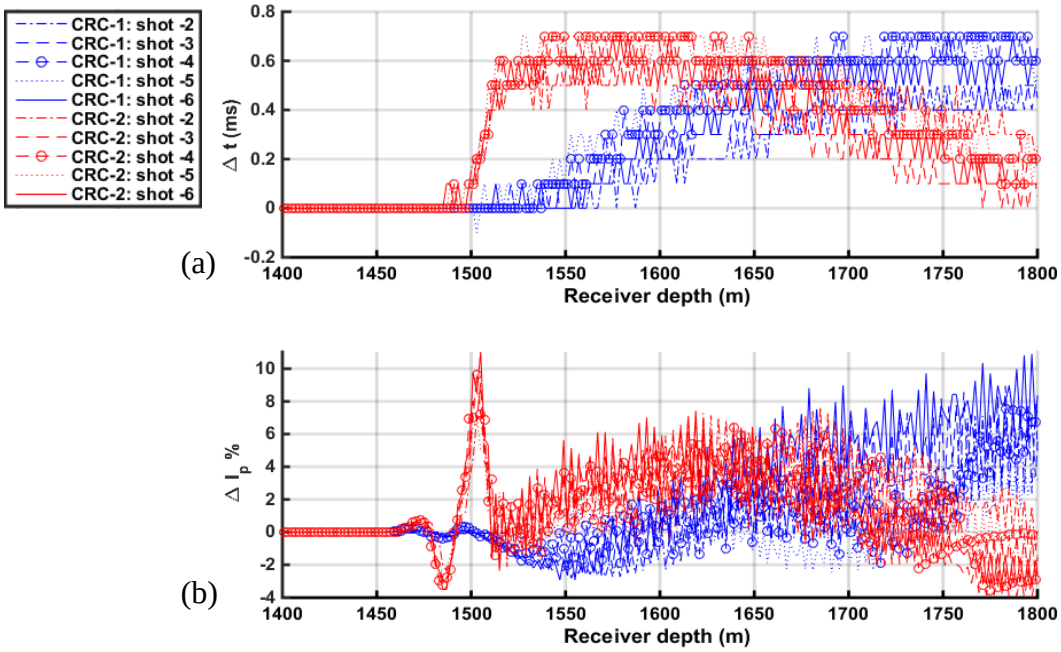

Figure 7-20: Far-offset shots (a) transit time delays and (b) transmission coefficient change for CRC-1 and CRC-2 wells.

7.3.5.3 Reflection amplitudes

For the near-offset shots the reflection amplitude is essentially coming from a lateral distance of less than 200 m around the receiver well. The amplitude is calculated as the RMS amplitude difference in a 60 ms window for the normalized amplitudes of both vintages (by the baseline maximum) for the reservoir reflection as:

$$\Delta A_{rms} = \frac{A_{rms\_post} - A_{rms\_pre}}{A_{rms\_pre}} \times 100 \qquad (7\text{-}1)$$

The reflections amplitude is expected to vary with changing receiver depth. As we have seen previously in the study of the reflection behaviour observed in the Frio case study in Chapter 4, as each receiver depth samples a different volume of the subsurface rock, the reflection is affected by the size of the Fresnel zone and gas plume geometry. The near-offset reflection response difference for CRC-1 and CRC-2 wells is shown in Figure 7-21. It can be seen that the change in amplitude for CRC-2 well is much stronger than CRC-1 well. This is because for these near-offset shot, the gas plume is not present around CRC-1 and only part of the seismic wavefield is affected by its presence.

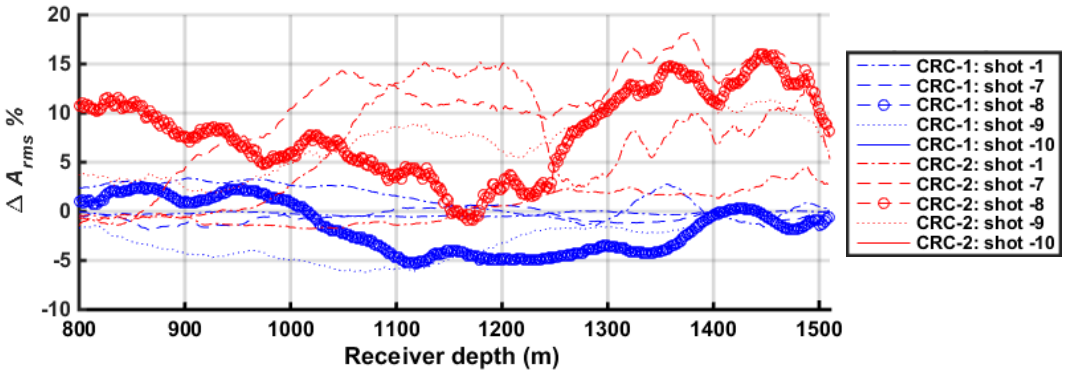

Figure 7-21: Reflection amplitude change in a 60 ms window calculated using equation (7-1) for near-offset shots at the reservoir interval in CRC-1 and CRC-2 wells for the reservoir reflection (smoothed).

7.4 DISCUSSION

We presented the processing and interpretation of a synthetic time-lapse VSP data for Otway stage 2C CO_2 injection project. The results provide the best case scenario of obtaining a time-lapse signal as the data set is noise free. If the injected gas behaved similar to that predicted by the reservoir modelling (lateral extent, changes in elastic properties with CO_2/CH_4 saturation etc.), then the following main observations can be made:

- Receivers in CRC-2 will provide information about the near and far offset response of the plume. However, receivers in CRC-1 will only provide information using the far-offset shots, while weak time-lapse signal is observed for the near-offset shots.
- The first arrivals contain information about the velocity changes caused by the gas plume for receivers in CRC-2 well, while for CRC-1, the majority of the seismic waves do not travel through the gas plume.
- First arrivals traveltime expected to be of the order of 0.4 ms (for a gas plume thickness of about 20 m), thus a high signal-to-noise ratio field data is required to effectively capture such subtle changes.
- First arrivals time delays in CRC-2 well could be utilized in containing the rock physics model, however, uncertainty in the obtained signal could make the results less effective in constraining the rock physics model.
- Reflection amplitudes are difficult to interpret, However, if the real data is compared to the synthetics, then, reflection amplitude could be used to constrain the quantitative and qualitative interpretation of the time-lapse signal.

The study in this chapter shows how each time-lapse survey is unique and that various factors control our ability to perform quantitative interpretation to constrain rock physics models such as, survey design, expected time-lapse signal strength and quality of the seismic data (resolution and signal-to-noise ratio). We expect the main controlling factor here to be the magnitude of velocity changes. The P-wave velocity changes of about 200 m/s for about 20 m plume thickness for the Otway 2C case, resulted in 0.4 ms time delay, this translate to a relative V_P change of 0.062±0.02 (with ±0.1 ms uncertainty in the time picks). Such a subtle change in the first arrivals time delays would be challenging to obtain in the real data.

7.5 CONCLUSION

This chapter presented a study on the induced elastic changes by CO_2 in the Otway 2C project and their seismic response for seismic monitoring using sparse-VSP geometry by means of a realistic 3D synthetic modelling. The synthetic VSP data have shown that it is possible to constrain the velocity changes in the reservoir if the receivers are set in the CRC-2 well with sufficient spacing. Moreover, good overall illumination of the plume is obtained for the northern azimuth. The velocity changes inferred from the first arrivals time delays and amplitude changes provide could be utilized to contain the rock physics model. However, because the velocity changes expected are small, the uncertainty is almost 25% that of the magnitude of the signal. The results show that for quantitative interpretation the magnitude of the velocity changes caused by CO_2 is a first order factor followed by the resolution of the seismic method. Both factors are expected to play a major role in utilizing borehole seismic data to contain the velocity saturation relation for the Otway 2C project.

CHAPTER 8. CONCLUSIONS

The objective of this thesis was the analysis of the effect of CO_2 saturation on the elastic properties of rocks using borehole seismic data. Seismic resolution, gas plume geometry, rock physics models applicability and adaptation to the effect of geochemical interactions on the rock frame were the main aspects in this research. To investigate these factors two CO_2 injection projects were investigated, the Frio project and Otway Stage 2C project (synthetic data).

For the Frio project the applicability of Gassmann's poroelasticity theory was investigated for quantitative interpretation of field time-lapse VSP and crosswell seismic. At first, to calibrate the rock physics model time-lapse measurements were extracted from time-lapse VSP data. The measured traveltime delay is found to be caused by a velocity reduction of 750±150 m/s in about 8.8 m interval at the injection well. Two other independent measurements, that is first arrivals amplitude changes and reflection amplitudes, as well as the 2.5D elastic, finite difference modelling results, supported the estimates of the magnitude of this velocity change at the injection well. The geophysical attribute from the time-lapse VSP provided a high accuracy measurement with redundancy that confirms the velocity changes caused by the CO_2. The effect of the seismic waves resolution on the quantitative analysis was also investigated in the modelling and was found to affect largely the reflection amplitude, while it had a negligible effect on the first arrivals (amplitudes and transit time). An interesting observation with the Frio VSP data is that the reflection response change is possibly caused by the geometry of the CO_2 plume, being at or below the tuning thickness and with a lateral extent comparable to the Fresnel zone. This allowed the estimate of approximate plume geometry in the subsurface for the Frio case study. Modelling is found to be an essential part to reveal resolution and reflector geometry related effects on the seismic waves response. Also, it assisted in the estimate of elastic seismic parameters such as P-wave and seismic impedance.

The site-specific rock physics model for the Frio "C" sandstone injection interval was created using petrophysical and baseline sonic logs and was constrained by the VSP measurements. Using Gassmann-Wood (uniform saturation) the maximum velocity reduction that could be obtained was 500 m/s for any CO_2 saturation. This is

much less than the 750 m/s velocity reduction observed in the field data. Thus, it became apparent that the rock physics model underestimates the velocity change obtained from field observations at the injection well. Given that input parameters for the Gassmann's equation were well constrained, we investigated Gassmann's assumptions as possible causes for this discrepancy. The assumptions of homogeneity and isotropy were anticipated to be satisfactory for the Frio "C" and even if present they are not expected to be responsible of such a large discrepancy in this case. Moreover, the assumption of fluids homogeneity was already assumed in the fluid substitution by using Gassmann-Wood and assuming a heterogeneous fluids distribution was only bound to increase the discrepancy. Thus, after investigation of several possible causes the most probable cause was formation frame weakening after CO_2 injection, which violates the assumption that the rock frame properties do not change with fluids replacement. To be able to investigate such a claim, we integrated the crosswell data which have a higher resolution results and offer the ability to use the change in both V_P and V_S, compared to the time-lapse VSP data.

The crosswell data offered an opportunity to investigate a topic of current interest in CO_2 injections projects, that is CO_2-fluid-rock interactions effect on the rock frame elastic properties. It has been demonstrated that rock frame weakening we suspected at the Frio site is supported by many field observations and other CO_2-rock-interactions experimental studies. Possible mechanisms responsible of frame weakening due to injecting a reactive fluid such as CO_2 were given which could occur individually or in combination. All given mechanisms are mostly related to rock frame cement, with dissolution of grain contact cement as the major cause suspected at the Frio CO_2 injection project. The ability to explain these changes required the use of models that can describe the rock microstructure and developing a workflow to estimate these changes quantitatively. The constant-cement model predicted that the grain contact cement present in the formation is about 0.1% before CO_2 injection. Using S-waves velocity changes, a reduction of 0.04% in grain contact cement was inferred in the reservoir area of interest after CO_2 injection on average. The results were consistent with frame weakening resulting from minute changes in the contact-cement percent that cause a large reduction in the frame elastic moduli as predicted by the cementation theory of high porosity sandstone. This small decrease in cement percent is furthermore consistent with geochemical field data acquired during CO_2 injection which shows that even though some mineral dissolution was present, it was not volumetrically significant.

To sum-up, integrating logs, VSP and crosswell with a rock physics model that is based on rock microstructure diagnostic which conforms with Gassmann's derived dry-frame properties we were able to explain the discrepancy by introducing a time- and space- varying rock frame weakening in the form of contact cement change. The rock frame weakening map between the wells derived using crosswell S-wave velocity change and the constant-cement model shows that the Gassmann's consistent model fails at the injection well only. However, at the observation well, the model does not contradict with the data and predicted the velocity change due to saturation using a patchy saturation model. The VSR at both the wells predicts the same patch size for the crosswell and VSP if only the frame properties were changed based on the magnitude of the rock frame weakening in the form of contact cement percent change. Although the uncertainty was difficult to estimate, the results obtained conform with the field data for both the crosswell and VSP. A broad look at the results of the Frio CO_2 injection project shows the power of data integration in time-lapse seismic monitoring for CO_2 sequestration. Adaptation of existing theoretical models guided by recent geochemical experimental results was a key to explaining observed time-lapse responses.

The Frio project case study illustrated that time-lapse VSP can be used to obtain quantitative measurement of velocity change upon CO_2 injection and constrain the velocity-saturation relation. The learnings from the field measurement analysis, rock physics modelling and seismic modelling studies showed a potential to apply to Australia's Otway 2C project. The two projects have many similarities such as depth and the injection into a brine aquifer. The synthetic VSP data from the Otway 2C showed that it is possible to obtain quantitative measurement of velocity changes caused by the injected gas if the receivers are deployed in CRC-2 well using traveltime delays. However, first arrivals amplitudes were not usable due to the large uncertainty involved compared to the expected signal as predicted by the rock physics model. On the other hand, if the receivers are deployed only in CRC-1 well, then measurements from the first arrivals are only present for far-offset shots, and are difficult to constrain for quantitative interpretation. Thus, in such case, only reflection amplitudes for the CRC-1 far offset shots could be used for analysis. The sensitivity study shows that for the rock physics model used the seismic wave velocity change that is of the order of 200 m/s, that is about 0.4 ms for a 20 m thick plume. Such a small transit time change

would require high signal-to-noise ratio data to be performed in the real data. Comparison between the Frio project and Otway 2C showed that both the survey geometry and magnitude of the heterogeneity (e.g., P-wave velocity changes, thickness of the gas plume) in the subsurface control our ability to obtain quantitative geophysical data for rock physics modelling.

The key objectives of this thesis were using time-lapse borehole seismic data for CO_2 monitoring in the subsurface and constraining rock physics models for quantitative estimation of CO_2 saturation. We utilized the concept the Fresnel zone in CO_2 monitoring to constrain the geometry of the CO_2 plume of the Frio project. We have shown that it is possible to use time-lapse VSP and crosswell seismic to investigate the applicability of rock physics models for field scale studies. Gassmann's poroelasticity theory is found to be sufficient if rock frame changes are not induced. Moreover, a methodology to quantitatively estimate possible rock frame changes has been developed and performed on the Frio data. Finally, a prediction of the time-lapse signal for offset VSP data and the ability to constrain the rock physics model was accomplished for the Otway 2C project.

The methodologies developed in this research for utilizing borehole seismic data could be employed in current and future CO_2 sequestration projects to better constrain the velocity-saturation relation and thus allows better quantitative interpretation of time-lapse seismic data.

References

Adam, L., J. MacFarlane, K. v. Wijk*, J. Shragge, and K. Higgs. 2015, Monitoring the effects of CO_2 injection on carbonate-cemented sandstones with elastic waves. In 2015 SEG Annual Meeting.

Ajo-Franklin, J. B., B. J. Minsley, and T. M. Daley. 2007, Applying compactness constraints to differential traveltime tomography. Geophysics, **72**, no. 4,R67-R75. doi: 10.1190/1.2742496.

Ajo-Franklin, J. B., J. Peterson, J. Doetsch, and T. M. Daley. 2013, High-resolution characterization of a CO_2 plume using crosswell seismic tomography: Cranfield, MS, USA. International Journal of Greenhouse Gas Control, **18**,497-509. doi: 10.1016/j.ijggc.2012.12.018.

Aki, K., and P. G. Richards. 1980, Quantitative seismology. San Francisco.

Al Hosni, M., E. Caspari, R. Pevzner, T. M. Daley, and B. Gurevich. 2015, Using time-lapse VSP data to constrain velocity-saturation relations. ASEG Extended Abstracts, **2015**, no. 1,1-4.

Al Hosni, M., E. Caspari, R. Pevzner, T. M. Daley, and B. Gurevich. 2016, Using time-lapse VSP data to constrain velocity-saturation relations: the Frio brine pilot CO_2 injection. Geophysical prospecting, **(Accepted)**.

Al Hosni, M., B. Gurevich, and T. M. Daley. 2015, Effect of CO_2 on bulk and shear moduli of rocks: Frio crosswell case study. In 3rd International Workshop on Rock Physics. Perth, Western Australia.

Al Hosni, M., B. Gurevich, S. Vialle, and T. M. Daley. 2015, Effect of CO_2 on Rock Properties: Frio Crosswell Case Study. In Third EAGE Workshop on Rock Physics. Istanbul: EAGE.

Arts, R., O. Eiken, A. Chadwick, P. Zweigel, L. van der Meer, and B. Zinszner. 2004, Monitoring of CO_2 injected at Sleipner using time-lapse seismic data. Energy, **29**, no. 9-10,1383-1392. doi: 10.1016/j.energy.2004.03.072.

Avseth, P., and R. Bachrach. 2005, Seismic properties of unconsolidated sands: Tangential stiffness, Vp/Vs ratios and diagenesis. In SEG Expanded Abstract.

Avseth, P., J. Dvorkin, G. Mavko, and J. Rykkje. 2000, Rock physics diagnostic of north sea sands: Link between microstructure and seismic properties. Geophysical Research Letters, **27**, no. 17,2761-2764. doi: 10.1029/1999GL008468.

Avseth, P., T. Mukerji, and G. Mavko. 2010, Quantitative seismic interpretation : applying rock physics tools to reduce interpretation risk. Paperback ed: Cambridge University Press.

Avseth, P., and N. Skji. 2011, Rock physics modeling of static and dynamic reservoir properties—a heuristic approach for cemented sandstone reservoirs. The Leading Edge, **30**, no. 1,90-96. doi: doi:10.1190/1.3535437.

Azuma, H., C. Konishi, and Z. Xue. 2013, Introduction and application of the modified patchy saturation for evaluating CO_2 saturation by seismic velocity. Energy Procedia, **37**,4024-4032.

Bachrach, R., J. Dvorkin, and A. Nur. 2000, Seismic velocities and Poisson's ratio of shallow unconsolidated sands. Geophysics, **65**, no. 2,559-564. doi: 10.1190/1.1444751.

Bachu, S., and J. Adams. 2003, Sequestration of CO_2 in geological media in response to climate change: capacity of deep saline aquifers to sequester CO_2 in solution. Energy Conversion and Management, **44**, no. 20,3151-3175.

Bachu, S., W. Gunter, and E. Perkins. 1994, Aquifer disposal of CO_2: Hydrodynamic and mineral trapping. Energy Conversion and Management, **35**, no. 4,269-279.

Balch, A., M. Lee, J. Miller, and R. T. Ryder. 1982, The use of vertical seismic profiles in seismic investigations of the earth. Geophysics, **47**, no. 6,906-918.

Batzle, M., and Z. J. Wang. 1992, Seismic Properties of Pore Fluids. Geophysics, **57**, no. 11,1396-1408. doi: Doi 10.1190/1.1443207.

Bednar, J., and T. Watt. 1984, Alpha-trimmed means and their relationship to median filters. Acoustics, Speech and Signal Processing, IEEE Transactions on, **32**, no. 1,145-153.

Bemer, E., and J. Lombard. 2010, From Injectivity to Integrity Studies of CO2 Geological Storage-Chemical Alteration Effects on Carbonates Petrophysical and Geomechanical Properties. Oil & Gas Science and Technology–Revue de l'Institut Français du Pétrole, **65**, no. 3,445-459.

Benson, S. M., and D. R. Cole. 2008, CO_2 Sequestration in Deep Sedimentary Formations. Elements, **4**, no. 5,325-331.

Berryman, J. G. 1999, Origin of Gassmann's equations. Geophysics, **64**, no. 5,1627-1629.

Bildstein, O., C. Kervévan, V. Lagneau, P. Delaplace, A. Crédoz, P. Audigane, E. Perfetti, N. Jacquemet, and M. Jullien. 2010, Integrative modeling of caprock

integrity in the context of CO2 storage: evolution of transport and geochemical properties and impact on performance and safety assessment. Oil & Gas Science and Technology–Revue de l'Institut Français du Pétrole, **65**, no. 3,485-502.

Biot, M. A. 1956, Theory of propagation of elastic waves in a fluid-saturated porous solid. I. Low-frequency range. The Journal of the Acoustical Society of America, **28**, no. 2,168. doi: 10.1121/1.1908239.

Biot, M. A. 1962, Mechanics of deformation and acoustic propagation in porous media. Journal of applied physics, **33**, no. 4,1482.

Bohlen, T. 2002, Parallel 3-D viscoelastic finite difference seismic modelling. Computers & Geosciences, **28**, no. 8,887-899.

Bohlen, T., D. De Nil, D. Kohn, and S. Jetschny. 2015, SOFI 3D: seismic modelling with finite differences 3D - acoustic and viscoelastic version.

Bregman, N., R. Bailey, and C. Chapman. 1989, Crosshole seismic tomography. Geophysics, **54**, no. 2,200-215.

Brown, R. J., and J. Korringa. 1975, On the dependence of the elastic properties of a porous rock on the compressibility of the pore fluid. Geophysics, **40**, no. 4,608-616.

Cairns, G., H. Jakubowicz, L. Lonergan, and A. Muggeridge. 2010, Issues regarding the use of time-lapse seismic surveys to monitor CO_2 sequestration. In 2010 SEG Annual Meeting.

Canal, J., J. Delgado-Martín, V. Barrientos, R. Juncosa, B. Rodríguez-Cedrún, and I. Falcón-Suarez. 2014, Effect of supercritical CO_2 on the Corvio sandstone in a flow-thru triaxial experiment.

Carcione, J., H. Helle, and N. Pham. 2003, White's model for wave propagation in partially saturated rocks: Comparison with poroelastic numerical experiments. GEOPHYSICS, **68**, no. 4,1389-1398. doi: doi:10.1190/1.1598132.

Carcione, J. M., G. C. Herman, and A. Ten Kroode. 2002, Seismic modeling. Geophysics, **67**, no. 4,1304-1325.

Caspari, E. 2013, Effect of scale and saturation on effective properties of porous rocks for seismic monitoring of CO_2 sequestration. Ph.D., Curtin University.

Caspari, E., T. M. Müller, and B. Gurevich. 2011, Time-lapse sonic logs reveal patchy CO2 saturation in-situ. Geophysical Research Letters, **38**, no. 13,L13301. doi: 10.1029/2011GL046959.

Caspari, E., R. Pevzner, B. Gurevich, T. Dance, J. Ennis-King, Y. Cinar, and M. Lebedev. 2015, Feasibility of CO_2 plume detection using 4D seismic: CO2CRC Otway Project case study—Part 1: Rock-physics modeling. Geophysics, **80**, no. 4,B95-B104.

Chadwick, A., G. Williams, N. Delepine, V. Clochard, K. Labat, S. Sturton, M. Buddensiek, M. Dillen, M. Nickel, A. Lima, R. Arts, F. Neele, and G. Rossi. 2010, Quantitative analysis of time-lapse seismic monitoring data at the Sleipner storage operation. The Leading Edge, **29**, no. 2,170-177. doi: doi:10.1190/1.3304820.

Chen, J.-Y., Z.-J. Zhang, G.-J. Wang, L.-G. Han, and Y.-G. Wu. 2000, CDP mapping and image reconstruction by using offset VSP data. Acta Seismologica Sinica, **13**, no. 1,98-104. doi: 10.1007/s11589-000-0087-7.

Chen, Y., Y. Li, H. Zhao, X. Gao, and Y. Qiu. 2013, Study of First Arrival Time of VSP Data, Near Surface Geophysics Asia Pacific Conference, Beijing, China 17-19 July 2013. 97-101.

Cheng, A., L. Huang, and J. Rutledge. 2010, Time-lapse VSP data processing for monitoring injection. The Leading Edge, **29**, no. 2,196-199. doi: doi:10.1190/1.3304824.

CO2CRC. 2015. The Cooperative Research Centre for Greenhouse Gas Technologies 2015 [cited 15 January 2015]. Available from http://www.co2crc.com.au/otway/operations.html.

CO2CRC. 2016. The Cooperative Research Centre for Greenhouse Gas Technologies 2016 [cited 15 January 2016]. Available from http://www.co2crc.com.au/.

Cook, P. 2014, Geologically storing carbon: learning from the Otway Project experience: CSIRO PUBLISHING.

Costa, J., F. S. Neto, and A. Novais. 2006, 2.5 D Elastic finite-difference modeling. In 68th EAGE Conference & Exhibition: EAGE.

Daley, T., L. Myer, and E. Majer. 2005, Acquisition of time-lapse, 6-component, P- and S-wave, crosswell seismic survey with orbital vibrator and of time-lapse VSP for CO_2 injection monitoring. In 2005 SEG Annual Meeting.

Daley, T. M., and D. Cox. 2001, Orbital vibrator seismic source for simultaneous P- and S-wave crosswell acquisition. Geophysics, **66**, no. 5,1471-1480.

Daley, T. M., L. Myer, J. E. Peterson, E. L. Majer, and G. M. Hoversten. 2008, Time-lapse crosswell seismic and VSP monitoring of injected CO_2 in a brine aquifer.

Environmental Geology, **54**, no. 8,1657-1665. doi: 10.1007/s00254-007-0943-z.

Delshad, M., X. Kong, R. Tavakoli, S. A. Hosseini, and M. F. Wheeler. 2013, Modeling and simulation of carbon sequestration at Cranfield incorporating new physical models. International Journal of Greenhouse Gas Control, no. 0. doi: http://dx.doi.org/10.1016/j.ijggc.2013.03.019.

Dillon, P., and V. Collyer. 1985, On timing the VSP first arrival. Geophysical prospecting, **33**, no. 8,1174-1194.

Dillon, P., and R. Thomson. 1984, Offset Source Vsp Surveys and Their Image RECONSTRUCTION*. Geophysical Prospecting, **32**, no. 5,790-811.

Doughty, C., B. M. Freifeld, and R. C. Trautz. 2008, Site characterization for CO_2 geologic storage and vice versa: the Frio brine pilot, Texas, USA as a case study. Environmental Geology, **54**, no. 8,1635-1656.

Dutta, N., and H. Odé. 1979, Attenuation and dispersion of compressional waves in fluid-filled porous rocks with partial gas saturation (White model)-Part I: Biot theory. Geophysics, **44**, no. 11,1777-1788.

Dvorkin, J., G. Mavko, and B. Gurevich. 2007, Fluid substitution in shaley sediment using effective porosity. Geophysics, **72**, no. 3,O1-O8. doi: 10.1190/1.2565256.

Dvorkin, J., G. Mavko, and A. Nur. 1991, The effect of cementation on the elastic properties of granular material. Mechanics of Materials, **12**, no. 3,207-217.

Dvorkin, J., and A. Nur. 1996, Elasticity of high-porosity sandstones: Theory for two North Sea data sets. Geophysics, **61**, no. 5,1363-1370.

Dvorkin, J., and A. Nur. 2002, Chapter 4: Critical-Porosity Models. AAPG Memoir 76,33-41.

Dvorkin, J., A. Nur, and H. Yin. 1994, Effective properties of cemented granular materials. Mechanics of materials, **18**, no. 4,351-366.

Eberhart-Phillips, D., D.-H. Han, and M. D. Zoback. 1989, Empirical relationships among seismic velocity, effective pressure, porosity, and clay content in sandstone. Geophysics, **54**, no. 1,82-89.

Engelmark, F. 2002, Error propagation in Gassmann modeling for 4D feasibility studies. The Leading Edge, **21**, no. 10,984-987.

Espinoza, D. N., S. H. Kim, and J. C. Santamarina. 2011, CO2 geological storage — Geotechnical implications. KSCE Journal of Civil Engineering, **15**, no. 4,707-719. doi: 10.1007/s12205-011-0011-9.

Fleury, M., J. Pironon, Y.-M. Le Nindre, O. Bildstein, P. Berne, V. Lagneau, D. Broseta, T. Pichery, S. Fillacier, and M. Lescanne. 2010, Evaluating sealing efficiency of caprocks for CO2 storage: An overview of the geocarbone-integrity program and results. Oil & Gas Science and Technology–Revue de l'Institut Français du Pétrole, **65**, no. 3,435-444.

Freifeld, B. M., T. M. Daley, S. D. Hovorka, J. Henninges, J. Underschultz, and S. Sharma. 2009, Recent advances in well-based monitoring of CO_2 sequestration. Energy Procedia, **1**, no. 1,2277-2284.

Galloway, W. E., D. K. Hobday, and K. Magara. 1982, Frio formation of the Texas Gulf Coast Basin: depositional systems, structural framework, and hydrocarbon origin, migration, distribution, and exploration potential: Bureau of Economic Geology, University of Texas at Austin.

Gassmann, F. 1951, Elastic waves through a packing of spheres. Geophysics, **16**, no. 4,673-685.

Gaus, I., M. Azaroual, and I. Czernichowski-Lauriol. 2005, Reactive transport modelling of the impact of CO 2 injection on the clayey cap rock at Sleipner (North Sea). Chemical Geology, **217**, no. 3,319-337.

Gershenzon, N. I., M. R. Soltanian, R. W. Ritzi Jr, and D. F. Dominic. 2014, Influence of small scale heterogeneity on CO2 trapping processes in deep saline aquifers. arXiv preprint arXiv:1407.0369.

Ghomian, Y., G. A. Pope, and K. Sepehrnoori. 2008, Reservoir simulation of CO_2 sequestration pilot in Frio brine formation, USA Gulf Coast. Energy, **33**, no. 7,1055-1067.

Glubokovskikh, S., R. Pevzner, T. Dance, E. Caspari, D. Popik, V. Shulakova, and B. Gurevich. 2016, Seismic monitoring of CO 2 geosequestration: CO2CRC Otway case study using full 4D FDTD approach. International Journal of Greenhouse Gas Control, **49**,201-216.

Greenberg, M., and J. Castagna. 1992, SHEAR-WAVE VELOCITY ESTIMATION IN POROUS ROCKS: THEORETICAL FORMULATION, PRELIMINARY VERIFICATION AND APPLICATIONS1. Geophysical prospecting, **40**, no. 2,195-209.

Grochau, M., and B. Gurevich. 2009, Testing Gassmann fluid substitution: sonic logs versus ultrasonic core measurements. Geophysical Prospecting, **57**, no. 1,75-79. doi: 10.1111/j.1365-2478.2008.00726.x.

Guoping, L. 1994, Crosswell Seismic Processing: Automatic Velocity Analysis, Filtering, and Reflection Imaging, THE UNIVERSITY OF CALGARY.

Gurevich , B., R. Pevzner, M. Urosevic, A. Kepic, V. Shulakova, and E. Caspari. 2014, 2D and 3D seismic investigations for Stage 1 and 2C in Peter Cook, ed., Geologically storing carbon: learning from the Otway Project experience: CSIRO PUBLISHING. 155-196.

Han, De-hua, and M. L. Batzle. 2004, Gassmann's equation and fluid-saturation effects on seismic velocities. Geophysics, **69**, no. 2,398-405.

Hangx, S., C. Spiers, and C. Peach. 2010, Creep of simulated reservoir sands and coupled chemical-mechanical effects of CO_2 injection. Journal of Geophysical Research: Solid Earth (1978–2012), **115**, no. B9.

Hangx, S., A. van der Linden, F. Marcelis, and A. Bauer. 2013, The effect of CO 2 on the mechanical properties of the captain sandstone: geological storage of CO 2 at the Goldeneye field (UK). International Journal of Greenhouse Gas Control, **19**,609-619.

Hardage, B. A. 1985, Vertical seismic profiling. Vol. 14A: Pergamon Press.

Hardage, B. A. 1992, Crosswell seismology & reverse VSP. Vol. 1: Geophysical Press.

Hashin, Z., and S. Shtrikman. 1963, A variational approach to the theory of the elastic behaviour of multiphase materials. Journal of the Mechanics and Physics of Solids, **11**, no. 2,127-140.

Holtz, M. 2002, Residual gas saturation to aquifer influx: A calculation method for 3-D computer reservoir model construction. Paper read at SPE Gas Technology Symposium.

Hosseini, S. A., H. Lashgari, J. W. Choi, J.-P. Nicot, J. Lu, and S. D. Hovorka. 2012, Static and dynamic reservoir modeling for geological CO2 sequestration at Cranfield, Mississippi, U.S.A. International Journal of Greenhouse Gas Control, no. 0. doi: http://dx.doi.org/10.1016/j.ijggc.2012.11.009.

Hottman, B., B. Cornish, M. Curtis, and N. Maerefat. 2000, A risk analysis spreadsheet for both time-lapse VSP and 4D seismic reservoir monitoring.

Hovorka, S. 2009, Frio brine pilot: The first US sequestration test. Southwest Hydrology, **8**, no. 5,26-31.

Hovorka, S., C. Doughty, P. Knox, C. Green, K. Pruess, and S. Benson. 2001, Evaluation of brine-bearing sands of the Frio formation, upper Texas gulf coast for geological sequestration of CO2. Paper read at First National Conference on Carbon Sequestration.

Hovorka, S. D., S. M. Benson, C. Doughty, B. M. Freifeld, S. Sakurai, T. M. Daley, Y. K. Kharaka, M. H. Holtz, R. C. Trautz, and H. S. Nance. 2006, Measuring permanence of CO_2 storage in saline formations: the Frio experiment. Environmental Geosciences, **13**, no. 2,105-121.

Hovorka, S. D., and K. Cohen. 2006, Update on the Frio Brine Pilot: 15 months after injection. Paper read at International Workshop on CO2 Geological Storage, at Tokyo.

Hovorka, S. D., C. Doughty, and M. Holtz. 2004, Testing efficiency of storage in the subsurface: frio brine pilot experiment.

Hovorka, S. D., and P. R. Knox. 2003, Frio brine sequestration pilot in the Texas Gulf Coast. Greenhouse Gas Control Technologies, **1**,583-586.

Hovorka, S. D., S. Sakurai, Y. K. Kharaka, H. S. Nance, C. Doughty, S. M. Benson, B. M. Freifeld, R. C. Trautz, T. Phelps, and T. M. Daley. 2006, Monitoring CO_2 storage in brine formations: lessons learned from the Frio field test one year post injection. Gulf coast carbon center publication library, Bookshelf.

Ilgen, A. G., and R. T. Cygan. 2016, Mineral dissolution and precipitation during CO_2 injection at the Frio-I Brine Pilot: Geochemical modeling and uncertainty analysis. International Journal of Greenhouse Gas Control, **44**,166-174.

Ivanova, A., A. Kashubin, N. Juhojuntti, J. Kummerow, J. Henninges, C. Juhlin, S. Lüth, and M. Ivandic. 2012, Monitoring and volumetric estimation of injected CO_2 using 4D seismic, petrophysical data, core measurements and well logging: a case study at Ketzin, Germany. Geophysical Prospecting, **60**, no. 5,957-973. doi: 10.1111/j.1365-2478.2012.01045.x.

Ivansson, S. 1986, Seismic borehole tomography—theory and computational methods. Proceedings of the IEEE, **74**, no. 2,328-338.

JafarGandomi, A., and A. Curtis. 2012, Assessing the monitorability of CO2 saturation in subsurface saline aquifers. International Journal of Greenhouse Gas Control, **7**, no. 0,244-260. doi: http://dx.doi.org/10.1016/j.ijggc.2011.10.015.

Jalal Khazanehdari, N. D., and Jorg Herwanger. 2010, The next generation of rock physics models.

Jenkins, C. R., P. J. Cook, J. Ennis-King, J. Undershultz, C. Boreham, T. Dance, P. de Caritat, D. M. Etheridge, B. M. Freifeld, and A. Hortle. 2012, Safe storage and effective monitoring of CO2 in depleted gas fields. Proceedings of the National Academy of Sciences, **109**, no. 2,E35-E41.

Johansen, T., E. Jensen, G. Mavko, and J. Dvorkin. 2013, Inverse rock physics modeling for reservoir quality prediction. GEOPHYSICS, **78**, no. 2,M1-M18. doi: doi:10.1190/geo2012-0215.1.

Johnson, D. L. 2001, Theory of frequency dependent acoustics in patchy-saturated porous media. The Journal of the Acoustical Society of America, **110**,682.

Johnston, D. H. 2013, Practical applications of time-lapse seismic data. Distinguished Instructor Series, Society of Exploration Geophysicists.

Joy, C., T. Vanorio, and M. K. Sen. 2011, Differentiating chemical effects and pressure effects on the elastic properties of the lower Tuscaloosa sandstone in Cranfield, Mississippi by injecting carbon dioxide rich brine. Paper read at 2011 SEG Annual Meeting.

Kampman, N., M. Bickle, M. Wigley, and B. Dubacq. 2014, Fluid flow and CO_2–fluid–mineral interactions during CO_2-storage in sedimentary basins. Chemical Geology, **369**,22-50.

Kazemeini, S. H., C. Juhlin, and S. Fomel. 2010, Monitoring CO_2 response on surface seismic data; a rock physics and seismic modeling feasibility study at the CO_2 sequestration site, Ketzin, Germany. Journal of Applied Geophysics, **71**, no. 4,109-124. doi: http://dx.doi.org/10.1016/j.jappgeo.2010.05.004.

Kharaka, Y., D. Cole, S. Hovorka, W. Gunter, K. Knauss, and B. Freifeld. 2006, Gas-water-rock interactions in Frio Formation following CO_2 injection: Implications for the storage of greenhouse gases in sedimentary basins. Geology, **34**, no. 7,577-580.

Kharaka, Y. K., J. J. Thordsen, S. D. Hovorka, H. Seay Nance, D. R. Cole, T. J. Phelps, and K. G. Knauss. 2009, Potential environmental issues of CO_2 storage in deep saline aquifers: Geochemical results from the Frio-I Brine Pilot test, Texas, USA. Applied Geochemistry, **24**, no. 6,1106-1112. doi: http://dx.doi.org/10.1016/j.apgeochem.2009.02.010.

Kikuta, K., S. Hongo, D. Tanase, and T. Ohsumi. 2005, Field test of CO2 injection in Nagaoka, Japan. Paper read at Proceedings of seventh international conference on greenhouse gas control technologies.

Klein, E., M. De Lucia, T. Kempka, and M. Kühn. 2013, Evaluation of long-term mineral trapping at the Ketzin pilot site for CO2 storage: An integrative approach using geochemical modelling and reservoir simulation. International Journal of Greenhouse Gas Control, no. 0. doi: http://dx.doi.org/10.1016/j.ijggc.2013.05.014.

Knapp, R. 1991, Fresnel zones in the light of broadband data. Geophysics, **56**, no. 3,354-359.

Knight, R., and R. Nolen-Hoeksema. 1990, A laboratory study of the dependence of elastic wave velocities on pore scale fluid distribution. Geophysical Research Letters, **17**, no. 10,1529-1532. doi: 10.1029/GL017i010p01529.

Kommedal, J., and B. Tjøstheim. 1989, A Study of Different Methods of Wavefield Separation for Application to VSP Data. Geophysical prospecting, **37**, no. 2,117-142.

Konishi, C., H. Azuma, D. Nobuoka, Z. Xue, and J. Watanabe. 2008, Estimation of CO_2 saturation considering patchy saturation at Nagaoka. Paper read at 70th EAGE Conference & Exhibition.

Kosloff, D., and D. Kessler. 1990, Seismic numerical modeling. Oceanographic and Geophysical Tomography, Houches Summer Session, Elsevier Science, Les Houches, France,249-312.

Kostyukevych, A., N. Marmalevskyi, Y. Roganov, and V. Tulchinsky. 2008, Anisotropic 2.5 D-3C finite-difference modeling. In 70th EAGE Conference & Exhibition.

Kragh, E., and P. Christie. 2002, Seismic repeatability, normalized rms, and predictability. The Leading Edge, **21**, no. 7,640-647.

Kramer, D. 1996, Multicomponent multioffset VSP processing. Paper read at SEG expanded abstract, Houston meeting, BG2.

Le Guen, Y., F. Renard, R. Hellmann, E. Brosse, M. Collombet, D. Tisserand, and J. P. Gratier. 2007, Enhanced deformation of limestone and sandstone in the presence of high fluids. Journal of Geophysical Research: Solid Earth (1978–2012), **112**, no. B5.

Lebedev, M., M. E. Wilson, and V. Mikhaltsevitch. 2014, An experimental study of solid matrix weakening in water-saturated Savonnières limestone. Geophysical Prospecting, **62**, no. 6,1253-1265.

Lumley, D. 2010, 4D seismic monitoring of CO_2 sequestration. The Leading Edge, **29**, no. 2,150-155. doi: 10.1190/1.3304817.

Lumley, D., D. Adams, R. Wright, D. Markus, and S. Cole. 2008, Seismic monitoring of CO_2 geo-sequestration: realistic capabilities and limitations, SEG Technical Program Expanded Abstracts 2008. 2841-2845.

Lumley, D. E. 2001, Time-lapse seismic reservoir monitoring. Geophysics, **66**, no. 1,50-53.

Luquot, L., M. Andreani, P. Gouze, and P. Camps. 2012, CO_2 percolation experiment through chlorite/zeolite-rich sandstone (Pretty Hill Formation–Otway Basin–Australia). Chemical geology, **294**,75-88.

Lüth, S., P. Bergmann, C. Cosma, N. Enescu, R. Giese, J. Götz, A. Ivanova, C. Juhlin, A. Kashubin, C. Yang, and F. Zhang. 2011, Time-lapse seismic surface and down-hole measurements for monitoring CO_2 storage in the CO_2SINK project (Ketzin, Germany). Energy Procedia, **4**, no. 0,3435-3442. doi: 10.1016/j.egypro.2011.02.268.

Makse, H. A., N. Gland, D. L. Johnson, and L. Schwartz. 2004, Granular packings: Nonlinear elasticity, sound propagation, and collective relaxation dynamics. Physical Review E, **70**, no. 6,061302.

Makse, H. A., N. Gland, D. L. Johnson, and L. M. Schwartz. 1999, Why effective medium theory fails in granular materials. Physical Review Letters, **83**, no. 24,5070.

Marbler, H., K. P. Erickson, M. Schmidt, C. Lempp, and H. Pöllmann. 2013, Geomechanical and geochemical effects on sandstones caused by the reaction with supercritical CO_2: an experimental approach to in situ conditions in deep geological reservoirs. Environmental earth sciences, **69**, no. 6,1981-1998.

Marini, L. 2006, Geological sequestration of carbon dioxide: thermodynamics, kinetics, and reaction path modeling. Vol. 11: Elsevier.

Masson, Y., and S. Pride. 2011, Seismic attenuation due to patchy saturation. Journal of Geophysical Research: Solid Earth (1978–2012), **116**, no. B3.

Mavko, G., T. Mukerji, and J. Dvorkin. 2009, The Rock Physics Handbook : Tools for Seismic Analysis of Porous Media. 2 ed: Cambridge University Press.

Maxim Lebedev, O. B., Vassili Mikhaltsevitch, Marina Pervukhina, Boris Gurevich 2013, Laboratory measurements of ultrasonic velocities in CO_2 saturated brines. Energy Procedia.

McGuire, K. A. 2009, CO_2 injection and reservoir characterization : an integrated petrographic and geochemical study of the Frio Formation, Texas. M.S. dissertation, Ball State University.

Michael, K., A. Golab, V. Shulakova, J. Ennis-King, G. Allinson, S. Sharma, and T. Aiken. 2010, Geological storage of CO_2 in saline aquifers—A review of the experience from existing storage operations. International Journal of Greenhouse Gas Control, **4**, no. 4,659-667.

Molins, S., D. Trebotich, C. I. Steefel, and C. Shen. 2012, An investigation of the effect of pore scale flow on average geochemical reaction rates using direct numerical simulation. Water Resources Research, **48**, no. 3.

Müller, T. M., and B. Gurevich. 2004, One-dimensional random patchy saturation model for velocity and attenuation in porous rocks. Geophysics, **69**, no. 5,1166-1172. doi: 10.1190/1.1801934.

Murphy, W. F. 1982, Effects of microstructure and pore fluids on the acoustic properties of granular sedimentary materials: Stanford University.

Nazari, S. 2014, Assessing Uncertainty and Repeatability in Time-Lapse VSP Monitoring of CO_2 Injection in a Brine Aquifer, Frio Formation, Texas (A Case Study).

Nguyen, M., E. Bemer, and L. Dormieux. 2011, Micromechanical modeling of carbonate geomechanical properties evolution during acid gas injection. In 45th US Rock Mechanics/Geomechanics Symposium: American Rock Mechanics Association.

Nolen-Hoeksema, R. C. 2000, Modulus-porosity relations, Gassmann's equations, and the low-frequency elastic-wave response to fluids. Geophysics, **65**, no. 5,1355-1363.

Nur, A., G. Mavko, J. Dvorkin, and D. Galmudi. 1998, Critical porosity: A key to relating physical properties to porosity in rocks. The Leading Edge, **17**, no. 3,357-362.

O'Brien, J., F. Kilbride, and F. Lim. 2004, Time-lapse VSP reservoir monitoring. The Leading Edge, **23**, no. 11,1178-1184. doi: doi:10.1190/1.1825943.

Onishi, K., T. Ueyama, T. Matsuoka, D. Nobuoka, H. Saito, H. Azuma, and Z. Xue. 2009, Application of crosswell seismic tomography using difference analysis with data normalization to monitor CO_2 flooding in an aquifer. International

Journal of Greenhouse Gas Control, **3**, no. 3,311-321. doi: http://dx.doi.org/10.1016/j.ijggc.2008.08.003.

Peterson, J. E., B. N. Paulsson, and T. V. McEvilly. 1985, Applications of algebraic reconstruction techniques to crosshole seismic data. Geophysics, **50**, no. 10,1566-1580.

Pevzner, R., E. Caspari, B. Gurevich, T. Dance, and Y. Cinar. 2015, Feasibility of CO_2 plume detection using 4D seismic: CO2CRC Otway Project case study—Part 2: Detectability analysis. Geophysics, **80**, no. 4,B105-B114.

Pevzner, R., M. Urosevic, E. Caspari, R. J. Galvin, M. Madadi, T. Dance, V. Shulakova, B. Gurevich, V. Tcheverda, and Y. Cinar. 2013, Feasibility of Time-lapse Seismic Methodology for Monitoring the Injection of Small Quantities of CO2 into a Saline Formation, CO2CRC Otway Project. Energy Procedia, **37**,4336-4343. doi: 10.1016/j.egypro.2013.06.336.

Pevzner, R., M. Urosevic, and B. Gurevich. 2015, Borehole Seismic Monitoring of a Small-scale CO2 Injection-The CO2CRC Otway Project Feasibility Study. Paper read at 77th EAGE Conference and Exhibition 2015.

Pevzner, R., M. Urosevic, and S. Nakanishi. 2010, Applicability of zero-offset and offset VSP for time-lapse monitoring–CO2CRC Otway project case study. Paper read at 72nd EAGE Conference & Exhibition.

Picotti, S., J. M. Carcione, D. Gei, G. Rossi, and J. E. Santos. 2012, Seismic modeling to monitor CO2 geological storage: The Atzbach-Schwanenstadt gas field. Journal of Geophysical Research: Solid Earth, **117**, no. B6,B06103. doi: 10.1029/2011JB008540.

Ross, G. D., A. C. Todd, J. A. Tweedie, and A. G. Will. 1982, The dissolution effects of CO_2-brine systems on the permeability of UK and North Sea calcareous sandstones. In SPE Enhanced Oil Recovery Symposium: Society of Petroleum Engineers.

Saadatpoor, E., S. L. Bryant, and K. Sepehrnoori. 2010, New trapping mechanism in carbon sequestration. Transport in porous media, **82**, no. 1,3-17.

Saito, H., D. Nobuoka, H. Azuma, Z. Xue, and D. Tanase. 2006, Time-lapse crosswell seismic tomography for monitoring injected CO_2 in an onshore aquifer, Nagaoka, Japan. Exploration Geophysics, **37**, no. 1,30-36.

Sakurai, S., T. Ramakrishnan, A. Boyd, N. Mueller, and S. Hovorka. 2006, Monitoring saturation changes for CO_2 sequestration: petrophysical support of the Frio brine pilot experiment. Petrophysics, **47**, no. 6,483-496.

Saul, M., and D. Lumley. 2015, The combined effects of pressure and cementation on 4D seismic data. Geophysics, **80**, no. 2,WA135-WA148.

Schmidt, H., and G. Tango. 1986, Efficient global matrix approach to the computation of synthetic seismograms. Geophysical Journal International, **84**, no. 2,331-359.

Simm, R., M. Bacon, and M. Bacon. 2014, Seismic Amplitude: An Interpreter's Handbook: Cambridge University Press.

Smith, T., C. Sondergeld, and C. Rai. 2003, Gassmann fluid substitutions: A tutorial. GEOPHYSICS, **68**, no. 2,430-440. doi: 10.1190/1.1567211.

Span, R., and W. Wagner. 1996, A new equation of state for carbon dioxide covering the fluid region from the triple-point temperature to 1100 K at pressures up to 800 MPa. Journal of physical and chemical reference data, **25**,1509.

Spetzler, J., and R. Snieder. 2004, The Fresnel volume and transmitted waves. Geophysics, **69**, no. 3,653-663.

Steefel, C. I., and K. Maher. 2009, Fluid-rock interaction: A reactive transport approach. Reviews in mineralogy and geochemistry, **70**, no. 1,485-532.

Stewart, R. R., and S. N. Domenico. 1991, Exploration seismic tomography: Fundamentals. Vol. 3: Society of Exploration Geophysicists.

Sun, S., and J. C. Bancroft. 2002, Amplitude within the Fresnel zone for the zero-offset case. University of Calgary.

Tabakov, A. A., and K. V. Baranov. 2007, Integrated land seismic and VSP survey geometries offer improved imaging solution. First Break, **25**, no. 9.

Technologies', T. 2016, Finite-difference solution of Wave Equation in Tesseral. Tesseral Technologies 20122016]. Available from www.tesseral-geo.com.

The National Institute of Standards and Technology. 2014, Thermophysical Properties of Carbon dioxide. The National Institute of Standards and Technology 2014 [cited 28 December 2014]. Available from http://webbook.nist.gov/cgi/fluid.cgi?ID=C124389&Action=Page.

Toms, J., T. M. Mueller, and B. Gurevich. 2007, Seismic attenuation in porous rocks with random patchy saturation. Geophysical Prospecting, **55**, no. 5,671-678. doi: 10.1111/j.1365-2478.2007.00644.x.

Toms, J., T. Müller, R. Ciz, and B. Gurevich. 2006, Comparative review of theoretical models for elastic wave attenuation and dispersion in partially saturated rocks. Soil Dynamics and Earthquake Engineering, **26**, no. 6,548-565.

Toms, J., T. Müller, and B. Gurevich. 2005, 3D random patchy saturation model for velocity and attenuation in porous rocks, SEG Technical Program Expanded Abstracts 2005: Society of Exploration Geophysicists. 1747-1750.

Vanorio, T., A. Nur, and Y. Ebert. 2011, Rock physics analysis and time-lapse rock imaging of geochemical effects due to the injection of into reservoir rocks. GEOPHYSICS, **76**, no. 5,O23-O33. doi: 10.1190/geo2010-0390.1.

Vialle, S., J. Dvorkin, and G. Mavko. 2013, Implications of pore microgeometry heterogeneity for the movement and chemical reactivity of CO_2 in carbonates. GEOPHYSICS, **78**, no. 5,L69-L86. doi: 10.1190/geo2012-0458.1.

Vialle, S., and T. Vanorio. 2011, Laboratory measurements of elastic properties of carbonate rocks during injection of reactive CO_2-saturated water. Geophysical Research Letters, **38**, no. 1. doi: 10.1029/2010GL045606.

Wellman, T. P., R. B. Grigg, B. J. McPherson, R. K. Svec, and P. C. Lichtner. 2003, Evaluation of CO_2-brine-reservoir rock interaction with laboratory flow tests and reactive transport modeling. In International symposium on oilfield chemistry: Society of Petroleum Engineers.

White, J. 1975, Computed seismic speeds and attenuation in rocks with partial gas saturation. Geophysics, **40**, no. 2,224-232.

Wiggins, W., P. Ng, and A. Manzur. 1986, The relation between the VSP-CDP transformation and VSP migration. Paper read at 1986 SEG Annual Meeting.

Wildenborg, T., A. Chadwick, J.-P. Deflandre, O. Eiken, A. Mathieson, R. Metcalfe, C. S. Hattenberger, and J. Wollenweber. 2013, Key Messages from Active CO_2 Storage Sites. Energy Procedia, **37**, no. 0,6317-6325. doi: http://dx.doi.org/10.1016/j.egypro.2013.06.560.

Wood, A. B. 1955, A TEXTBOOK OF SOUND: THE PHYSICS OF VIBRATIONS: Bell and Sons.

Xiong, J., Y. Lin, A. Abubakar, and T. Habashy. 2013, 2.5-D forward and inverse modelling of full-waveform elastic seismic survey. Geophysical Journal International,ggt013.

Xu, T., J. A. Apps, and K. Pruess. 2004, Numerical simulation of CO2 disposal by mineral trapping in deep aquifers. Applied Geochemistry, **19**, no. 6,917-936. doi: http://dx.doi.org/10.1016/j.apgeochem.2003.11.003.

Xu, T., Y. K. Kharaka, C. Doughty, B. M. Freifeld, and T. M. Daley. 2010, Reactive transport modeling to study changes in water chemistry induced by CO_2 injection at the Frio-I Brine Pilot. Chemical Geology, **271**, no. 3,153-164. doi: 10.1016/j.chemgeo.2010.01.006.

Yam, H., and D. R. Schmitt. 2011, Co2 rock physics: A laboratory study. Canadian Well Logging Society Insite Magazine, **30**,13-16.

Yang, D., A. Malcolm, M. Fehler, and L. Huang. 2014, Time-lapse walkaway vertical seismic profile monitoring for CO_2 injection at the SACROC enhanced oil recovery field: A case study. Geophysics, **79**, no. 2,B51-B61.

Yilmaz, Ö. 2001a, Seismic data analysis. Vol. 1: Society of Exploration Geophysicists Tulsa.

Yilmaz, Ö. 2001b, Seismic data analysis. Vol. 2: Society of Exploration Geophysicists Tulsa.

Zhou, H. 2003, Multiscale traveltime tomography. GEOPHYSICS, **68**, no. 5,1639-1649. doi: doi:10.1190/1.1620638.

Zhou, H., J. Mendoza, C. Link, J. Jech, and J. McDonald. 1993, Crosswell imaging in a shallow unconsolidated reservoir. The Leading Edge, **12**, no. 1,32-36. doi: 10.1190/1.1436910.

Zhou, R. 2010, Coda-wave interferometry analysis of time-lapse VSP data for monitoring geological carbon sequestration.

Zhu, X., and G. A. McMechan. 1990, Direct estimation of the bulk modulus of the frame in a fluid-saturated elastic medium by Biot theory. In 60th Ann. Internat. Mtg., SEG Expanded Abstracts.

List of Figures

List of Tables

APPENDIX A. FRIO REAL DATA

Here we present the final processed VSP shots for the Frio case study which have been used in the analysis. Shots 2, 4 and 5 are presented in Figures A-1, A-2 and A-3, respectively. Other shots were excluded due to their low signal-to-noise ratio.

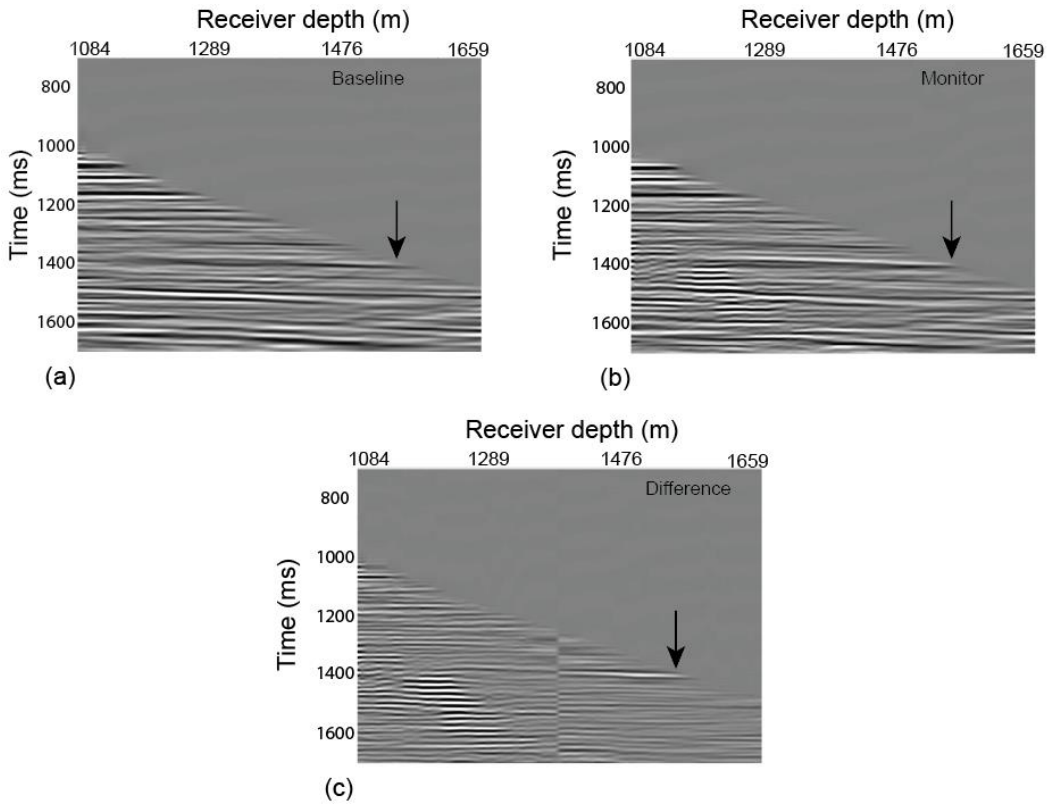

Figure A-1: VSP data for shot 2 after NMO correction for (a) baseline, (b) monitor and (c) difference record. The reservoir reflection is indicated by the arrows.

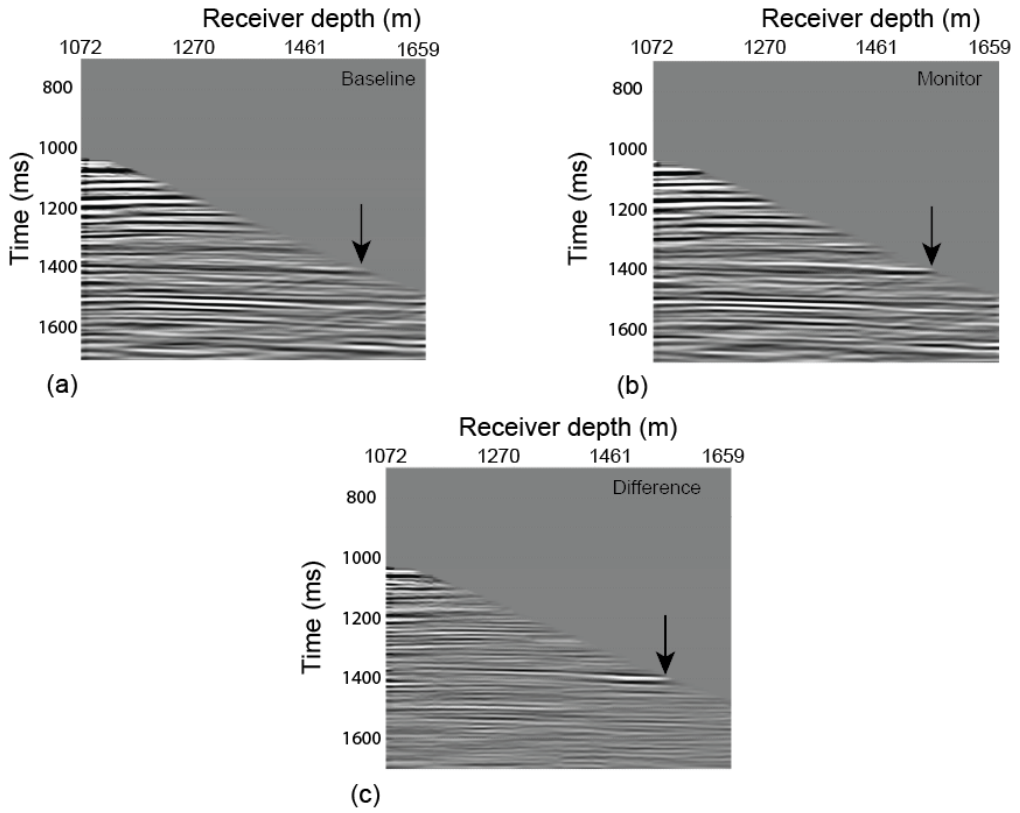

Figure A-2: VSP data for shot 4 after NMO correction for (a) baseline, (b) monitor and (c) difference record. The reservoir reflection is indicated by the arrows.

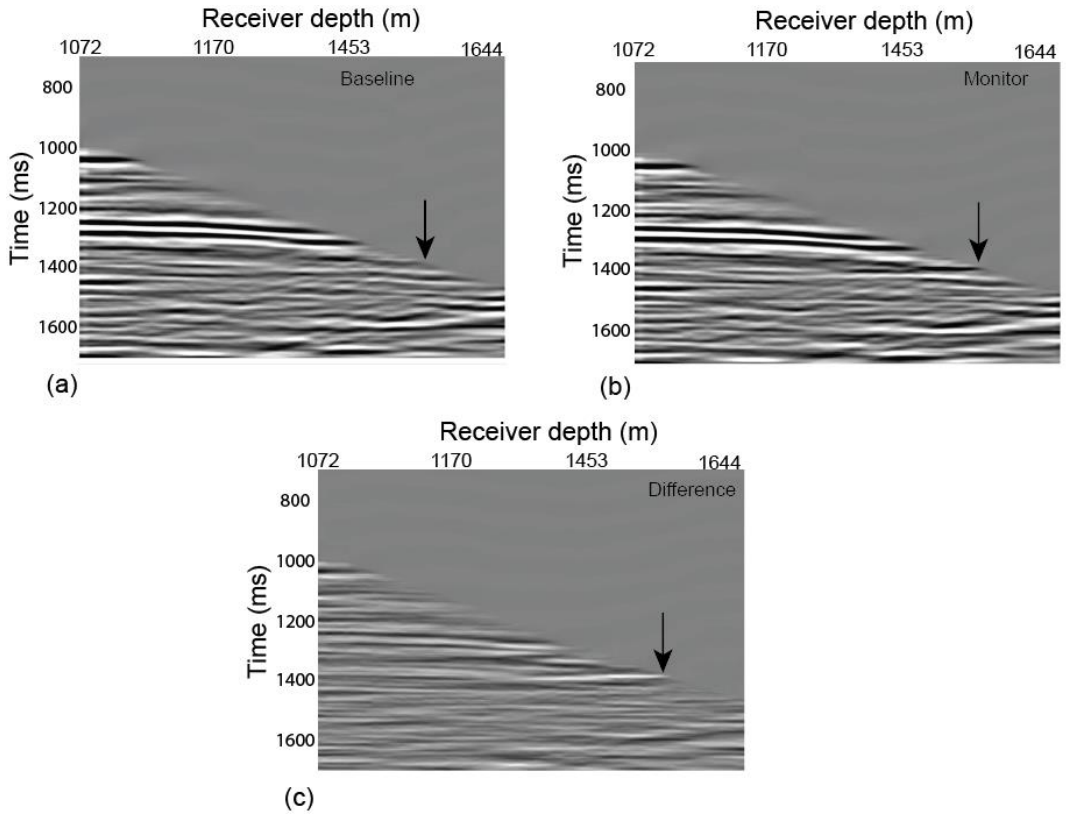

Figure A-3: VSP data for shot 5 after NMO correction for (a) baseline, (b) monitor and (c) difference record. The reservoir reflection is indicated by the arrows.

APPENDIX B. COPYRIGHT CONSENT

Permission 1

From: Carla.Flores@csiro.au [mailto:Carla.Flores@csiro.au]
Sent: Monday, 3 August 2015 12:09 PM
To: smart_88@live.com
Subject: RE: Copyright consent of ASEG Abstract-Our Ref: CP2015-143

Dear Mohammed Al-Hosni,

First of all, please note that copyright to this journals (*Exploration Geophysics* and *ASEG Extended Abstracts)* belongs to the Australian Society of Exploration Geophysicists (ASEG) (https://aseg.org.au/).

Secondly, as the publisher of these journals, we act as the clearing house for all permissions to use any parts of these journals.

Finally, on behalf of ASEG and CSIRO Publishing, I am pleased to grant you permission to include your co-authored paper (described below) as a chapter in your PhD thesis, with the appropriate acknowledgement of the source and a link back to this paper on our website, which is on: http://www.publish.csiro.au/?paper=ASEG2015ab153. As well, the copyright notice – ©ASEG 2015 – must accompany this paper in your thesis.

This permission is granted in this instance only. Any subsequent use will require a separate permission from ASEG/CSIRO Publishing.

Thank you for seeking consent.

Good luck with your dissertation.

With best wishes,

Carla

Carla Flores

Rights & Permissions

CSIRO PUBLISHING

E carla.flores@csiro.au **T** (03) 9545 8426 **F** (03) 9545 8550

Street Address: Unipark, Building 1 Level 1, 195 Wellington Road, Clayton, Victoria 3168

Postal Address: **CSIRO** PUBLISHING, Locked Bag 10, Clayton South, Victoria 3169

ABN 41 687 119 230

www.csiro.au

www.publish.csiro.au

From: Smart_oman [mailto:smart_88@live.com]

Sent: Tuesday, 28 July 2015 12:05 PM

To: PUBLISHING - General Info

Subject: Copyright consent of ASEG Abstract

Dear **associate publisher ,**

It is my understanding that CSIRO publishing is copyright holder of the following material:

Al Hosni, M., Caspari, E., Pevzner, R., Daley, T. M., & Gurevich, B. (2015). Using time-lapse VSP data to constrain velocity-saturation relations. *ASEG Extended Abstracts, 2015*(1), 1-4.

DOI: 10.1071/ASEG2015ab153

I would like to reproduce this work (Figures/caption and text) in a doctoral thesis which I am currently undertaken at Curtin University in Perth, Western Australia. I intend to integrate the article into a thesis chapter, so the formatting will be of my thesis. The current title of my thesis is “velocity-saturation relation at various scales and frequencies for CO2 sequestration”.

Once completed, the thesis will be made available in a hard-copy form in the Curtin library and in a digital form via the Australian Digital Thesis Program. The material will be provided strictly for educational purposes and on a non-commercial basis. Further information on the ADT program can be found at http://adt.caul.edu.au.

I would be most grateful for you consent to the copying and communication of the work as proposed. Full acknowledgment of the ownership of the copyright and the source of the material will be provided with the material. I would be willing to use a specific form if acknowledgment that you may require and communicate any conditions realting to its use.

If you are not the copyright owner of the material in question, I would be grateful for any information you can provide as to who is likely to hold the copyright. I look forward to hearing from you and thank you in advance for your consideration of my request.

Yours sincerely

Mohammed Al-Hosni

Mohammed Al-Hosni **| PhD candidate**
BSc, MSc
Department of Exploration Geophysics | Western Australia School of Mines
Curtin University

[**Postal Address**: GPO Box U1987, Perth, Western Australia, 6845] [Bld 613, Rm 2H15]
[**Street Address**: ARRC/CSIRO Building, H Block, Level 2, 26 Dick Perry Avenue, Kensington 6151, Western Australia]
Tel | +61 0 4023 70746
Fax | +61 8 9266 3407
Mobile | +61 40237 0746
Email | m.alhosni@student.curtin.edu.au
Web | http://student.curtin.edu.au/~15818748

Permission 2

SEG publishes journals, books, and conference papers with the primary aim of facilitating innovation in applied geophysics. Consistent with this objective, the Society provides mechanisms for those who seek to reuse or republish material from SEG publications as it ensures the viability of the SEG publications program. Any questions about permissions that are not answered on this page can be sent via e-mail to the SEG Publications Department at permissions@seg.org.

Republication rights available without explicit permission

SEG follows STM permissions guidelines, to which many publishers of scholarly works are signatories. Under this framework, it is not necessary for authors, editors, or publishers to obtain explicit written permission from SEG to republish the following amounts of content from Society publications with respect to a particular journal article, conference paper, book, or derivative work being prepared for publication and/or distribution:

- up to three figures (including tables) from a journal article or book chapter, but:
  - not more than five figures from a whole book or journal issue/edition;
  - not more than six figures from an annual journal volume; and
  - not more than three figures from an SEG article, and not more than three figures from works published in an SEG book chapter (and in total not more than thirty SEG figures for republication in a book, including a multivolume book, with different authors per chapter)
- single text extracts of fewer than 400 words from a journal article or book chapter, but
  - not more than a total of 800 words from a whole book or journal issue/edition.

There are no fees associated with permission grants for republication of SEG material in quantities consistent with the guidelines above. Authors or instructors who need documentation that SEG is extending this permission are encouraged to print this page. Those who require further documentation should contact the SEG publications director.

SEG requires that full acknowledgment of the source, including a DOI-based permalink (live in electronic versions), be used in any new work that includes SEG material. If SEG has cited a publication for which it is not the publisher, and a third party seeks permission to republish material from that publication, permission should be obtained from the original publisher.

Permission 3

USAGE PERMISSIONS

AGU grants permission for individuals to use figures, tables, and short quotes from AGU journal and books for republication in academic works and to make single copies for personal use in research, study, or teaching provided full attribution is included. There is no need to request this permission from AGU.

This permission does not extend to public posting of the PDF or HTML created by AGU for publication. AGU journal content after 1996 is now freely available 24 months after publication; AGU encourages linking to this content directly. There is no charge or additional permissions needed for any of these uses, but the material must be cited appropriately.

For information on requesting permission for commercial reuse of AGU content, please click on the "permissions" link on any journal or book home page in the **Wiley Online Library**.

http://publications.agu.org/author-resource-center/usage-permissions/#repository

Permission 4

From: Laura van Kal [mailto:lkl@eage.org]

Sent: Tuesday, 3 May 2016 3:29 PM

To: Mohammed Saif Salim Al Hosni <m.alhosni@postgrad.curtin.edu.au>

Subject: RE: EAGE permission to reproduce in a PhD thesis

Dear Mohammed Al-Hosni,

You are herby granted permission to reproduce figures/captions/text from the mentioned work as long as full acknowledgment of the ownership of the copyright and the source of the material will be provided.

Kind regards,

Laura van Kal
Publications Coordinator
European Association of Geoscientists & Engineers (EAGE)
PO Box 59
3990 DB Houten
The Netherlands

Tel: +31 889955055
Fax: +31 30 6343524
Email: lkl@eage.org

From: Mohammed Saif Salim Al Hosni [mailto:m.alhosni@postgrad.curtin.edu.au]

Sent: vrijdag 29 april 2016 10:18

To: Laura van Kal <lkl@eage.org>

Subject: EAGE permission to reproduce in a PhD thesis

Dear **publisher,**

It is my understanding that EAGE is the copyright holder of the following material:

1- Extended abstract:

Al-Hosni, M., Vialle, S., Gurevich, B. and Daley, T., 2015, November. Effect of CO_2 on Rock Properties: Frio Crosswell Case Study. In Third EAGE Workshop on Rock Physics. Doi: 10.3997/2214-4609.201414393

2- Journal paper (soon to be published – in production AID GPR12386).

Al Hosni, M., E. Caspari, R. Pevzner, T. M. Daley, and B. Gurevich, 2016, Using time-lapse VSP data to constrain velocity-saturation relations: the Frio brine pilot CO2 injection: Geophysical prospecting, (Accepted).

I would like to reproduce this work (Figures/caption and text) in a doctoral thesis which I am currently undertaken at Curtin University in Perth, Western Australia. I intend to integrate the article into a thesis chapter, so the formatting will be of my thesis. The current title of my thesis is "Analysis of the effect of CO_2 saturation on elastic properties of rocks using borehole seismic data from pilot carbon storage projects".

Once completed, the thesis will be made available in a hard-copy form in the Curtin library and in a digital form via the Australian Digital Thesis Program. The material will be provided strictly for educational purposes and on a non-commercial basis. Further information on the ADT program can be found at http://adt.caul.edu.au.

I would be most grateful for you consent to the copying and communication of the work as proposed. Full acknowledgment of the ownership of the copyright and the source of the material will be provided with the material. I would be willing to use a specific form if acknowledgment that you may require and communicate any conditions realting to its use.

If you are not the copyright owner of the material in question, I would be grateful for any information you can provide as to who is likely to hold the copyright. I look forward to hearing from you and thank you in advance for your consideration of my request.

Yours sincerely

Mohammed Al-Hosni

Mohammed Al-Hosni **| PhD candidate**

BSc, MSc

Department of Exploration Geophysics | Western Australia School of Mines

Curtin University

[**Postal Address**: GPO Box U1987, Perth, Western Australia, 6845] [Bld 613, Rm 2H15]

[**Street Address**: ARRC/CSIRO Building, H Block, Level 2, 26 Dick Perry Avenue, Kensington 6151, Western Australia]

Tel | +61 0 4023 70746

Fax | +61 8 9266 3407

Mobile | +61 40237 0746

Email | m.alhosni@student.curtin.edu.au

Web | http://student.curtin.edu.au/~15818748

Permission 5

This Agreement between Mohammed Al Hosni ("You") and Springer ("Springer") consists of your license details and the terms and conditions provided by Springer and Copyright Clearance Center.

License Number
3864591282515
License date
May 09, 2016
Licensed Content Publisher
Springer
Licensed Content Publication
Environmental Geology
Licensed Content Title
Site characterization for CO2 geologic storage and vice versa: the Frio brine pilot, Texas, USA as a case study
Licensed Content Author
Christine Doughty
Licensed Content Date
Jan 1, 2007
Licensed Content Volume Number
54
Licensed Content Issue Number
8
Type of Use
Thesis/Dissertation
Portion
Figures/tables/illustrations
Number of figures/tables/illustrations
1
Author of this Springer article
No
Order reference number
None
Original figure numbers
Figure 3
Title of your thesis / dissertation
Analysis of the effect of CO2 saturation on elastic properties of rocks using borehole seismic data from pilot carbon storage projects
Expected completion date
May 2016
Estimated size(pages)
260
Requestor Location
Mohammed Al Hosni
32/80 King geroge st victoria park
Perth, Australia 6100
Attn: Mohammed Al Hosni
Billing Type
Invoice
Billing Address
Mohammed Al Hosni
32/80 King geroge st victoria park
Perth, Australia 6100
Attn: Mohammed Al Hosni
Total
0.00 AUD
Terms and Conditions

Introduction

The publisher for this copyrighted material is Springer. By clicking "accept" in

connection with completing this licensing transaction, you agree that the following terms and conditions apply to this transaction (along with the Billing and Payment terms and conditions established by Copyright Clearance Center, Inc. ("CCC"), at the time that you opened your Rightslink account and that are available at any time at http://myaccount.copyright.com).

Limited License

With reference to your request to reuse material on which Springer controls the copyright, permission is granted for the use indicated in your enquiry under the following conditions:

- Licenses are for one-time use only with a maximum distribution equal to the number stated in your request.

- Springer material represents original material which does not carry references to other sources. If the material in question appears with a credit to another source, this permission is not valid and authorization has to be obtained from the original copyright holder.

- This permission

• is non-exclusive

• is only valid if no personal rights, trademarks, or competitive products are infringed.

• explicitly excludes the right for derivatives.

- Springer does not supply original artwork or content.

- According to the format which you have selected, the following conditions apply accordingly:

• Print and Electronic: This License include use in electronic form provided it is password protected, on intranet, or CD-Rom/DVD or E-book/E-journal. It may not be republished in electronic open access.

• Print: This License excludes use in electronic form.

• Electronic: This License only pertains to use in electronic form provided it is password protected, on intranet, or CD-Rom/DVD or E-book/E-journal. It may not be republished in electronic open access.

For any electronic use not mentioned, please contact Springer at permissions.springer@spi-global.com.

- Although Springer controls the copyright to the material and is entitled to negotiate on rights, this license is only valid subject to courtesy information to the author (address is given in the article/chapter).

- If you are an STM Signatory or your work will be published by an STM Signatory and you are requesting to reuse figures/tables/illustrations or single text extracts, permission is granted according to STM Permissions Guidelines: http://www.stm-assoc.org/permissions-guidelines/

For any electronic use not mentioned in the Guidelines, please contact Springer atpermissions.springer@spi-global.com. If you request to reuse more content than stipulated in the STM Permissions Guidelines, you will be charged a permission fee for the excess content.

Permission is valid upon payment of the fee as indicated in the licensing process. If permission is granted free of charge on this occasion, that does not prejudice any rights we might have to charge for reproduction of our copyrighted material in the future.

-If your request is for reuse in a Thesis, permission is granted free of charge under the following conditions:

This license is valid for one-time use only for the purpose of defending your thesis and with a maximum of 100 extra copies in paper. If the thesis is going to be published, permission needs to be reobtained.
- includes use in an electronic form, provided it is an author-created version of the thesis on his/her own website and his/her university's repository, including UMI (according to the definition on the Sherpa website: http://www.sherpa.ac.uk/romeo/);
- is subject to courtesy information to the co-author or corresponding author.

Geographic Rights: Scope

Licenses may be exercised anywhere in the world.

Altering/Modifying Material: Not Permitted

Figures, tables, and illustrations may be altered minimally to serve your work. You may not alter or modify text in any manner. Abbreviations, additions, deletions and/or any other alterations shall be made only with prior written authorization of the author(s).

Reservation of Rights

Springer reserves all rights not specifically granted in the combination of (i) the license details provided by you and accepted in the course of this licensing transaction and (ii) these terms and conditions and (iii) CCC's Billing and Payment terms and conditions.

License Contingent on Payment

While you may exercise the rights licensed immediately upon issuance of the license at the end of the licensing process for the transaction, provided that you have disclosed complete and accurate details of your proposed use, no license is finally effective unless and until full payment is received from you (either by Springer or by CCC) as provided in CCC's Billing and Payment terms and conditions. If full payment is not received by the date due, then any license preliminarily granted shall be deemed automatically revoked and shall be void as if never granted. Further, in the event that you breach any of these terms and conditions or any of CCC's Billing and Payment terms and conditions, the license is automatically revoked and shall be void as if never granted. Use of materials as described in a revoked license, as well as any use of the materials beyond the scope of an unrevoked license, may constitute copyright infringement and Springer reserves the right to take any and all action to protect its copyright in the materials.

Copyright Notice: Disclaimer

You must include the following copyright and permission notice in connection with any reproduction of the licensed material:
"Springer book/journal title, chapter/article title, volume, year of publication, page, name(s) of author(s), (original copyright notice as given in the publication in which the material was originally published) "With permission of Springer"
In case of use of a graph or illustration, the caption of the graph or illustration must be included, as it is indicated in the original publication.

Warranties: None

Springer makes no representations or warranties with respect to the licensed material and adopts on its own behalf the limitations and disclaimers established by CCC on its behalf in its Billing and Payment terms and conditions for this licensing transaction.

Indemnity

You hereby indemnify and agree to hold harmless Springer and CCC, and their respective officers, directors, employees and agents, from and against any and all

claims arising out of your use of the licensed material other than as specifically authorized pursuant to this license.

No Transfer of License

This license is personal to you and may not be sublicensed, assigned, or transferred by you without Springer's written permission.

No Amendment Except in Writing

This license may not be amended except in a writing signed by both parties (or, in the case of Springer, by CCC on Springer's behalf).

Objection to Contrary Terms

Springer hereby objects to any terms contained in any purchase order, acknowledgment, check endorsement or other writing prepared by you, which terms are inconsistent with these terms and conditions or CCC's Billing and Payment terms and conditions. These terms and conditions, together with CCC's Billing and Payment terms and conditions (which are incorporated herein), comprise the entire agreement between you and Springer (and CCC) concerning this licensing transaction. In the event of any conflict between your obligations established by these terms and conditions and those established by CCC's Billing and Payment terms and conditions, these terms and conditions shall control.

Jurisdiction

All disputes that may arise in connection with this present License, or the breach thereof, shall be settled exclusively by arbitration, to be held in the Federal Republic of Germany, in accordance with German law.

Other conditions:

V 12AUG2015

Questions? customercare@copyright.com or +1-855-239-3415 (toll free in the US) or +1-978-646-2777.

Permission 5

This Agreement between Mohammed Al Hosni ("You") and American Association of Petroleum Geologists ("American Association of Petroleum Geologists") consists of your order details and the terms and conditions provided by American Association of Petroleum Geologists and Copyright Clearance Center.

License number	Reference confirmation email for license number
License date	May 09, 2016
Licensed content publisher	American Association of Petroleum Geologists
Licensed content title	Environmental geosciences
Licensed content date	Jan 1, 1994
Type of use	Thesis/Dissertation
Requestor type	Academic institution
Format	Electronic
Portion	image/photo
Number of images/photos requested	1
Title or numeric reference of the portion(s)	Figure 6
Title of the article or chapter the portion is from	Measuring permanence of CO2 storage in saline formations: the Frio experiment
Editor of portion(s)	N/A
Author of portion(s)	Hovorka, Susan D Benson, Sally M Doughty, Christine Freifeld, Barry M Sakurai, Shinichi Daley, Thomas M Kharaka, Yousif K Holtz, Mark H Trautz, Robert C Nance, H Seay
Volume of serial or monograph	13
Issue, if republishing an article from a serial	2
Page range of portion	105-121
Publication date of portion	2006
Rights for	Main product
Duration of use	Life of current edition
Creation of copies for the disabled	no
With minor editing privileges	no
For distribution to	U.K. and Commonwealth (excluding Canada)

In the following language(s)	Original language of publication
With incidental promotional use	no
Lifetime unit quantity of new product	Up to 499
Made available in the following markets	education
Specified additional information	I will only use one figure in my PhD thesis
The requesting person/organization	Mohammed Al Hosni
Order reference number	None
Author/Editor	Mohammed Al Hosni
The standard identifier	Analysis of the effect of CO2 saturation on elastic properties of rocks using borehole seismic data from pilot carbon storage projects
The proposed price	0
Title	Analysis of the effect of CO2 saturation on elastic properties of rocks using borehole seismic data from pilot carbon storage projects
Publisher	Curtin University
Expected publication date	May 2016
Estimated size (pages)	260
Requestor Location	Mohammed Al Hosni 32/80 King geroge st victoria park Perth, Australia 6100 Attn: Mohammed Al Hosni
Billing Type	Invoice
Billing address	Mohammed Al Hosni 32/80 King geroge st victoria park Perth, Australia 6100 Attn: Mohammed Al Hosni
Total (may include CCC user fee)	0.00 USD
Total	0.00 USD